UNIVERSITY OF SOUTHAMPTON

Mechanisms of Subantarctic Mode Water re-emergence in a hybrid-coordinate global GCM

Hao Zuo

A thesis submitted in candidature for the degree of
Doctor of Philosophy

Faculty of Engineering, Science and Mathematics
School of Ocean & Earth Science

December 2009

UNIVERSITY OF SOUTHAMPTON

Abstract

Faculty of Engineering, Science and Mathematics
School of Ocean & Earth Science

Doctor of Philosophy

Mechanisms of Subantarctic Mode Water re-emergence in a hybrid-coordinate global GCM

by Hao Zuo

This study seeks to investigate the global circulation and re-emergence of Subantarctic Mode Water (SAMW), which is thought to be important in providing the source of nutrients to drive biological production over large proportions of the world ocean. For this purpose, the HYbrid isopycnic-cartesian Coordinate Ocean general circulation Model (HYCOM) is configured to simulate the global ocean circulation for timescales of up to centuries. After development and validation of the model, a control run of 120 years is undertaken in order to reach a near-equilibrium. A tracer is then injected into the SAMW formation regions and used to track the global circulation of SAMW for a further 150 years. The upwelling regions in which SAMW is returned to the upper-ocean mixed layer are identified, and the importance of different mechanisms of SAMW/nutrient re-emergence north of the Southern Ocean is assessed. It is found that for the global ocean north of $30°S$, entrainment driven by surface buoyancy loss and/or wind stirring is the most important mechanism for SAMW re-emergence in the model (accounting for 33% of the total SAMW upwelling). Substantial regional variation in upwelling mechanisms exists though. Regridding mixing driven by the Ekman pumping effect and shear-induced mixing dominate SAMW upwelling in the equatorial oceans. Induction at isopycnal outcrops is critical to SAMW upwelling in the high-latitude North Atlantic.

It is found that SAMW has little influence in the North Pacific when compared with the North Atlantic and the different circulation and upwelling patterns of SAMW in the Northern Hemisphere are investigated in the model. The confined penetration distance of SAMW to the North Pacific is found to be associated with the relatively lighter density levels that the SAMW core resides at in the Pacific Ocean, and the different vertical extensions of the Equatorial Under Current (EUC) and Kuroshio Current (KC) there. The mechanisms of nutrient supply into the North Atlantic Ocean in association with the SAMW has been studied in more detail with a set of perturbation experiments. Intercomparison shows that the relatively high nutrient concentrations and primary production in the upper thermocline isopycnals and surface within the Gulf Stream (GS) are likely to be associated with the imported nutrients through isopycnal transport, and diapycnal mixing need not to be invoked to explain the Gulf Stream's high nutrient concentrations. Based on the tracer experiment, a new nutrient circulation and upwelling model is proposed for the North Atlantic Ocean, which comprises four steps following the seasonal cycle of the thermocline.

Contents

List of Figures

List of Tables

Declaration of Authorship

I, *Hao Zuo*, declare that this thesis titled, '*Mechanisms of Subantarctic Mode Water re-emergence in a hybrid-coordinate global GCM*' and the work presented in it are my own. I confirm that:

- This work was done wholly or mainly while in candidature for a research degree at this University.
- Where any part of this thesis has previously been submitted for a degree or any other qualification at this University or any other institution, this has been clearly stated.
- Where I have consulted the published work of others, this is always clearly attributed.
- Where I have quoted from the work of others, the source is always given. With the exception of such quotations, this thesis is entirely my own work.
- I have acknowledged all main sources of help.
- Where the thesis is based on work done by myself jointly with others, I have made clear exactly what was done by others and what I have contributed myself.
- None of this work has been published before submission.

Signed: _____

Date: _____

Acknowledgements

I want to give my most sincere thanks to all my supervisors, Alberto N. Garabato (NOC), Adrian L. New (NOC) and Andreas Oschlies (Kiel University, Germany), whose guidances and supports during my study in the National Oceanography Centre proved to be invaluable for me.

Alex Megann from NOC helped me building up research region for HYCOM and the following model development. Vassil M. Roussenov from Liverpool University helped me tuning HYCOM and constructing bathymetry during model configuration. George Nurser from NOC helped me diagnosing spurious tracer mixing. James Ledwell from MIT supervised me for three months and helped me understanding the tracer mixing in ocean. Alan J. Wallcraft, Rainer Bleck, Shan Sun *et al*. from HYCOM community also gave me lots of help in developing the diagnostic scheme for tracer experiment in the model.

I want to give my thanks to my office mates too: Richard Myerscough, Ben Wards, Laure Grignon, Polly Hill and Sue-Ann Waston, as well as all my friends in the National Oceanography Centre: Craig Wallace, Nina Rothe, Katharine Cox, David Spofforth, Cynthia Dumousseaud, Yining Chen, Liao Chang, Xiang Zhao, Tongcheng Han, (sorry I cannot let this list go on forever) . . . , who have also helped me, not only in scientific research, but more importantly in getting me involved in the social life here in NOC. Without them it would be much harder for me to set down so quickly in U.K. in the first year. I would like to thank the basketball community in NOC (I consider myself one of the cofounder for this community) for all the happy times I had with them.

In the end I would like to thank my girl friend Yao Cheng, who always has confidence in me and has always been supporting me, even in the hardest times of my PhD.

Abbreviations

SAMW	**S**ub**A**ntarctic **M**ode **W**ater
AAIW	**Ant**A**r**ctic **I**ntermediate **W**ater
NPIW	**N**orth **P**acific **I**ntermediate **W**ater
STMW	**S**ubtropical **M**ode **W**ater
MOC	**M**eridional **O**verturning **C**irculation
AMOC	**A**tlantic **M**eridional **O**verturning **C**irculation
WBC	**W**estern **B**oundary **C**urrent
EUC	**E**quatorial **U**nder **C**urrent
SEC	**S**outh **E**quatorial **C**urrent
NAC	**N**orth **A**tlantic **C**urrent
EAC	**E**ast **A**ustralian **C**urrent
KC	**K**uroshio **C**urrent
GS	**G**ulf **S**tream
ITF	**I**ndonesian **T**hrough **F**low
ACC	**A**ntarctic **C**ircumpolar **C**urrent
WOCE	**W**orld **O**cean **C**irculation **E**xperiment
OGCM	**O**cean **G**eneral **C**irculation **M**odel
HYCOM	**HY**brid **C**oordinate **Ocean** **M**odel
MICOM	**M**iami **I**sopycnic **C**oordinate **O**cean **M**odel
KPP	**K**-**P**rofile **P**arameterization
PV	**P**otential **V**orticity
MLD	**M**ixed **L**ayer **D**epth
BLD	**B**oundary **L**ayer **D**epth

Symbols

K_T	tracer diffusivity coefficient
p_k	layer interface depth
Ri	Richardson number
R_ρ	density ratio
N^2	buoyancy frequency
h_b	boundary layer depth
h_{mix}	mixed layer depth
h_E	Ekman length scale
c_p	specific heat
f	Coriolis coefficient
Q_t	tracer upwelling flux

υ	eddy viscosity/diffusivity coefficient
ζ	relative vorticity
ρ	potential density
α	potential specific volume
ϕ	geopotential
ν	diapycnal diffusivity
$\mathbf{v}$	horizontal velocity
κ	von Karman constant
α	thermal expansion coefficient
β	haline contraction coefficient
Δ_k	specified minimum layer thickness

Dedicated to my parents, Zuo Jisheng and Liu xianyuan,
who have always been my spirit guides for the last 28 years
. . .

Chapter 1

Introduction

1.1 Physical transport of nutrients and nutrient circulation

The carbon cycle (i.e. the biogeochemical cycle by which carbon is exchanged between land, ocean and atmosphere) plays an important role in global climate in maintaining the global temperatures within certain bounds through adjusting the atmospheric concentration of carbon dioxide. By fixing carbon through photosynthesis in chlorophyll pigment and making it available for higher trophic levels, phytoplankton consequently control the organic carbon export into the ocean interior and play a important role in global carbon circulation. The population of phytoplankton affects the global climate and lowers the average temperature by reducing the volume of greenhouse gases (primarily carbon dioxide) in the atmosphere. The major environmental factors that influence the phytoplankton growth in the surface ocean are light (Marra, 1978), the circulation of dissolved inorganic carbon from the atmosphere and inorganic nutrients input mainly from below the surface boundary layer. As the exchange process at the surface can provide plenty of carbon dioxide from the overlying atmosphere, it is the supply of inorganic nutrients (*e.g.*, NO_3, NH_4, PO_4, $Si(OH)_3$ and Fe, which are constantly removed from the surface waters by growing phytoplankton) that controls the biological production in the euphotic zone, and ultimately affects global atmospheric carbon levels and climate.

The oceanic distribution of nutrients and patterns of biological production are controlled by the interplay of biogeochemical and physical processes, and external sources (*e.g.*, atmospheric decomposition and river runoff). Biological and chemical processes lead to the transformation of nutrients between inorganic and organic forms, and also between dissolved and particulate forms. Physical processes redistribute nutrients horizontally and vertically through advection and mixing (Fig. 1.1). The traditional one-dimensional view of the biological pump (Longhurst and Harrison, 1989) in the ocean can be understood as the set of processes below: (1) the phytoplankton consume the inorganic nutrients in growth and biological production is limited by either the supply of the inorganic nutrients or the light conditions (restricted to the euphotic layer); (2) the phytoplankton are consumed locally by zooplankton (grazing), organic matter is exported to the deep sea through the settling of dead cells and detritus of zooplankton (particulate fallout) and by downwelling or mixing (dissolved); (3) this export organic matter is assimilated by bacteria and is regenerated into inorganic forms (through respiration and excretion); (4) these inorganic nutrients are supplied into the surface euphotic zone again by diapycnal diffusion, upwelling and convection. A sharp vertical gradient of nutrients (nutricline) is created due to this biological pump, with minimum nutrient concentrations in the surface and maximum concentrations between 500 and 1000 m due to remineralization (Fig. 1.1).

However, the observations of diapycnal mixing rate in the upper ocean (Ledwell et al., 1998) suggest that diapycnic diffusivity itself is not large enough to support the water upwelling from the deep ocean over much of the ocean interior in such a one-dimensional view. Considering the physical mechanisms affecting the nutrient supply to the euphotic zone in a three-dimensional way, then both global-scale processes (*e.g.*, the overturning circulation) and smaller-scale processes (*e.g.*, Ekman upwelling, entrainment, diapycnal mixing, upwelling associated with eddies and fronts) can be significant (Fig. 1.2). The large-scale ocean circulation redistributes nutrients between different ocean basins (*e.g.* nutrients sink in the Southern Ocean and are transported to the Indian, Pacific and North Atlantic oceans by lateral advection) below the surface boundary layer and supports upwelling by outcropping isopycnal layers in the high-latitude regions (Williams et al., 2006). Eddy sustainment of the nutrient supply to the surface can be achieved by eddy pumping effects (McGillicuddy and Robinson, 1997; McGillicuddy et al., 1998).

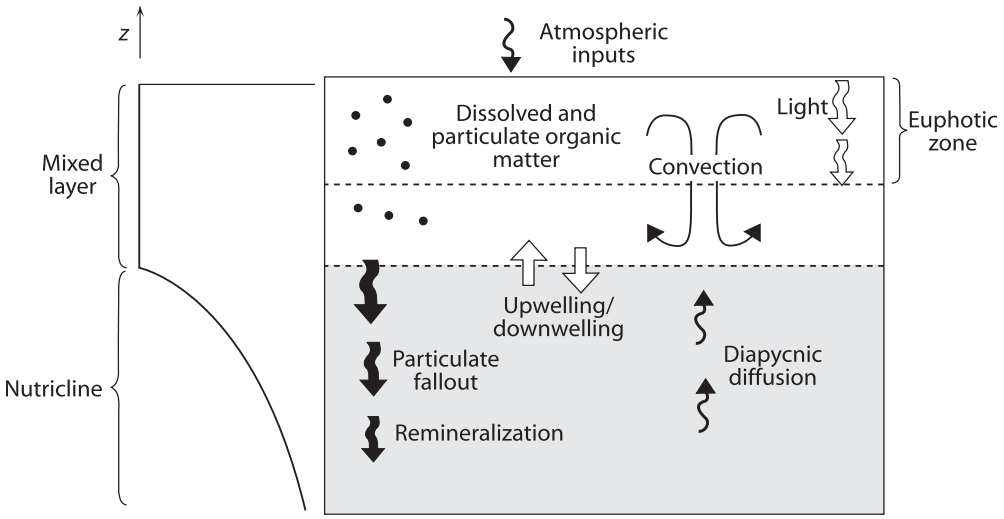

FIGURE 1.1: Schematic figure displaying a one-dimensional view of the physical processes affecting the surface biological production. Three basic processes are advection, diapycnal diffusion and convection (Williams and Follows, 2003).

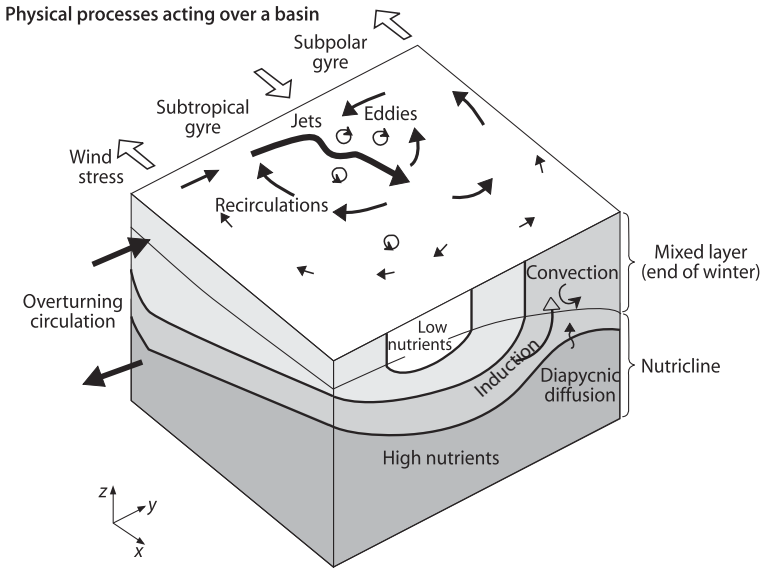

FIGURE 1.2: Schematic figure displaying a three-dimensional view of the physical processes affecting biological production, involving contributions from the overturning, gyre, eddy and frontal circulations, as well as involving induction in winter outcropping regions (after Williams and Follows (2003)).

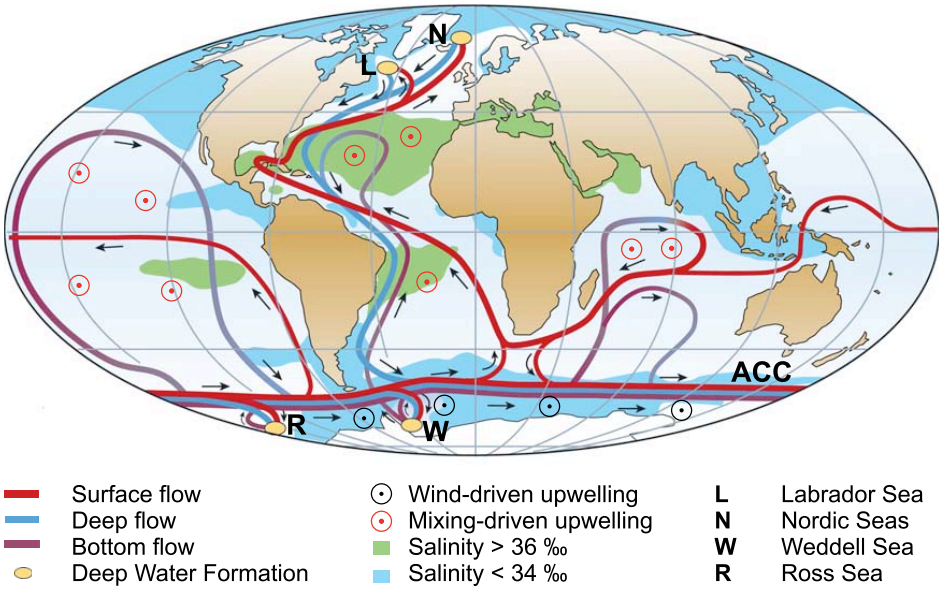

FIGURE 1.3: Strongly simplified sketch of the global overturning circulation system (Kuhlbrodt et al., 2007). In the Atlantic, warm, saline and nutrient rich waters flow northward in the subsurface all the way from the Southern Ocean into the Labrador and Nordic Seas, where they become cold, nutrient depleted and are transformed to deep waters. In contrast, there is no deepwater formation in the North Pacific, and water masses are advected from the Southern Ocean into the Pacific Ocean as surface flow and eventually return southwards at mid-depths. Inter-basin transports can be found via through the Indonesian Through Flow (ITF), Agulhas Current and by crossing the Drake Passage and following the eastward Antarctic Circumpolar Current (ACC).

Overturning circulation in individual ocean basins and the Antarctic Circumpolar Current (ACC, see reviews by Schmitz (1995) and Zenk (2001)) play a dominant role in transporting nutrients from their source region (most notably, the Southern Ocean) to the global ocean on the multi-annual to centennial time scales. A schematic illustration of the global ocean circulation from Kuhlbrodt et al. (2007) is shown in Fig. 1.3. Taking the North Atlantic as a starting point, the surface waters in the North Atlantic are nutrient depleted and are transformed to North Atlantic Deep Water (NADW) at high latitudes (*e.g.*, in Labrador Sea and Nordic Seas). This deep water mass flows southwards and gradually enriches nutrients by the accumulation of remineralized nutrients from organic fallout. Upon reaching the Southern Ocean, this nutrient-rich NADW gets mixed with AABW when flowing eastward by following the ACC. Some of NADW returns to the surface via upwelling around Antarctic and returns to the North Atlantic through the northward flux of Subantarctic Mode

Water (SAMW), Antarctic Intermediate Water (AAIW) and Antarctic Bottom Water (AABW). This upper branch of the northward nutrient circulation is primarily achieved by narrow Western Boundary Currents (WBC) and recirculating subtropical and subpolar gyres. In the North Atlantic and also in the subtropical and subpolar oceans, the intensified transport of nutrients following the WBC and its extension (Pelegrí et al., 1996) becomes important for sustaining the primary production in both subtropical and subpolar gyres. The source of the nutrients is suggested to be associated with the mode water formed in the Southern Ocean (Sarmiento et al., 2004; Williams et al., 2006; Palter and Lozier, 2008).

On smaller length scales and seasonal timescales, convection (entrainment) and upwelling driven by surface buoyancy fluxes and wind stress (Marshall and Schott, 1999; Williams and Follows, 1998) are important in transporting nutrients vertically from the thermocline into the overlying euphotic zone. Nutrients are entrained into the surface boundary layer via convection whenever the mixed layer thickens due to surface cooling and/or enhancement of the surface wind stress. Williams et al. (2000) estimated the annual convective supply of nitrate to the euphotic zone based on climatological data and suggested that convective nutrient supply due to surface buoyancy flux dominated over lateral Ekman term in the subpolar gyre of North Atlantic Ocean. A similar magnitude of the entrainment supply of nutrients has also been diagnosed from in situ observations at Bermuda of 0.1 $mol\ N\ m^{-2} yr^{-1}$ (Michaels et al., 1994). The Ekman upwelling is driven by the divergence of the Ekman volume flux over the surface (Ekman) layer induced by the the atmospheric winds. Over the tropics, the westward and equatorward surface Trade winds drive a polewards Ekman volume flux on either side of the equator and an off-shore Ekman flux along the eastern boundary of an ocean basin. Consequently, the divergence of this horizontal Ekman volume flux drives a band of upwelling along the equator (Wyrtki, 1981; Johnson et al., 2001) and in the eastern boundary regions (Smith, 1995; Hutchings et al., 1995). As for the North Atlantic circulations, the subpolar gyres are characterized by a cyclonic circulation, upwelling and an uplifted nutricline with high primary production in the surface (Behrenfeld and Falkowski, 1997; Williams and Follows, 1998). Conversely, subtropical gyres are associated an anticyclonic circulation, downwelling and a depressed nutricline with low chlorophyll concentrations in the surface (Fig. 1.4). This wind-driven Ekman volume flux is also important in transferring nutrients between mixed

layer/seasonal boundary layer and the underlying thermocline (Marshall et al., 1993; Williams, 2001).

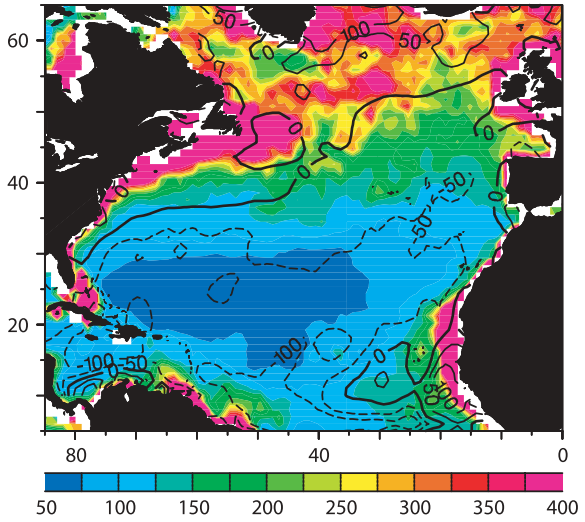

FIGURE 1.4: Annual primary production (color shaded in $mol\ C\ m^{-2}yr^{-1}$) and wind-induced (Ekman) upwelling (contours in $m\ yr^{-1}$) in the North Atlantic Ocean. The annual primary productivity is inferred from satellite observations of surface chlorophyll by Sathyendranathan et al. (1995) and the upwelling inferred from a wind-stress climatology (reproduced from (Williams and Follows, 1998)).

Jenkins (1988) showed that there is a discrepancy between the large rates of export of organic matter estimated from biogeochemical budgets in the oligotrophic North Atlantic subtropical gyre compared with the lower rates of measured productivity. A large number of studies has then been undertaken and the mesoscale eddy field (with length scales of 100 km or less in the horizontal) was proposed as the missing physical mechanism that can generate additional nutrient supply to close the nutrient budget generated by phytoplankton production (see Garcon et al. (2001); Martin (2003) and Lévy (2008) for detailed reviews). A good illustration of these studies is the eddy pumping paradigm proposed by McGillicuddy and Robinson (1997) and McGillicuddy et al. (1998), in which the time evolution of the eddy anomaly has been directly related to the vertical transport of nutrients. This eddy induced enhancement of nutrient supply to the euphotic zone can be explained by Fig. 1.5, in which the cyclonic eddies lift the thermocline and raise nutrient-rich isopycnal surfaces into the euphotic zone (assuming that the nutricline and thermocline are coincident), instead the anticyclonic eddies induce a depressed thermocline

and move nutrient-rich isopycnals out of the euphotic zone. The role of eddy pumping of nutrients in cyclonic eddies has been investigated and confirmed by several other studies that used moored instrumentations and shipboard surveys (Robinson et al., 1993; Allen et al., 1996; McGillicuddy et al., 1999). Through a coupled physical-biogeochemical numerical model, Mahadevan and Archer (2000) show a vast increase of the primary production when the model resolution is refined from 40 km to 10 km. Such an impact of the spatial resolution was also addressed by McGillicuddy et al. (2003), who found that 20% to 30% of the total vertical fluxes of nitrate can be explained by the mesoscale eddies. This increase was shown to be entirely due to a much better representation of the vertical advection of nutrients (more undulation of isopycnal surfaces and in an increased length of the frontal zone) in high-resolution models. Another view points out the possibility of vertical pumping directly at small scales, *e.g.*, within the sub-mesoscale structures (< 10 km in the horizontal) such as filaments that are produced by the mesoscale eddy-eddy interactions. By increasing the model resolution from 10 km to 2 km, Lévy (2001) found that the primary production was doubled due to enhanced variance of vertical velocity captured within filaments of strong vorticity gradients surrounding the eddies or ejected by eddies, leading to small-scale hot spots of upwellings within sub-mesoscale structures. Lapeyre and Klein (2006) also quantify the potential impact of the sub-mesoscale structures far off the eddies, which could eventually close the nutrient budgets. In addition to changing the vertical velocity structure, eddies can also alter the mixed layer thickness, change the light limitation for phytoplankton and hence alter the ecosystem. The mixed layer depths in a eddy-resolving model ($\frac{1}{9}^\circ$ resolution) are significant shallower than in a eddy-permiting model ($\frac{1}{3}^\circ$) in the mid and high latitudes (Oschlies, 2001). Despite all these advantages in a eddy-resolving model ($< \frac{1}{9}^\circ$), coarse resolution GCMs ($> \frac{1}{2}^\circ$), in planetary scale and for timescales of decades, are still the only computationally efficient way of simulating the global nutrient circulation. Results from these models (Williams et al., 2006; Sen Gupta and England, 2007) provide vital information in helping us understand the sustainment of surface primary production in respect to the nutrient supply from the deep ocean, as the lateral advection and overturning circulation still dominate over these spatial and temporal scales.

Even though the physical mechanisms that affect the nutrient transport in the ocean interior have been investigated extensively, the relative importance of

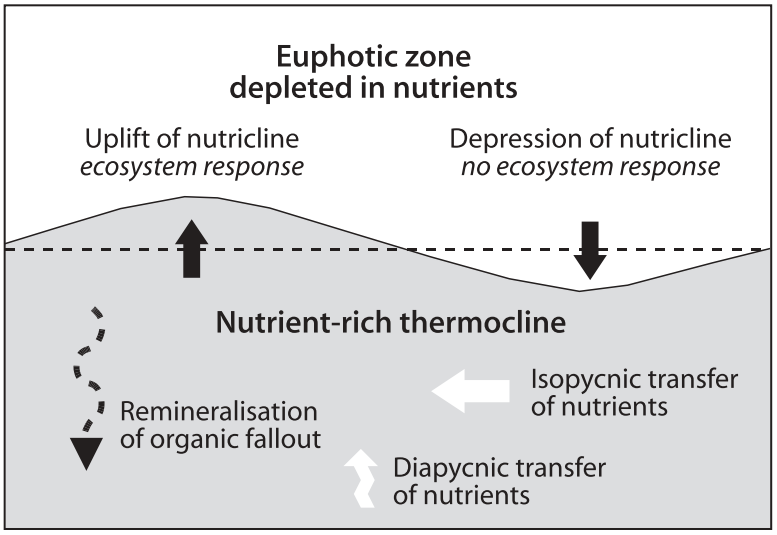

FIGURE 1.5: Schematic representation of the eddy-induced upwelling mechanism. When nutrient-rich isopycnals are raised into the euphotic zone, there is biological production. Conversely, when the nutrient-rich isopycnals are pushed into the interior, there is no biological response. In order for the transient upwelling to persist, there needs to be a process maintaining the nutrient concentrations in the thermocline, which might be achieved by remineralization of organic fallout, diapycnal mixing or a lateral influx of nutrients from the time-mean or time-varying circulations. After Williams and Follows (2003).

the mechanisms that bring up nutrients into the euphotic zone remains largely unexplained. Take the nutrient circulation in the North Atlantic Ocean for example, which has been a topic of great interest over the last several decades (Pelegrí and Csanady, 1991; Marshall et al., 1993; Jenkins and Doney, 2003; Williams et al., 2006; Palter and Lozier, 2008; Kremeur et al., 2009). It has been proposed that the primary production in both subtropical and subpolar gyres is sustained by the Gulf Stream as a "Nutrient Stream" (Pelegrí and Csanady, 1991), and the variability in the gyre's productivity may depend on variability in the upstream conditions that set the nutrient concentrations of the Gulf Stream source waters. However, the sources and the mechanisms that sustain the relatively high nutrient concentrations within the Gulf Stream are under debate, as two different hypotheses have been proposed (Jenkins and Doney, 2003; Williams et al., 2006).

Jenkins and Doney (2003) suggest that high nutrient concentration is a result of strong diapycnal mixing along the length of the Gulf Stream and proposed a

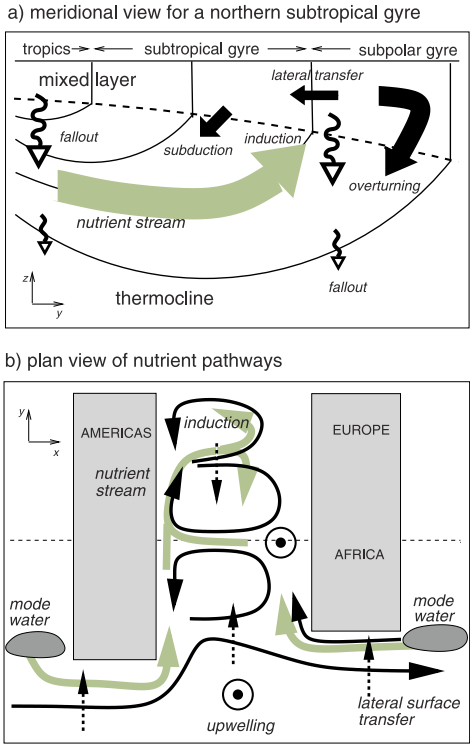

FIGURE 1.6: Schematic of nutrient circulation in the Atlantic Ocean (Williams et al., 2006): (top) meridional nutrient stream and induction of nutrients into the mixed layer; (bottom) possible nutrient pathways in the Atlantic Ocean and sources from the Southern Ocean (as SAMW).

"Nutrient Spiral" model to investigate nutrient supply to the subtropical gyre in the North Atlantic Ocean. In this conceptual model the subtropical nutrient cycle comprises a sequence of 4 steps: (1) build up of the nutrients in the thermocline due to remineralization of export production following the recirculation in the gyre; (2) recirculation and entrainment of these water masses with ample nutrients into the Gulf Stream; (3) enhanced diapycnal mixing due to strong velocity shear along the WBC, lifting a fraction of these nutrients into the surface mixed layer; and (4) nutrient consumption in the euphotic zone, followed by fallout into the thermocline. In addition, Kremeur et al. (2009) propose that the gyre-scale nutrient cycle and replenishment of the nutrients to the WBC is accomplished via the recirculation of the Sub-Tropical Mode Water (STMW) in the North Atlantic. However, the contribution of enhanced diapycnal mixing in moving up the nutrients onto light density along the western boundary current has been questioned by Palter and Lozier (2008), as a decline of nutrient concentration along the length of WBC has been observed based on hydrographic

sections from WOCE and the CLIVAR Mode Water Dynamics Experiment. Williams et al. (2006) also investigated the importance of the Gulf Stream as a conduit for nutrient transport into both the subpolar and subtropical North Atlantic through climatological diagnostics and numerical simulations via a isopycnal GCM. However, they argued that these nutrients are originated from the tropical and South Atlantic and that the main mechanism responsible for nutrient upwelling is the "induction" that results from the advection of the nutricline into the winter mixed layer following the gyre circulation (Fig. 1.6). Their results support the importance of the Gulf Stream and North Atlantic Current (NAC) in sustaining high primary production in the Subpolar gyres and suggest a relationship between these waters with high nutrient concentration water and mode water of Southern Ocean origin (Sarmiento et al., 2004). Nutrient circulation and upwelling in other ocean basins still remain largely unexplained at moment.

1.2 Subantarctic Mode Water

Winter convection north of the Subantarctic Front (SAF) of the ACC forms a deep, well-mixed layer with high oxygen concentration known as the Subantarctic Mode Water. This water mass encircles the Southern Ocean and the formation is considered to occur most strongly in the southeast Indian (Ribbe and Tomczak, 1997) and mid to southeast Pacific Oceans (McCartney, 1977, 1982), coinciding with regions of strong convection in the Subantarctic Zone (SAZ) between the Subtropical Front at about $40-45°S$ and the Subantarctic Front at about $45-55°S$ (Fig. 1.7). The warmest and most saline SAMW (15° C, 35.8 psu, 26.5 σ_θ) is formed where the SAF is furthest north, in the western Atlantic. The coldest and freshest SAMW ($4-5°$ C, 34.2 psu, 27.1 σ_θ) occurs just west of Drake Passage in the South Pacific (Hanawa and Talley, 2001).

There is a wide range in the thickness of SAMW at formation (reflected in the mixed layer depth), with the thickest layers being found in the eastern South Indian Ocean and across the South Pacific Ocean (Hanawa and Talley, 2001), and somewhat shallower layers in the South Atlantic and western Indian Ocean (Piola and Georgi, 1982). Deepening of the Mixed Layer Depth (MLD) from the western Atlantic to the eastern Pacific is not gradual but with some sudden depth increases (*e.g.*, in the east of the Kerguelen Plateau) (Karstensen and

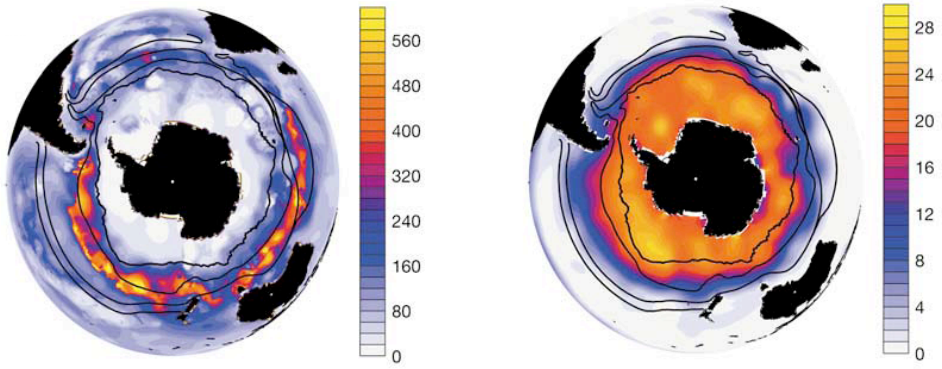

FIGURE 1.7: Maps of upper ocean (adopted from Sarmiento et al. (2004)): (left) winter mixed layer thickness averaged over the July-Spetember period; (right) annual mean nitrate concentration. The southerly line denotes the mean position of the Polar Front. In sequence from south to north, the remaining lines denote the position of the Subantarctic Front, the Southern Subtropical Front, and the Northern Subtropical Front. Nutrient data are from Levitus (1998); the mixed layer thickness data are from Kara et al. (2003)

Quadfasel, 2002). Based on Argo float data, Dong et al. (2008) investigate the spatial and temporal variability of the SAMW thickness. The deepest mixed layers ($> 400\ m$) are found from June to October in the Pacific and Indian oceans within and just north of the ACC. In contrast in the Atlantic the mixed layer depth is relatively shallow with wintertime maximum of about 150 m. As the ACC shifts southward from the Indian Ocean to the Drake Passage, the surface density for the SAMW formation regions (with MLD $> 400\ m$) increases from 26.57 σ_θ to 27.04 σ_θ, and temperature decreases from 13.3° C to 4.3° C (Fig. 1.8). Aoki et al. (2007) suggest that the distributions of this eastward deepening and local maxima of MLD are affected by near-surface geostrophic flow associated with the major bottom topographic obstacles. Their results show that southward deflection of geostrophic flow is favorable in deepening the mixed layer and northward deflection in the western Southern Pacific leads to shoaling of the mixed layer.

Deep convection imprints the SAMW with low potential vorticity and high oxygen concentration. These tracers allow the SAMW to be traced from its formation regions to the Southern Hemisphere subtropical gyres, where they renew the waters of the lower thermocline (McCartney, 1982). High-quality hydrographic and tracer section collected during World Ocean Circulation Experiment (WOCE) show that within the Indian and Pacific ocean basins, the

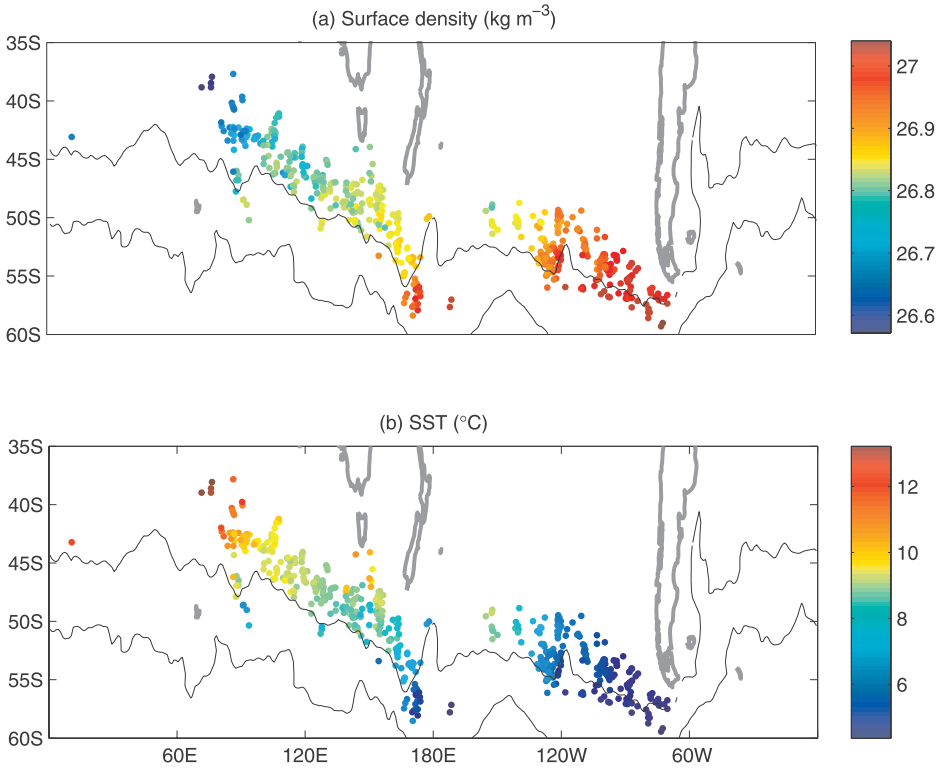

FIGURE 1.8: Spatial distribution of the near surface (a) density (σ_θ) and (b) temperature ($^\circ C$) for mixed layer depths that exceed 400 m (Dong et al., 2008). The black curves donate the southern and northern boundaries of the ACC.

lighter SAMW varieties are injected further west and are restricted to the southwest corner of the subtropical gyre, while the dense varieties entering the subtropical gyres on their eastern sides travel around the gyres and extend to lower latitudes. Following the continuous cooling, freshening and loss of buoyancy by air-sea fluxes (McCartney, 1982) along the eastward SAMW circulation path across the Indian and Pacific sections of the Southern Ocean, the densest SAMWs are transformed into AAIW in the southeast Pacific and southwest Atlantic after crossing the Drake Passage (England et al., 1993; Talley, 1996). This part of modified SAMW and AAIW enter the lower thermocline of the Atlantic subtropical gyre mainly in the southeast quadrant by following the Benguela Current (Sloyan and Rintoul, 2001a).

The northward circulation of SAMW and AAIW in the Atlantic Ocean is believed to be crucial in balancing the southward branch of North Atlantic Deep

Water (NADW) and therefore plays a important role in closing the thermocline circulation (THC) in global ocean. The eastward transport of cold fresh SAMW and AAIW across the Drake Passage has been identified as the cold return route for the THC (Rintoul, 1991). You (2002) suggested that this part of the return route is predominant in closing the thermohaline circulation in the Atlantic Ocean. Another return route has been identified as the westward transport of warmer water from south of South Africa by Agulhas Current System (Gordon, 1986), which is associated with the Indonesian Through Flow (ITF) (Schmitz, 1995) and the so called "Tasman Leakage" (Speich et al., 2001, 2002). Sloyan and Rintoul (2000, 2001a) have used a box inverse model constrained by Southern Ocean hydrographic sections together with independent estimates of diapycnal and air-sea fluxes, to examine the formation and circulation of SAMW and AAIW in the Southern Hemisphere (Fig. 1.9). The SAMW has been found to participate in an Indian-Pacific 'throughflow gyre', in which SAMW is carried from the Indian to the Pacific by the ACC, where it is modified by mixing and air-sea exchange, and ultimately returns to the Indian basin via the Indonesian passages (Gordon, 2001).

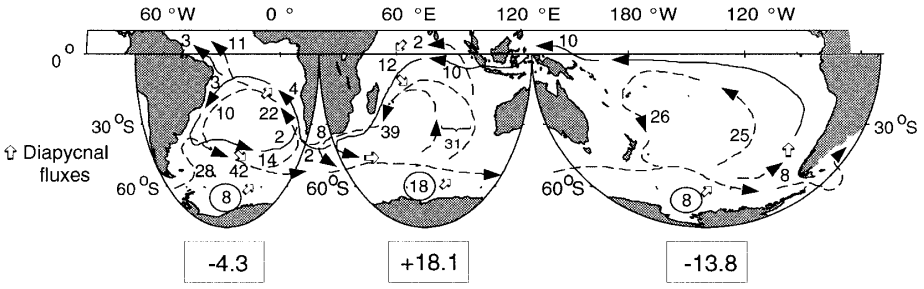

FIGURE 1.9: A summary of circulation and formation of SAMW and AAIW, from the inverse model of Sloyan and Rintoul (2001a). Numbers give volume fluxes in Sv of thermocline water (solid line, neutral density $< 26.0\ kg\ m^{-3}$) and intermediate water (SAMW/AAIW, dashed line, neutral density $26.0 < \gamma_n < 27.4\ kg\ m^{-3}$). Open arrows represent diapycnal fluxes driven by air-sea exchange and interior mixing. Circled numbers in each of the Southern Ocean sectors represent conversion of Upper Circumpolar Deep Water to SAMW and AAIW. Bold numbers below figure are the net convergence (+ve) or divergence (-ve) of SAMW/AAIW in each sector of the Southern Ocean due to meridional and diapycnal fluxes; mass is conserved by a compensating divergence in zonal transport of the ACC.

The biological pump would eventually deplete the surface and thermocline waters of nutrients if there was no return path of nutrients from deep waters. Through combining the distributions of both silicic acid and nitrate, Sarmiento

et al. (2004) tracked main nutrient return path from deep waters by upwelling in the Southern Ocean, where it has long been recognized as playing a central role in the global carbon cycle and biological productivity (Sarmiento et al., 1998; Sigman and Boyle, 2000). Their results show that it is the SAMW, which forms in the nutrient-rich SAZ (Fig. 1.7) and subsequently subducts and spreads through-out the entire Southern Hemisphere and North Atlantic Ocean, that plays a key role in determining how Southern Ocean processes affect the supply of nutrients to the world thermocline and low latitude productivity (the exception was found in the northwest corner of the Pacific Ocean and was associated with the formation of the North Pacific Intermediate Water (Talley, 1997; Yasuda et al., 2002)). This role of SAMW as the main conduit of nutrients from the Southern Ocean to the upwelling regions of the equatorial Pacific and off South America has been investigated by Toggweiler et al. (1991). Williams et al. (2006) used an isopycnal OGCM configured for the Atlantic Ocean to investigate the source for the nutrient supply into the North Atlantic Ocean and suggested that the relatively high nutrient concentration along the Gulf Stream may also have its source from the SAMW. As a result, investigating the formation of this specific mode water in the Southern Ocean, its subsurface spreading pathways in the world ocean and eventually its re-emergence in the three major ocean basins becomes crucial in understanding the nutrient return path in a three-dimensional manner and the connection between the nutrient upwelling in the Southern Ocean and the biological production in the global ocean euphotic zone.

In order to model mode waters and their variations accurately, various processes must be correctly simulated, including: frontal systems, mixed-layer processes given adequate surface forcing, eddy activity in the formation area, subduction/advection/upwelling processes and isopycnal/diapycnal mixing. At the same time, reproducing the mode water distribution, circulation and variability in numerical models will assist improvement of the numerical models themselves. Using a high-resolution numerical model, Ribbe and Tomczak (1997) examine the ventilation pathway of SAMW in the Southern Ocean ($< 12°S$) through off-line tracer experiments. Sloyan and Kamenkovich (2007) evaluate the simulation of SAMW and AAIW in eight IPCC climate models relative to the Commonwealth Scientific and Industrial Research Organization (CSIRO) Atlas of Regional Seas 2006 (CARS2006), but also confined their study to the Southern Hemisphere. A further attempt has been made by Sen Gupta and

England (2007) through a globally configured eddy-permitting model with a passive tracer released in different regions in the Southern Ocean. An important source of error in those ocean models is the inadequate representation of the subgrid-scale mixing processes in the Southern Ocean, as realistic representation of the boundary layer mixing is crucial for adequate simulation of the mixed layer (Large et al., 1994), which in turn determines the formation of the SAMW during winter. The northward transports of the SAMW and AAIW after subduction in the Southern Ocean as simulated in these models are also under question due to significant spurious mixing in the advection scheme unavoidable introduced by their z-level models (Griffies et al., 2000). Above all, the diapycnal tracer fluxes across the base of the surface boundary layer (tracer upwelling) cannot be resolved as neither an off-line tracer method nor a simplified vertical/lateral mixing scheme has been implemented in these climate models. Investigation of SAMW re-emergence pattern and the corresponding driving mechanisms through OGCM simulation have not yet been addressed.

In order to study the formation, subduction and re-emergence of the SAMW in the world ocean, a globally configured GCM with adequate representation of boundary layer mixing as well as diapycnal/isopycnal diffusion in the interior ocean is required. The HYbrid Coordinate system Ocean circulation Model (HYCOM) (Bleck, 2002) with a K-Profile Parameterization (KPP) mixing scheme (Large et al., 1994) is arguably an optimal choice of model for tracking the circulation and upwelling of a specific water mass in the global ocean, due to the following reasons: (1) the isopycnic representation of this model in the ocean interior is optimally suited to represent water mass transport along isopycnal surfaces and the induction process at the outcrops of isopycnal layers; (2) tracer mixing and stirring are handled more concisely due to the isopycnic nature of this model, consequently it reduces the spurious mixing that occurs in all z-level models due to the horizontal transport of tracer; (3) the advanced vertical mixing scheme (KPP) can be decomposed into different mixing types according to their driving mechanisms and can be applied for the whole water column, hence, both the surface boundary mixing (for the formation of SAMW) and diapycnal fluxes across the base of the mixed layer (re-emergence of the SAMW) can be resolved properly in this model; (4) the possibility of repeating the tracer experiments within the range of a set of plausible vertical mixing schemes implemented in this model allow us to assess the SAMW upwelling with respect to different vertical diffusivity profiles.

1.3 HYbrid Coordinate Ocean Model

Studies of ocean circulation by means of Ocean General Circulation Models (OGCMs) have proliferated in the last several decades, fueled both by the recognition of an increasing realism of the model solutions and by the increases in computing power (see McWilliams (1996) for a review). Currently, there are three main vertical coordinates in use. Most traditional OGCMs are based on a Bryan-Cox type model (Bryan, 1969; Cox, 1984) which is constructed such that coordinate surfaces coincide with geopotential levels and is named as a Cartesian z-coordinates model. This kind of model is convenient to solve the thermohaline circulation and small-scale convection, however, it can not represent topographically controlled flows well (Roberts et al., 1996) due to their deficient staircase representation of topography. Isopycnic coordinate systems were created (Bleck et al., 1992; Oberhuber, 1993) in order to simulate the epipycnal (along isopycnal) flow of fluid. Such a representation is optimally suited to represent water mass transports that occur along isopycnal surfaces, a traditional concept in oceanography that has ample support from observations. Another important vertical coordinate system developed is the so called terrain-following coordinate system (Haidvogel et al., 1991), in which the model coordinate smoothly conforms to the irregular ocean bottom and is most suitable when topographic influence plays the key role in the research. Among these three, isopycnal layers are best in the deep stratified ocean, z-levels (constant fixed depths) are best in the surface mixed layer, and terrain-following coordinates are often the best choice in shallow coastal regions. However, no single vertical coordinate–depth, density, or terrain-following–can by itself be optimal everywhere in the ocean, as demonstrated by model comparison exercises (Willebrand et al., 2001). Hence, many developers have been motivated to pursue research into hybrid approaches, which leads to the creation of HYbrid Coordinate Ocean Model (HYCOM) (Halliwell, 1998; Bleck, 2002).

HYCOM is a primitive equation ocean general circulation model that evolved from the Miami Isopycnic-Coordinate Ocean Model (MICOM) and has been described by Bleck (2002). As one of the widely used ocean models, MICOM has been validated (Chassignet, 1996; Roberts et al., 1996) and used in numerous ocean climate studies (New et al., 1995; Halliwell, 1998; Paiva et al., 2000). However, MICOM provides inadequate vertical resolution in regions with weak stratication (*e.g.*, the surface mixed layer) and is suboptimal in the

coastal ocean and shallow seas where topographic changes are large and bottom boundary layer dynamics is usually important. The HYCOM's hybrid coordinate algorithm was developed to overcome these limitations of MICOM by placing different vertical coordinates types in those regions where they are quasi-optimum, and thus permitting the use of more sophisticated turbulence closures. HYCOM has become one of the primary ocean models in use today, having been used in both basin scale studies (Chassignet et al., 2003; Halliwell, 2004; Shaji et al., 2005; Kara et al., 2008) and in the shelf sea research (Winther and Evensen, 2006). Development of the data assimilative system as well as ocean prediction through HYCOM have also been discussed by Chassignet et al. (2006, 2007).

Vertical coordinates in HYCOM remain isopycnic in the open, stratified ocean. However, they smoothly transition to z coordinates in the weakly-stratified upper-ocean mixed layer, to terrain-following sigma coordinate in shallow water regions, and back to level coordinates in very shallow water. Like MICOM, HYCOM contains five prognostic equations, including two horizontal velocity components equations (Eq. 1.1); a mass continuity equation (Eq. 1.2) and two other conservation equations (Eq. 1.3) for a pair of thermodynamic variables (chosen from density, salinity and temperature). Following Bleck et al. (1992), the model equations are listed below

$$\frac{\partial \mathbf{v}}{\partial t_s} + \nabla_s \frac{\mathbf{v}^2}{2} + (\zeta + f)\mathbf{k} \times \mathbf{v} + (\dot{s}\frac{\partial p}{\partial s})\frac{\partial \mathbf{v}}{\partial p} + \nabla_s M - p\nabla_s \alpha = -g\frac{\partial \tau}{\partial p} + (\frac{\partial p}{\partial s})^{-1}\nabla_s \cdot (\upsilon \frac{\partial p}{\partial s}\nabla_s \mathbf{v}), \tag{1.1}$$

$$\frac{\partial}{\partial t_s}(\frac{\partial p}{\partial s}) + \nabla_s \cdot (\mathbf{v}\frac{\partial p}{\partial s}) + \frac{\partial}{\partial s}(\dot{s}\frac{\partial p}{\partial s}) = 0, \tag{1.2}$$

$$\frac{\partial}{\partial t_s}(\frac{\partial p}{\partial s}\theta) + \nabla_s \cdot (\mathbf{v}\frac{\partial p}{\partial s}\theta) + \frac{\partial}{\partial s}(\dot{s}\frac{\partial p}{\partial s}\theta) = \nabla_s \cdot (\nu \frac{\partial p}{\partial s}\nabla_s \theta) + H_\theta \tag{1.3}$$

Where s is the vertical coordinate of HYCOM, $\dot{s}$ is the time derivative of s, $\mathbf{v} = (u, v)$ is the horizontal velocity vector, p is the pressure, θ represents any one of the model's thermodynamic variables, $\alpha = \rho_{\text{pot}}^{-1}$ is the potential specific volume, $\zeta \equiv \frac{\partial v}{\partial x_s} - \frac{\partial u}{\partial y_s}$ is the relative vorticity, $M \equiv gz + p\alpha$ is the Montgomery potential, $gz \equiv \phi$ is the geopotential, f is the Coriolis parameter, $\mathbf{k}$ is the vertical unit vector, υ is the eddy viscosity, ν is the diffusivity coefficient, and τ

is the wind and bottom drag induced shear stress vector. H_θ represents the sum of diabatic source terms, including diapycnal mixing, acting on θ. Subscripts indicate which variable is held constant during partial differentiation.

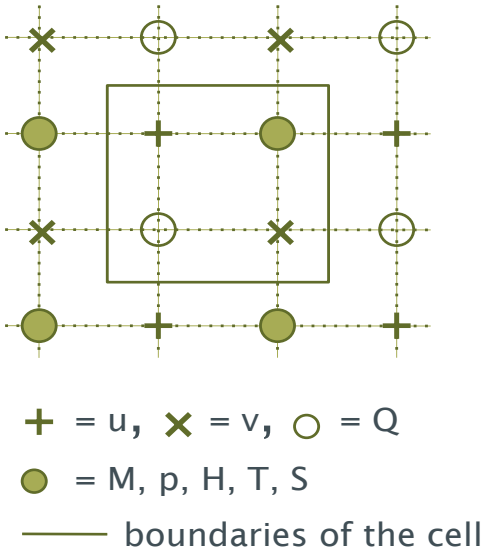

FIGURE 1.10: C-grid horizontal coordinate system used in HYCOM. u and v are velocity, Q is vorticity, p for pressure.

The above prognostic equations are complemented by three diagnostic equations, including the hydrostatic equation ($\frac{\partial M}{\partial \alpha} = p$); the equation of state and an equation prescribing the vertical mass flux $\dot{s}\frac{\partial p}{\partial s}$ through an s surface. The last equation controls both spacing and movement of layer interfaces and thus is the algorithm for the remapping scheme, or "grid generator", which will be described in detail in Chapter 3. All prognostic equations are time-integrated using the split-explicit treatment of barotropic and baroclinic modes developed by Bleck and Smith (1990). The horizontal mass fluxes are computed using the Flux Corrected Transport (FCT) scheme (Zalesak, 1979) while horizontal tracer transport is treated in flux form and handled by a variant of the MP-DATA scheme (Drange and Bleck, 1997). All HYCOM variables are stored on Arakawa C-grid, with momentum components carried at u and v grid points and thermodynamical variables plus tracers stored at pressure (p) grid points (Fig. 1.10).

The parameterization of vertical mixing is a limiting factor in all types of ocean models. OGCM studies are typically conducted using one set of parameterizations to govern vertical mixing, including the strong mixing in the near surface

TABLE 1.1: Vertical mixing scheme embedded in HYCOM (Halliwell, 2004).

Mixing model	Description	Supplemental interior diapycnal mixing algorithms
KPP (K-Profile Parameterization)	Nonlocal differential model	Not required
GISS (NASA Goddard Institute for Space Studies)	local differential Reynolds stress model; level 2 turbulence closure	Not required
MY(Mellor-Yamada)	Local differential Reynolds stress model; level 2.5 turbulence closure	Not required
PWP(Price-Weller-Pinkel)	Slab mixed layer; static instability; bulk and gradient Richardson number instabilities	Explicit (MICOM-like) for hybrid coordinates
KTA(Full Kraus-Turner for hybrid coordinates)	Slab model, vertically integrated TKE balance	1) Explicit (MICOM-like) for hybrid coordinates; 2) Implicit (KPP-like) for hybrid coordinates.
KTB (Simplified Kraus-Turner for hybrid coordinates)	Slab model, vertically integrated TKE balance	1) Explicit (MICOM-like) for hybrid coordinates; 2) Implicit (KPP-like) for hybrid coordinates.
KTC [Kraus-Turner for isopycnic coordinates (MICOM model)]	Slab model, vertically integrated TKE balance (from MICOM 2.8)	Explicit for isopycnic coordinates (from MICOM 2.8)

mixed layer, the relatively weak mixing in the ocean interior, and in some cases the enhanced mixing of the bottom boundary layer. However, no single vertical mixing model exists that is clearly the optimum choice to use in all ocean models. Therefore, HYCOM is equipped with several vertical mixing turbulence closure schemes with the purpose of testing model behaviors subject to different vertical mixing models implemented. The full set of vertical mixing options embedded in HYCOM is summarized in Table. 1.1. There are five primary vertical mixing algorithms, of which three are "continuous" vertical diffusion models and two are bulk (slab) models. The three differential models are the nonlocal K-Profile-Parameterization (KPP; Large et al. (1994)), the NASA Goddard Institute for Space Studies level 2 turbulence closure (GISS;

Canuto et al. (2001, 2002)), and the MellorYamada level 2.5 turbulence closure (MY; Mellor and Yamada (1982)). These models govern vertical mixing throughout the water column. The bulk models include the dynamical instability model of Price et al. (1986) (PWP) and three versions of the Kraus-Turner model (Kraus and Turner, 1967) (KT).

The full suite of model capabilities is presented in the HYCOM Users Manual Bleck et al. (2002). This manual, along with other model information, publications, and ongoing research summaries, is available on the HYCOM website.

SUMMARY

The photosynthesis process by phytoplankton in the surface water consumes nutrients and exports them into the thermocline and deep waters. This biological pump would eventually deplete the surface and thermocline waters of nutrients if there was no return path of nutrients from the deep waters. The Southern Ocean has long been recognized as playing a central role in the global carbon cycle and biological productivity, and in the response of these to climate change. Sarmiento et al. (2004) identified that it is specifically the SAMW that formed in the SAZ that is most crucial in determining how Southern Ocean processes affect the supply of nutrients to the main thermocline and low latitude productivity. Attempts have been made for simulating the subduction and spreading of this nutrient-rich mode water through climate models, however the previous simulations either only include the Southern Hemisphere or are implemented with simplified vertical/lateral mixing schemes. The upwelling locations and the driving mechanisms that are responsible for the re-emergence of SAMW in global ocean have never been investigated before in a global model context. Therefore, a hybrid coordinate system ocean general circulation model (HYCOM) with an advanced vertical mixing scheme (KPP) has been chosen for the purpose of addressing the return path of nutrients in a three-dimensional way. In this thesis, I will investigate the relationship between nutrient upwelling in the Southern Ocean and the sustainment of biological production in the global euphotic zone, by studying the formation, subduction, spreading and re-emergence of the SAMW in the global ocean over multi-annual to centennial time scales.

Chapter 2

Configuration of Numerical Model

All numerical models are subject to a considerable number of model settings: details of model topography, climatological surface forcing, boundary conditions or mixing parameterizations can all have a significant impact on the behavior of the modelled ocean circulation. In the remainder of this section, the principal elements of our 3° HYCOM configuration are described, as are the sensitivity experiments which are undertaken for almost all the important model choices.

2.1 Model domain and bathymetry

2.1.1 Horizontal grid

The domain is spanned by a mesh consisting of 120 points in the E-W direction and 50 points in the N-S direction with a horizontal grid of resolution 3° in longitude and 3° in latitude. This covers a horizontal domain from $78°S$ to $69°N$, and $0°W$ to $360°E$ with a uniform projection. The research domain includes the whole Southern Ocean and accounts at least partially for the high latitudes of the northern North Atlantic (including the Greenland-Iceland-Scotland ridge). The Mediterranean Sea is preserved in this configuration but without a channel connecting to the Atlantic Ocean, because it has a narrow

(15 km wide, subgrid-scale) outflow through the Gibraltar Straits. Mediterranean overflow water in the Atlantic is present in the initial conditions and preserved by boundary relaxation. The resolution of the longitudinal axis of the grid box varies from 333.5 km at the equator to 69.3 km at $78°S$, while the length of the latitudinal axis is always 333.5 km. Two closed walls are placed in the northern and southern boundaries and there are no fluxes crossing them.

2.1.2 Bathymetry

The bathymetry for the model was derived by A. Megann from the 5 min ETOPO5 database. A simple interpolation algorithm was used by taking the median of all bathymetric data within each grid box as the bathymetry value for the corresponding model grid, with no additional smoothing applied. The minimum depth of the ocean was set to 10 m. However, we found that there are some abnormal northward bottom flows transporting water from the Antarctic region into the Pacific and Indian Ocean basins through some sills (the deepest points across an ocean ridge) and straits in several key regions. This suggests that the depths of these critical points (*e.g.*, the connection between the Ross Sea and the South Pacific) are unsatisfactorily described in the model (minimum 3° width due to the model's coarse resolution) and certain subjective modifications have been applied in three sills by setting the bathymetry with constant values of 3200 m in the middle of the Indian Ocean, 3000 m south of Australia and 3400 m in the Southern Pacific (Fig. 2.1). This made the sills shallower by approximately $200 \sim 500$ m.

It is quite clear that after adding adjustments to the topography of several key sill places, the deep cell in global meridional overturning associated with the AABW and NADW has been reduced from 45 Sv to 30 Sv (Fig. 2.2). At the same time the abnormal northward transport of the AABW has been stopped (not shown here), suggesting some significant improvements in the realism of the HYCOM results.

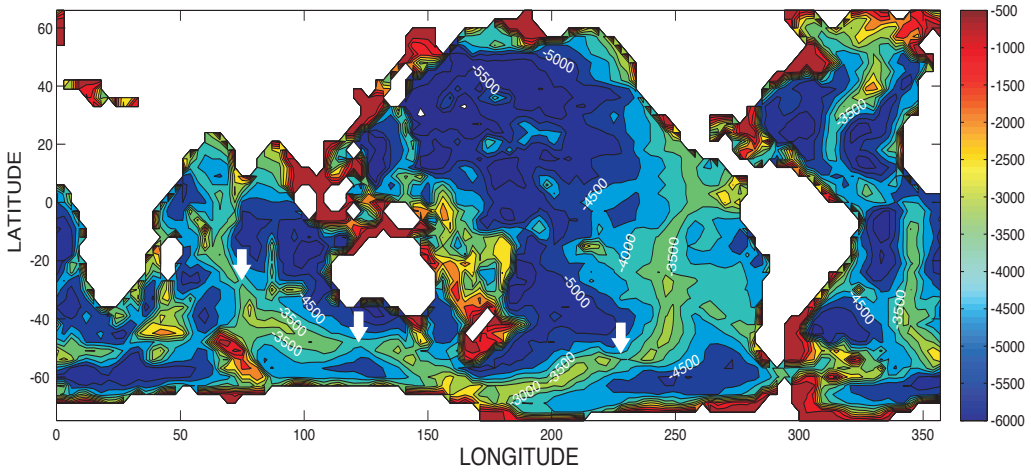

FIGURE 2.1: Domain and topography for the 3° global HYCOM, bathymetry data derived from Etopo5 database by averaging algorithm. Modifications have been applied in bathymetry in three critical sills (marked by the white arrows).

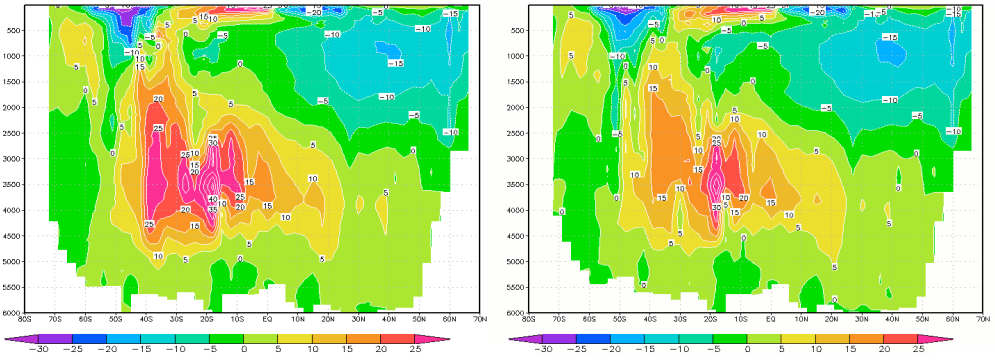

FIGURE 2.2: HYCOM output global overturning stream functions with (left) Etopo5 topography and (right) topography with adjusted sill depths. Volume transports were computed for 50 db pressure layers and zonally summed over longitude, transports were then integrated from the ocean bottom to the top to produce a stream function. No southern boundary relaxation has been applied in either run and no AABW is being generated.

2.2 Model architecture and initialization

2.2.1 Vertical coordinate system

Early experiments with HYCOM show that using the ocean surface as reference pressure for the potential density (σ_0) would lead to non-monotonic conditions in the deep Atlantic, so that the NADW has a higher σ_0 than AABW, even though the in-situ density of AABW is higher than that of NADW and therefore lies underneath the latter. Configured as a global model, we are especially interested in using HYCOM to investigate the role of the Southern Ocean originated SAMW in transporting nutrient to the high latitude North Atlantic (Sarmiento et al., 2004). Therefore, a reference pressure of 2000 dbar (≈ 2000 m) has been chosen for our configuration and the target densities of all coordinate layers are referenced to potential density σ_2. Such configurations make sure that most of the oceans (especially the Atlantic) is monotonic. The model comprises a total of 16 isopycnal layers of constant potential density (except for the surface fixed-coordinate regions), varying from 30.90 to 37.23 (See Appendix A). These values are chosen to represent water masses and thermocline structure as closely and evenly as possible.

2.2.2 Model initialization

The model has been initialized from a state of rest using the Levitus climatology dataset (Levitus, 1982) for the month of December. To do this, the Levitus native fixed z-levels climatology is first interpolated to the HYCOM horizontal grid by using a simple piecewise bilinear interpolation algorithm, then vertically mapped from z-levels to HYCOM isopycnal layers by converting one stair step set of profiles (in this case between z-levels) into another with prescribed density steps. All vertical instabilities have been removed in this interpolation process by repartitioning the temperature and salinity profiles between neighbouring pairs of levels.

The converted Levitus climatology has been used for three different purposes during the HYCOM simulations, including initializing HYCOM (Fig. 2.3), applying surface relaxation to augment surface atmospheric forcing, and applying lateral boundary nudging for the missing Mediterranean Water and exchange

processes across the northern Atlantic boundaries and at the southern boundary (a relaxation mask has been defined to specify where and how much relaxation to apply).

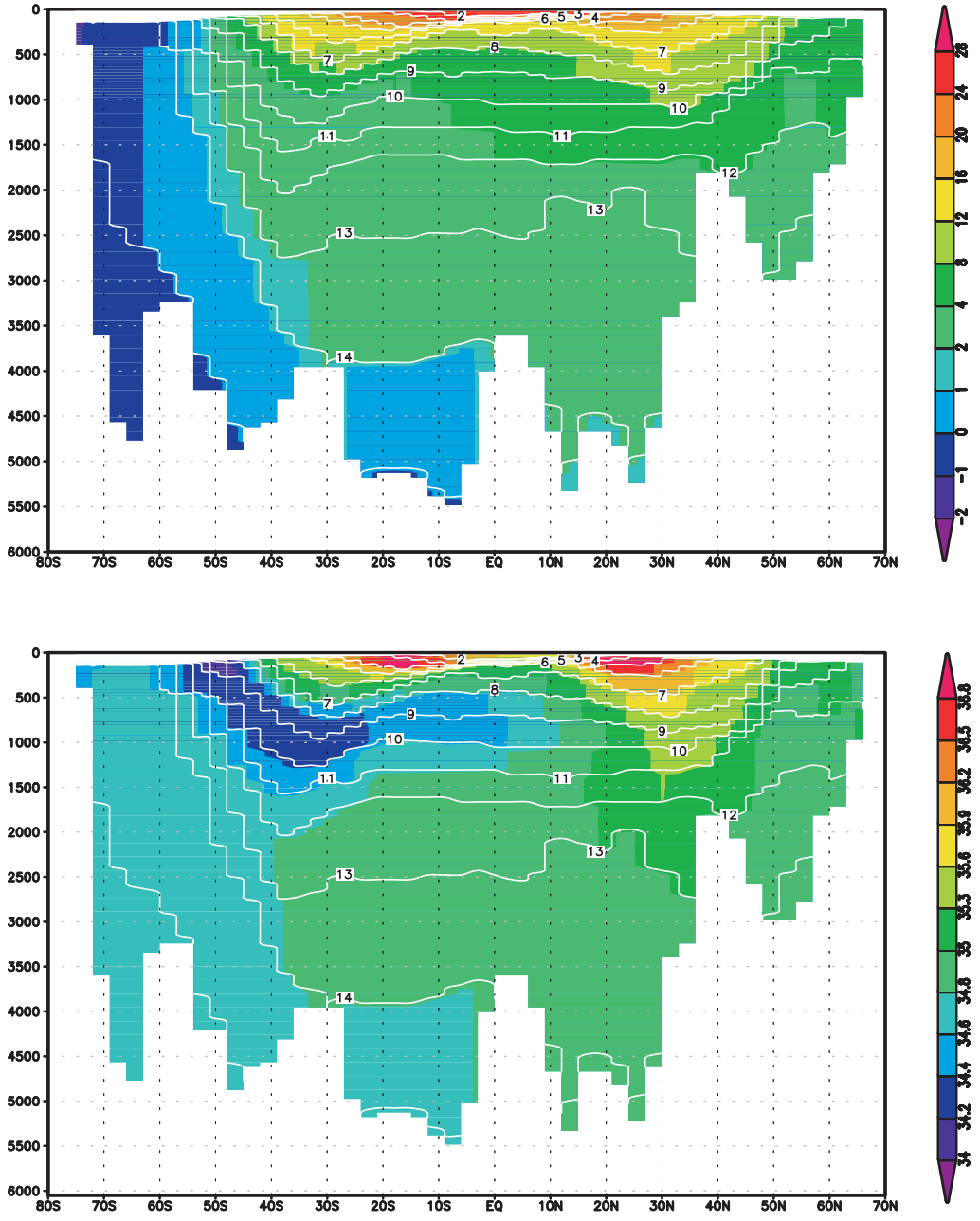

FIGURE 2.3: Meridional section of HYCOM initial (top) temperature and (bottom) salinity in the Atlantic Ocean following longitude 30°W (interpolated from Levitus dataset). Also shown are the layer interface depths in white contours with number representing overlaying layer.

2.3 Surface climatology

Two climatological data sets have been tested in an intercomparison: National Oceanography Centre (NOC) climatology and National Centers for Environmental Prediction (NCEP) climatology. The NOC climatology was generated by applying empirical flux formulae to the surface meteorological dataset of International Comprehensive Ocean-Atmosphere Dataset (ICOADS) covering the period of 1980 - 1993, merged with additional metadata from the WMO47 list of ships, and with additional bias corrections applied. Interest in including NCEP climatology as well originates from the poor data quality of the NOC climatology in the Southern Ocean region. The linearly extrapolated NOC air temperature close to Antarctic is too warm to form any ice even in the southern winter.

All NOC and NCEP forcing fields have been interpolated to exactly the same resolution ($3^\circ \times 3^\circ$) and grid locations (P points for HYCOM C-grid, see Fig. 1.10) to facilitate intercomparison. However, because the NOC climatology does not include any data fields south of $60^\circ S$, linear extrapolation from north of $60^\circ S$ has been applied to generate the atmospheric forcing fields in the missing region. A summary of climatological components in HYCOM sensitivity experiments can be found in Table 2.1. All other monthly-mean climatologies (sea surface temperature, sea surface salinity, precipitation, evaporation and air humidity above sea surface) are taken from the NCEP data set and remain the same in all sensitivity experiments.

Table 2.1: Summary of climatological components in HYCOM sensitivity experiments.

Experiments	Wind	Air temperature	Surface radiation
Case 1	NOC	NOC	NOC
Case 2	NOC	NCEP	NOC
Case 3	NOC	NCEP	NCEP
Case 4	NCEP	NCEP	NCEP

2.3.1 Air temperature

Due to the lack of observations south of $60°S$, the NOC air temperature is extrapolated there. In Fig. 2.4 we can see that the NCEP air temperature is much colder than that in the NOC climatology in the southern polar regions (minimum temperatures are $-1.8°C$ and $-40°C$ for the NOC and NCEP climatologies, respectively) because the NCEP climatology includes the dataset from the Antarctic region.

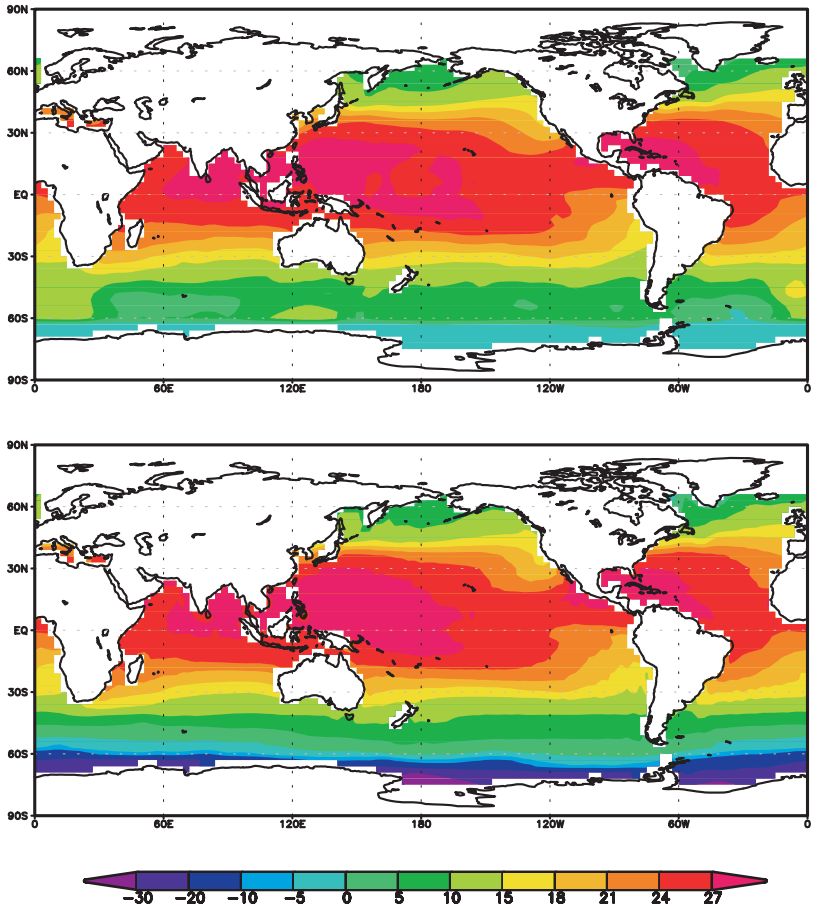

FIGURE 2.4: September surface air temperature in (top) NOC climatology and (bottom) NCEP climatology.

Sensitivity experiments have been carried out with different surface air temperature inputs (Cases 1 and 2 in Table 2.1). Model-generated sea surface heat flux and Mixed Layer Depth (MLD) in the Southern Ocean during the southern winter are unrealistic and incorrect when compared with observed values (Aoki et al., 2007; Dong et al., 2008), if NOC air temperature is applied as a surface

forcing in HYCOM. Fig. 2.5 shows that almost no deep mixing (except in the Weddell Sea) happens in the Southern Ocean during winter, indicating that there is not enough deep water formation. The reason for this phenomenon is explained by Fig. 2.6, as it shows that sea surface heat flux is almost always positive (heat flux from overlaying atmosphere to ocean) during the whole seasonal cycle. Therefore surface water will not sink and can not generate dense deep water even during the southern winter as they are not cold enough. A more realistic image has been achieved when NOC air temperature is replaced by NCEP air temperature (Figs. 2.5 and 2.6). The MLD is much deeper (1000 $\sim$ 2000 m) under the influence of NCEP cold air temperatures near the Antarctic continent, and strong heat loss occurs in this region due to the temperature difference between the sea surface and overlying air during the southern winter at rates of -200 to -300 Wm^{-2}.

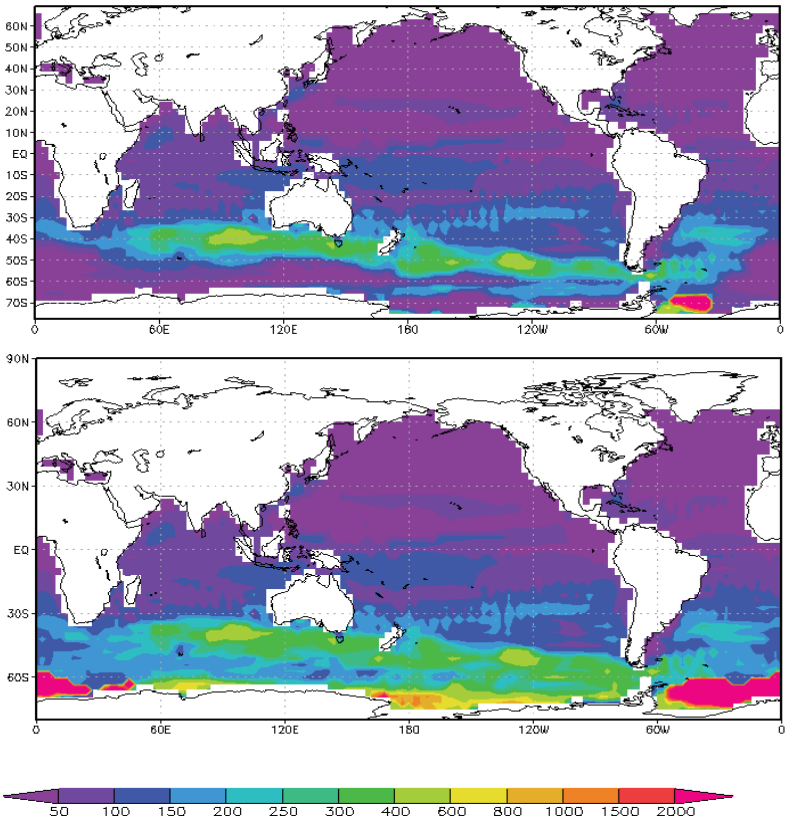

FIGURE 2.5: Model mixed layer depth (m) in September with (top) NOC (Case 1) and (bottom) NCEP air temperature (Case 2).

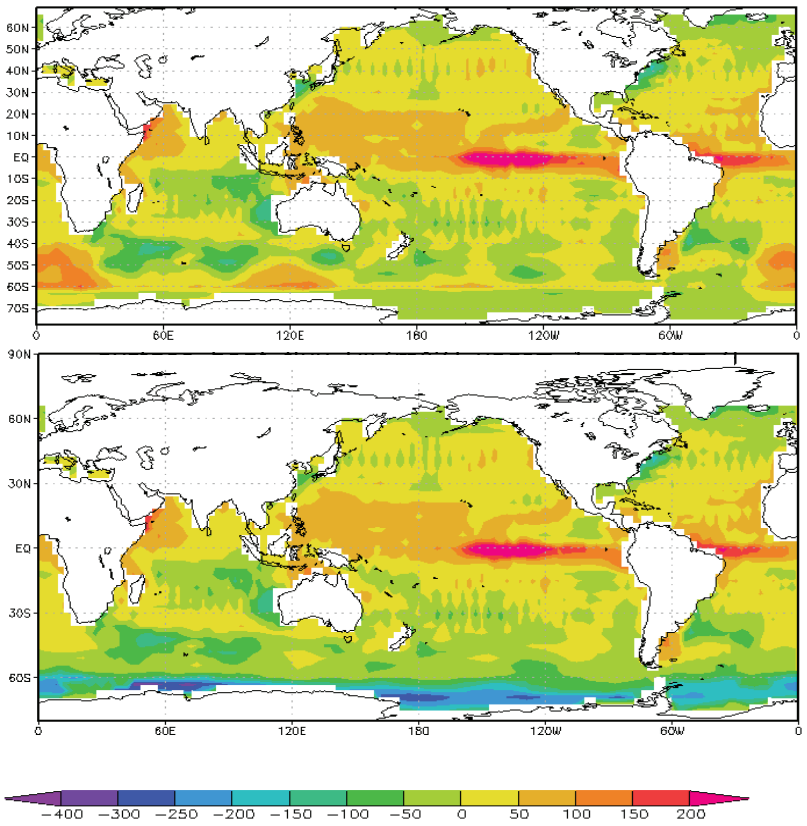

FIGURE 2.6: Model net surface heat fluxes (Wm^{-2}) in September with (top) NOC (Case 1) and (bottom) NCEP air temperature (Case 2), positive value means fluxes from atmosphere to ocean.

2.3.2 Net radiation flux

The shortwave radiations from the NOC and NCEP climatologies have similar spatial distribution patterns except close to the Antarctic continent. However, the extrapolated sea surface net radiation in NOC climatology is above zero even in the southern winter and ranges from 0 to 248 Wm^{-2}, while the NCEP net radiation varies between -49 to 205 Wm^{-2} (refer to monthly mean data in September). Such differences are mainly generated by the longwave radiation and may cause significant differences to winter radiation fluxes in the Southern Ocean (Fig. 2.7).

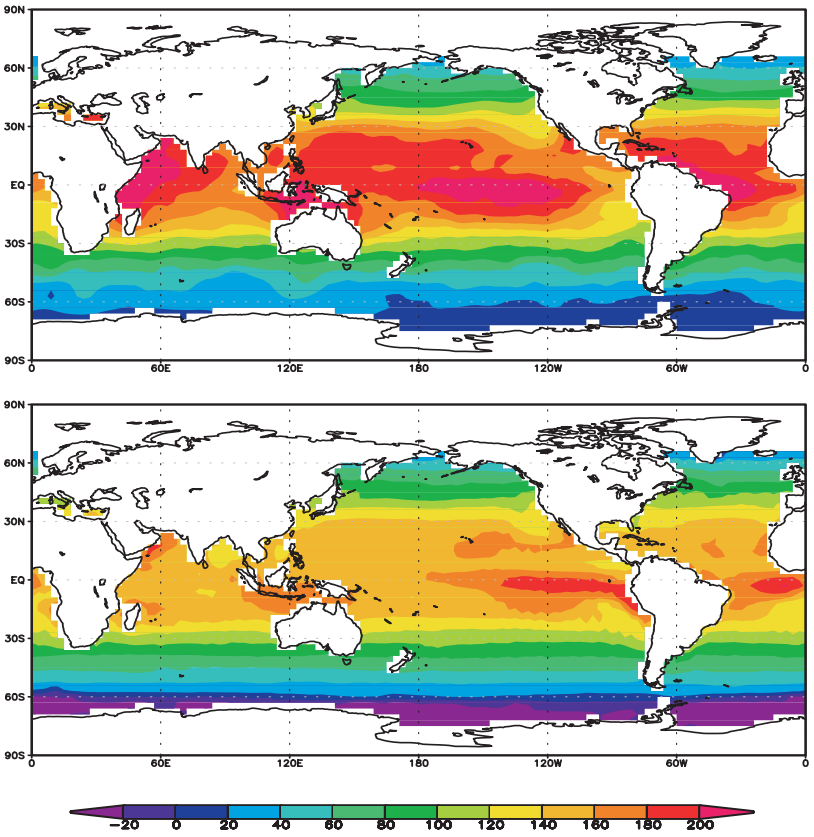

FIGURE 2.7: September surface net radiation (Wm^{-2}) in (top) NOC climatology and (bottom) NCEP climatology.

2.3.3 Wind

The NCEP wind stress is slightly weaker than that in the NOC climatology in a general way. In the Northern Atlantic and Pacific, the maximum NOC wind stresses reach as much as 0.24 Nm^{-2}, when the maximum NCEP wind stresses are only 0.14 - 0.16 Nm^{-2} (Fig. 2.8). However, as far as the wind stress in the vicinity of the Antarctic continent and westerly wind band region are concerned, the maximum NCEP wind stress is almost twice as large as that of NOC climatology in these regions.

It is also interesting to compare the wind speed field for these two climatologies too (Fig. 2.9). The NOC wind speed is much larger than NCEP wind speed in most regions. This is because the NCEP wind speed is derived from observations 10 m above the sea surface while NOC wind speed is derived from the measurement 2 m above the sea surface. The drag coefficients used when

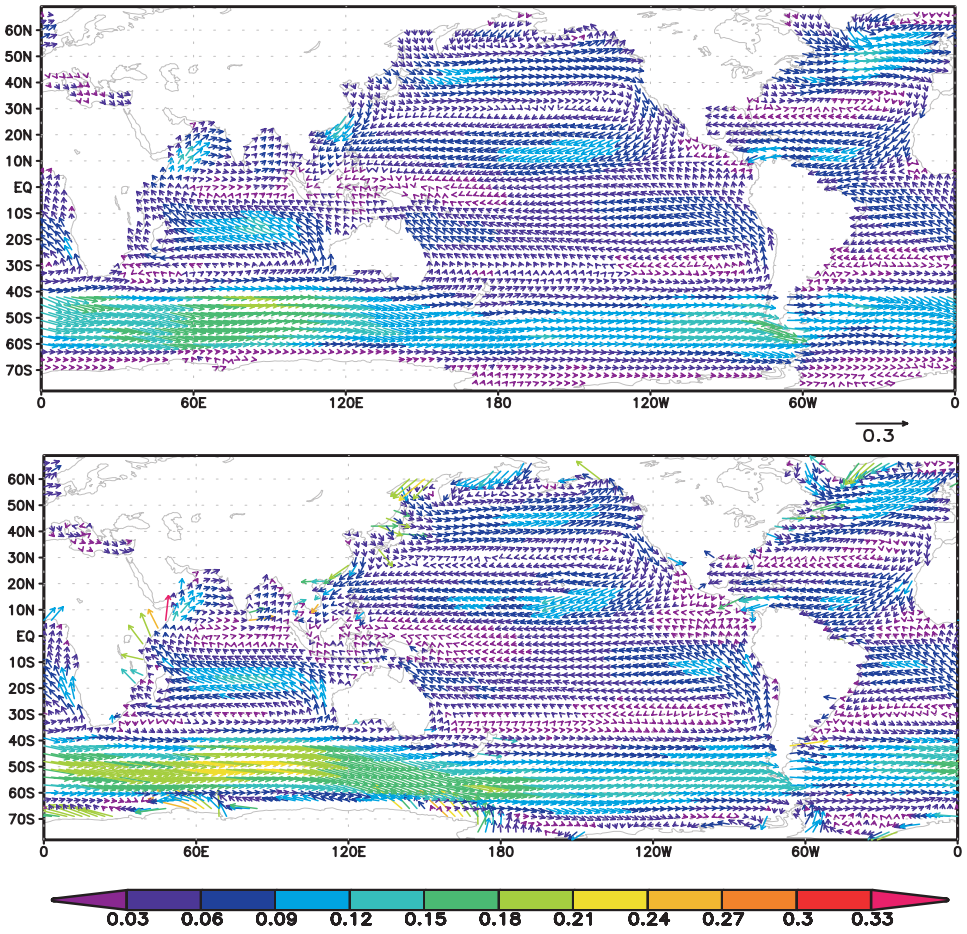

FIGURE 2.8: September surface wind stress (Nm^{-2}) in (top) NOC climatology and (bottom) NCEP climatology.

calculating wind stress from wind speed in these two climatologies are also different, which presumably explains why wind stresses are less different than wind speed.

Sensitivity experiments have been carried out with different surface wind forcing inputs (Cases 3 and 4 in Table 2.1) and several conclusions could be drawn from the model results: (1) Boreal winter MLD in the northern North Atlantic Ocean with the NOC wind is generally deeper (both in the northern boundary and in the subtropical gyre) than that with the NCEP wind (Fig. 2.10); (2) sea surface heat loss reaches its maximum over the Northern Hemisphere western boundary current regions (Gulf Stream and Kuroshio) in winter for both the NOC and NCEP wind forcings. However, the maximum heat loss (in the Gulf Stream area) is 350 Wm^{-2} with NOC winds and only 200 Wm^{-2} with NCEP

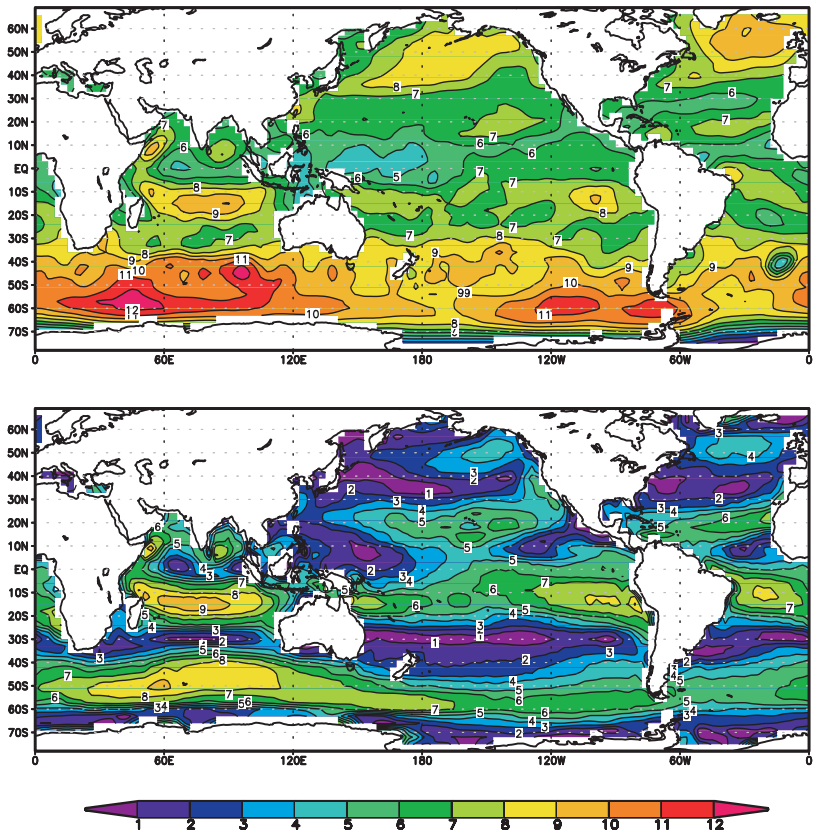

FIGURE 2.9: September surface wind speed (ms^{-1}) in (top) NOC climatology and (bottom) NCEP climatology.

winds (Fig. 2.11), a discrepancy that is mainly caused by the differences between wind speeds in those two climatologies (Fig. 2.9); (3) with stronger wind stress, NOC wind managed to maintain a comparatively stronger and deeper Atlantic MOC (not shown here).

The climatological forcing for HYCOM has a significant influence on the model's output and can greatly affect the simulated ocean circulation. Among all components, surface wind and air temperature seem to be most important. In order to keep a consistent climatology dataset while also optimally simulating ocean circulation in HYCOM, the NCEP climatology dataset has been used as the surface forcing in our control run.

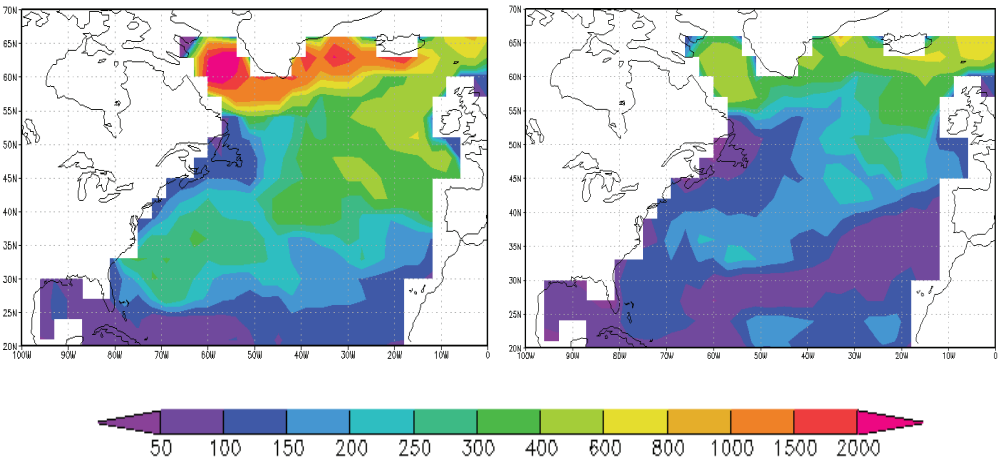

FIGURE 2.10: Boreal winter mixed layer depth (m) in the North Atlantic Ocean with (left) NOC wind forcing (Case 3) and (right) NCEP wind forcing (Case 4).

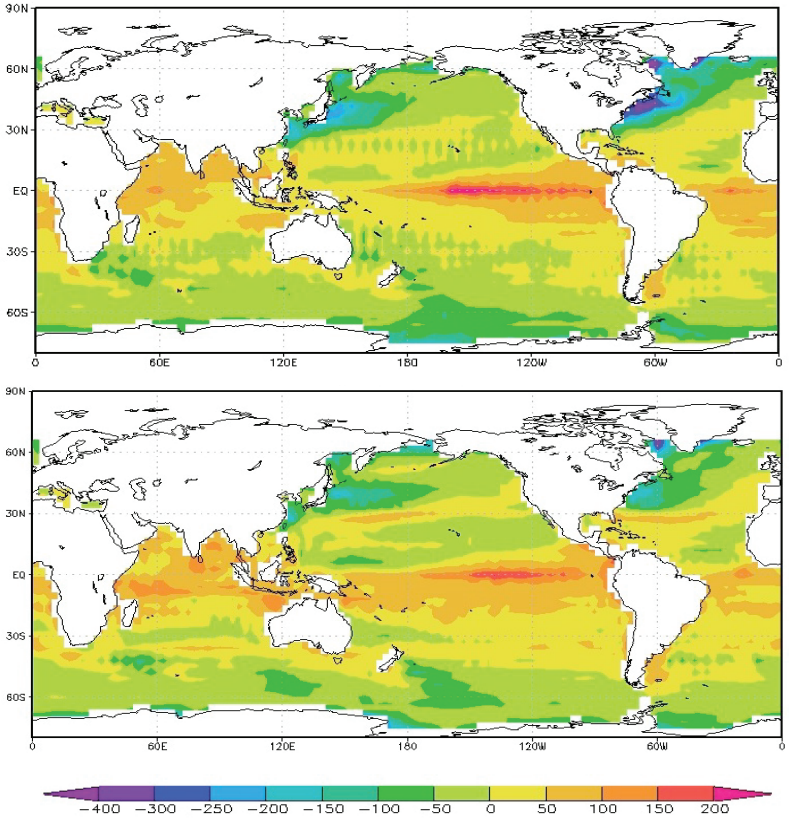

FIGURE 2.11: Boreal winter net surface heat fluxes (Wm^{-2}) with (top) NOC wind forcing (Case 3) and (bottom) NCEP wind forcing (Case 4).

2.4 Boundary conditions

2.4.1 Surface boundary conditions

In order to account for the surface freshwater forcing and prevent precipitation-evaporation induced model drift away from observed salinity, a relaxation of the model Sea Surface Salinity (SSS) to the climatological values provided by Levitus (1982) has been used. No direct Sea Surface Temperature (SST) relaxation has been applied because the bulk parameterizations used in HYCOM provide a physically-based tendency towards the observed SST. The strength of SSS relaxation is defined by the e-folding time scale (T_E in Eq. 2.1), which is 30 days times the model-calculated mixed layer depth (h_{mix}) divided by the reference mixed layer thickness (h_{REF}). By setting h_{REF} to 20 m, we obtain a time scale of around 5 months for 100 m mixed layer thickness:

$$T_E = 30days \times \frac{h_{\mathrm{mix}}}{h_{\mathrm{REF}}} \tag{2.1}$$

The thermodynamic fluxes applied to the model mixed layer are equal to the observed datasets plus a restoring term. For example, the form of the sea surface salinity flux is:

$$S_{\mathrm{flx}} = E(\frac{S_{\mathrm{mix}}}{q}) + T_E(S_{\mathrm{clm}} - S_{\mathrm{mod}}) \tag{2.2}$$

where S_{mix} stands for the mixed layer salinity, q is the reference value of specific volume (m^3kg^{-1}), E is the net evaporation, S_{clm} is the climatological surface salinity, and S_{mod} is the model surface salinity.

2.4.2 Lateral boundary conditions

We have been unsuccessful in applying any ice model in our study and the model domain for this global configuration does not include the Arctic, therefore cannot adequately simulate the formation of NADW in winter. The north Atlantic domain of the model extends only as far as the Greenland-Norwegian Sea at $70°N$ and the significant water mass formation north of the boundary could not be simulated in the model. Therefore the boundary conditions must

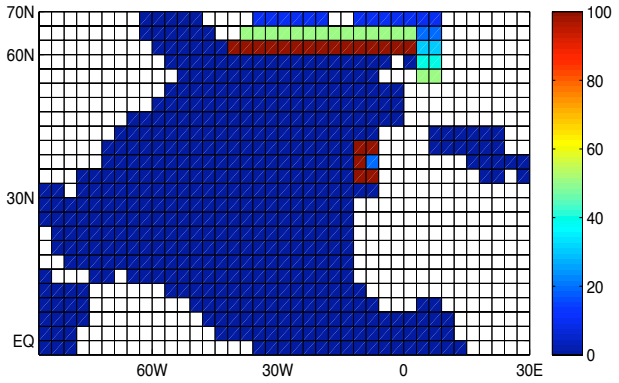

FIGURE 2.12: Timescales for the northern boundary and Mediterranean Water relaxation (days).

allow for important exchange processes across these boundaries. Furthermore, the influence of Mediterranean Water also needs to be simulated because there is no resolved connection between the North Atlantic Ocean and Mediterranean Sea due to the coarse model resolution. This has been achieved by restoring the temperature and salinity to monthly climatological values (Levitus, 1982) near the Greenland-Iceland-Scotland ridge. The relaxation timescale increases from 10 days at $70°N$ to 100 days at $58°N$ (3 grid rows). For Mid-Water relaxation, the timescale at the Strait of Gibraltar ($36°N$, $6°W$) is taken as 20 days (for only one grid cell) and increased to 100 days in the nearby grid cells (Fig. 2.12). All boundary relaxations were applied from the sea surface to the bottom for all 16 isopycnal layers. After applying the northern boundary relaxation, the simulation of North Atlantic Deep Water and Mediterranean Water formation has been successfully achieved (Figs 2.13 and 2.14).

A restoring forcing is also required at the Southern Boundary. If no restoring is applied, the HYCOM bottom layers will keep losing volume due to the diapycnal mixing. Correspondingly, the Antarctic Circumpolar Current (ACC) weakens quickly because not enough dense water in the Southern Ocean is produced in the model to maintain the density gradient across the ACC region. Once Southern Boundary Relaxation (SBR) is applied (Fig. 2.15) by restoring the whole water column to its initial state and forcing all isopycnal layers to stay in their initial positions, the AABW formation is maintained and the decreasing rate of the ACC is reduced (Fig. 2.16). The isopycnal bottom layers in the model will either gain mass or loss mass, depending on the magnitude

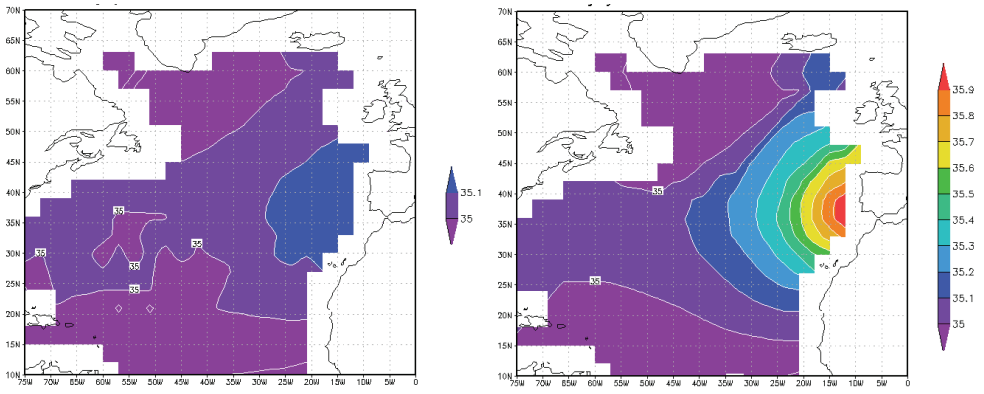

FIGURE 2.13: Spatial distribution of salinity at 1000 m depth in the North Atlantic of HYCOM: (left) without and (right) with Mediterranean Water relaxation.

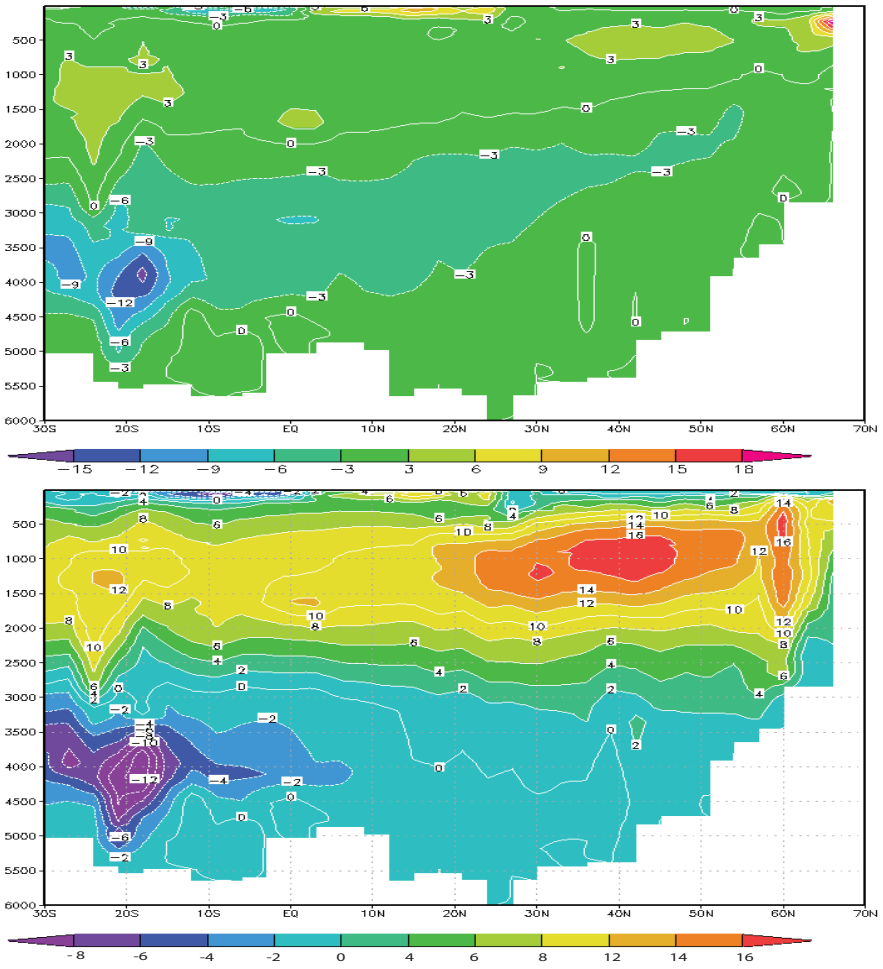

FIGURE 2.14: Meridional overturning stream function for Atlantic Ocean basin: (top) without and (bottom) with northern boundary relaxation.

of the SBR (Fig. 2.17). In addition, we notice that the magnitude of the output MOC is also very sensitive to the strength of applied SBR. An unrealistic enhanced southern deep cell in the global MOC normally suggests that the restoring forcing in the Southern Ocean is too strong to be realistic, and has produced more AABW than necessary. In order to identify the suitable SBR strength, four sensitivity experiments were carried out, as showed in Table 2.2.

TABLE 2.2: Summary of sensitivity experiments with different SBR. The strongest relaxation (least relaxation days) has been applied in the first model row from the south, close to the southern boundary (Fig. 2.15). Values under different ocean basins are the maximum MOC after 40 years of integration. All four experiments share the same initial and surface forcing conditions, except for the SBR. Unit for SBR is day, MOC and ACC transports are shown in Sv ($1\ Sv = 10^6\ m^3 s^{-1}$).

Experiments	SBR	Atlantic	Pacific	Indian	Global	ACC
Case 5	OFF	22	21	24	35	54
Case 6	500/1000	22	27	27	45	65
Case 7	360/720/1000	22	25	33	50	80
Case 8	200/300/500	22	27	33	50	90

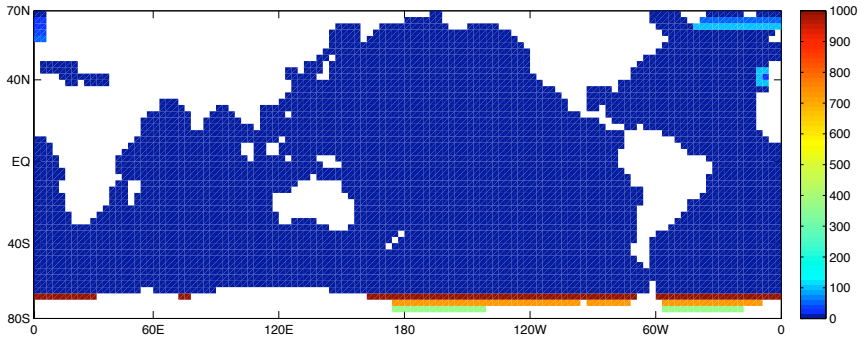

FIGURE 2.15: Timescales of boundary relaxation (days) in the model (for Case 7).

The strength of the geostrophic ACC current depends on the meridional density gradient (pressure gradient) in the Southern Ocean, which is represented by the sloping isopycnal layers in this region, and can be used as one of the criteria for selecting a suitable SBR. Other components that should be taken into consideration include the magnitude of the ITF, annual mean volume variation of bottom isopycnal layers and the magnitude of the lower limb of the MOC.

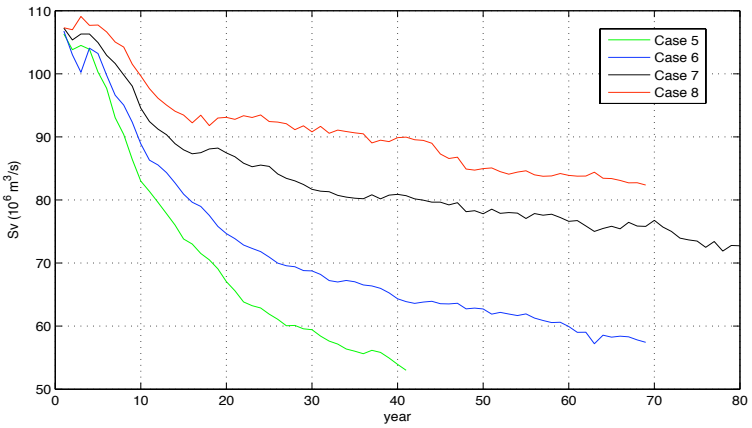

FIGURE 2.16: Magnitude of ACC transport (Sv) in sensitivity experiments with different SBR.

We can see that the magnitude of the ACC transport is proportional to the strength of SBR (Fig. 2.16). In model year 40, the magnitude of the ACC dropped from 108 Sv to 54 Sv when no southern boundary climatological nudging was applied and almost 50% of the flux crossing the Drake Passage was lost during this period. Correspondingly, with the increase of SBR in Cases 7 and 8, the rate of deceleration of the ACC was reduced and the magnitude of ACC at year 40 reached 80 Sv in Case 7 with intermediate SBR.

As mentioned before, if not enough deep water (in Cases 5 and 6) is generated during the southern winter, the total water volume in the bottom layers (layers 15 and 16) would keep dropping due to diapycnal mixing (Fig. 2.17)). However, a strong southern boundary nudging (in Case 8) would generate extra bottom water and lead to an annual mean mass gain in all bottom layers (layers 14 - 16). An important criterion for choosing the appropriate SBR strength depends on whether it can stabilize isopycnal bottom layers so that the time series of bottom layers' total volume stabilizes.

We identified the optimal SBR strength (Case 7) from the sensitivity experiments' results and applied it to the latter control run. The relaxation mask covers a region from $78°S$ to $72°S$ for 3 rows, with the relaxation timescale increasing from 360 days at $78°S$ to 1000 days at $72°S$ (and 720 days in the middle row). The rationale for this choice was to ensure a meridional overturning stream function as close to observations (Lumpkin and Speer, 2007)

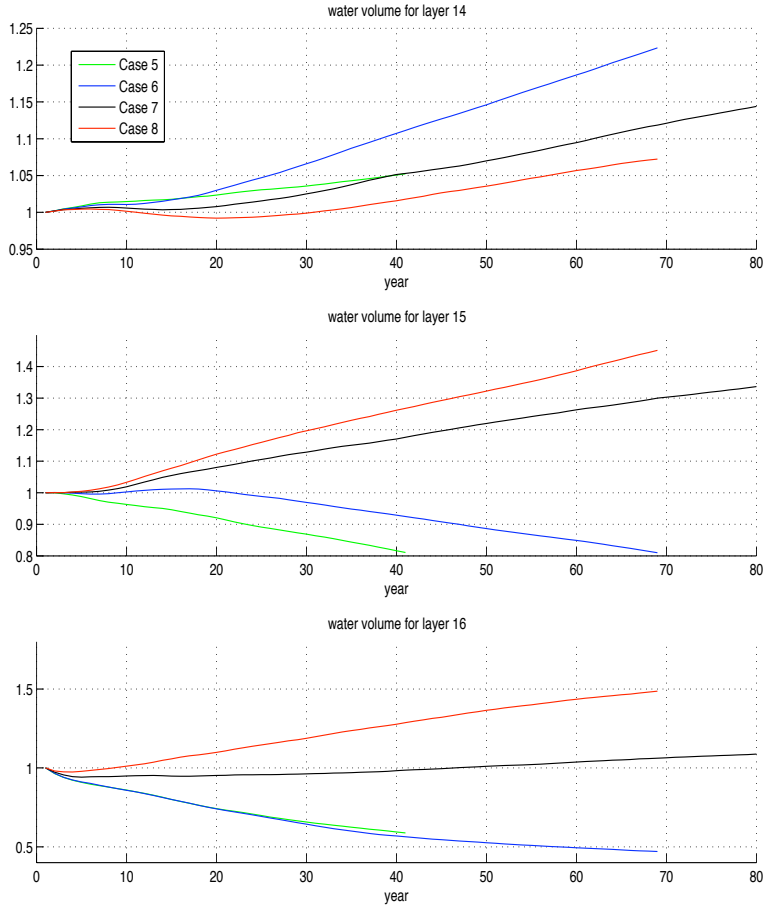

FIGURE 2.17: Annual-mean water volume of bottom isopycnal layers in the sensitivity experiments with different SBR, expressed as a fraction of their initial water volume.

as possible, while also optimising stable hydrography and circulations in the Southern Ocean.

2.5 Sub-grid scale parameterization

2.5.1 Lateral and vertical mixing

HYCOM uses the same fundamental algorithms for horizontal advection and diffusion that were used by MICOM. A Fickian law has been applied for the isopycnic exchange of momentum, and diffusion of both layer thickness and temperature/salinity. All coefficients are proportional to the grid spacing. The

value of 0.003 ms^{-1} was taken as the diffusion velocity (diffusivities divided by the grid spacing) for the thermodynamic variables, giving actual diffusivities of approximately 10^3 m^2s^{-1} around the equator for temperature and salinity. For the momentum equations, an eddy viscosity (υ) that reverts from a constant value plus one proportional to the total deformation in regions of large horizontal shear (Smagorinsky, 1963) has been used and defined as (Bleck et al., 1992)

$$\upsilon = max\{u_d \Delta X, \eta[(u_x - v_y)^2 + (v_x + u_y)^2]^{\frac{1}{2}} \Delta X\}, \tag{2.3}$$

where ΔX is the mesh size, u_d is a background diffusion velocity, and η is dimensionless factor for the shear-dependent terms.

The KPP scheme provides vertical mixing for the entire water column by matching the parameterization of the surface boundary layer mixing with ocean interior mixing. The detail about this mixing scheme will be discussed in Chapter 3, together with a decomposition scheme developed and implemented in the model. In the interior of the open ocean, diffusivities of potential temperature, salinity (scalars), and momentum (viscosity) are assumed to consist of three components. These are shear mixing, internal wave-generated mixing (background mixing) and double-diffusive mixing. Based on Large et al. (1994), a maximum value of 5×10^{-3} m^2s^{-1} has been chosen for the shear-induced diffusion, while the constant background diffusion is of 10^{-5} m^2s^{-1} (10^{-4} m^2s^{-1} for the viscosity).

2.5.2 Sensitivity experiments

A test run integrated over a period of 80 years shows that a weak eddy viscosity parameter would result in strong meridional velocity vertical shears (Fig. 2.18) from surface to ocean bottom in a band following $20^\circ S$ (especially in the Indian Ocean). The MOC stream function affected by this abnormal velocity would become unstable over time. It is also suggested that the resulting strong deep cell in the MOC may lift up the NADW during the simulation and thus affect the shape of the Atlantic MOC.

It is important here to understand the relationship between the barotropic velocity shear and artificially enhanced MOC stream function first. As stated

before, HYCOM is a hybrid coordinate system model (isopycnal in the deep ocean), so when calculating the meridional overturning stream function with reference to pressure levels, an interpolation of the northward fluxes from density-related vertical coordinates to pressure-related vertical coordinates within each isopycnal layer is essential. We need to sum up the interpolated northward velocity over longitude and integrate from the ocean bottom to the top thereafter. This algorithm normally works fine in most of the cases. However, when strong velocity shear exists within one deep isopycnal layer, together with some topographic bumps (see topographic bump around $90°E$ in Fig. 2.18), the regridding from isopycnal layers to a z-level coordinate system and the following zonal integration will result in a southward transport above the topographic bump and northward transport below the bump (Fig. 2.19) due to flux balance within the same isopycnal layer. This implies that an artificial overturning, which does not physically exist in the isopycnal model, would occur due to this barotropic shear and the numerical interpolation algorithm for calculating MOC. This explanation has also been confirmed by the time series of maximum density-referenced MOC in Fig. 2.20, which shows a stable MOC after 30 years of integration,while the maximum depth-referenced MOC becomes unstable and keeps increasing after 20 years of integration. However, this numerical issue is only vital if the model resolution is very coarse (3° in our case).

Sensitivity experiments have then been carried out with similar model configuration and forcing conditions, but with different isopycnal eddy viscosities (Table 2.3). It is very obvious that by increasing the eddy viscosity in the model we effectively reduced the barotropic velocity shear and thus suppressed the artificially enhanced southern deep cell in the global and Indian Ocean (Fig. 2.22). By increasing the Laplacian viscosity factor from 0.1 to 1.0, and also increasing biharmonic viscosity factor from 0 to 0.5 in Case 11, the MOC stream function has been significantly improved (Fig. 2.22) and instability of the maximum MOC has been suppressed (Fig. 2.21). The best combination of eddy viscosity factors would be $\eta_l = 1.0$ and $\eta_b = 0.5$ in our case and has been applied in the subsequent control run. Other combinations have also been tested but either would blow up the model immediately or just destabilize the MOC/ACC fluxes.

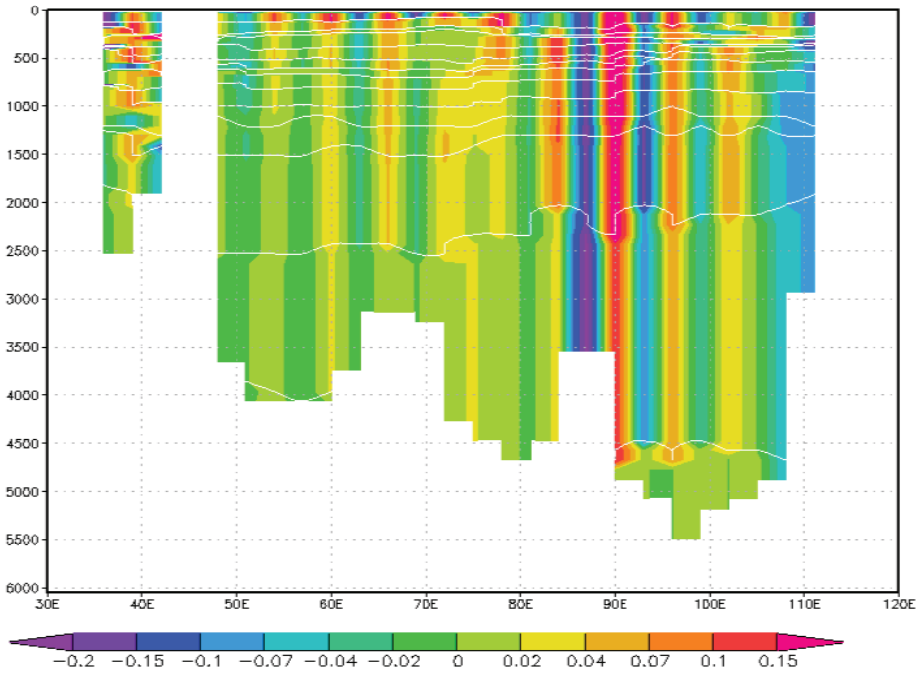

FIGURE 2.18: Zonal section of annual-mean northward volume flux (Sv) along latitude 20°S across the Indian Ocean, showing a barotropic velocity shear over a topographic bump.

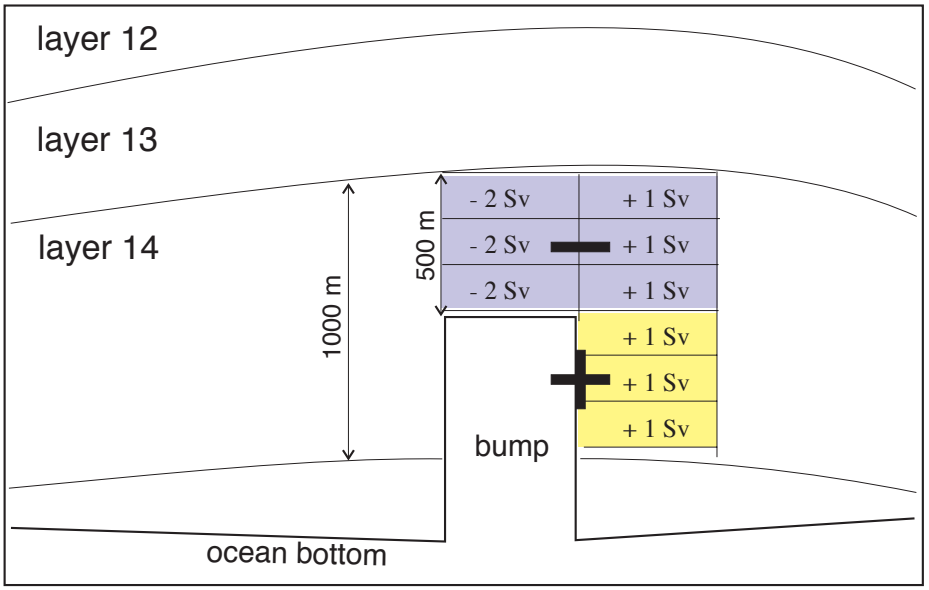

FIGURE 2.19: Schematic of the formation of an artificial overturning cell within one isopycnal layer, induced by a topographic bump and overlaying barotropic velocity shear. Positive value and '+' indicates northward flux, negative value and '−' represents southward flux.

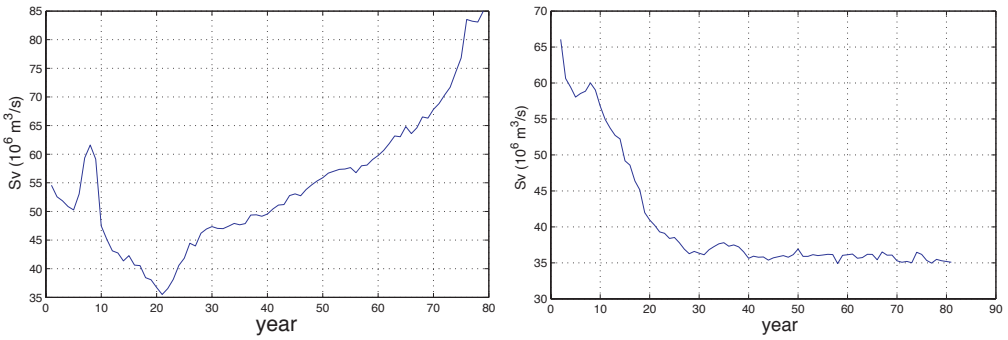

FIGURE 2.20: Maximum MOC with reference to (left) depth and (right) density. The instability of the depth-referenced MOC is induced by the barotropic velocity shear.

TABLE 2.3: Summary of sensitivity experiments with different eddy viscosity. η_l and η_b stand for Laplacian and biharmonic shear dependent factors, respectively

experiments	η_l	η_b
Case 9	0.1	0
Case 10	1	0
Case 11	1	0.5

Another model parameter that has been tuned during the sensitivity experiments is the diffusion velocity for layer thickness. In isopycnal layer models, computational modes can develop through interactions between velocity oscillations and interface oscillations, and the potential enstrophy-conserving momentum advection operator used in HYCOM provides a particularly effective feedback between mass and momentum fields and thus may aggravate this problem. Bleck (2002) suggests that the biharmonic layer thickness diffusion velocity, instead of Laplacian diffusion, is "more effective in removing this noise from the interface depth field and damping the interface undulations." Early experiments also show that the layer thickness diffusion velocity plays an important role in controlling the model's stable state in decade-scale run. Sensitivity experiments show that the optimal layer thickness diffusion is of about 0.1 ms^{-1}, which has been applied in the subsequent control run. In the end, the values of lateral mixing parameters that have been used in the control run and the corresponding equatorial diffusions are given in Table 2.4.

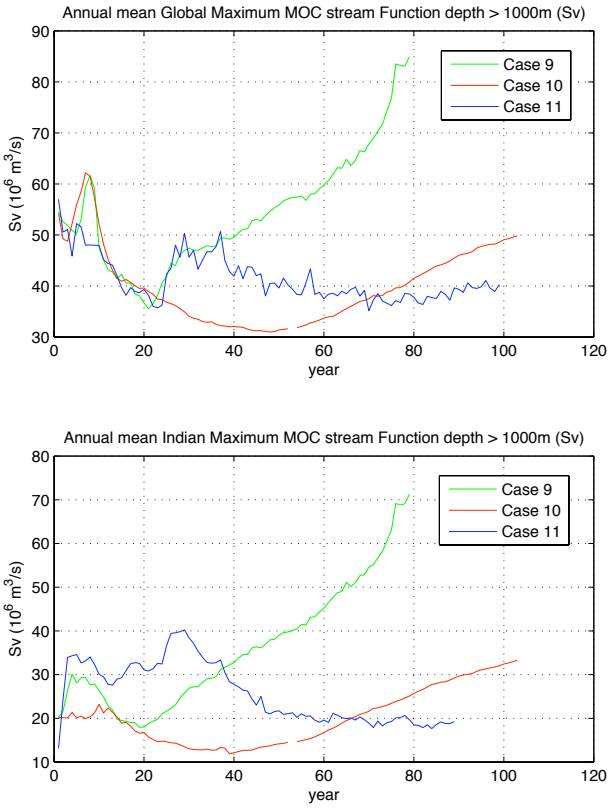

FIGURE 2.21: Time series of the maximum value of (top) global MOC and (bottom) Indian MOC in sensitivity experiments with different eddy viscosity coefficients (with reference to depth, unit Sv).

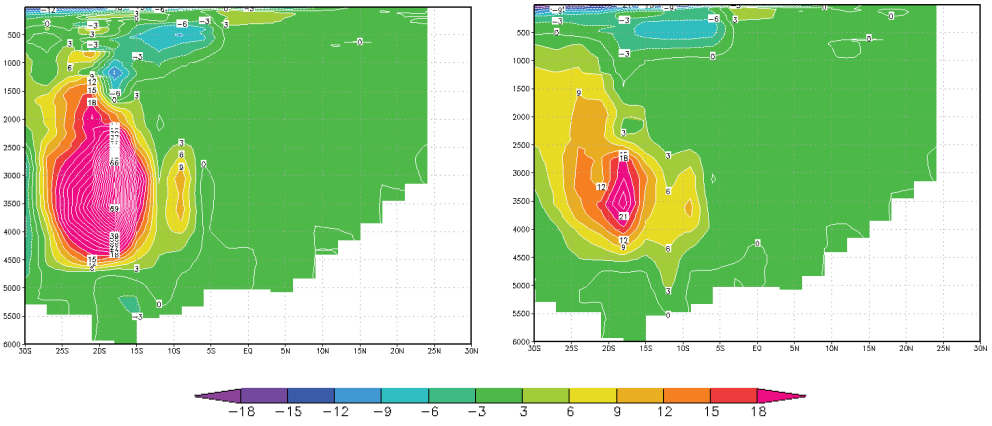

FIGURE 2.22: Meridional overturning stream function (Sv) in the Indian Ocean with (left) $\eta_l = 0.1$ (Case 9) and (left) $\eta_l = 1$ (Case 10). Vertical axis is depth (m).

TABLE 2.4: Summary of the mixing coefficients used in the control run.

	diffusion velocity
η_l (laplacian)	1
η_d (biharmonic)	0.5
u_d (laplacian)	0.03 ms^{-1}
u_d (biharmonic)	0.01 ms^{-1}
layer thickness diffusion (laplacian)	0
layer thickness diffusion (biharmonic)	0.1 ms^{-1}
thermodynamic diffusion	0.003 ms^{-1}

2.6 Integration of the control run

A control run has been undertaken for 120 years until the model reaches a quasi-equilibrium state. All main features of the general circulation will be discussed against observations, with the purpose of model validation. The equilibrium state of the model has been tested with respect to the stability of the meridional overturning and the ACC transport.

2.6.1 The meridional overturning circulation

The stream function of the Meridional Overturning Circulation is normally defined as the zonally-integrated transport above a certain geopotential level. The ability of the model to reproduce essential features of the MOC in the global ocean and regional ocean basins is one of the most important aspects in evaluating its performance and therefore has been checked carefully here. The meridional overturning streamfunction for the Atlantic, Pacific, and Indian Ocean are computed from the control run and the results are illustrated in Fig. 2.23. Three components of the global MOC can be identified, with an amplitude of about 37.5 Sv for the abyssal cell associated with the northward flow of AABW; and 17.5 Sv for the mid-depth cell associated with the southward flow of upper North Atlantic Deep Water (NADW). Two shallow wind-driven cells in the subtropical gyres are also well established in this model.

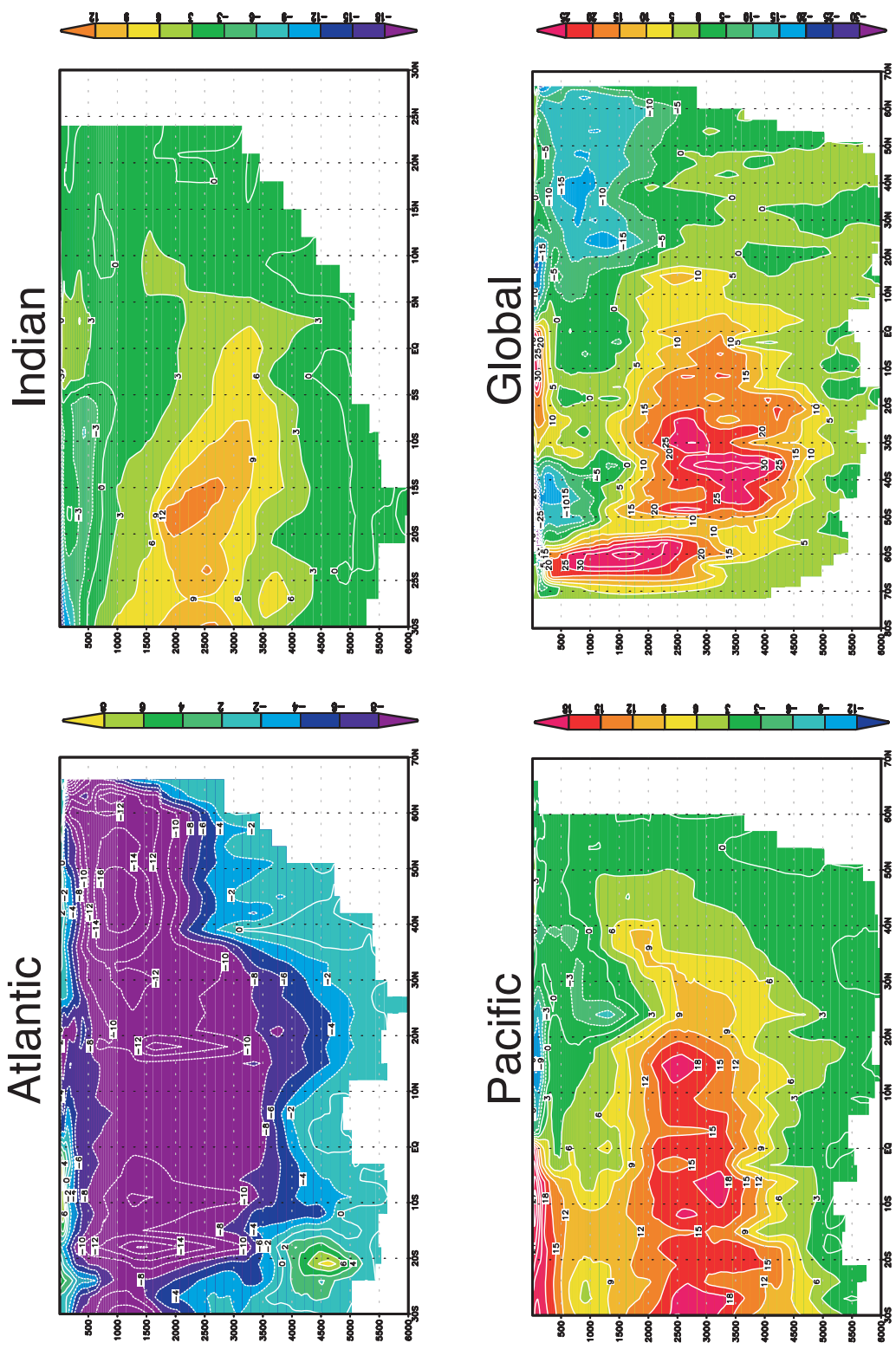

FIGURE 2.23: Meridional overturning stream functions (Sv) for the (A) Atlantic; (B) Indian and (C) Pacific and (D) Global oceans for the control run. Model has been integrated over a period of 120 years and reached a quasi-equilibrium state. Vertical axis is depth (m).

There are two global-scale counterrotating meridional cells that dominate the model solution's global overturning circulation (Fig. 2.23-(D)), while two smaller, shallow cells are associated with subtropical gyres. The magnitude of the positive cell (dense outflow of AABW accounts for most of the deep cell) is almost twice as large as the negative cell (NADW accounts for most of the shallow cell). The upper cell's magnitude in our model is almost exactly the same as that calculated by Lumpkin and Speer (2007), but the deep cell in our model is comparatively larger than most previous estimates (21 ± 6 Sv: Ganachaud (2003); 22 Sv: Talley et al. (2003); 20.9 ± 6.7 Sv: Lumpkin and Speer (2007)), while smaller than the O(50 Sv) overturning of Sloyan and Rintoul (2001a). However, it does not matter much for the formation of SAMW, which is the focus of this thesis.

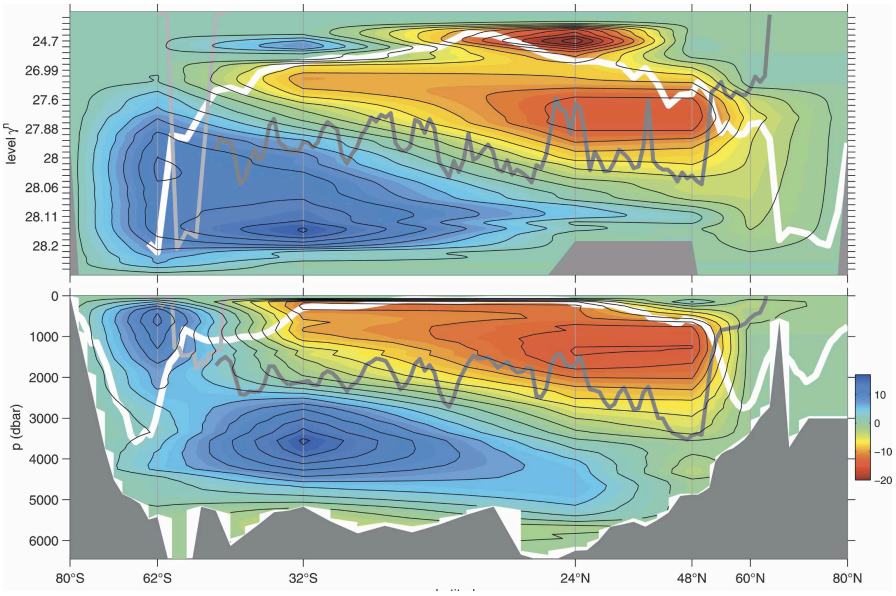

FIGURE 2.24: Zonally averaged global overturning stream function (Sv) derived from hydrographic sections in Lumpkin and Speer (2007): (top) in density and (bottom) in pressure levels.

The overflow of NADW across the northern ridges (Fig. 2.23-(A)) amounts to 8 Sv, and a further 4 Sv transport occurs north of $60°N$ through entrainment and sinking in the subpolar gyre. The NADW transport increases to a maximum of 16 Sv at $45°N$ and 1000 m depth. Two closed recirculations (in the latitude of $20°N$ and $23°S$, respectively) found in this clockwise cell at the depth of around 1500 m appear to be spurious and may be caused by

the lack of vertical resolution in these regions. Most of the NADW is originated in the high latitude northern hemisphere and sinks once it has crossed the Greenland-Iceland-Scotland sill north of $60°N$ (Fig. 2.23-(A)). In our case, this NADW accounts for about 14 Sv of the Atlantic MOC. In most cases the lower boundary of this Atlantic MOC should be level/rising once to the south of $50°N$ (Montoya et al., 2005), however our plot shows that there is another sinking event around $40°N$ and around 10 Sv of the NADW sinks from 2500 m to 4000 m depth there. It is because the main body of southward flowing NADW shifts from layer 13 ($\sigma_2 = 36.95$) to layer 14 ($\sigma_2 = 37.05$) at this region (Fig. 2.26) due to the inflation of layer 13, and corresponding deflation of layer 14 (Fig. 2.25), and is very possibly a result from the input of the Mediterranean Water. In the tropical South Atlantic, AABW transports of 3 - 5 Sv have been estimated (Speer and Zenk, 1993). McCartney and Curry (1993) estimated the cross-equatorial flow of AABW to be of the order of 4.3 Sv. However, only a closed recirculation of the order of 8 Sv appears in our Atlantic MOC stream function (Fig. 2.23-(A)), in the deep reverse cell around $20°S$ and does not cross the equator.

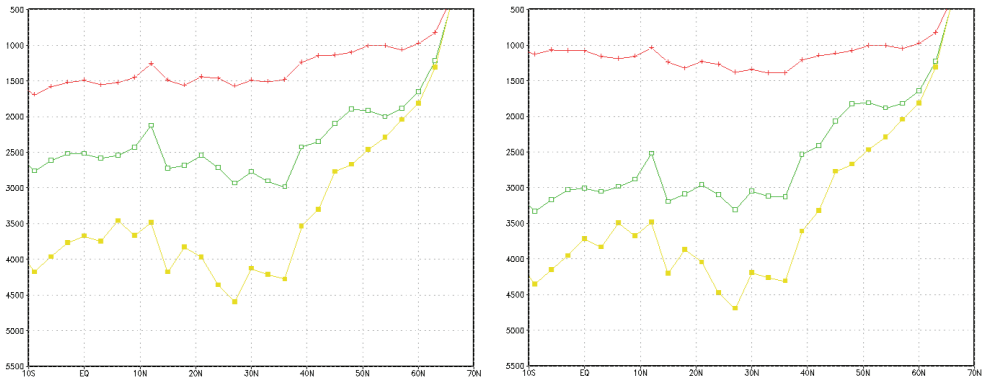

FIGURE 2.25: Zonally averaged annual mean model layer interface depths of layers 13 and 14, in the Atlantic Ocean for years (left) 20 and (right) 120. The red contour marks the upper interface of layer 13; the green contour is the interface between layers 13 and 14; the yellow contour represents the bottom interface of layer 14.

FIGURE 2.26: Zonally and annually averaged northward volume transports (Sv) in layers 13 and 14, in the Atlantic Ocean for years (left) 20 and (right) 120. The green contour marks the transports carried out by layer 13 and yellow contour represents layer 14.

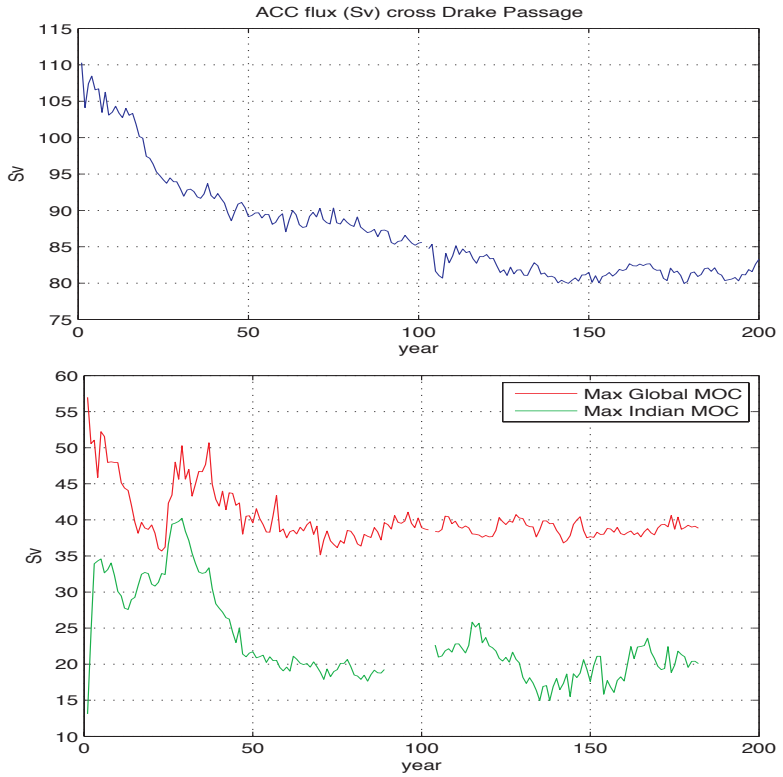

FIGURE 2.27: Time series of the (top) ACC transport (Sv) and (bottom) maximum MOC (Sv) in the global and the Indian oceans, as calculated from the control run.

2.6.2 Equilibrium state of the control run

In order to reach a quasi-equilibrium state for the model, a spin-up of 120 years has been undertaken. From Fig. 2.27, we can see that the meridional overturning is stabilized after 120 years of integration in the model. The maximum MOC in the deep cells ($> 1000\ m$) varies between 15 - 25 Sv for the Indian Ocean after spin-up, and is within the wide range of previous estimates (7 Sv in Ganachaud and Wunsch (2000); 12 Sv in Robbins and Toole (1997); 18 Sv in Talley et al. (2003); 23 Sv in Sloyan and Rintoul (2001b)). The maximum global MOC is of about 37 Sv, which is slightly higher than recent observational values (Lumpkin and Speer, 2007). The ACC transport gradually reduces during the spin-up period, but reaches a steady state value of around 80 Sv that is maintained until the end of the 200-year integration (Fig. 2.26). This value is smaller than observation-based estimates (112 ± 4 Sv in Sloyan and Rintoul (2001b); 140 ± 6 Sv in Ganachaud (2003)) but considered reasonable as a coarse resolution model's result. In the end, the conclusion can be drawn that HYCOM has reproduced the meridional overturning circulation reasonably well in our simulation, and a spin-up period of about 120 years is sufficient for the model to reach a quasi-equilibrium state. Other metrics like time series of ITF transports, global mean temperature, salinity and sea surface height trends all show a stable state after 120 years integration in the model (results not shown here).

SUMMARY

In this Chapter, aspects of the configuration of the HYCOM model have been described, including the model domain and bathymetry, model initialization, surface forcing, boundary conditions and sub-grid scale parameterizations. Both NOC and NCEP climatologies have been applied and tested as surface forcing fields in the model for intercomparison. Among all components, surface wind and air temperature show the greatest difference between these two data sets especially in the Southern Ocean and the vicinity of the Antarctic continent, as the NOC climatology within these regions is extrapolated. In order to keep a consistent climatology dataset while also optimally simulating ocean circulation in HYCOM, the NCEP climatology dataset has been used as the surface forcing in our control run. Sensitivity experiments have also

been carried out to test the behaviour and robustness of the model with respect to different boundary conditions and mixing coefficients. It is clear that the model's outputs (MOC, ACC, ITF and MLD) are very much subject to the prescribed boundary relaxation strength as well as the diffusion velocity. In the end, a set of optimal configurations for HYCOM have been chosen for the control run, which has been integrated over a period of 120 years until reaching a quasi-equilibrium state. Despite the coarse mesh grid, our model reproduced all main features of the physical ocean reasonably well, according to the intercomparison of our model outputs with observations and previous OGCM results.

Chapter 3

Tracer Experiment Setup

In this Chapter the setting up of a tracer tracking experiment with the purpose of mimicking the formation, subduction and re-emgence of the SAMW in the global ocean will be explained in detail. The formation region of the SAMW in the Southern Ocean is discussed first by comparing the model simulation results with observations, then the deployment algorithm for a salinity-like tracer in the formation region of SAMW and the algorithm of its consumption in the mixed layer will be examined. After release, a tracer diagnostic scheme is then developed for quantitatively assessing the influences of different upwelling mechanisms (induction, entrainment, diapycnal diffusion, numerical re-gridding mixing, etc) for SAMW re-emergence in the global ocean.

3.1 Tracer releasing scheme

3.1.1 Formation of the Subantarctic Mode Water

The formation of SAMW can be investigated by examining the spatial distribution of deep winter mixed layers in the Southern Ocean (Dong et al., 2008; Aoki et al., 2007). Considering HYCOM, the isopycnic nature of this model makes it very convenient for identifying and tracking the subduction and spreading of the SAMW into the ocean interior within each isopycnal layer.

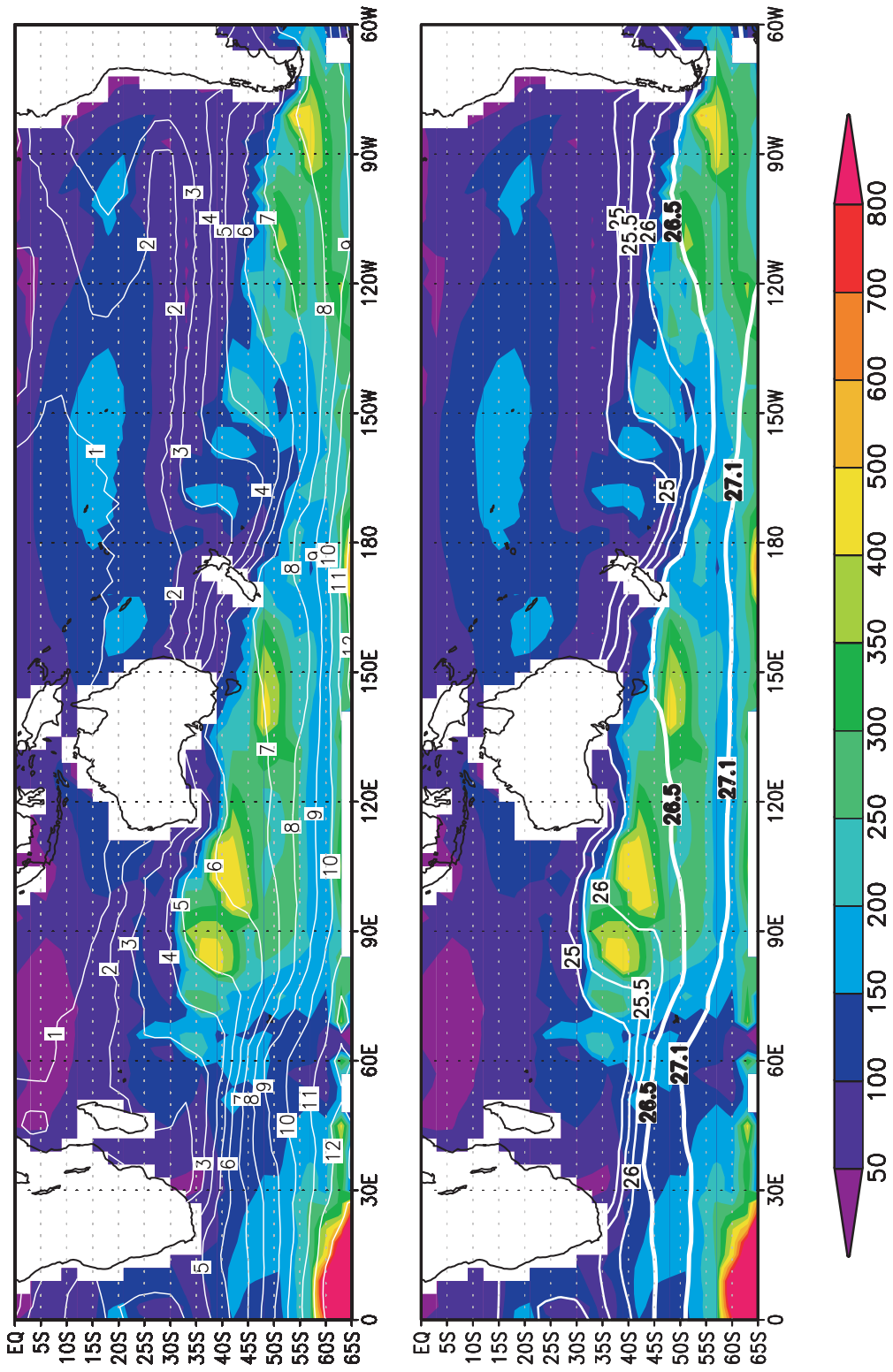

FIGURE 3.1: Spatial distribution of winter mixed layer depth in HYCOM's Control Run after 120 years spin-up: (A) with contours representing the intersection locations where isopycnal layer outcropped by winter deep mixed layer; (B) with contours marking the mixed layer potential density with reference to the sea surface (σ_0).

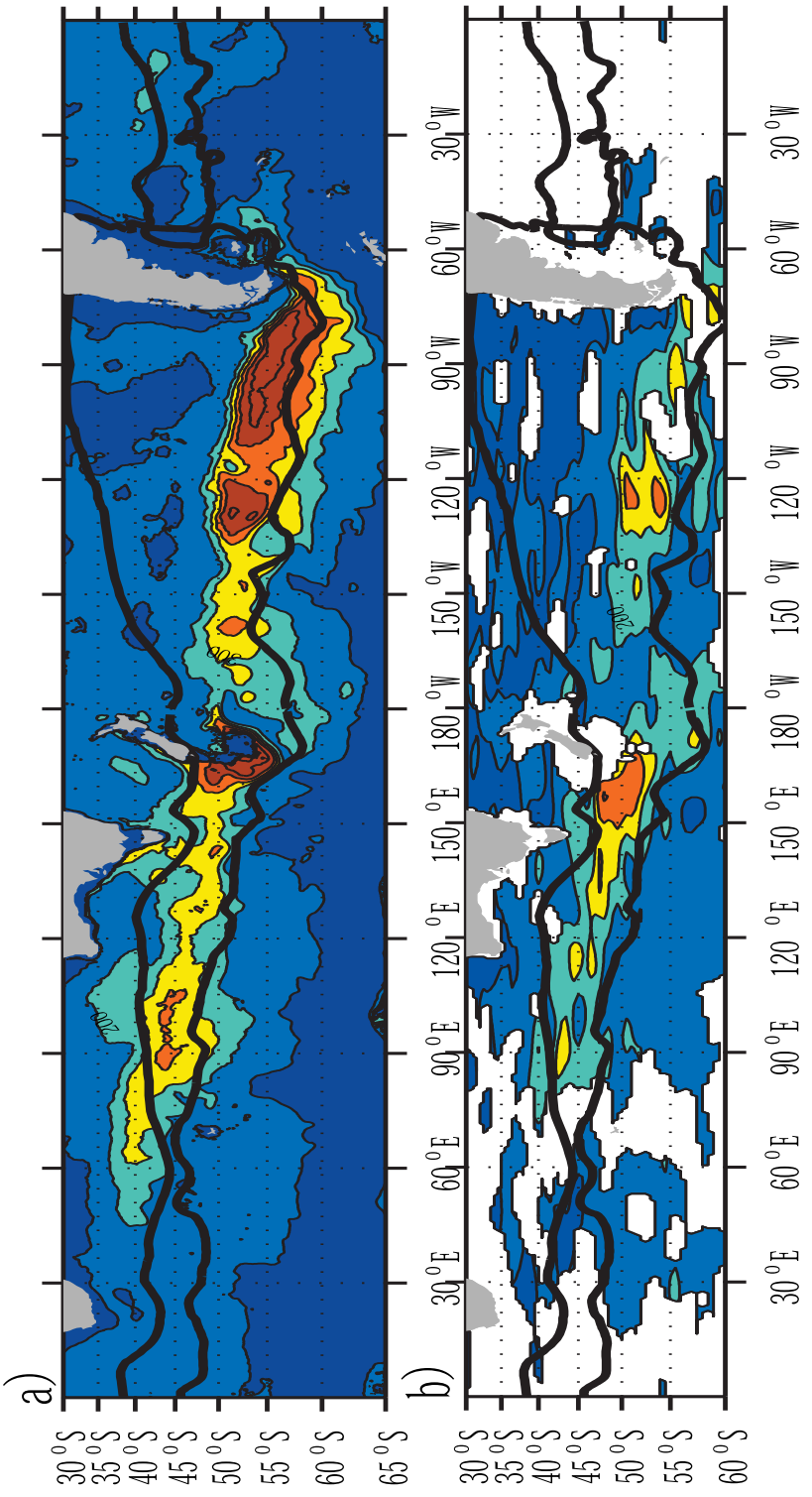

FIGURE 3.2: Distribution of winter mixed layer depth, derived from (a) Ocean general circulation model For the Earth Simulator (OFES) and (b) Argo float data with the same colour scale as in Fig. 3.1. Blank areas denote regions of inadequate sampling. Thick lines denote the Subtropical Font (STF) and Subantarctic Font (SAF). (Aoki et al., 2007)

After a 120 year spin-up, the model reached a near-equilibrium state. The winter mixed layer depth defined based on a prescribed density deviation ($\Delta\rho = 0.03\ kgm^{-3}$) from sea surface in the Southern Ocean can be seen in figure 3.1. HYCOM-simulated deep winter mixed layers ($> 250\ m$) are only significant in the southeast Indian Ocean and southeast Pacific Ocean, consistent with past observations and research (Hanawa and Talley, 2001; McCartney, 1977, 1982). Argo float data also show (Dong et al., 2008) that deep winter mixed layers from both density ($\Delta\rho = 0.03\ kgm^{-3}$) and temperature ($|\Delta T| = 0.2°C$) difference criteria, representing the thick SAMW are only found in the Indian and Pacific Oceans. The formation region of SAMW in the Atlantic is limited (McCartney, 1982) and the density definitions of SAMW from different studies are not clearly distinguished from the density definition of Subtropical Mode Water (STMW) in the Atlantic Ocean. Therefore, formation of SAMW in the Atlantic is not included here.

Comparison with Ocean general circulation model For the Earth Simulator (OFES) and Argo float data (Fig. 3.2) shows that they are in generally good agreement with the distribution of deep winter mixed layers in the Southern Ocean. The formation region of SAMW covers mainly the Southern Indian and Pacific Oceans between 30°S and 60°S. The corresponding isopycnal layers in HYCOM for SAMW formation are layers 4 - 7 (σ_2 = 33.54 - 35.37) in the Indian Ocean and layers 4 - 8 (σ_2 = 33.54 - 35.80) in the Pacific Ocean. For the purpose of comparison with observations and other climate model results, the potential density of HYCOM layers (in σ_2) are converted to σ_0 (calculated from local potential temperature, salinity and pressure). We found that simulated deep mixed layers in the southeast Indian ocean are within lighter densities range ($\sigma_0 = 26.0 - 27.1 kgm^{-3}$) than observed values ($\sigma_0 = 26.5 - 27.2 kgm^{-3}$ (Hanawa and Talley, 2001)). However, as suggested by Sloyan and Rintoul (2001b), this broad density definition of SAMW actually results in most models producing the SAMW potential vorticity within this neutral density range, as most climate model simulated SAMW is at lighter densities than observations (Sloyan and Kamenkovich, 2007). It can be seen in figure 3.1 that the density of SAMW increases eastwards from the southern Indian Ocean to the Pacific Ocean, which is also consistent with OFES and the Argo floats' inferences.

Potential Vorticity (PV) has been widely used in ocean circulation studies as a dynamical quantity with a tracer-like property. It is conserved within each

density layer as long as the effects of diabatic processes, friction and diapycnal mixing are weak with respect to isopycnal advection (Luyten et al., 1983). The SAMW is often identified by a PV minimum layer on the equatorward side of SAF, reflecting the low PV associated with deep winter mixed layers. A series of SAMW properties, including the distribution of PV, have been investigated by Sloyan and Kamenkovich (2007). In order to compare our model with them and validate the formation region of SAMW in HYCOM, we calculated PV within each isopycnal layer in our model

$$q = -\frac{1}{\rho}\frac{\partial \rho}{\partial z}(f + \zeta) \tag{3.1}$$

where q is potential vorticity, ρ is density, f is planetary vorticity and ζ is relative vorticity. Here, $\frac{\partial \rho}{\partial z}$ is the local stratification. The Coriolis parameter $f = 2\Omega\sin(\phi)$, where ϕ is the latitude and $\Omega = 7.29 \times 10^{-5} s^{-1}$. The minus sign in (3.1) is introduced so that PV is positive in the Northern Hemisphere. Relative vorticity $\zeta = \nabla \times \mathbf{v}$, and can be written in the form of

$$\zeta = \frac{\partial v}{\partial x} - \frac{\partial u}{\partial y} \tag{3.2}$$

For calculation of derivatives, centered finite differencing (weighted by distance as needed) was used and the horizontal velocity at four corner points were used to compute ζ at the center density points. On solid boundaries, zero velocity and zero normal gradients were assumed.

Assuming the vertical density gradient at the very top of the ocean is zero, the vertical derivative of potential density at layer k is

$$-\frac{1}{\rho}\frac{\partial \rho}{\partial z} = -\frac{1}{\rho_k}\frac{\rho_{\text{k-1}} - \rho_{\text{k+1}}}{h_k + 0.5 \times (h_{\text{k-1}} + h_{\text{k+1}})} \tag{3.3}$$

where h is the layer thickness. Calculation was carried out along isopycnal surfaces with reference to 2000 dbar and then linearly interpolated onto z-level coordinates for the purpose of section analysis. Resulting winter PV along isopycnal surfaces from 33.54 to 35.80 (σ_2) with layer numbers 4 to 8 are displayed in Fig. 3.3. It's clear that the location of minimum PV ($< 15 \times 10^{-11} m^{-1} s^{-1}$) in the Indian and Pacific Oceans both shift eastwards with increasing potential density, consistent with the density distribution and formation regions of SAMW identified by Aoki et al. (2007).

Sloyan and Kamenkovich (2007) compared the simulations of SAMW in eight climate models with an observation-based inverse model (The Commonwealth Scientific and Industrial Research Organization Atlas of Regional Seas 2006 (CARS)). The results show that although many models simulate the potential vorticity minimum layer of SAMW, this is generally thinner and at lighter densities than observation. Distribution of PV in the southern winter after our control run has reached its equilibrium state is displayed in Fig. 3.4 following the same meridional sections that were chosen in Sloyan and Kamenkovich (2007). In the Indian Ocean, our model produces a well established potential vorticity minimum layer on the northern boundary of the model ACC, with the minimum $|PV| < 15 \times 10^{-11}\ m^{-1}s^{-1}$. This simulated PV minimum layer sinks to a depth of about 500 m and extends northwards to about $23°S$. Comparing with the observations (CARS2006), which suggest that SAMW can sink to a depth of 650 m and extend northwards as far as $25°S$, our model-simulated SAMW is thinner but similar in extension distance, as most other climate models (Sloyan and Kamenkovich, 2007). Our simulated PV minimum value is also more pronounced than observations ($5 \times 10^{-11}\ m^{-1}s^{-1}$ in CARS2006), again similar to other models simulation. This discrepancy likely derives from the coarse resolution of our model and the inaccurate monthly mean surface forcing in the Southern Ocean deduced from the NCEP reanalysis climatology. In the eastern Pacific Ocean, our simulated minimum PV has shorter latitudinal extent and is also thinner than that observed.

For a ocean GCM with very coarse, non-eddy resolving resolution ($3° \times 3°$) and under the surface driving forces of monthly mean climatology, our model does a reasonably good job in simulating the formation region of SAMW as the maximum winter mixed layer and minimum PV layer, even when comparing with higher-resolution climate models reviewed by Sloyan and Kamenkovich (2007).

3.1.2 Tracer injection

A conservative tracer has been used for the purpose of tracking the ventilation and circulation of the SAMW throughout the global ocean, as well as identifying the upwelling locations and investigating mechanisms that return SAMW to the surface mixed layer. The tracer is injected as a one-off event in mid-September

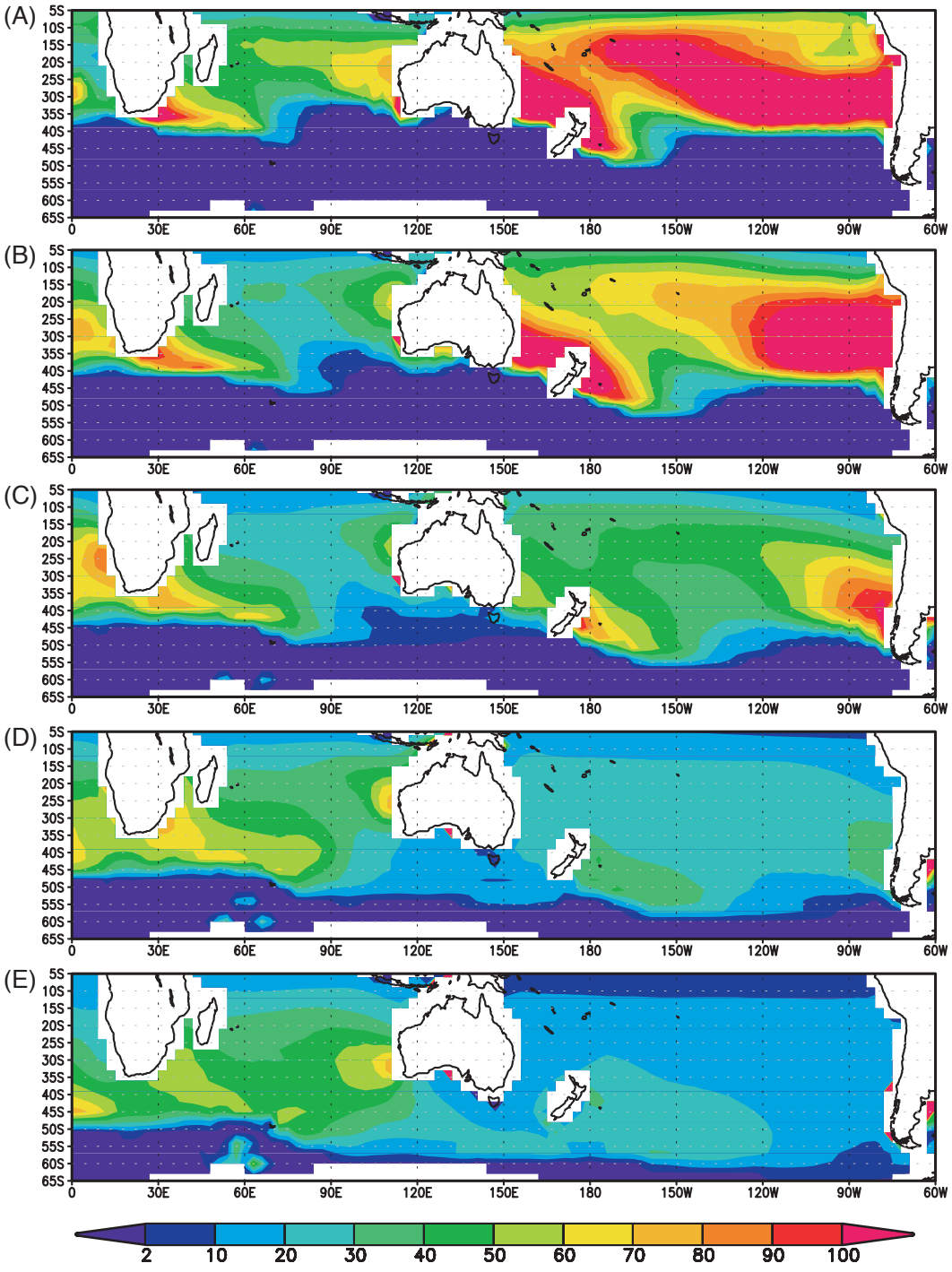

FIGURE 3.3: Winter spatial distribution of $|PV|$ $[\times 10^{-11}(\text{m s})^{-1}]$ in the Southern Ocean after quasi-equilibrium state has been reached in the control run: (A) PV in isopycnal layer 4 with potential density $\sigma_2 = 33.54$; (B) in layer 5 with $\sigma_2 = 34.24$; (C) in layer 6 with $\sigma_2 = 34.85$; (D) in layer 7 with $\sigma_2 = 35.37$ and (E) in layer 8 with $\sigma_2 = 35.80$.

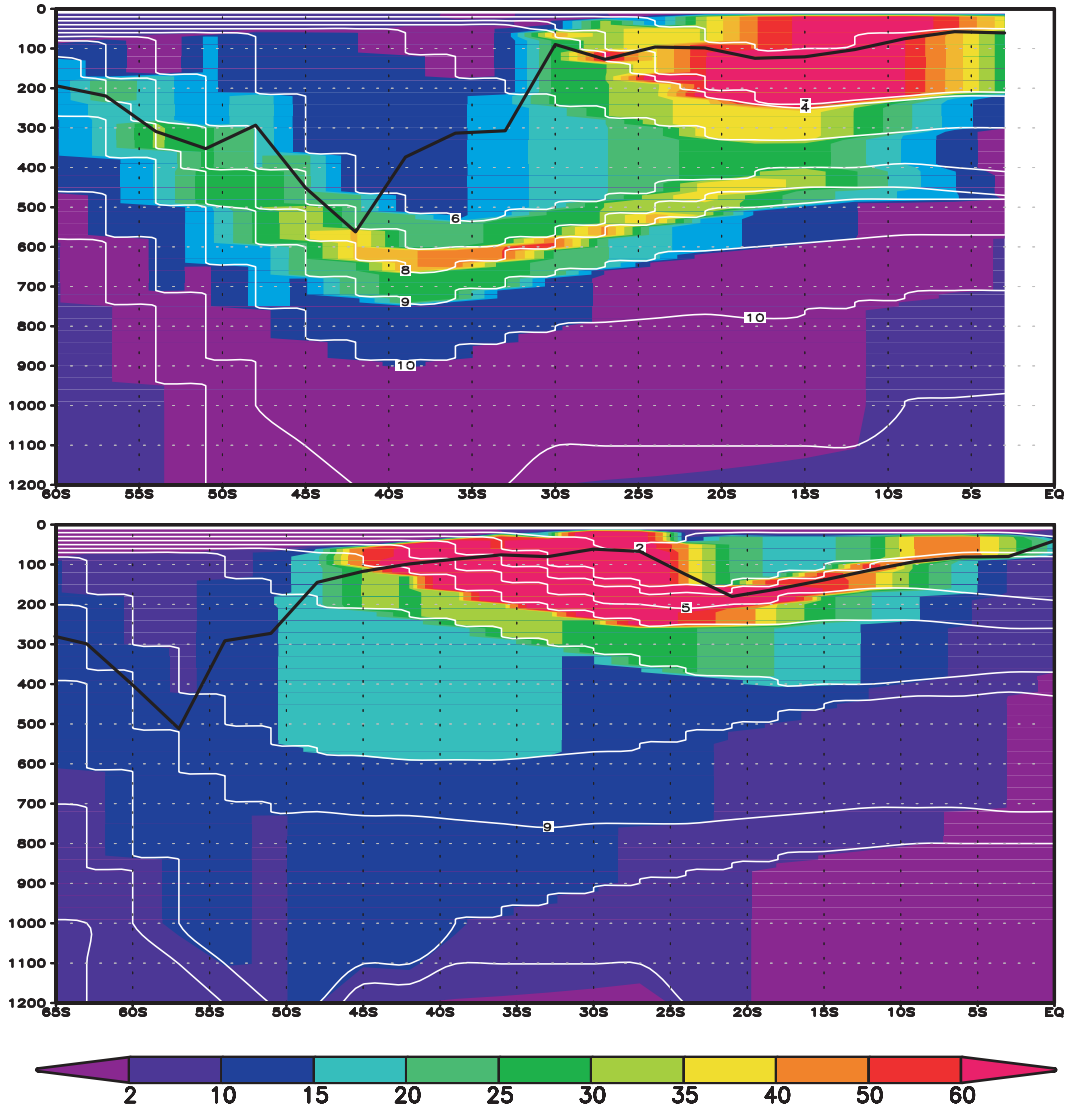

FIGURE 3.4: Winter distribution of potential vorticity $[\times -10^{-11}(m^{-1}s^{-1})]$ (top) in the eastern Indian Ocean ($100°E$) and (bottom) in the eastern Pacific Ocean ($90°W$) after quasi-equilibrium state has been reached in the control run. Also shown is the distribution of isopycnal layer interfaces (white contours) and winter mixed layer depth (bold black).

after the model has been integrated over a period of 120 years and reached a quasi-equilibrium state, in a manner that mimics a physical tracer release experiment in the ocean. The injection region of tracer has been carefully chosen so that it represents the region of SAMW formation in the model as closely as possible.

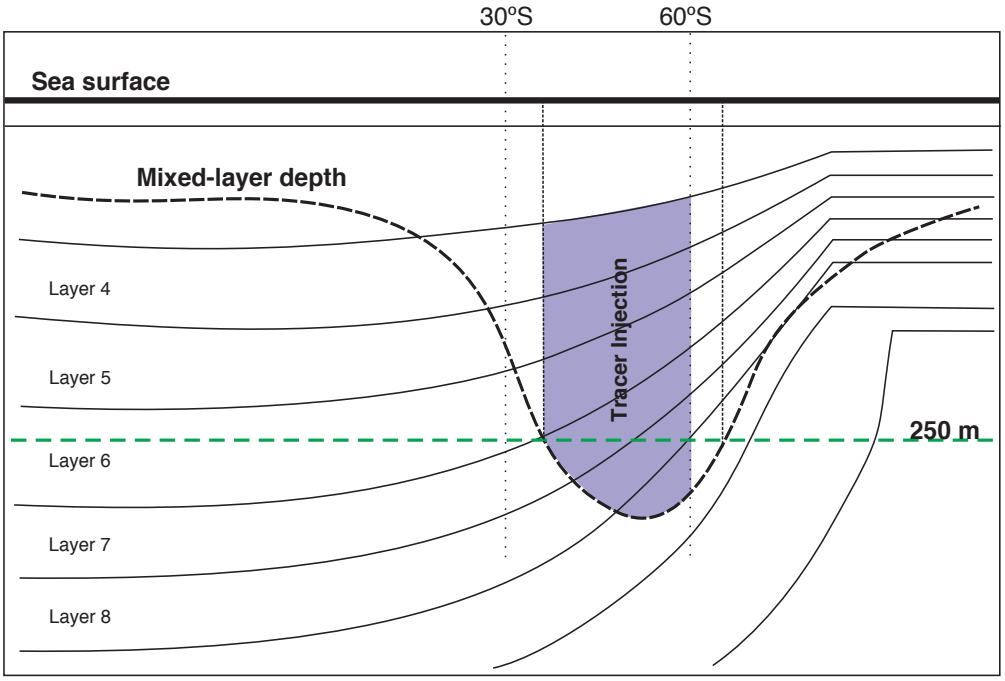

FIGURE 3.5: Schematic of tracer release region in the Southern Ocean. Injection takes place in the first September after spin-up and is defined with boundaries of mixed-layer depth, isopycnal layer interfaces and latitudes.

For a model region to be included in the tracer deployment domain, or in other words, in the SAMW formation region, the following criteria must be fulfilled:

1. The region must be within a rectangular area between 30°S – 60°S and 40°E – 360°E in the Southern Ocean.

2. It must be within the mixed layer and only in a region where later winter (i.e. Sep) mixed layer depths exceed 250 m.

3. It must be within the density range of SAMW in HYCOM (from layers 4 to 8 in model with density $\sigma_2 = 33.54 - 35.80$) when comparing with OFES and Argo float data (Aoki et al., 2007).

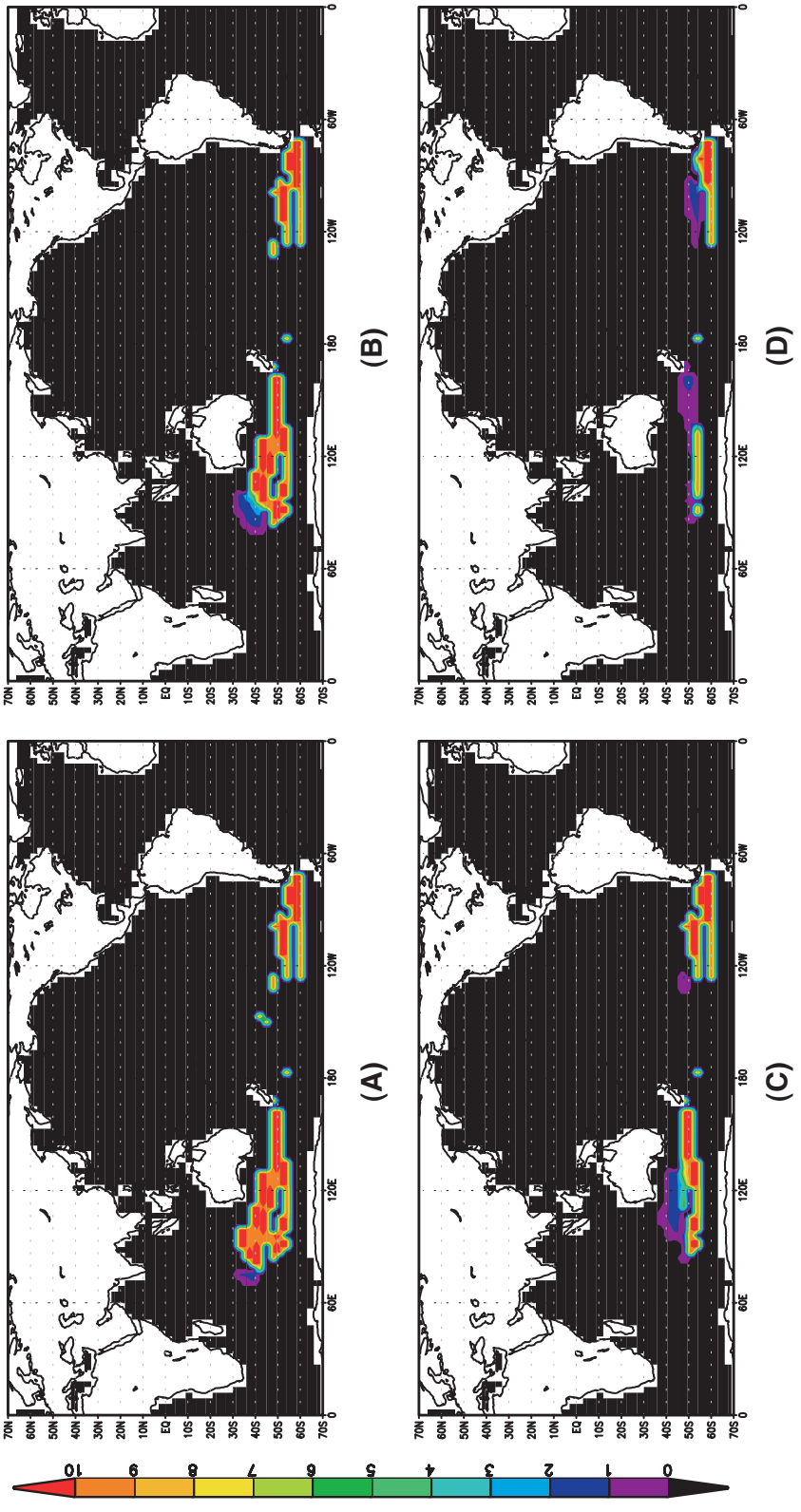

FIGURE 3.6: Tracer concentration in different isopycnal layers (HYCOM) one step after injection: (A) layer 5 with density $\sigma_2 = 34.24$; (B) layer 6 with density $\sigma_2 = 34.85$; (C) layer 7 with density $\sigma_2 = 35.37$; (D) layer 8 with density $\sigma_2 = 35.80$.

This tracer releasing scheme is illustrated by Fig 3.5. The concentration of tracer within each isopycal layer is given by:

$$C_{\mathrm{trc}} = \begin{cases} 10 & \text{if } P_{\mathrm{n+1}} \leq P_{\mathrm{mix}} \\ 10 \times \frac{P_{\mathrm{mix}} - P_{\mathrm{n}}}{P_{\mathrm{n+1}} - P_{\mathrm{n}}} & \text{if } P_{\mathrm{n}} \leq P_{\mathrm{mix}} < P_{\mathrm{n+1}} \\ 0 & \text{if } P_{\mathrm{mix}} < P_{\mathrm{n}} \end{cases} \tag{3.4}$$

where C_{trc} is the tracer concentration (*tracer unit* m^{-3}) and P_n is the depth of the isopycnal layer interfaces. The subscripts here represent the layer number (P_{n} and $P_{\mathrm{n+1}}$ are the top and bottom interface depths for layer number n). P_{mix} is the maximum depth of the winter mixed layer.

This algorithm ensures that any layer outcropping in the surface mixed layer within the SAMW formation region has tracer injected. The concentration of tracer equals 10 if the concerned isopycnal layer totally outcrops into the mixed layer, or 0 if the layer is below the mixed layer. A value between 0 and 10 will be assigned to a layer that only partially outcrops into the surface mixed layer. After release the tracer is conservative and not subject to any imposed decay, apart from when it re-emerges into the surface mixed layer. The result of tracer initialization field in model can be seen in Fig 3.6.

3.1.3 Tracer consumption

The purpose of this research is to track the ventilation circulation and, in particular, the upwelling of SAMW in the global ocean, with a view to model the role of SAMW in global nutrient supply to the mixed layer (Sarmiento et al., 2004). However the oceanic distributions of nutrients are controlled by both physical and biogeochemical processes, as well as external sources. Eventually, there are significant differences between the nutrient and water mass distributions, with nutrients generally showing stronger vertical and basin-to-basin contrasts. Biological production is a major factor in determining these greater nutrient contrasts, with inorganic nutrients consumed and converted to organic matter in the surface, sunlit ocean (euphotic zone). In order to mimic the consumption of nutrient in the surface, we introduced the following tracer consumption/removal scheme in our model.

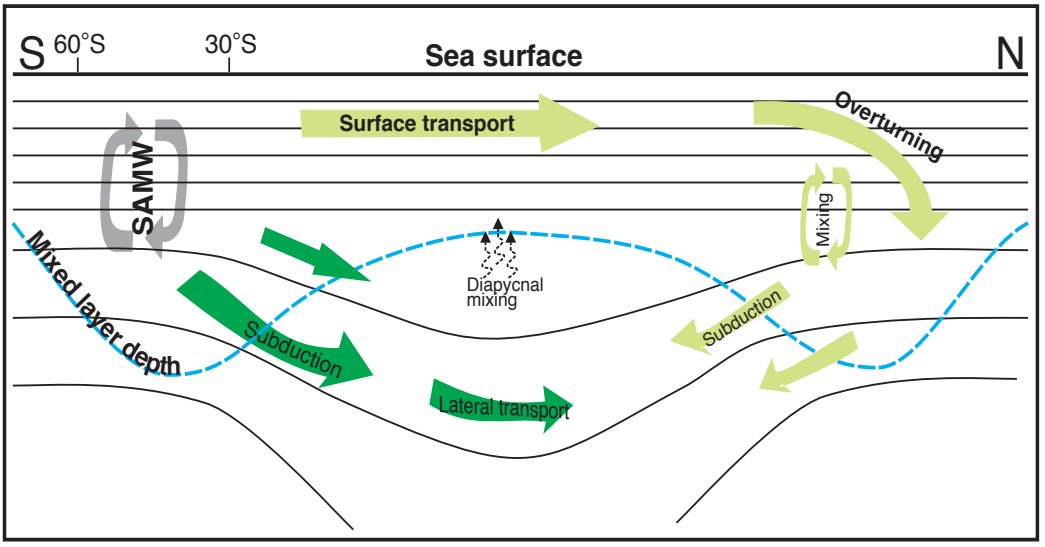

FIGURE 3.7: Schematic of tracer circulation and transport after release in the Southern Ocean, in the absence of a surface consumption mechanism.

After release, the tracer spreads from the source region into the whole mixed layer through vertical convection, and then is subducted into the pycnocline and advected northwards largely following different isopycnal surfaces. In surface layers (potential density $\sigma_2 = 30.90 - 32.75$), tracer always moves faster than within the SAMW layers (potential density $\sigma_2 = 33.54 - 35.80$). The consequence is that before the tracer transported isopycnally along the SAMW layers reaches the high latitudes in the northern hemisphere (eg. the North Atlantic), the surface tracer would already has reached there, and the subsequent mixed-layer subduction in the high latitude of North Atlantic winter outcropped region makes it impossible to identify the upwelling regions of the SAMW there, or anywhere else in the Northern Hemisphere (as outlined in Fig. 3.7).

Although it's not possible to replicate all biogeochemical processes that affect nutrient transport within the SAMW in a general ocean circulation model like HYCOM, it is possible to track and isolate the effect of the physical circulation of SAMW in nutrient transport in the model. Once the tracer reaches the bottom of the surface mixed layer from below, vertical convection will spread it upwards through-out the boundary layer and into the euphotic zone. Therefore, we can consider any tracer/nutrient entering the mixed layer as being

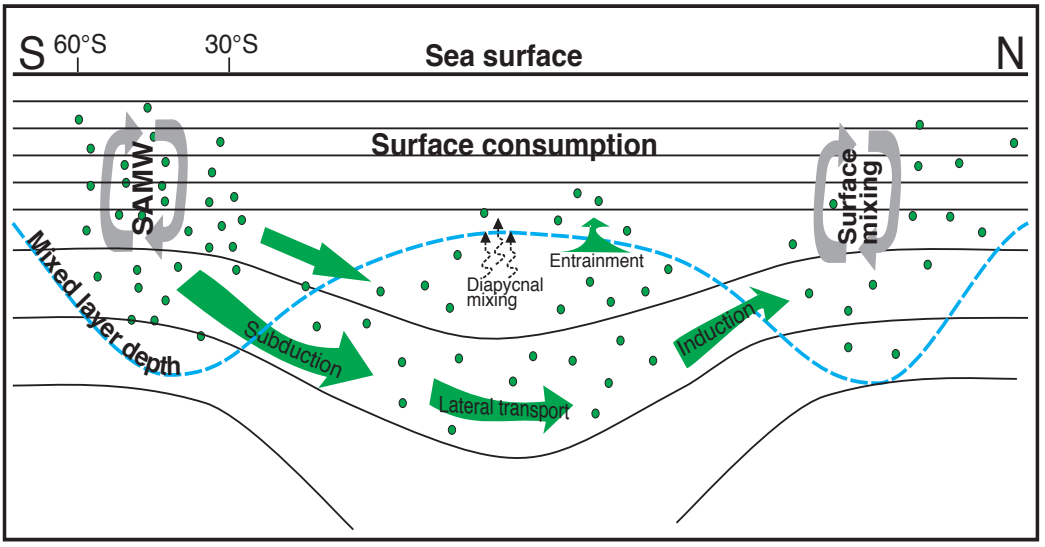

FIGURE 3.8: Schematic of tracer circulation and transport with surface consumption

consumed rapidly by primary producers in the euphotic zone. A tracer consumption scheme for removing surface tracer in order to mimic the biological consumption of nutrient as well as solving the surface contamination problem (Figure 3.7) was developed and implemented into HYCOM. This algorithm is similar to the "eddy rectification" model proposed by McGillicuddy and Robinson (1997), in which the uplift of tracer/nutrient-rich SAMW into the mixed layer is followed by a rapid nutrient utilization and subsequent lowering of nutrient/tracer depleted waters resulting in a net upward flux of tracer/nutrient. In our scheme after release, tracer would be transported freely without applying any artifical intervener so that tracer can be subducted into the thermocline. Technically, this surface removal algorithm is introduced one year after the release and any tracer reaching the mixed layer at anytime thereafter is removed immediately (reset tracer concentration to 0). Except for the tracer that is initially within the mixed layer and is removed for the first time that the removal algorithm is applied, a tracer budget is recorded thereafter. In this way, the accumulated volume of tracer re-emerged into the mixed layer at each geographical position in the model domain is recorded, in terms of each modelled upwelling mechanism at each time step (Figure 3.8). As we will see, this information contains important lessons for both how SAMW mediates nutrient supply to the mixed layer in the ocean and how this supply is separated in climate-role ocean models.

3.2 Diagnosis of basic tracer upwelling fluxes

Before we explain the tracer diagnostic scheme implemented in the model, the concept about the mixed layer must be made clear. HYCOM calculates the mixed layer depth by the density discrepancy criterion (0.03 kgm^{-3} from the surface) as a diagnostic value, so the formation region of SAMW in our model can be compared with the observational data. However, this definition does not imply that active mixing is occurring in this depth range at all times in the model. Another concept used more commonly is the surface boundary layer depth, which is determined by the critical Richardson number in HYCOM and with convection being active in this layer. This surface Boundary Layer Depth (BLD) in HYCOM, as a diagnostic value is not restricted by the vertical resolution and could be inside a isopycnal layer. However, the numerical model cannot resolve the prognostic processes inside coordinate layers. Therefore, we introduce a new definition of the Mixed Layer Depth (MLD) in HYCOM as bounded below by the lower interface of the coordinate layer that contains the BLD (details of this definition are discussed in section 3.3.2). The reader must keep in mind that this MLD has nothing to do with the diagnostic value determined by the density deviation in HYCOM, nor does it share any similarity with the mixed layer depth used in MICOM (the predecessor of HYCOM), which is always identical to the depth of first surface coordinate layer. Thereafter whenever we mention "mixed layer" we actually mean the surface active mixing layer in the model so it is consistent with the tracer diagnostic scheme developed as below.

3.2.1 Mathematical definition and numerical application

HYCOM is a primitive-equation model and calculates all thermodynamic variables (including tracer) within its main loop in the sequence of 9 different subroutines (Fig. 3.9), which are based on 5 prognostic equations (Bleck, 2002). In isopycnic coordinates, the thermal evolution equation for tracer takes the form

$$\frac{\partial}{\partial t}T\Delta p + \underbrace{\nabla\cdot(\mathbf{v}T\Delta p)}_{\text{advec}} + \underbrace{\left(\dot{s}\frac{\partial p}{\partial s}T\right)_{\text{bot}} - \left(\dot{s}\frac{\partial p}{\partial s}T\right)_{\text{top}}}_{\text{dia - flux}} = \underbrace{\nabla\cdot(\upsilon_s\Delta p\nabla T)}_{\text{iso - diff}} + H_T \tag{3.5}$$

Where Δp is the thickness of layer k with tracer T, s is the vertical coordinate of HYCOM, $\dot{s}$ is the time derivative of s, $\mathbf{v} = (u, v)$ is the isopycnal velocity vector, υ_s is a spatially variable (latitude dependent) eddy viscosity/diffusivity coefficient. The expression $\left(\dot{s}\frac{\partial p}{\partial s}\right)$ is the entrainment velocity in pressure per unit time across isopycnal layer interfaces and the subscripts s indicate that the generalized vertical coordinate is held constant during partial differentiation. The radiative exchanges (diabatic source terms) are represented by the term H_T.

For the mixed layer, there is no vertical tracer flux across the sea surface ($\left(\dot{s}\frac{\partial p}{\partial s}T\right)_{\text{top}} = 0$) and no surface diabatic term for the tracer ($H_T = 0$). Eq.(3.5) becomes

$$\frac{\partial}{\partial t}T\Delta h = \underbrace{\nabla \cdot (\upsilon_s \Delta h \nabla T)}_{\text{iso - diff}} - \underbrace{\nabla \cdot (\mathbf{v}T\Delta h)}_{\text{advec}} - \underbrace{\left(\dot{s}\frac{\partial p}{\partial s}T\right)_{\text{bot}}}_{\text{dia - flux}} + H_{\text{m}} \tag{3.6}$$

where $\Delta h = (\mathbf{x}, t)$ is the mixed layer depth and H_{m} is the extra mixing flux due to regridding neutral surfaces in HYCOM's layer generator.

If we define **trcflx** as the time integral of total tracer flux that re-emerged into the ocean mixed layer at a particular grid point; **indflx** as the tracer induction flux into the mixed layer driven by isopycnal advection and diffusion; **kppflx** as the diapycnal tracer flux when considering the mixed layer bottom entrainment and diapycnal diffusion; **hybflx** as the tracer flux into the mixed layer introduced by HYCOM's regridding process, then from Eq.(3.6) we get

$$trcflx = indflx + kppflx + hybflx. \tag{3.7}$$

Now considering the ventilation of a salinity-like tracer, the following subroutines in HYCOM (Figure 3.9) are important:

Advec subroutine isopycnally advects/diffuses tracer from interior of the ocean into the surface boundary layer and thus represents induction.

Thermf subroutine accounts for surface diabatic term and boundary variables' relaxation (T/S/P), based on model-predicted values and this difference from climatological values.

Trcupd subroutine initializes tracer in the SAMW formation region, and applies tracer relaxation if required.

Mxkprf subroutine calculates diapycnal diffusion for thermodynamic variables and tracer according to the K-Profile Parameterization (KPP) mixing scheme (Large et al., 1994).

Hybgen subroutine is the hybrid layer generator for HYCOM and is responsible for remapping isopycnal layer interfaces near the surface after mass fluxes. This process inevitably introduces numerical mixing and its effect has been calculated.

Therefore, the three basic tracer upwelling fluxes described as in Eq.(3.7) can be estimated accordingly in different HYCOM subroutines, by simply comparing tracer patterns before and after calling each subroutine, and then integrating with time. The time integral of total tracer upwelling flux ($trcflx$) is obtained in the end of the main loop (Figure 3.9) when all tracer remaining in the ocean mixed-layer is removed.

3.2.2 Tracer integration method under the leapfrog scheme

For the purpose of saving computational time, HYCOM as well as MICOM, use a time splitting system that calculate advective terms with larger time steps (baroclinic time step) while using smaller time steps (barotropic time step) to resolve the fast-propagating gravity waves. To avoid linear instability, the barotropic time step Δt must be strictly less than or equal to the Courant-Friedrich-Levy (CFL) limit, the value of which depends on the fastest wave propagation speed and advection. However, for $\Delta t = \Delta x/C$ (C is the gravity wave speed and Δx is the minimum horizontal grid spacing), the model blew up after a few time steps due to the varying maximum advection velocity. Therefore a Δt= 75% of the CFL limit has been chosen for our simulations. The baroclinic time step is often an order of magnitude longer than the barotropic time step. Now considering the tracer advection in a one dimensional case with an uniform velocity u, Eq. 3.5 becomes

$$\frac{\partial T}{\partial t} + u\frac{\partial T}{\partial x} = 0. \tag{3.8}$$

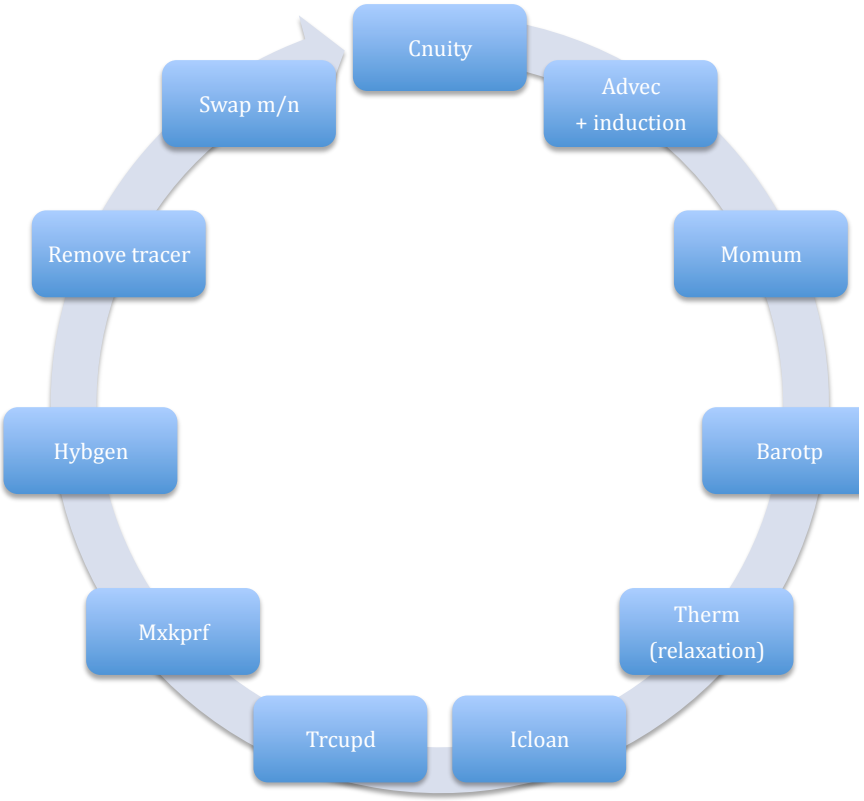

FIGURE 3.9: Schematic Plot of HYCOM Main Loop: (1) Cnuity - continuity equation (2) advec - advection and lateral diffusion (3) Momum - momentum equation (4) Barotp - barotropic solution (5) Therm - surface forcing and relaxation (6) Trcupd - tracer initialization and relaxation (7) Mxkprf - KPP mixing scheme (8) Hybgen - hybrid layer generator. Tracer was injected in the middle of September when mixed-layer depth reaches its maximum value in the Southern Ocean. After that, tracer would be subducted into the ocean interior following the advection/diffusion of the SAMW and ventilate freely for one year, before the surface removal algorithm is applied. In the end of the HYCOM main loop, the model would calculate the time integral of tracer mass that reaches the mixed layer and reset all tracer concentration to zero within the mixed layer.

With the leapfrog scheme (midpoint rule) and space-centered differencing, the numerical solution for Eq. 3.8 through space and time discretization can be written as

$$T_j^{\mathrm{n+1}} = T_j^{\mathrm{n\text{-}1}} + 2\Delta t \frac{(uT_{\mathrm{j+1}}^n - uT_{\mathrm{j\text{-}1}}^n)}{2\Delta x} \tag{3.9}$$

where, T_j^n denotes $T(t_n, x_j)$ is the tracer concentration, Δt and Δx are the time and space increments, respectively. As for the momentum equation, HYCOM introduces a temporal scheme that mixes Euler forward-backward scheme with the second order centered leapfrog scheme. The Euler forward-backward scheme is only applied during the barotropic time step for momentum integration and leapfrog scheme is applied during baroclinic time step.

Though neutrally stable and accurate in second-order, the leapfrog scheme also has some disadvantages. First, the time march per integration is Δt and not $2\Delta t$ because the integration is forwarded from levels $n-1$ to n to $n+1$ rather than directly from $n-1$ to $n+1$. Second, it suffers from computational instabilities due to the odd and even time levels, which makes the leapfrog scheme difficult to use for treating long-term integration and problems with strong nonlinearities (*e.g.*, the strong nonlinearity of tracer concentration in the surface mixed layer due to our tracer releasing and removing scheme). As a result, HYCOM includes the Asselin filter (Asselin, 1972) as a smoothing technology in order to suppress this computational mode. However, this smoothing algorithm can not treat abrupt non-linear events very well as Asselin filter will try to "restore" consumed surface tracer the instant the surface tracer removal scheme applies. As a drawback, the tracer budget is not conserved after applying this smoothing algorithm in HYCOM due to the instantaneous (unphysical) removal of tracer in the mixed layer.

Figure 3.10 shows the time series of total tracer mass inside the mixed layer following the main loop of HYCOM subroutines (Fig. 3.9) and can be used for separating tracer upwelling fluxes due to different mechanisms. The leapfrog's odd and even time levels are referred to as "current" and "previous" time levels in HYCOM. The current time level advances forward and switches between "active" - when tracer upwelling and surface removal scheme apply (blue solid line in Fig. 3.10); and "idle" phases (green dashed line in Fig. 3.10).

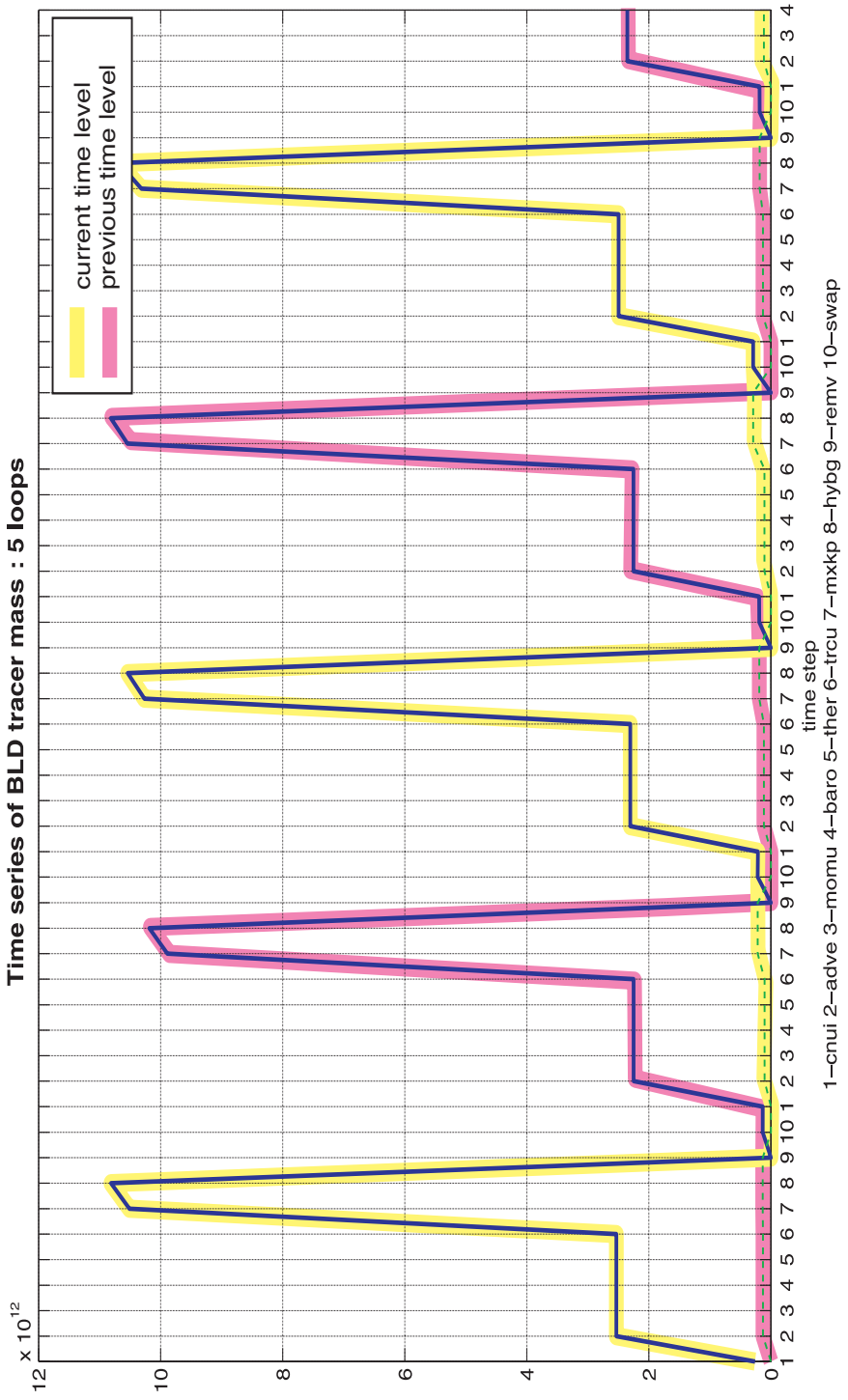

FIGURE 3.10: Time series of tracer mass within the mixed layer. The numerical values following the time axis represent the sequence of different HYCOM sub-routines (see Fig. fig:hycomloop). The blue solid line represents the "active" phase of time level and the dashed green line is the "idle" phase of time level.

For diagnosing the tracer budget within the mixed layer we can simply follow the current time level (yellow thick line in Fig 3.10). During the active phase, tracer is injected into the mixed layer in the sequence of advection/lateral diffusion (calculated as $indflx_{\mathrm{i}}$ from subroutine 2), diapycnal diffusion/entrainment (calculated as $kppflx_{\mathrm{i}}$ from subroutine 7), regridding mixing (calculated as $hybflx_{\mathrm{i}}$ in subroutine 8) and is removed in the end of the phase (calculated as $trcflx$ from subroutine 9). After switching to the "idle" phase, tracer concentration within the mixed layer should remain zero except with some winter time entrainment due to the update of the MLD (calculated as $kppflx_{\mathrm{ii}}$ from subroutine 7 in the idle phase). However, with the Asselin filter on part of the removed tracer in the surface mixed layer is restored (small rise during subroutine 2 in the idle phase) and therefore tracer budget is not conserved. Because the Asselin smoothing parameter has been hard-wired into the HYCOM code, we have no choice but to disable this filter when calculating the tracer prognostic equation. The tracer budget is conserved after the Asselin filter has been turned off and the conservation equation of tracer (Eq. (3.7)) becomes

$$trcflx = indflx_{\mathrm{i}} + kppflx_{\mathrm{i}} + hybflx_{\mathrm{i}} + kppflx_{\mathrm{ii}} \tag{3.10}$$

where the subscript i/ii represents active/idle phase, respectively.

3.2.3 Validation of the basic diagnostic scheme

Based on the diagnosing scheme described above, the standard experiment was integrated over a period of 150 years. The integration time was chosen with care while considering both the computing efficiency and the time scale of SAMW ventilation in the model.

It is clear that after release in the middle of the first September, the global mean tracer concentration stays constant until it has been removed in the surface boundary layer (re-emergence) one year after the release (Fig. 3.11). The time integral of the total re-emergence of this salinity-like tracer ($trcflx$) gradually increases while the amount of tracer remaining in the interior of the ocean decreases ($tracer$). The wave-like rising pattern of $trcflx$ curve represents the seasonal variation of tracer upwelling rate in the Southern Ocean: the regions where the slope of the curve is steep corresponds to fast upwelling during the southern winter, while regions with flat slope correspond to slow

upwelling during the southern summer. During the experiment total tracer mass ($trcflx + tracer$) is always conserved and Eq. (3.10) is satisfied (Fig. 3.12).

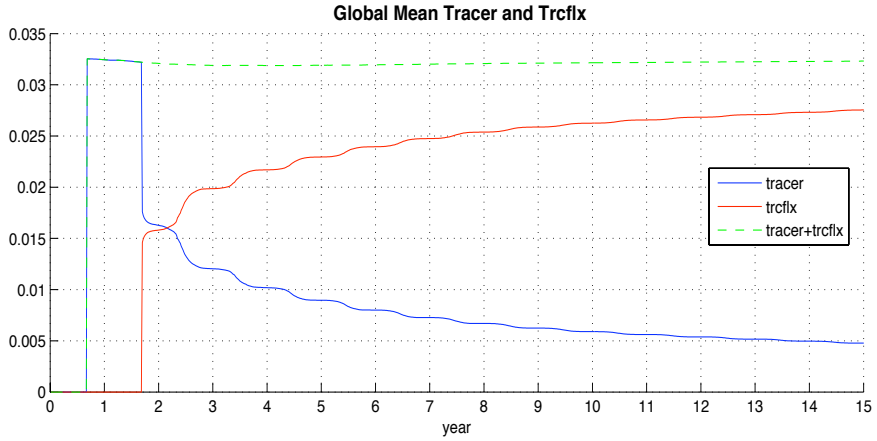

FIGURE 3.11: Time series of global mean tracer concentration (in tracer unit/m^3). The dashed green line represents the sum of tracer that remains in the interior of ocean and tracer re-emergence into the mixed layer.

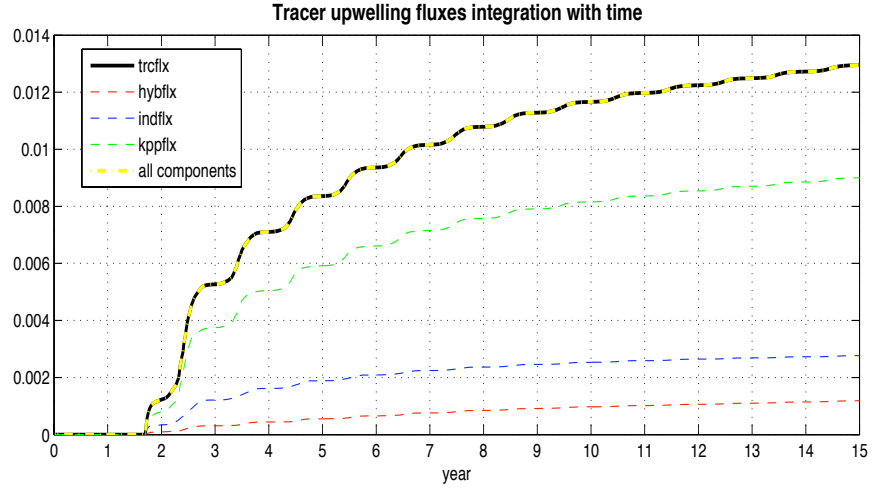

FIGURE 3.12: Time integral of tracer fluxes (in tracer unit/m^3) that gets into the mixed layer due to different upwelling mechanisms

3.3 Diagnosis of diapycnal tracer fluxes

Although the Kraus-Turner (KT) mixing model was used in the global simulation of Bleck (2002), we chose the nonlocal K-Profile Parameterization model (Large et al., 1994) for our tracer ventilation experiment. This observationally based algorithm was initially designed to work with fixed coordinate system but can be applied to the whole water column in HYCOM. Technical details of the implementation of these vertical mixing algorithms have been included in the HYCOM Users Manual (Bleck et al., 2002).

3.3.1 KPP mixing scheme

The K-Profile Parameterization (KPP) model is described in detail in Large et al. (1994). The key idea of the KPP mixing scheme is to separate the ocean into two parts: an ocean surface region with strong mixing (refered as Surface Boundary Layer thereafter) under a variety of surface forcing conditions, and an interior region of weak mixing under the influence of internal waves, shear instability, and double diffusion. The diffusivity is formulated to agree with similarity theory of turbulence in the surface layer and is subject to the conditions that both it and its vertical gradient match the interior values at the bottom of the boundary layer. To summarize the implementation of KPP mixing and how it affects tracer upwelling in HYCOM, we need to understand the diagnosis of this surface boundary layer depth introduced by Large et al. (1994) first.

In the KPP mixing scheme, the Surface Boundary Layer thickness (h_b) is defined as the depth range over which turbulent boundary layer eddies can penetrate before becoming stable relative to the local buoyancy and velocity. It is estimated as the minimum depth at which the bulk Richardson number Ri_b exceeds a critical value (set to $Ri_c = 0.45$ in our standard experiment). This bulk Richardson number is a variable of layer number and can be calculated by using the following equation

$$Ri_b = \frac{(B_r - B)d}{(\overline{\mathbf{v}}_r - \overline{\mathbf{v}})^2 + V_t^2} \tag{3.11}$$

where B is buoyancy, d is depth , the subscript r denotes reference values, and where the two terms in the denominator represent the influence of resolved vertical shear ($(\overline{\mathbf{v}}_r - \overline{\mathbf{v}})^2$) and unresolved turbulent velocity shear (V_t^2), respectively. Reference values are averaged over the depth range εd, where $\varepsilon = 0.1$. At depth $d = h_b$, the reference depth (εd) represents the thickness of surface layer where Monin-Obukhov similarity theory applies.

The unresolved turbulent velocity shear in the denominator of (3.11) is estimated from

$$V_t^2 = \frac{(-\beta_T)^{1/2}}{Ri_c \kappa^2} (c_s \varepsilon)^{-1/2} d N w_s \tag{3.12}$$

where c_s is a constant between 1 and 2 to account for smoothing of the buoyancy profile caused by mixing. β_T is the ratio of entrainment buoyancy flux to surface buoyancy flux, $\kappa = 0.4$ is the von Karman constant, and w_s is the tracer/salinity turbulent velocity scale.

The Richardson number is calculated for each layer and increases with the depth (layer number) when moving downward from the surface. When the first layer is reached where $Ri_b > Ri_c$, the thickness of Surface Boundary Layer (h_b) is estimated by linear interpolation between the central depths of that layer and the layer above.

After defining the ocean into two distinct regimes, vertical mixing in the ocean interior beyond the boundary layer is regarded as the superposition of three processes: local Richardson number instability due to resolved vertical shear, internal wave breaking and double diffusion. Model variables are first decomposed into mean (denoted by a overbar) and turbulent (denoted by a prime) components. Diapycnal diffusivities for a salinity-like tracer are parameterized in the ocean interior as follows:

$$\overline{w'T'} = -\nu_T \frac{\partial \overline{T}}{\partial z} \tag{3.13}$$

$$\nu_T = \nu_T^s + \nu_T^w + \nu_T^d \tag{3.14}$$

where ν_T is the interior diffusivity of tracer, which consists of three components: ν_T^s is the contribution of resolved shear instability, ν_T^w is the contribution of unresolved shear instability due to background internal wave field, and ν_T^d is the contribution of double diffusion.

The contribution of shear instability is parameterized in terms of the gradient Richardson number calculated at isopycnal layer interfaces:

$$Ri_g = \frac{N^2}{\left(\frac{\partial \overline{u}}{\partial z}\right)^2 + \left(\frac{\partial \overline{v}}{\partial z}\right)^2} \tag{3.15}$$

where N^2 is the buoyancy frequency and mixing is triggered when $Ri_g = Ri_0 < 0.7$. Vertical derivatives are estimated at model interfaces as follows: Given model layer k bounded by interfaces k and $k+1$, the vertical derivative of $\overline{u}$ at interface k is estimated as

$$\frac{\partial \overline{u}}{\partial z} = \frac{\overline{u}^{k-1} - \overline{u}^{k}}{0.5(h^k + h^{k-1})} \tag{3.16}$$

where h^k is the thickness of layers k. The contribution of shear instability for tracer (all scalars) diffusion is given by

$$\nu_T^s = \begin{cases} \nu_T^0 & Ri_g < 0 \\ \nu_T^0 \left[1 - \left(\frac{Ri_g}{Ri_0}\right)^2\right]^P & 0 < Ri_g < Ri_0 \\ 0 & Ri_g > Ri_0 \end{cases} \tag{3.17}$$

where $\nu_T^0 = 50 \times 10^{-4} m^2 s^{-1}$, is the maximum value of diffusion due to shear instability and is chosen to fall within the range of maximum observed diffusivities reported for the seasonal thermocline; $Ri_0 = 0.7$, is the critical Richardson number and $P = 3$.

The diffusivity that results from the unresolved background internal wave shear used in our run is constant and $\nu_T^w = 10^{-5} m^2 s^{-1}$. Double diffusive mixing can occur when the vertical gradient of density is stable but the vertical gradient of either salinity or temperature is unstable in its contribution to density. Though most numerical turbulence closure schemes commonly employed in numerical

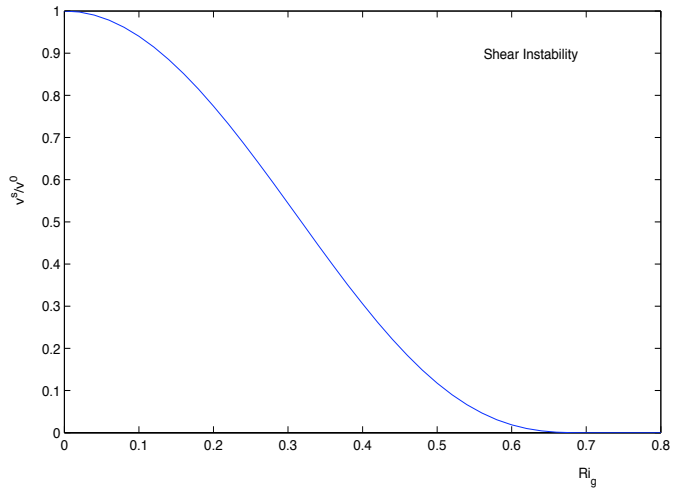

FIGURE 3.13: Interior diffusivity due to shear instability mixing, normalized by its maximum value ν_T^0, as a function of local gradient Richardson number (Large et al., 1994).

models have neglected double diffusion induced mixing, it has been suggested that salt-fingering instabilities generate substantial nutrient fluxes of similar magnitude to the fluxes associated with mechanically induced turbulence or with mesoscale eddies (Oschlies et al., 2003; Glessmer et al., 2008). Zhang et al. (1998) developed a double diffusion mixing scheme based on density ratio and has been incorporated here in the KPP mixing scheme. Regions where double diffusive processes are important are identified using the double diffusion density ratio calculated at model interfaces:

$$R_\rho = \frac{\alpha \frac{\partial \overline{\theta}}{\partial z}}{\beta \frac{\partial \overline{S}}{\partial z}} \tag{3.18}$$

where $\alpha = -\frac{1}{\rho}\frac{\partial \rho}{\partial T}$ is the thermal expansion coefficient, $\beta = -\frac{1}{\rho}\frac{\partial \rho}{\partial S}$ is the haline contraction coefficient. For salt fingering (warm, salty water overlying cold, fresh water), tracer/salinity diffusivity is given by

$$\nu_T^d = \begin{cases} \nu_f \left[1 - \left(\frac{R_\rho - 1}{R_\rho^0 - 1}\right)^2\right]^P & 1.0 < R_\rho < R_\rho^0 \\ 0 & R_\rho \geq R_\rho^0 \end{cases} \tag{3.19}$$

where $\nu_f = 10 \times 10^{-4} m^2 s^{-1}$, $R_\rho^0 = 1.9$ and $P = 3$. For diffusive convection

(cold, fresh water overlying warm, salty water), tracer/salinity diffusivity is given by

$$\nu_T^d = \begin{cases} \nu_\theta^d(1.85 - 0.85R_\rho^{-1})R_\rho & 0.5 \leq R_\rho \leq 1 \\ \nu_\theta^d(0.15R_\rho) & R_\rho < 0.5 \end{cases} \tag{3.20}$$

where $\nu_\theta^d$is temperature diffusivity due to diffusive convection and is given by

$$\frac{\nu_\theta^d}{\upsilon_m} = 0.909\exp\{4.6\exp[-0.54(R_\rho^{-1} - 1)]\} \tag{3.21}$$

where υ_m is the molecular viscosity for temperature (see Fig. 3.14).

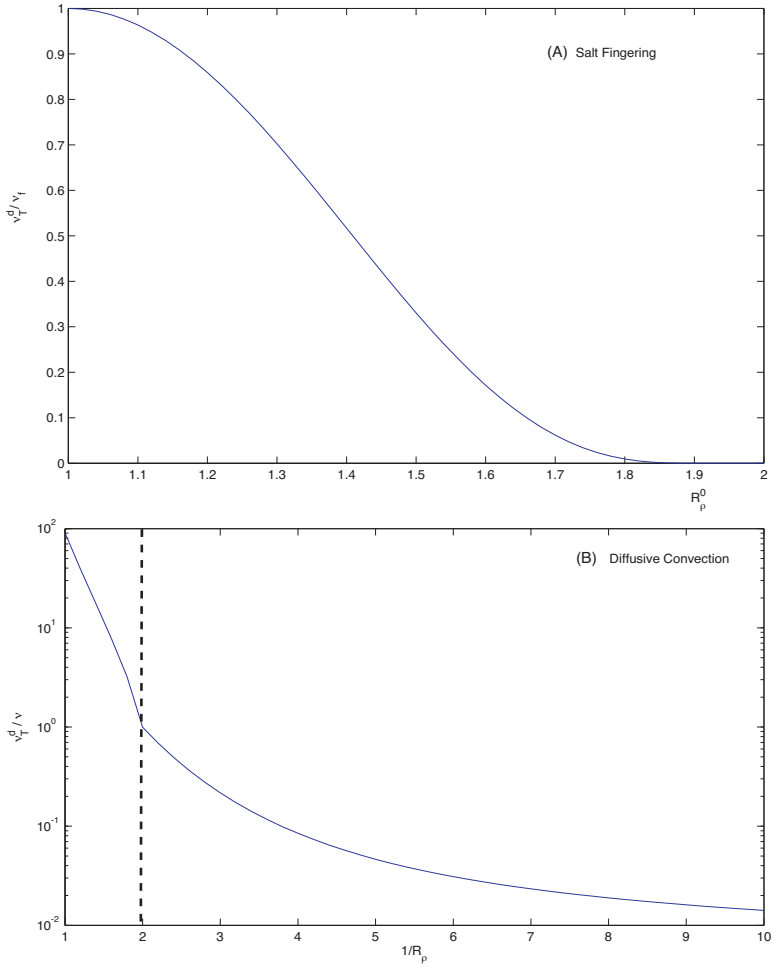

FIGURE 3.14: Interior diffusivity for double diffusion due to (a) salt fingering (Eq. (3.19)), and (b) diffusive convection (Eq. (3.20)).

The diffusivity profiles within the surface boundary layer depend on surface forcing (wind stress, radiation and freshwater fluxes) and the magnitude and the gradient of the interior mixing at the boundary layer base. They are parameterized as :

$$K_T(\sigma) = h_b w_T(\sigma) G_T(\sigma) \tag{3.22}$$

where $\sigma = d/h_b$ and d is the depth from surface, w_T is the scalar turbulent velocity scale. G is a smooth shape function represented by a third-order polynomial function

$$G(\sigma) = a_0 + a_1\sigma + a_2\sigma^2 + a_3\sigma^3. \tag{3.23}$$

Since turbulent eddies do not cross the ocean surface, all K coefficients are zero there, which requires that $a_0 = 0$. The remaining coefficients of the shape function are chosen to satisfy requirements of Monin-Obukhov similarity theory, and also to ensure that the resulting value and first vertical derivative of the boundary layer K-profile match the value and first derivative of the interior diffusivity profile (calculated from Eq. (3.17), (3.19) and (3.20)). At model interfaces within surface boundary layer, the K profile diffusivity for tracer is provided by Eq. (3.22). At model interfaces below the boundary layer, the K profile equals the interior diffusivity ($K_T = \nu_T$).

3.3.2 Diapycnal diffusion and entrainment

Following the tracer releasing/integration scheme described before, any tracer re-emergence north of the $30°S$ into the surface active mixing layer would be integrated over time as an upwelling flux, and be consumed/removed immediately in order to avoid surface contamination. According to the K-profile parameterization scheme, this active mixing layer is actually defined as the Surface Boundary Layer over which turbulent surface eddies can penetrate before becoming stable relative to the local buoyancy and velocity in HYCOM (Eq. (3.11)).

In ocean circulation studies, the depth of the mixed layer is often determined by two criteria based on temperature and potential density. The mixed layer depth is defined as the position where the temperature/density deviates from the surface temperature/density by a prescribed value. As for Levitus (1982),

this value is 0.5 degrees Celsius for temperature and 0.125 of σ_t for potential density, respectively. However, neither criterion implies that active mixing is occurring in the mixed layer depth range at all times. Therefore, we introduced a new definition of mixed layer depth here, which is bounded below by the lower interface of the coordinate layer that contains the Surface Boundary Layer Depth:

$$h_b = p_{\mathrm{k}} + a(p_{\mathrm{k+1}} - p_{\mathrm{k}}) \qquad \text{if} \quad Ri_b^{\mathrm{k}} < Ri_c < Ri_b^{\mathrm{k+1}} \tag{3.24}$$

$$h_{\mathrm{mix}} = p_{\mathrm{k+1}} \qquad \text{if} \quad p_{\mathrm{k}} < h_b < p_{\mathrm{k+1}} \tag{3.25}$$

where h_b is the Boundary Layer Depth (BLD) defined by the bulk Richardson number Ri_b, $a = (Ri_c - Ri_b^k)/(Ri_b^{\mathrm{k+1}} - Ri_b^k)$, h_{mix} is the Mixed Layer Depth (MLD), p_k is the isopycnal layer interface depth in pressure (unit dbar) and subscript/superscript k denotes layer number. This definition of mixed layer depth is consistent with the vertical mixing scheme used in HYCOM, which splits ocean into two different regions with different diffusivity profiles. However, we need to keep in mind that this MLD can be either deeper or shallower than the Ekman layer depth. For example, if the net heat flux into the ocean is positive, the diagnosed value of h_b is required to be smaller than both the Ekman length scale $h_E = 0.7u^*/f$ (u^* is the drag velocity and f is the Coriolis coefficient) and the Monin-Obukhov length

$$L = \frac{(u^*)^3}{\kappa \cdot \frac{g}{T_0} \cdot \frac{q}{c_p \cdot \rho}} \tag{3.26}$$

where $\kappa = 0.4$ is von Karman constant, T_0 is surface temperature, q is kinematical heat flux and c_p specific heat.

There are three primary sources of energy for driving turbulent mixing within the mixed layer: breaking of surface waves, wind-driven velocity shears and surface cooling. Among them the final two processes have been included in our model in the form of surface buoyancy fluxes (radiative exchanges, heat convection, precipitation and evaporation) and mechanical energy transfers into the ocean, and have been demonstrated by Eq. (3.11) in the KPP mixing scheme. These surface fluxes are applied as a set of climatological surface forcing fields. A seasonal thermocline and MLD appear in our experiment following the seasonal cycle of the climatological surface forcing fields. Now considering

some combination of these surface fluxes, the BLD for a fixed location in the open ocean may shift up or down within the water column, depending on the relative strengths of stabilizing (positive heat flux into the ocean) and destabilizing (strong wind forcing or negative heat flux into the ocean) surface forcings. Therefore, the updated MLD may change relative to the previous MLD before diapycnal mixing is applied in the KPP scheme, and one of three cases will apply:

1. Surface forcing is stabilizing via surface warming and/or wind stress getting weaker, leading to rise of the BLD ($h_b^{n+1} < h_b^n$) and MLD ($h_{\text{mix}}^{n+1} < h_{\text{mix}}^n$, superscript n denotes time step).

2. Surface forcing maintains stratification and turbulent eddies, therefore both BLD and MLD stay at their previous positions ($h_b^{n+1} = h_b^n$, $h_{\text{mix}}^{n+1} = h_{\text{mix}}^n$).

3. Surface forcing is destabilizing via surface cooling and/or wind stress getting stronger, leading to the descent of the BLD ($h_b^{n+1} > h_b^n$) and MLD ($h_{\text{mix}}^{n+1} > h_{\text{mix}}^n$).

The above three cases are demonstrated by Fig. 3.15. Considering a fixed location in the open ocean, the mixed layer contains 3 surface layers (layer 1,2,3) before applying the vertical mixing scheme in the model. Tracer transports follow isopycnal surfaces below the mixed layer through advection and lateral diffusion. Within the mixed layer there is strong boundary layer mixing (convection) and no tracer due to the tracer consumption/integral scheme. Tracer can get to the surface mixed layer through diapycnal diffusion and induction crossing the lower interface of mixed layer, or by entrainment due to deepening of the MLD. After re-evaluating surface forcing and re-calculating BLD in KPP scheme, the above three cases apply:

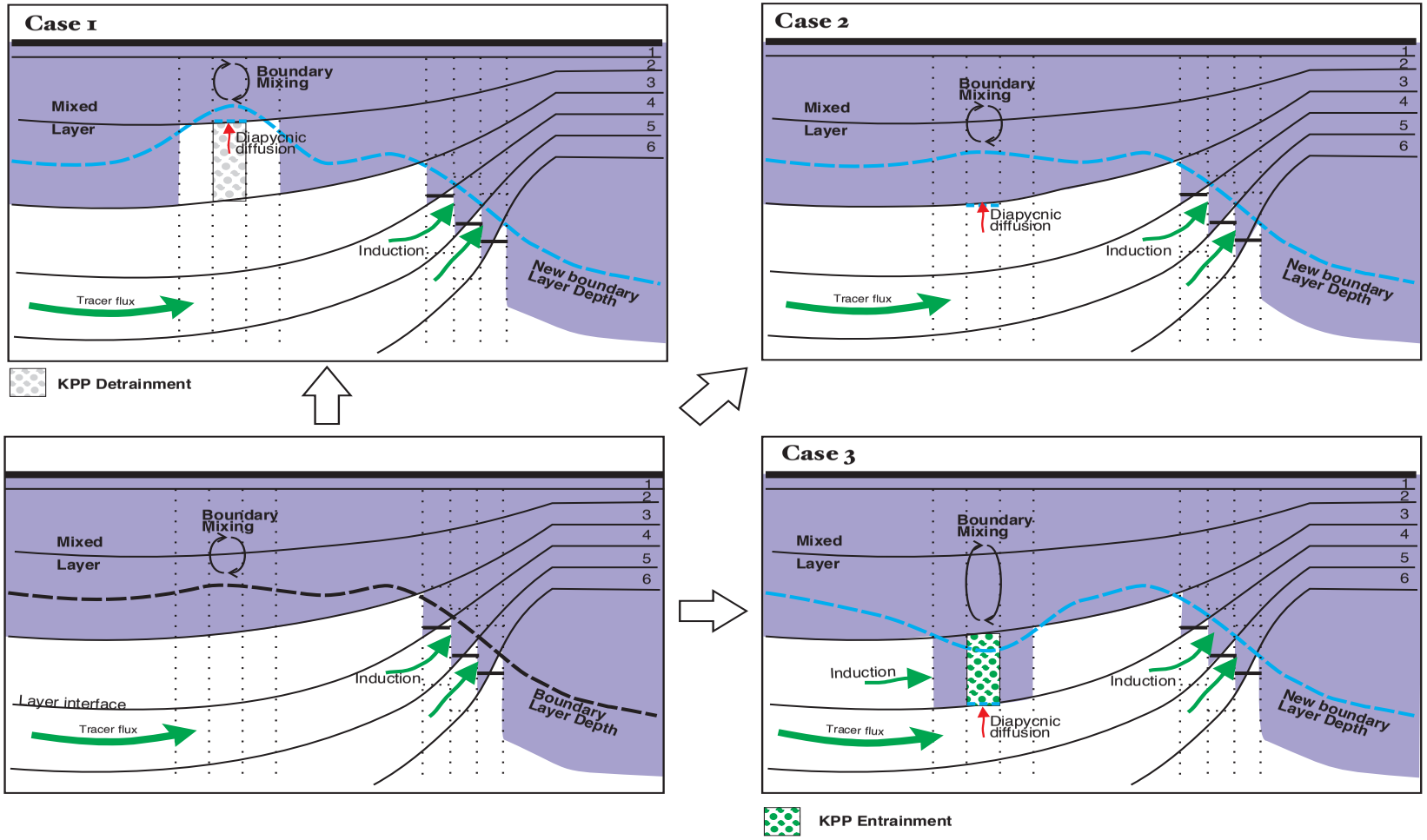

FIGURE 3.15: Tracer upwelling diagnostic scheme for KPP mixing generated diapycnal fluxes cross the base of mixed layer: (a) Case 1, $N_b^{n+1} = N_b^n - 1$; (b) Case 2, $N_b^{n+1} = N_b^n$ and (c) Case 3, $N_b^{n+1} = N_b^n + 1$. N represents the deepest isopycnal layer number within the mixed layer and superscript n here denotes time step. Blue shaded region represents the mixed layer in the surface.

- Case-1, Mixed layer getting thinner after vertical mixing and water mass in layer 3 has been detrained away (KPP detrainment). The differences of total tracer within the mixed layer before and after calling the KPP subroutine is only the result of diapycnic diffusion flux (integrated as $diaflx$) crossing the new mixed layer bottom.

- Case-2, there is no entrainment or detrainment after re-calculating BLD, all tracer upwelling is due to diapycnic diffusion.

- Case-3, due to surface cooling the new BLD penetrates into layer 4 and the new mixed layer includes 4 surface layers (layer 1, 2, 3 and 4). Water mass within layer 4 is completely entrained (KPP entrainment) into the mixed layer, as well as any tracer within this layer. This entrained tracer upwelling flux was integrated as $entflx$. If any of the neighboring grid in layer 4 is not included in mixed layer, then lateral advection in this layer may also generate some tracer upwelling into the mixed layer ($indflx$) in the loop. Therefore, difference of tracer within the mixed layer before and after calling KPP subroutine is actually the results of both diapycnic diffusion and KPP entrainment.

In summary, $kppflx$ can be written in the form of

$$kppflx = \begin{cases} diaflx & N^{n+1} \leq N^{n} \\ diaflx + entflx & N^{n+1} > N^{n} \end{cases} \tag{3.27}$$

where $N = f(x, y)$ is the layer number that contains the BLD and superscript n denotes time step. $kppflx$ is the total tracer upwelling flux generated by KPP mixing scheme; $diaflx$ is the tracer flux that gets to the mixed layer via diapycnic diffusion; $entflx$ is the entrained tracer flux.

Because the diapycnic diffusion generated tracer upwelling fluxes are calculated based on the vertical diffusivity at the bottom of the surface boundary layer, the value of K-profile diffusivity there equals the interior diffusivity. According to the KPP mixing scheme, this value is the sum of 3 terms (Eq. (3.14)). Combining Eq. (3.13) and Eq. (3.14) we get:

$$\underbrace{\overline{w'T'}}_{\text{diaflx}} = \underbrace{-\nu_T^s \frac{\partial \overline{T}}{\partial z}}_{\text{shrflx}} \underbrace{-\nu_T^w \frac{\partial \overline{T}}{\partial z}}_{\text{bckflx}} \underbrace{-\nu_T^d \frac{\partial \overline{T}}{\partial z}}_{\text{ddflx}} \tag{3.28}$$

where $shrflx$, $bckflx$ and $ddflx$ are tracer upwelling fluxes due to resolved velocity shear, background diffusion (internal wave) and double diffusion, respectively. Considering that the magnitude of $diaflx$ is already known and values of ν_T^s and ν_T^d can be calculated by Eq. (3.17), (3.19) and (3.20), then the contributions of shear, background and double diffusion to tracer upwelling fluxes can be calculated with the following equations:

$$shrflx = diaflx \cdot \frac{\nu_T^s}{\nu_T} \tag{3.29}$$

$$bckflx = diaflx \cdot \frac{\nu_T^w}{\nu_T} \tag{3.30}$$

$$ddflx = diaflx \cdot \frac{\nu_T^d}{\nu_T} \tag{3.31}$$

where $\nu_T = \nu_T^s + \nu_T^w + \nu_T^d$. Because the basic tracer diagnostic scheme already calculates the $kppflx$ and $diaflx$, combining Eq. (3.27) and (3.29) - (3.31) we can calculate the 4 terms of $kppflx$.

Validation of this advanced diagnostic scheme has been carried out in a model run with the same initial condition and tracer release/integration scheme, and model has been integrated over a period of 150 years again. According to the physical mechanisms responsible for the re-mergence, $kppflx$ decomposes into 4 different tracer fluxes: $bckflx$ due to background diffusion, $shrflx$ due to shear diffusion, $ddflx$ due to double diffusion effects, and $entflx$ due to seasonal cycle of the mixed layer thickness and corresponding entrainment. During our experiment global tracer is fully accounted for by these collective terms, as shown in Fig. 3.16.

3.4 Interpretation of regridding upwelling in terms of physical process and numerical mixing

3.4.1 Hybrid Layer Generator

The grid generator is the final algorithm executed during each model time step. Bleck (2002) described the hybrid vertical coordinate grid generator and its implementation in HYCOM. The two key features of this scheme are: (1) to restore isopycnic conditions in coordinate layers according to prescribed target densities; (2) maintain finite layer thickness of coordinate layers at the price

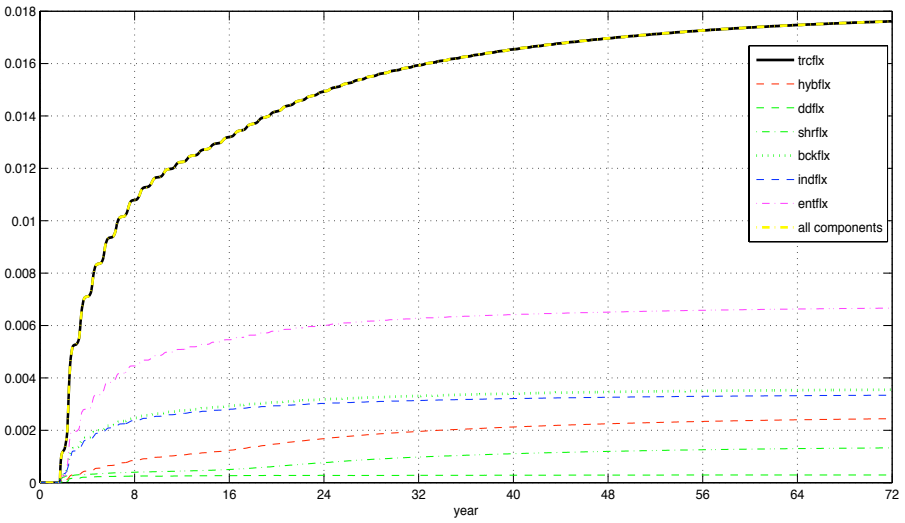

FIGURE 3.16: Time integral of tracer fluxes (in tracer unit/m^3) that re-emerge into the mixed layer due to different upwelling mechanisms

of allowing them to become nonisopycnic in the upper ocean, where lack of stratification would cause isopycnic layers to collapse to zero thickness. If a density discrepancy appears, or a layer is getting too thin, two basic strategies were adopted in HYCOM for satisfying the above features by (1) diluting the layer with water from the layer above/below; or by (2) dividing the layer whose density should be modified into two sublayers of different densities and expelling one sublayer into neighboring layers. The process of moving layer interfaces due to either the minimum layer thickness criterion or target density criterion here is called "regridding".

Because the lateral transports are resolved in the advection subroutine, considering only the vertical fluxes there are two physical processes that are involved in introducing density discrepancies into HYCOM surface layers: air-sea buoyancy exchanges and/or diapycnal mixing of thermodynamic variables (temperature and salinity) across the lower interface of the mixed layer. Currently the non-local K-profile Parameterization model has been used as the vertical mixing scheme for the surface boundary layer in HYCOM, while a supplemental mixing algorithm (McDougall and Dewar, 1998) has been adopted for the interior diapycnal mixing. Unlike McDougall-Dewar's scheme, the K-Profile Parameterization scheme was originally developed for fixed-grid models and is only responsible for mixing of thermodynamic variables and momentum without moving water mass between layers. As a result, potential densities within

the mixed layer may deviate from the target values after diapycnal mixing of temperature and salinity (KPP) and an additional coordinate layer remapping algorithm must be applied in HYCOM as a supplement to the KPP scheme. Because this vertical remapping required to restore reference density is a process not found in fixed-grid models, it would probably introduce a dissipative effect.

Now consider two regridding cases caused only by restoring density and excluding the contribution from wind-induced Ekman volume divergence, which will be discussed separately in Chapter 4. The remapping algorithm used in HYCOM for this hybrid layer generator is summarized here. Consider three consecutive isopycnic layers labeled k-1, k and k+1 in a stratified water column and layer k is at the base of the mixed layer (Fig. 3.17). The specific volume (α_k) of layer k would decrease and become smaller than its isopycnic reference value $\hat{\alpha}_k$ if there is a oceanic buoyancy loss due to surface cooling and/or if the diapycnal mixing across the lower interface of the mixed layer tends to increase the density of the surface layers. To restore isopycnic conditions, it is necessary to re-discretize the water column by moving the upper interface (p_k) upward to entrain less dense water from layer k-1 into layer k (Fig. 3.17). It is clear that this process would not introduce additional diapycnal tracer upwelling into the mixed layer because both layers are within the mixed layer.

For $\alpha_k < \hat{\alpha}_k$, conservation of $\int \alpha \, dp$ in the water column requires that the new position for the layer interface p_k be

$$\hat{p}_k = \frac{p_k(\alpha_{\text{k-1}} - \alpha_k) + p_{\text{k+1}}(\alpha_k - \hat{\alpha}_k)}{\alpha_{\text{k-1}} - \hat{\alpha}_k}. \tag{3.32}$$

Without additional constraints layer k-1 would get thinner and eventually collapse to zero thickness due to the lack of stratification. However, HYCOM will try to maintain a finite layer thickness by replacing $\hat{p}_k$ by

$$\tilde{p}_k = min[p_{\text{k+1}}, max(\hat{p}_k, p_{\text{k-1}} + \Delta_{\text{k-1}})], \tag{3.33}$$

where $\Delta_{\text{k-1}}$ is a specified minimum layer thickness for layer k-1. As a result, layers near the surface with densities exceeding their reference values cannot have isopycnic conditions restored and density surfaces then bend upwards and eventually intersect the sea surface. Following Bleck and Benjamin (1993), this

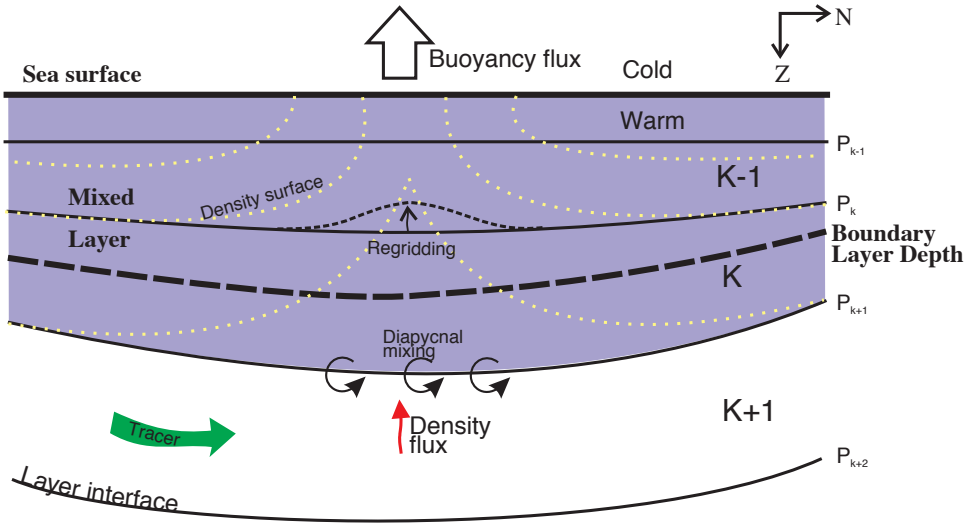

FIGURE 3.17: Schematic of HYCOM regridding process due to density discrepancy, case one: surface cooling and/or diapycnal mixing increase the potential density of layer k. Black contours denote the model layer interfaces before (solid) and after (dashed) the regridding process. Yellow dash contours denote the bending density surfaces after the regridding due to the minimum layer thickness constraint. There is no extra tracer upwelling in this case.

minimum thickness is determined by a constant minimum thickness δ_k using a cushion function that produces a smooth transition from the isopycnic to the surface p domain. Here we have chosen a constant value of 10 m for δ_k as both small or large values of δ_k can cause inadequate representation of the vertical resolution in the mixed layer due to the seasonal cycle of the simulated thermocline. Preservation of the minimum layer thickness always overrides attempts to restore isopycnic conditions in HYCOM.

If the surface buoyancy flux is positive into the ocean (surface warming) and/or diapycnal mixing at the base of the mixed layer tends to decrease the density of the surface layers, then layer k becomes too light ($\alpha_k > \hat{\alpha}_k$) and the lower interface ($p_{\mathrm{k+1}}$) needs to move downward to entrain denser water from layer k+1 into layer k. The new pressure level to which the interface must be relocated is

$$\hat{p}_{\mathrm{k+1}} = \frac{p_k(\hat{\alpha}_k - \alpha_k) + p_{\mathrm{k+1}}(\alpha_k - \alpha_{\mathrm{k+1}})}{\hat{\alpha}_k - \alpha_{\mathrm{k+1}}}. \tag{3.34}$$

To maintain the minimum thickness of layer k+1, $\hat{p}_{\mathrm{k+1}}$ is replaced by

$$\tilde{p}_{\mathrm{k+1}} = min(\hat{p}_{\mathrm{k+1}}, p_{\mathrm{k+2}} - \Delta_{\mathrm{k+1}}), \tag{3.35}$$

As shown in Fig. 3.18, this regridding process introduces tracer entrainment into the mixed layer. This extra tracer upwelling term due to restoring the density is originally induced by both air-sea buoyancy exchange and interior diapycnal mixing. Although the magnitude of this extra tracer upwelling flux can be calculated, it is not possible to separate the contributions of surface buoyancy input from the KPP mixing in the current version of HYCOM.

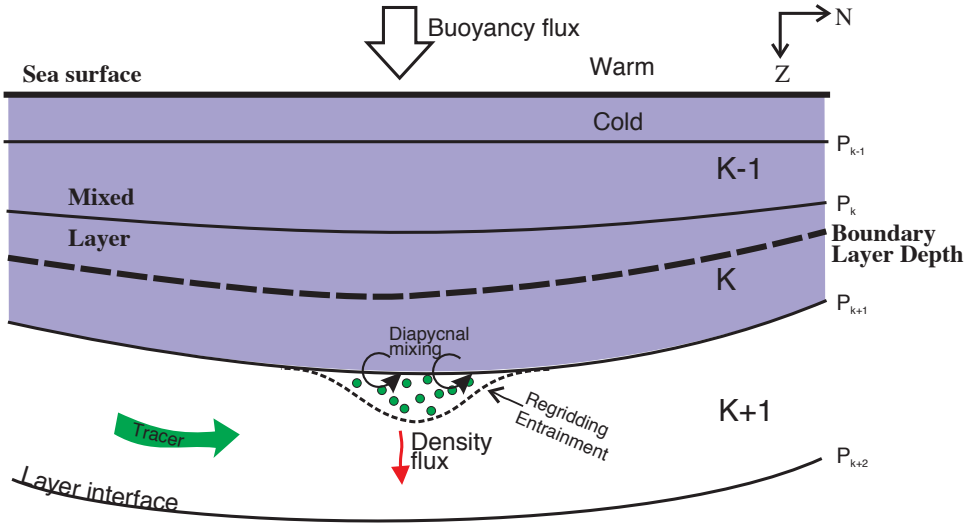

FIGURE 3.18: Schematic of HYCOM regridding process due to density discrepancy, case two: surface warming and/or diapycnal mixing decreases the potential density of layer k. The lower interface moves downward to entrain denser water from layer k+1 into layer k but restricted by the minimum layer thickness constraint. Additional tracer upwelling is introduced in this case by entraining tracer from the interior to the mixed layer via regridding the lower interface of the mixed layer.

If layer k is the deepest layer with nonzero thickness and is too light, the interface with pressure $p_{\mathrm{k+1}}$ cannot move downward to restore isopycnic conditions and the above diluting algorithm would not be applied. Instead, an unmixing algorithm would be employed to split the water in layer k into two sublayers. The density of the upper sublayer exactly equals the density of layer k-1 and the density of the lower sublayer is close to the desired reference density. The interface k is relocated using

$$\hat{p}_k = p_k + q(p_{\mathrm{k+1}} - p_k), \tag{3.36}$$

and the conservation of mass implies that

$$q = \frac{\alpha_k - \hat{\alpha}_k}{\alpha_{\text{k-1}} - \hat{\alpha}_k}.$$

Thermodynamical variables and tracer in the lower sublayer are then calculated using

$$\hat{T}_k = T_k - (\frac{q}{1-q})(T_k - T_{\text{k-1}}). \tag{3.37}$$

The general idea of this hybrid layer generator is demonstrated in the flow chart in Fig. 3.19.

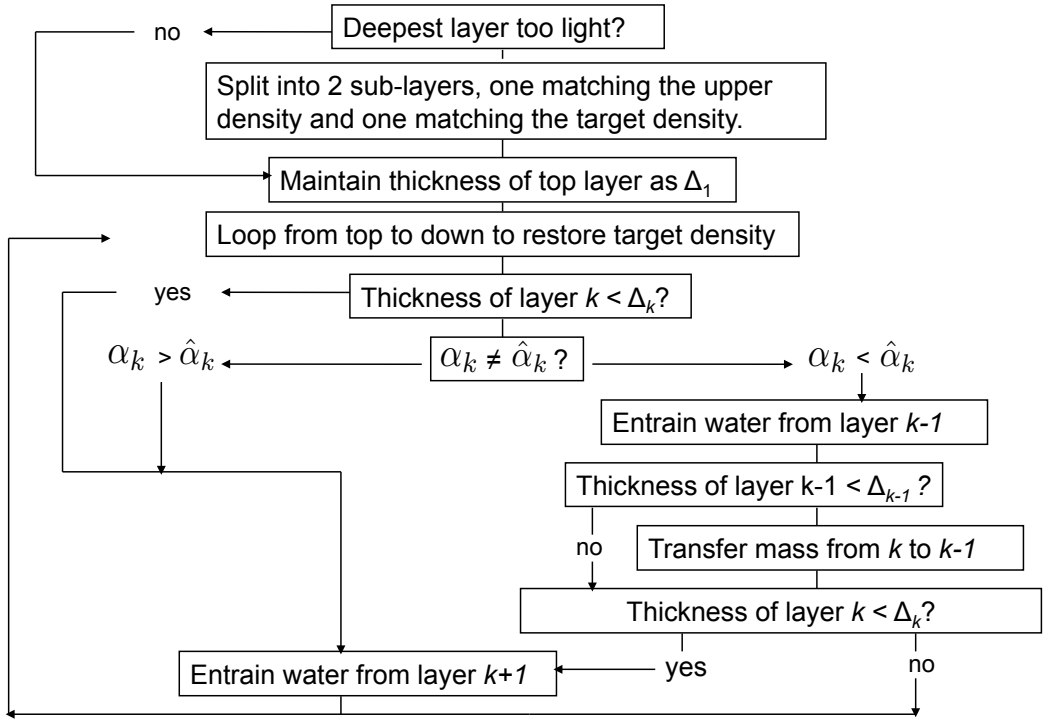

FIGURE 3.19: Flow chart of hybrid vertical coordinate generator used in HYCOM

Once the adjustment of vertical coordinates is performed at the pressure grid points using the above procedures, all model thermodynamical variables (including tracer) and momentum will be regridded by 1$^{\text{st}}$ or 2$^{\text{nd}}$ order vertical advection scheme (PCM, PLM and PPM). The adjustment of these variables must conserve their vertically averaged values and restore density as closely to the reference value as possible. Three vertical advection schemes that have been developed for HYCOM are summarized here:

PCM : Piecewise Constant Method scheme can only be applied in the isopycnic interior ocean where mixing is very weak. It is a non-direction dependent scheme but can generate large numerical diffusion near the surface.

PLM : Piecewise Linear Method scheme developed by A. J. Wallcraft from Naval Research Laboratory for using within the near surface non-isopycnic domain where distances over which interfaces are relocated are relatively large, and numerical diffusion is thus expected to be large. This scheme is non-direction dependent and supposed to be less diffusive than PCM (Donor Cell) scheme. However, PLM scheme may change values of layer variables within a layer when fluid is only detrained from that layer.

PPM : Piecewise Parabolic Method is a finite volume scheme and can be applied for the whole water column in HYCOM. During vertical interpolation of the variables, a monotonic parabola is fit to the zonal average of each dependent variable using information from neighboring zonal averages. PPM is developed for the purpose of reducing unwanted numerical mixing in HYCOM's regridding process and is the least diffusive scheme of the three.

Currently the most up-to-date PPM scheme has been employed in our setting for the tracer ventilation experiment as this 2^{nd} order vertical advection scheme is supposed to suppress unwanted vertical mixing, and thus reduce vertical numerical mixing as much as possible.

3.4.2 Decomposition of regridding mixing in HYCOM

The total regridding-introduced upwelling tracer flux was integrated over time as $hybflx$. The magnitude of this tracer upwelling flux is controlled by the grid layer generator as well as by the vertical advection scheme that has been applied after re-gridding layer interfaces. Numerically, according to its triggering mechanisms, $hybflx$ can be decomposed into two components, namely, $denflx$: regridding entrainment triggered by restoring isopycnic conditions, which is physically driven by both surface buoyancy fluxes and diapycnal mixing at the base of the mixed layer; and $mltflx$: regridding entrainment triggered by maintaining the minimum layer thickness (MLT) in the near-surface layers, which is physically driven by volume flux divergence within the mixed layer.

As described in the last section, part of the $denflx$ is actually driven by density fluxes across the lower interface of the mixed layer due to applying the fixed-coordinate KPP scheme in a hybrid-coordinate model (HYCOM). Therefore this fraction of the $denflx$ is actually a supplement to the KPP mixing scheme (changing layer thickness after adjustment of T and S) and should be considered as physical. The ultimate solution for HYCOM vertical mixing, however, should be to use KPP to determine a vertical mixing coefficient profile but let McDougall-Dewar's scheme do the actual mixing. This is because McDougall-Dewar's scheme modifies temperature, salinity and layer thickness (Δp) simultaneously whereas the conventional KPP only modifies temperature and salinity but does not modify layer thickness. This solution would not modify potential density for each coordinate layer and therefore would reduce the magnitude of $denflx$. However, even though there is no density flux across the base of the mixed layer, surface buoyancy loss can still generate a density discrepancy at layer k and as a result would induce extra tracer entrainment into the mixed layer as $denflx$ due to the vertical remapping process. Further diagnosis of this flux into physical and numerical components is very challenging, if not impossible, within the current model frame and is not included in this thesis.

Apart from restoring the isopycnic conditions in coordinate layers, regridding would also apply to stop a layer from collapsing to zero thickness by allowing it to become nonisopycnic in the upper ocean. Tracer upwelling generated by this regridding process has been integrated as $mltflx$. In the mixed layer, coordinate layers may become thinner if their water is entrained by the layer above and/or below, for the purpose of restoring these layers' densities to prescribed values; or simply because of the continuous Ekman divergent volume flux within the Ekman layer, if we assume that the Ekman depth is deeper than the mixed layer depth and instantaneous geostrophic velocity divergence is insignificant in the Ekman layer. In the first case, when layer k at the base of the mixed layer becomes thinner due to restoring the densities of the neighboring layers (Figs. 3.17 and 3.18), additional tracer upwelling is never generated. Integrated tracer upwelling flux of $mltflx$ only increases when the mixed layer base rises up due to Ekman divergence and violates the MLT constraint (Fig. 3.20). Therefore, this part of regridding induced tracer upwelling flux ($mltflx$), even though is generated by a numerical constraint, is initially driven by a physical process (Ekman divergence). It happens because there is an imbalance between Ekman

upwelling and resolved diabatic mixing process. Further diagnosis about the Ekman upwelling in our model will be discussed in Chapter 4.

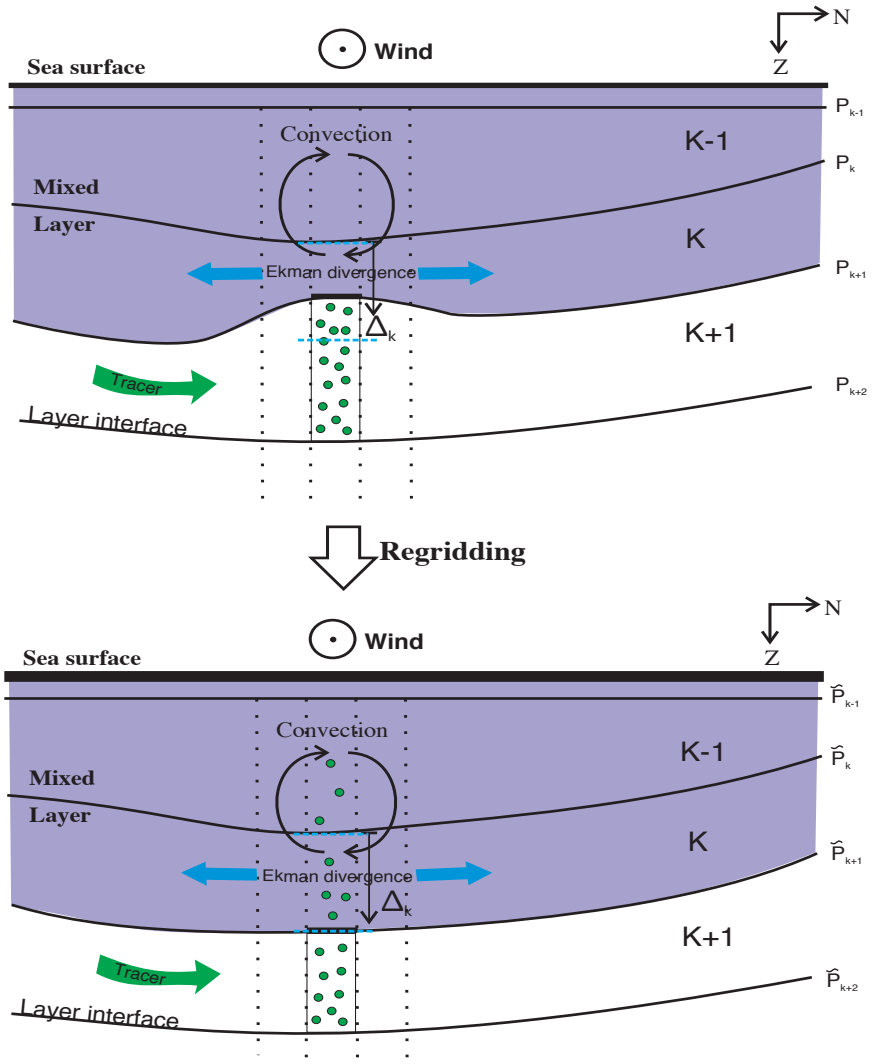

FIGURE 3.20: Schematic of Ekman divergence-induced regridding process and vertical mixing in HYCOM: (top) isopycnal layer interfaces before regridding and (bottom) after regridding process.

The algorithm used in our diagnosis for separating these two types of regridding mixing fluxes ($mltflx$ and $denflx$) is explained here. Consider two continuous coordinate layers labeled as k and $k+1$ with the mixed layer depth following p_{k+1} (which is also the lower interface of layer k in Fig. 3.21). If the minimum layer thickness constraint was triggered when remapping the mixed layer boundary, then according to Eq. (3.33) after remapping either $\Delta p_k = \Delta_k$

or $\Delta p_{\mathrm{k+1}} = \Delta_{\mathrm{k+1}}$ must appear (Δp_k is the thickness of layer k). Combining these two scenarios together with relocation of $p_{\mathrm{k+1}}$ we get four different cases:

- Case 1: $\tilde{p}_{\mathrm{k+1}} > p_{\mathrm{k+1}}$ and $\Delta p_k = \Delta_k$ (the lower interface of layer k becomes deeper after regridding), where $p_{\mathrm{k+1}}$ and $\tilde{p}_{\mathrm{k+1}}$ are the pressures of layer interface $k+1$ before and after regridding, respectively.
- Case 2: $\tilde{p}_{\mathrm{k+1}} > p_{\mathrm{k+1}}$ and $\Delta p_{\mathrm{k+1}} = \Delta_{\mathrm{k+1}}$. In this case water in layer k is too light ($\alpha_k > \hat{\alpha}_k$) and entrainment from layer $k+1$ is required. However, maintaining the minimum thickness of layer $k+1$ will prevent α_{k} from restoring to $\hat{\alpha}_{\mathrm{k}}$ and layer interface $p_{\mathrm{k+1}}$ ends up in $\tilde{p}_{\mathrm{k+1}}$ instead of $\hat{p}_{\mathrm{k+1}}$ (see Eq. (3.32) and (3.33)).
- Case 3: $\tilde{p}_{\mathrm{k+1}} < p_{\mathrm{k+1}}$ and $\Delta p_k = \Delta_k$. In this case water in layer $k+1$ is too dense ($\alpha_k < \hat{\alpha}_k$) and entrainment of less dense water from layer k is needed. Again the minimum thickness constraint applies and prevents $\alpha_{\mathrm{k+1}}$ from restoring to $\hat{\alpha}_{\mathrm{k+1}}$.
- Case 4: $\tilde{p}_{\mathrm{k+1}} < p_{\mathrm{k+1}}$ and $\Delta p_{\mathrm{k+1}} = \Delta_{\mathrm{k+1}}$.

The four cases of vertical regridding process are illustrated in Fig. 3.21. The mixed layer entrains water from below ($hybflx > 0$) in both Cases 1 and 2, but due to different reasons. Entrainment in Case 1 is due to restoring the minimum layer thickness and therefore is defined as $mltflx$. In Case 2 the grid generator relocates the mixed layer boundary $p_{\mathrm{k+1}}$ to $\tilde{p}_{\mathrm{k+1}}$ due to restoring the potential density in layer $k+1$ to its reference value and $hybflx$ is ascribed as $denflx$. Similar situations exist in Case 3 and 4 but only with negative $hybflx$.

$$hybflx = \begin{cases} mltflx > 0 & \text{in Case 1} \\ denflx > 0 & \text{in Case 2} \\ denflx < 0 & \text{in Case 3} \\ mltflx < 0 & \text{in Case 4} \end{cases}$$

Tracer conservation also requires that the time integral of these fluxes satisfies:

$$\int hybflx\, dt = \int denflx\, dt + \int mltflx\, dt \tag{3.38}$$

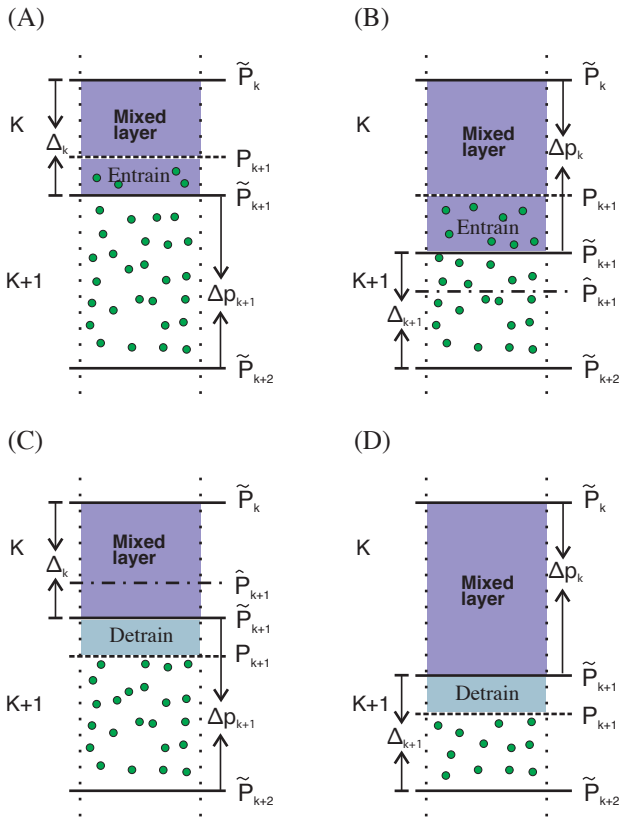

FIGURE 3.21: Schematic of numerical vertical mixing in HYCOM, introduced by hybrid grid generator and the regridding process (green dot represents tracer) : (A) numerical entrainment in Case 1; (B) regridding entrainment in Case 2; (C) regridding detrainment in Case 3 and (D) numerical detrainment in Case 4.

In the end, combination of Eqs. (3.7), (3.27), (3.28) and (3.38) leads to

$$Q_t = Q_{\text{ind}} + Q_{\text{dd}} + Q_{\text{shr}} + Q_{\text{bck}} + Q_{\text{ent}} + Q_{\text{den}} + Q_{\text{mlt}} \tag{3.39}$$

where Q_t is the time integral of the total tracer upwelling flux ($trcflx$), Q_{ind} for induction, Q_{dd} for double diffusion, Q_{shr} for shear diffusion, Q_{bck} for background diffusion, Q_{ent} for entrainment induced by deepening of the mixed layer, Q_{den} for regridding mixing induced by density restoration and Q_{mlt} for regridding mixing induced by the MLT constraint.

This final version of tracer diagnostic scheme has been embedded in HYCOM and a tracer experiment has been integrated over a period of 150 years, to ensure that tracer released from the Southern Ocean has enough time to ventilate to the high-latitude North Atlantic Ocean. The build up of all seven tracer

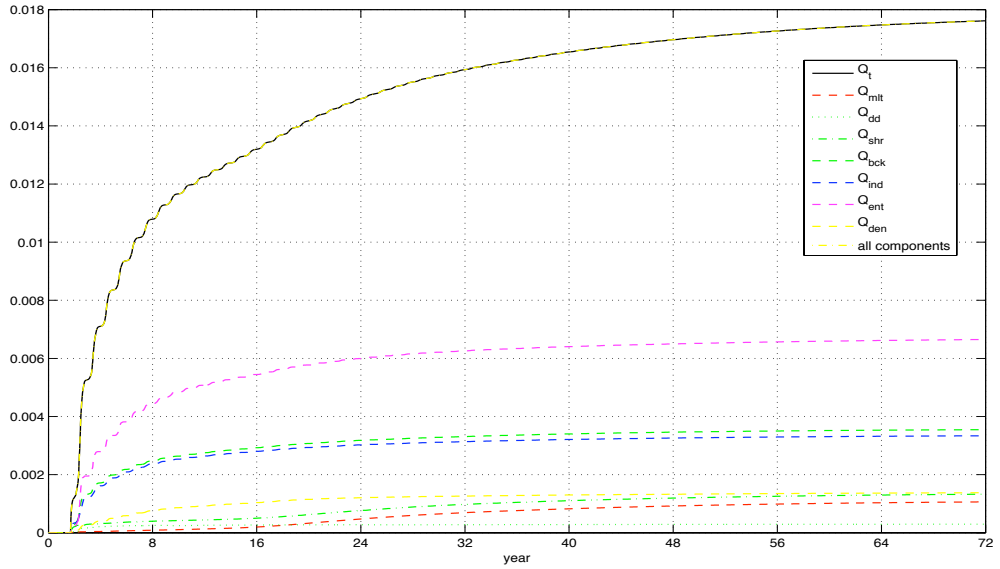

FIGURE 3.22: Time integral of tracer upwelling fluxes (in global mean *tracer unit* m^{-3}) that re-emerge into the mixed layer in global ocean due to different upwelling mechanisms

upwelling fluxes is shown in Fig. 3.22. Tracer mass was always conserved during our experiment.

SUMMARY

In order to explore the circulation of Southern Ocean-originated nutrients in the global scale, a tracer experiment has been set up mimicking the formation and transport of the SAMW, which is believed to be the main water mass responsible for supplying nutrient to the Northern Hemisphere thermocline (Sarmiento et al., 2004) and is thought to play an important role in maintaining the high primary production in the subpolar gyre and high latitude of the North Atlantic Ocean (Williams et al., 2006; Palter and Lozier, 2008). In this Chapter the details of our tracer experiment setup have been discussed. A conservative tracer was released once in the formation region of SAMW after the model reached a quasi-equilibrium state. A consumption algorithm was then applied in the mixed layer to mimic the biogeochemical process affecting nutrient in the surface. A diagnostic scheme has been developed for interpreting tracer upwelling fluxes in terms of physical and numerical driving mechanisms, and has been applied in a hybrid coordinate system model (HYCOM) for an integration period of 150 years. Results of the time integrations of these tracer

upwelling flux components will be shown in the following Chapter, as well as the advection pattern of the SAMW in the global ocean.

Chapter 4

Results and Discussion

In this Chapter the results of the standard tracer experiments are discussed. While the focus here is on the diapycnal tracer re-emergence due to different upwelling mechanisms, first an overview of the tracer circulation pattern in the global ocean is given to familiarize the readers with the gross feature of the model-simulated SAMW ventilation and to contrast this with results from observation-based inverse models and previous GCM simulations (Sloyan and Rintoul, 2001a; Sloyan and Kamenkovich, 2007). The relationship between adiabatic upwelling (Ekman divergence induced upwelling) and diabatic upwelling (entrainment) in the equatorial Pacific regions is discussed in the end of the Chapter.

4.1 Tracer circulation

First we will examine SAMW-related tracer circulation in the Southern Ocean and in three different ocean basins. Following the global thermohaline circulation and the surface wind-induced transport, the inter-basin pathway of tracer circulation is presented and the current systems it is associated with are discussed. Validation of the tracer circulation has been done by comparing the model results with previous GCM simulations and observations.

4.1.1 Atlantic and Southern Ocean

The SAMW formed in the Southern Ocean is transported following the eastward flow of the ACC and the northward Ekman flow into the adjacent subtropical gyres. In the Atlantic Ocean, SAMW initially moves northward with the Malvinas Current adjacent to the South American continent, but the southward flow of Brazil Current along the western boundary blocks its penetration into the subtropical gyre (Schmitz, 1995). SAMW that circulates eastwards follows the South Atlantic Current (SAC), which turns northward and feeds into the Benguela Current as part of the subtropical gyre (Stramma and Peterson, 1990; Peterson and Stramma, 1991). Similar pathways of intermediate water in the Atlantic have been suggested by Sloyan and Rintoul (2001a), amongst others, based on the results of an inverse model combining hydrographic sections. Sloyan and Rintoul (2001a) suggest that about $32.7 \pm 0.5 \times 10^6 m^3 s^{-1}$ of intermediate water (including SAMW and AAIW) enter the Atlantic Ocean through Drake Passage. According to their diagnosed circulation, most of the lighter part of this water (SAMW) is immediately captured by the Malvinas Current and turns northward following the western boundary in the Argentine Basin, while part of the dense fraction (AAIW) continues eastward with the ACC. After reaching about $35°S$, the northward-moving part turns offshore to form the SAC (Stramma and Peterson, 1990), which moves eastward across the mid-Atlantic ridge and transports modified and recirculating SAMW and AAIW southeastward to the eastern boundary. There these water masses exit the Benguela Current and flow into the subtropical gyre. However, Sloyan and Rintoul (2001a) do not comment on the volume of SAMW that turns eastward after entering the Malvinas current .

Another important pathway of SAMW from the Pacific to the Atlantic is the so-called "Tasman leakage". This pathway was first identified in the analysis of Sloyan and Rintoul (2001a), and then supported by trajectory experiments in three different General Circulation Models (Speich et al., 2002). Considered an important element for the upper branch of global thermohaline circulation, Speich et al. (2001) suggested that this pathway is responsible for transporting about $3Sv$ of SAMW and AAIW from the Pacific into the North Atlantic. After being entrained into the Tasman outflow in the Southwest Pacific, these Tasman waters first flow westward close to the South Australian Plateau and then cross the Indian Ocean northwestward as part of the northern branch of the Indian

subtropical gyre upon reaching the African Margin. They then flow southward following the Agulhas Current system and enter the South Atlantic, where they are captured by the Benguela Current and form part of the northward return flow of the thermohaline circulation (Speich et al., 2002).

In our simulation, after release in the SAMW formation region in Pacific and Indian (Fig. 3.6), the tracer circulation is under the strong influence of the surface wind field and follows mainly three major circulation features: the eastward-flowing ACC system, the anticyclonic subtropical gyres, and the northward Ekman flow. As demonstrated by Fig. 4.1, the tracer carried by the ACC crossed Drake Passage and entered the Atlantic Ocean one year after release. Surface consumption of tracer commenced in year two. Therefore, tracer following lighter density class of SAMW (with density σ_2 in the range 33.54 - 34.85, following model layer 4 - 6; hereafter referred to as SAMW-light tracer) can only flow through Drake Passage during southern summer when the mixed layer is shallowest and isopycnal layer is not outcropped (not shown here). This part of the SAMW supply into the Atlantic through the ACC can be viewed as a seasonal pump (Fig. 4.2). The dense fraction of SAMW and the AAIW transferred from SAMW due to progressive cooling and freshening following the ACC (McCartney, 1977) (with density range 35.37 - 36.43, among layer numbers 7 - 10; referred, SAMW-dense tracer) can maintain a steady flow from the Pacific to the Atlantic through Drake Passage even in southern winter, when the mixed layer is deepest. Therefore, it supplies much more tracer to the Atlantic than the SAMW-light class (Fig. 4.3).

After entering the Atlantic, the eastward-flowing tracer flux bifurcates into two branches: the northward-flowing branch follows the Malvinas Current and the eastward-flowing branch follows the SAC. Unlike the hypothesis of Stramma and Peterson (1990) and the research of Sloyan and Rintoul (2001a), who suggest that the presence of the southward Brazil Current prevents northward flow of SAMW and forces the SAMW eastward across the Atlantic as the SAC at the Brazil-Malvinas confluence between 38° and 33°S, our simulation shows that a noticeable part of SAMW-light tracer spreads northward from the Malvinas Current, reaching as far as the Equator (layers 4-6 in Fig. 4.2). It is probably because that the Brazil Current is too weak in our simulation due to the coarse mesh grid used in the model (not shown here). In the equatorial Atlantic Ocean, this part of the tracer was captured by the Atlantic Equatorial

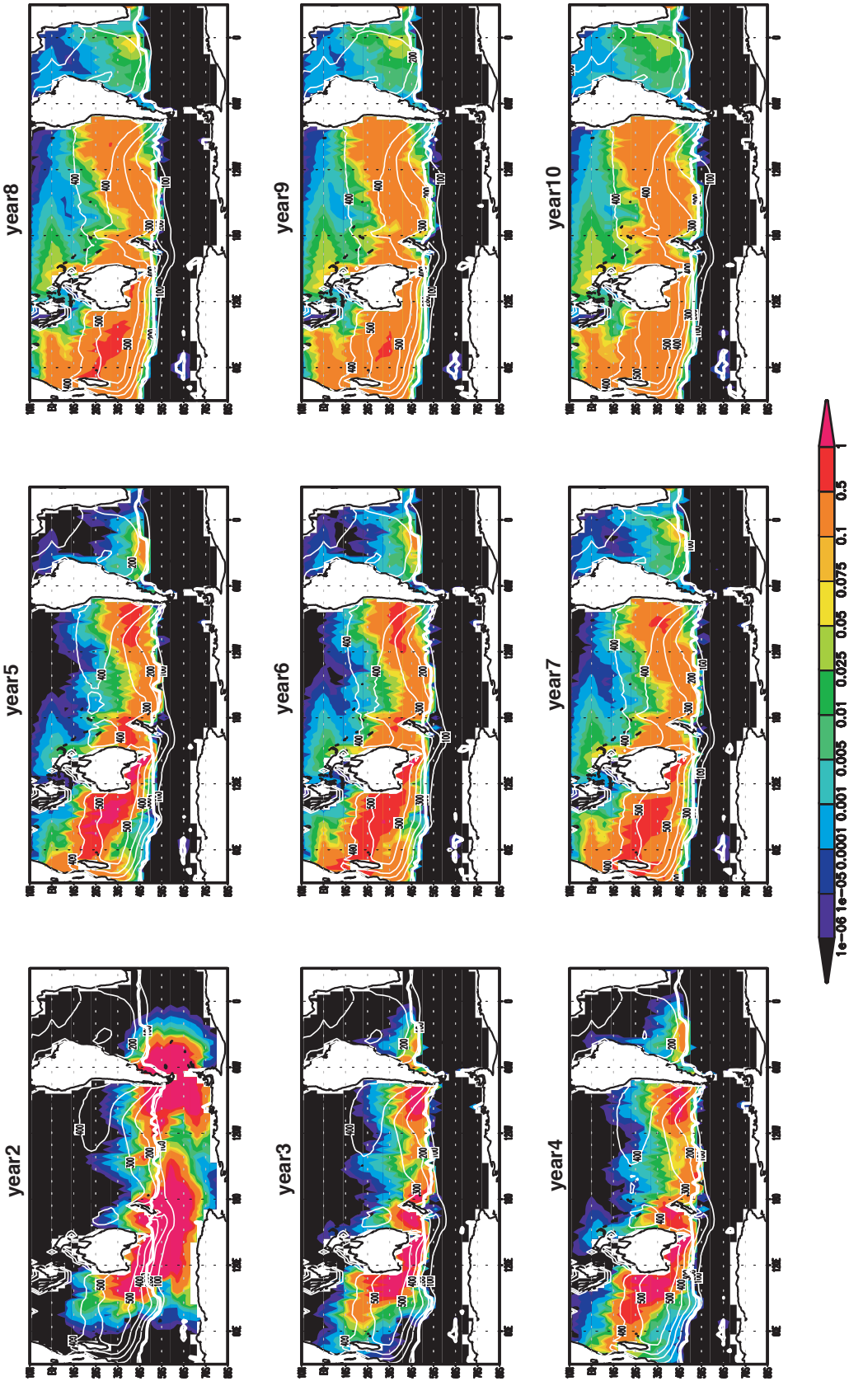

FIGURE 4.1: Tracer concentration for the southern winter (September) following layer six with potential density $\sigma_2 = 34.85$. The thick white lines denote the outcrops and the thin white contours show layer depths (with contour interval = 100 m).

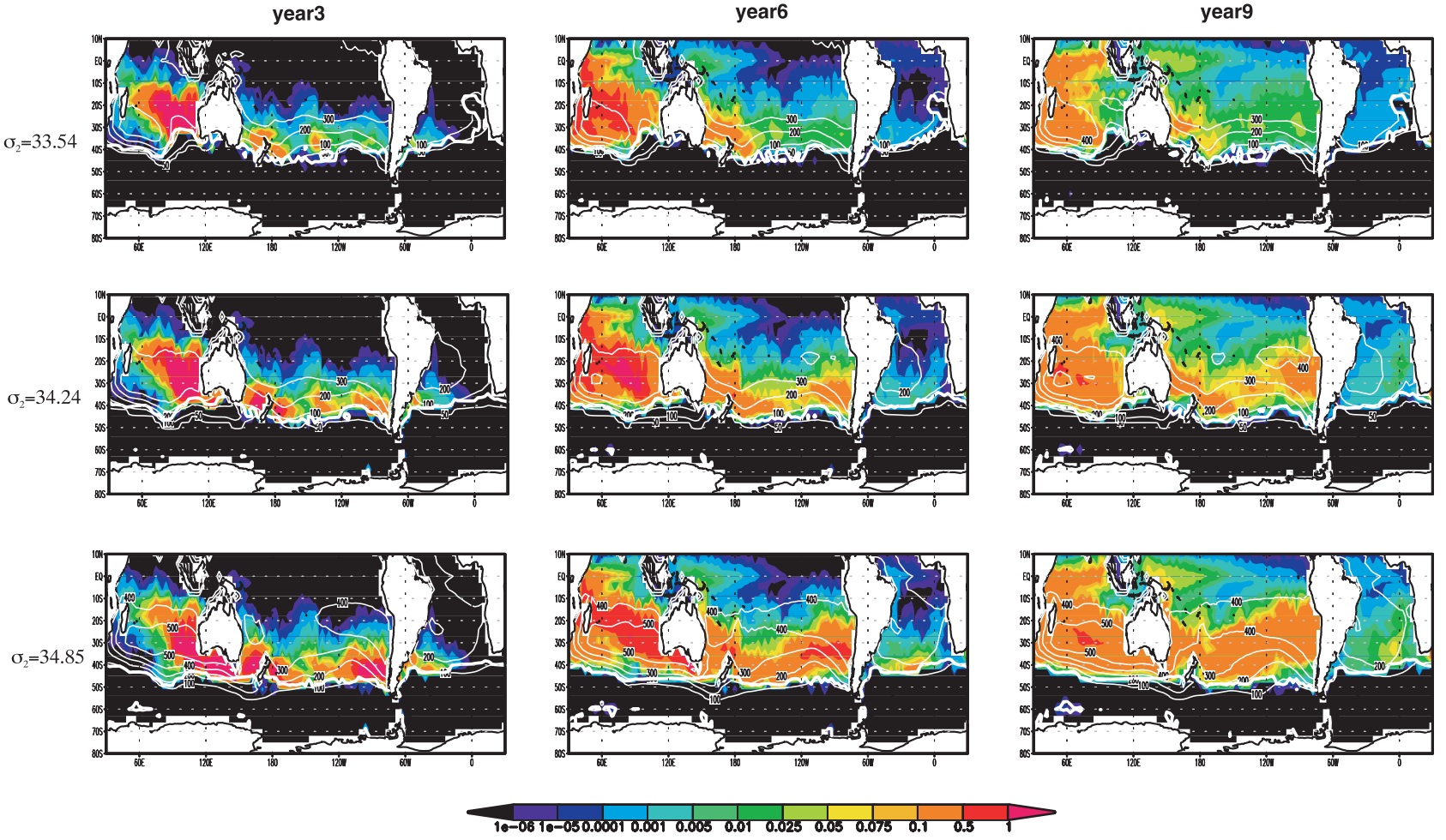

FIGURE 4.2: Tracer concentration for (Sep) following SAMW related isopycnals: (top) coordinate layer 4 with potential density $\sigma_2 = 33.54$, (middle) layer 5 with $\sigma_2 = 34.24$, and (bottom) layer 6 with $\sigma_2 = 34.85$ in the first ten years. The thick white lines denote the outcrops and the thin white contours show layer depths (with contour interval = 100 m).

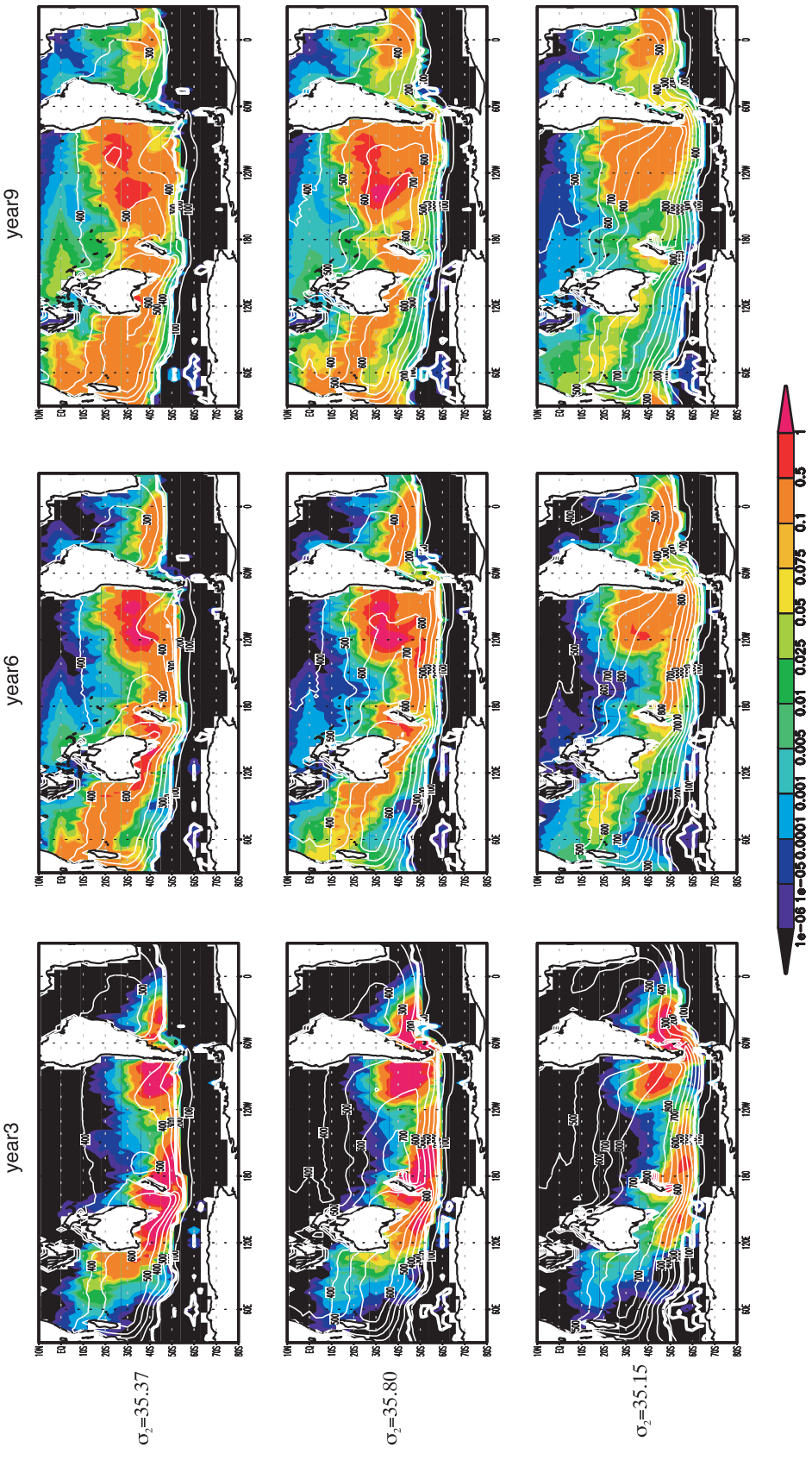

FIGURE 4.3: Tracer concentration for the southern winter (Sep) following SAMW related isopycnals: (top) coordinate layer 7 with potential density $\sigma_2 = 35.37$, (middle) layer 8 with $\sigma_2 = 35.80$, and (bottom) layer 9 with $\sigma_2 = 36.15$.

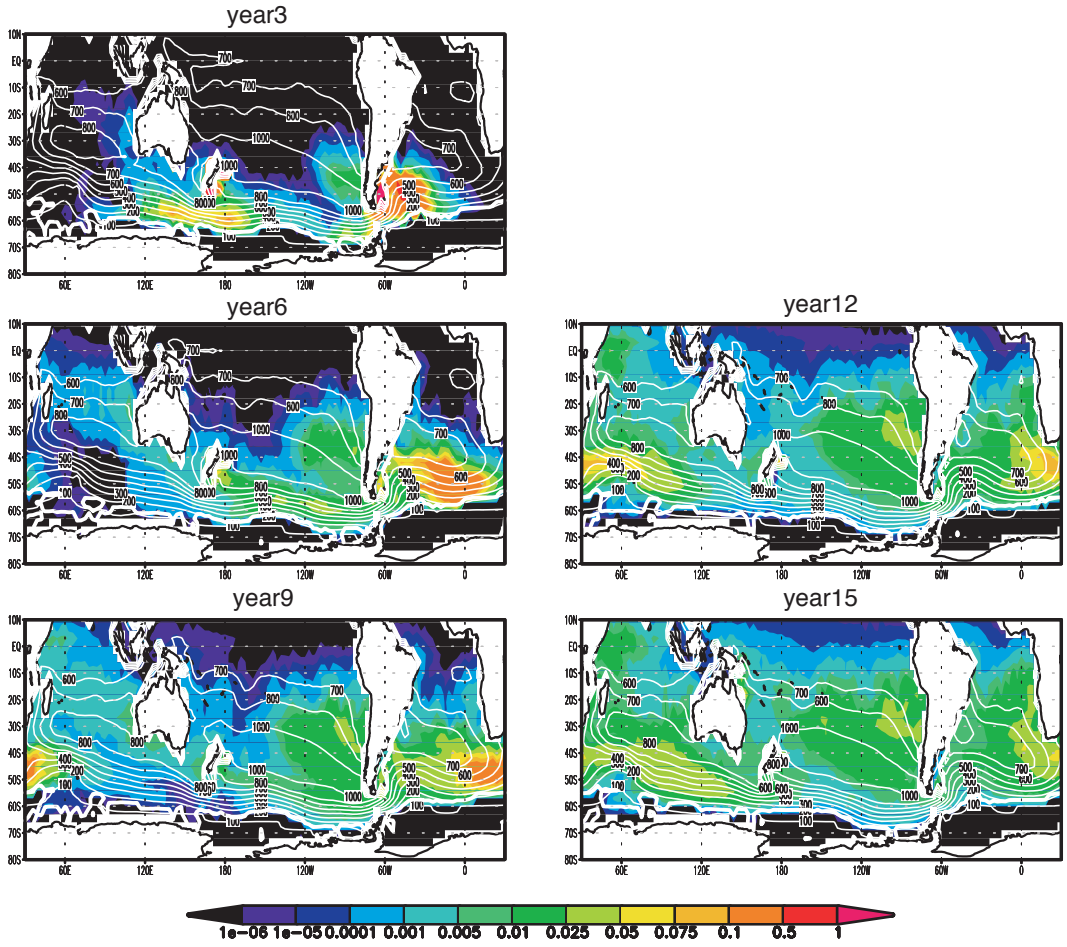

FIGURE 4.4: Tracer concentration for the southern winter (September) following layer ten with potential density $\sigma_2 = 36.43$.

Current System and flowed eastward across the Atlantic as far as the West African coast. The rest of the SAMW-light tracer, though, followed the eastward SAC first and entered the subtropical gyre after crossing the mid-Atlantic ridge, as suggested by Stramma and Peterson (1990) and Sloyan and Rintoul (2001a). The relative importance of these two tracer pathways in the Atlantic changes with density: more tracer flows northward adjacent to the Southern American margin in the lighter layers than in the dense layers in our simulation. Even though there is also some northward transport away from the Malvinas Current, most of the SAMW-dense tracer flows eastward after crossing the Drake Passage, following the SAC. However, upon crossing the Atlantic, only a small fraction of this water enters the Benguela Current and contributes to the return of the thermohaline circulation (Fig. 4.3). The greater part of SAMW-dense tracer continues eastward with the ACC south of Africa and enters the

Indian Ocean. With the increase of density, the fraction of tracer that remains in the ACC also increases. This tracer pathway becomes most significant in the model layer ten (with $\sigma_2 = 36.43$), in which the mode water tracer can be tracked back to the ventilation in the southwest Pacific (Fig. 4.4). This result is in good agreement with Sen Gupta and England (2007)'s off-line tracer experiment, although they found no tracer directly ventilates north of the Atlantic subtropical gyre unless it recirculates back from the Indian Ocean by the Agulhas Current system.

Even though tracer was originally only released in layer 4 - 8, the winter mixed layer in the Southeast Pacific reaches to a depth occupying layers 1 - 10. Therefore, strong vertical convection in the surface boundary layer mixes tracer within the mixed layer and injects a fraction of the tracer into layers 9 and 10. Fig. 4.5 demonstrates how the tracer follows the ACC and circulates across the Southern Ocean. Once released, tracer trapped in ACC moves southeastwards until it reaches the Drake Passage around $65°W$. Due to continued cooling and freshening, isopycnal surfaces gradually deepen eastwards within south Indian and Pacific basin. The core of the maximum tracer concentration lies within layers 8 and 9 ($\sigma_2 = 35.80 - 36.15$) in the South Pacific and sinks from 250 m to 500 m eastward before reaching Drake Passage. These isopycnal surfaces shoal abruptly after crossing Drake Passage and the tracer maximum concentration transfers into layers 10 - 12 ($\sigma_2 = 36.43 - 36.81$) as a result of densification by continuous deep winter mixing in Drake Passage and the Scotia Sea. While most of the SAMW-light tracer flux veers northward following the Malvinas Current in the Atlantic, a significant fraction of the SAMW-dense tracer remains in the ACC and makes its way back into the Southwest Pacific after about 18 years of circulation, most noticeably in layer 10 with potential density $\sigma_2 = 36.43$. Along the meridional section at $0°E$ in the eastern Atlantic Ocean (Fig. 4.6 [bottom]), a distinct tracer maximum appears after 5 years and penetrates north to the equatorial Atlantic after 10 years. This maximum tracer tongue is mostly comprised of isopycnal surfaces between $\sigma_2 = 34.85$ - 36.15 and covers layers 6 to 9. These surfaces initially lie between 200 - 700 m in the eastern subtropical gyre as far as $40°S$, and then tilt upward approaching the equator to a depth of 400 m. The deepest penetration occurs at $45°S$ to a depth of about 800 m. A local tracer maximum appears in layers 6 and 7 at the equatorial Atlantic and is disconnected from the main northward tracer tongue (not shown here). It is associated with the western boundary tracer branch

adjacent to the South American continent, which turns eastward following the South Equatorial Counter Current (SECC).

As expected, our model does not capture the feature of the Agulhas leakage adequately, partly because of the tracer consumption algorithm that has been applied in the mixed layer. As we can see in Fig. 4.2, thick winter mixed layers block the bulk of the pathway of the Agulhas Current south of Africa from layers 4 - 5 and therefore no tracer can enter the Atlantic from the leakage of Agulhas waters in these layers (though weak Agulhas leakage does appear in layer 6 and below). An additional difficulty is the coarse mesh of the model grid, which is insufficient to resolve the turbulent process of the Agulhas Current. As a important pathway for the return of global thermohaline circulation into the Atlantic Ocean ("warm route"), improperly resolved Agulhas leakage may affect the AMOC and model estimation of the SAMW transport into the Atlantic Ocean by modifying the Indian and Tasmania Sea pathways (Speich et al., 2001), leading to reduced tracer advection into the Atlantic Ocean.

4.1.2 Pacific and Indian

The tracer ventilation within the Pacific Ocean can be separated into two branches according to their source regions (Figs. 4.2 and 4.3). The eastern branch, which originates from the SAMW formation region in Southeast Pacific, generally follows the northward flow of the subtropical gyre with a core centered between σ_2 = 34.24 - 36.15. The ventilation pattern changes gradually with increasing potential density for this branch of tracer flux. Although all moving northward, the upper part of this eastern branch (from the σ_2 = 34.24 to 34.85) flows predominantly under the influence of prevailing wind and reaches as far north as $10°S$ mainly as an Ekman current (Fig. 4.2). The bottom part (from the σ_2 = 35.37 - 36.15), however, is initially confined to the subtropical South Pacific gyre system. It follows the Chilean coast, turning west to the north of $40°S$ and then following the northern limb of the deep subtropical gyre to the western basin, where part of it recirculates southward and returns to the Southern Ocean via the East Australian Current and is then transported westward into the Indian Ocean via the Tasman outflow. A meridional section across the tracer plume in the East Pacific can be found in Fig. 4.6[middle]. The core of tracer maximum lies mainly in layers 5 - 9

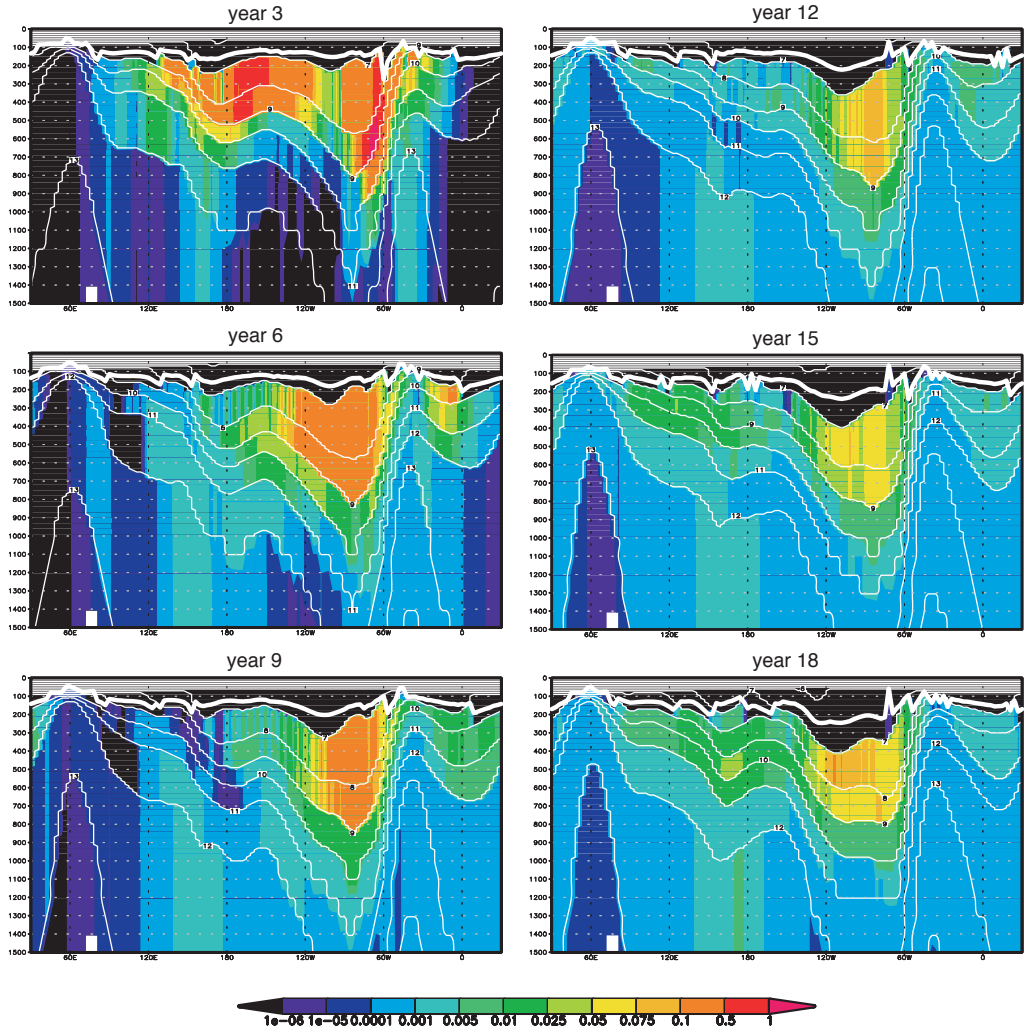

FIGURE 4.5: Longitudinal section of tracer distribution in the Southern Ocean along $57°S$ for the southern winter (September). Also shown are the layer interface depths (white contours with number representing overlaying layer number) and winter mixed layer depth (thick white contour). Drake Passage is between $60°W$ and $65°W$ in the model.

and penetrates to a greater depth than in the Atlantic Ocean (around 900 m) at $47°S$. Deep isopycnal surfaces (layers 8 - 9) gradually rise upwards while moving northward and the front of the tracer tongue following these isopycnals reaches $10°S$ after 10 yr. Unlike its eastern counterpart, the western tracer branch in the Pacific originates from the tracer released in the southeast Indian Ocean and south of Australia. Tracer circulates northward along the eastern coast of Australia in the shallower layers above $\sigma_2 = 34.85$ ($> 500\ m$ and above the bottom southward tracer flux, in Fig. 4.2). This is partly because the model simulated East Australian Current is too weak. This subsurface

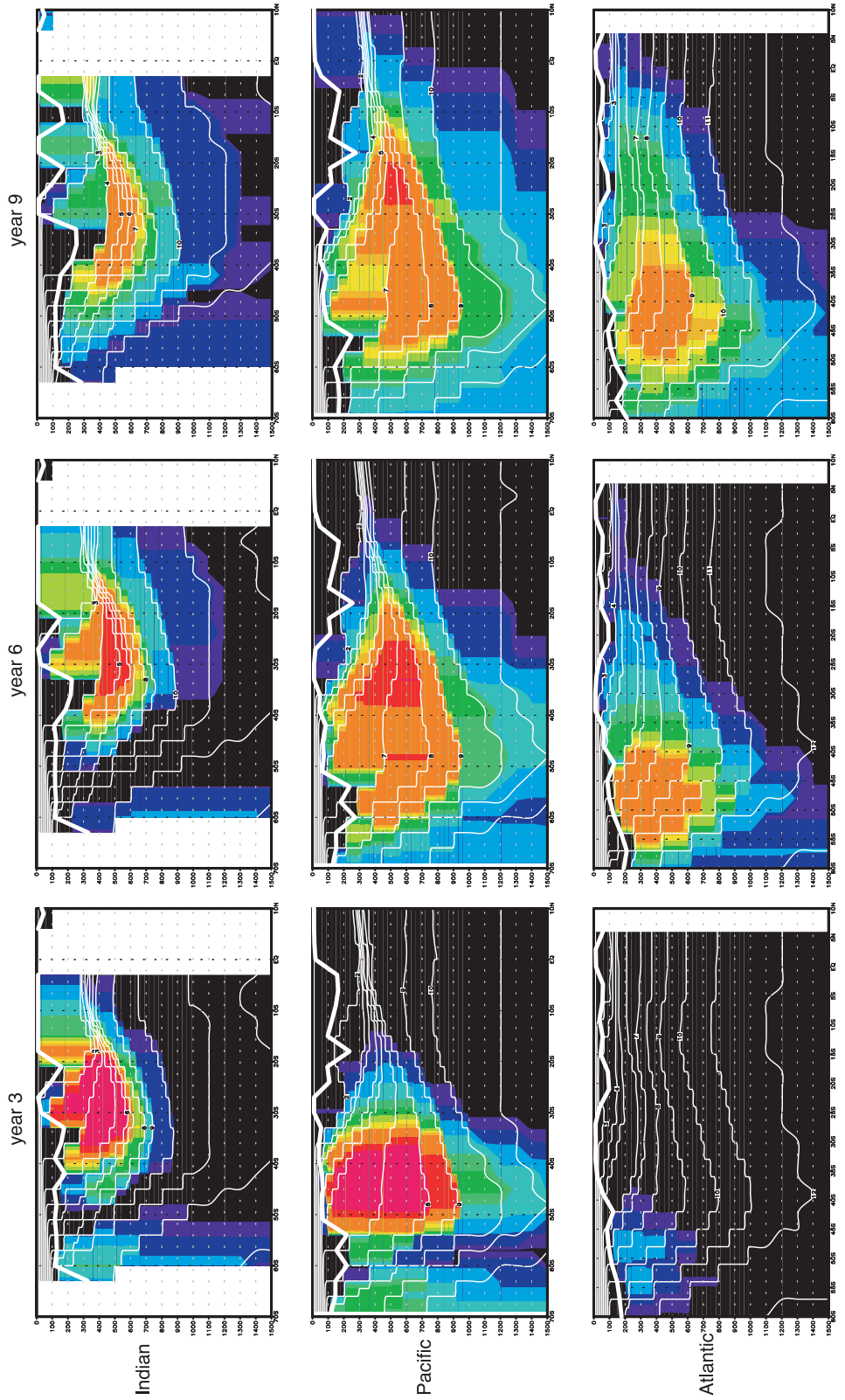

FIGURE 4.6: Meridional section of tracer distribution in: (top) the eastern Indian Ocean ($100^\circ E$), (middle) the eastern Pacific Ocean ($100^\circ W$) and (bottom) the eastern Atlantic Ocean ($0^\circ E$). Also shown are the layer interface depths (in white contours representing the number of the overlying layer) and winter mixed layer depth (in thick white contour).

northward-flowing eastern branch extends as far north as the Philippines, and then turns eastward following the Equatorial Countercurrent System after about 10 yr.

As demonstrated by Fig. 4.3, from the injection south of Australia there is a significant transport of tracer westward along the South Australia margin and into the Indian Ocean, centered at $\sigma_2 = 35.80$. This pathway of tracer ventilation follows the westward Tasman outflow (Speich et al., 2001, 2002) and is responsible for transporting SAMW and AAIW from the Pacific to the Indian ocean, and finally into the Atlantic Ocean. The formation of deep winter mixed layers south of Australia blocks this channel between $\sigma_2 = 33.54$ - 34.85 during the Southern Winter (Fig. 4.2) and thus limits the Tasman Leakage to a seasonal supply. Similar to the pathway as predicted by Sen Gupta and England (2007) with a high resolution GCM, tracer that enters the Indian Ocean through the Tasman outflow and that released in the southeast Indian Ocean in our model initially flow northward, then turn westward north of $20°S$ and leave the northwestern tip of the Australian continent to cross the Indian Ocean as part of the northern branch of the Indian subtropical gyre. This pathway is significant in almost all SAMW-related isopycnals (from $\sigma_2 = 33.54$ - 35.80) and is centered between 450 m - 650 m (Fig. 4.6).

The tracer circulation within the Indian Ocean is also in good agreement with previous research (Hanawa and Talley, 2001) and other GCM models' results (Speich et al., 2001; Sen Gupta and England, 2007; New et al., 2007). After reaching the Mascarene Plateau east of Madagascar the pathway bifurcates into two branches: the northward branch first follows the East African Coastal Current northwards and then veers eastward with the Equatorial Countercurrent; the southward branch flows as the East Madagascar Current and ultimately joins the Agulhas Current in the Southwestern Indian Ocean with some recirculation to the east into the subtropical gyre. Fig. 4.6[top] illustrates how tracer circulates meridionally along a section in the eastern Indian basin ($100°E$). The core of the tracer plume sits at a shallower depth (500 m) when comparing with the Pacific section and is thinnest (200 m) among all three meridional sections. The downward sloping isopycnals extend northward without tilting upwards again until reaching $35°S$.

By comparing the tracer ventilation in different ocean basins in our simulation with the observations and other GCM results, we have shown that the our

model reproduced a reasonably realistic circulation pattern for the SAMW, despite the coarse mesh of the model grid. The re-emergence of the SAMW diagnosed from the tracer upwelling in global ocean will then be discussed in the following section.

4.2 Re-emergence of SAMW diagnosed from tracer upwelling

Tracer upwelling fluxes have been separated into 7 terms based on the mechanisms (physical or numerical) responsible for SAMW re-emergence, as described in Chapter 3. The spatial and temporal statistics of their contributions in total upwelling will be discussed first. The geographical distribution of these upwelling terms will then be outlined and discussed within each ocean basin.

4.2.1 Tracer upwelling budget and fluxes contributions

Of the total injected tracer (SAMW), 45.6% still remains in the mixed layer after a year of circulation and has been removed before any genuine upwelling has occurred (in the first time step after consumption algorithm has been applied). The rest of the tracer (about 54.4%) is subducted into the ocean interior and is thereafter used as the reference value (T_{sub}) for upwelling diagnostics. Unless specified otherwise, all percentage values used in the following diagnostics are with reference to this total tracer mass that has been subducted into the ocean interior.

After integrating for a period of 150 years, over 97% of the total subducted tracer has returned to the mixed layer (Fig. 4.7). As for the upwelling in different ocean basins, $\sim 0.55\ T_{\mathrm{sub}}$ of tracer returns to the surface within the Pacific, making it the most important ocean basin for SAMW re-emergence; about $0.31\ T_{\mathrm{sub}}$ of tracer is transported back into the Indian Ocean, and the rest to the Atlantic ($\sim 0.12\ T_{\mathrm{sub}}$). Because tracer was only injected within the Pacific and Indian sections of the Southern Ocean, where winter mixed layer depths exceed 250 meters in the model, any tracer getting to the Atlantic must do so either via the ACC flow through the Drake Passage (dominant part in our simulation), or via the Agulhas leakage. The magnitude of total

tracer re-emergence in different ocean basins after 70/150 years of integration is displayed in Table 4.1, for the purpose of a temporal comparison. Only 2% T_{sub} upwelling is observed during the integration between years 70 and 150, and half of this takes place on the equatorial Pacific Ocean. However, when considering the temporal contribution of tracer re-emergence for each ocean basin, a significant increase of tracer upwelling has been observed during this later period of integration for the North Atlantic Ocean, which accounts for about 40% of the total tracer that re-entered the mixed layer within this region.

After crossing the equator, the tracer tongue penetrates into the North Hemisphere largely following the western boundary currents but with different patterns in the Atlantic and Pacific oceans (Fig. 4.17-A). The tracer re-emergence in the North Atlantic and the North Pacific are similar in magnitude for the first 70 years, with 0.003 $T_{\text{sub}}$for N. Atlantic and 0.002 T_{sub} for N. Pacific, respectively. However, the ratio of the upwelled tracer within N. Atlantic to that re-emerged in the N. Pacific increases to 2.5 by the end of year 150 due to continuous upwelling in N. Atlantic basin even in the later period of integration, when there is almost no upwelling occurring in the N. Pacific (Fig. 4.7). Furthermore, the N. Atlantic plays a much more important role for tracer upwelling in the Atlantic basin than that of the N. Pacific for the Pacific basin. Among all tracer re-emergence within the Atlantic Ocean, $\sim 4\%$ happens in the N. Atlantic ($> 20°N$), while the same partial contribution from the N. Pacific is less than 0.4% for the Pacific basin.

TABLE 4.1: Tracer re-emergence in different ocean basins after 70/150 years of integration (Equatorial $> -10°S$ and $< 10°N$, unit in T_{sub}).

	N. of $30°S$	S. of $30°S$	Equatorial	N. of $20°N$
Global	0.254/0.268	0.704/0.706	0.141/0.151	0.005/0.007
Atlantic	0.01/0.014	0.093/0.103	0.006/0.007	0.003/0.005
Pacific	0.141/0.151	0.395/0.396	0.098/0.105	0.002/0.002
Indian	0.102/0.102	0.207/0.207	0.038/0.039	

Of the total tracer subducted into the ocean interior, about 65% re-enters the mixed layer within the first 10 years (Fig. 4.8). During this period most (~ 0.56 T_{sub}) upwelling occurs in the area close to the tracer release regions, that is,

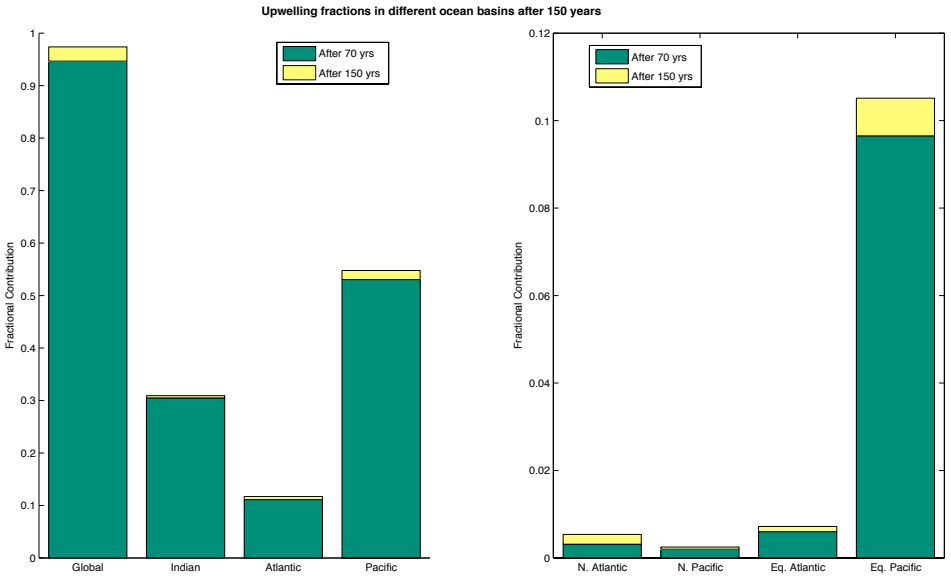

FIGURE 4.7: Fractional contribution of tracer upwelling fluxes in different ocean basins with reference to total tracer that subducted into the interior of the ocean (T_{sub}). Model has been integrated over a period of 150 years. (North Atlantic/Pacific $> 20°N$; Equatorial Atlantic/Pacific $> -10°S$ and $< 10°N$).

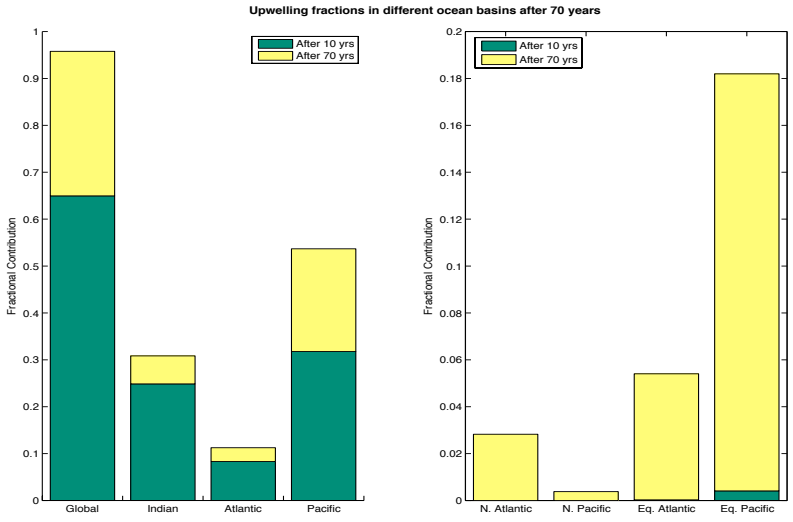

FIGURE 4.8: Fractional contribution of tracer upwelling fluxes in different ocean regions with reference (left) to global total subducted tracer (T_{sub}), and (right) to total tracer upwelling within the Atlantic or Pacific ocean basins (i. e. here N. Atlantic accounts for $\sim 2.8\%$ of the total upwelling in the Atlantic basin). Model has been integrated over a period of 70 years after tracer release in the Southern Ocean.

between $30°S$ and $60°S$ (Fig. 4.9) in the Southern Ocean. The latitudinal distribution of tracer upwelling flux comprises two peaks south of $30°S$ that consist of contributions from different ocean basins. The dominant part indicates upwelling in the Pacific and Atlantic oceans and is centered at $\sim 50°S$, while the second peak is the tracer re-emergence in the Indian Ocean centered at $\sim 38°S$. The different latitudinal upwelling belts between Indian and Pacific oceans are a result of the different tracer release regions within these ocean basins: tracer is released further equatorward in the Indian Ocean (the northern tip of tracer patch is located at $\sim 35°S$) compared with that in the Pacific Ocean (northern tip located at $\sim 50°S$).

About 0.31 T_{sub} returns to the surface between year 10 and 70. Of this, over 55% ($\sim$ 0.17 T_{sub}) occurs to the north of $30°S$. It takes about 20 years for tracer to arrive at the equator in the Pacific Ocean, and even longer in the Atlantic Ocean (about 25 years). Upwelling in the equatorial area (between $10°S$ and $10°N$) becomes the most significant part of SAMW re-ermergence during this period. It is easy to notice (Table. 4.1) that tracer re-emergence in the equatorial Pacific plays a dominant role and accounts for $\sim$0.1 T_{sub}, while the total global upwelling north of the $30°S$ is only 0.25 T_{sub} after 70 years of integration.

After separating the total tracer upwelling flux ($trcflx$) into three basic upwelling fluxes (Eq. 3.7), we find that the most important mechanism responsible for tracer re-emergence in the model is the entrainment due to surface wind forcing, heat flux and diapycnal diffusion across the mixed layer base. In fact, this tracer upwelling flux ($kppflx$) contributes over 60% of the total tracer upwelling in almost all latitudes (Fig. 4.10), except for the equatorial Pacific, where regridding mixing ($hybflx$) still gives significant contributions, and high-latitude of North Atlantic ($> 55°N$), where lateral advection is responsible for strong induction ($indflx$) into the mixed layer due to downstream deepening of the mixed layer. Further diagnostics separates $kppflx$ into 4 terms in Eq. 3.39, accounting for the influence of double diffusion different (Q_{dd}), background diffusion (Q_{bck}), shear diffusion (Q_{shr}) and entrainments due to deepening of the mixed layer (Q_{ent}). Regridding mixing ($hybflx$) has also been separated into 2 terms ($Q_{\text{den}} + Q_{\text{mlt}}$), representing the contributions from density restoration and minimum layer thickness constraint. Therefore, Fig. 4.10 can be re-plotted

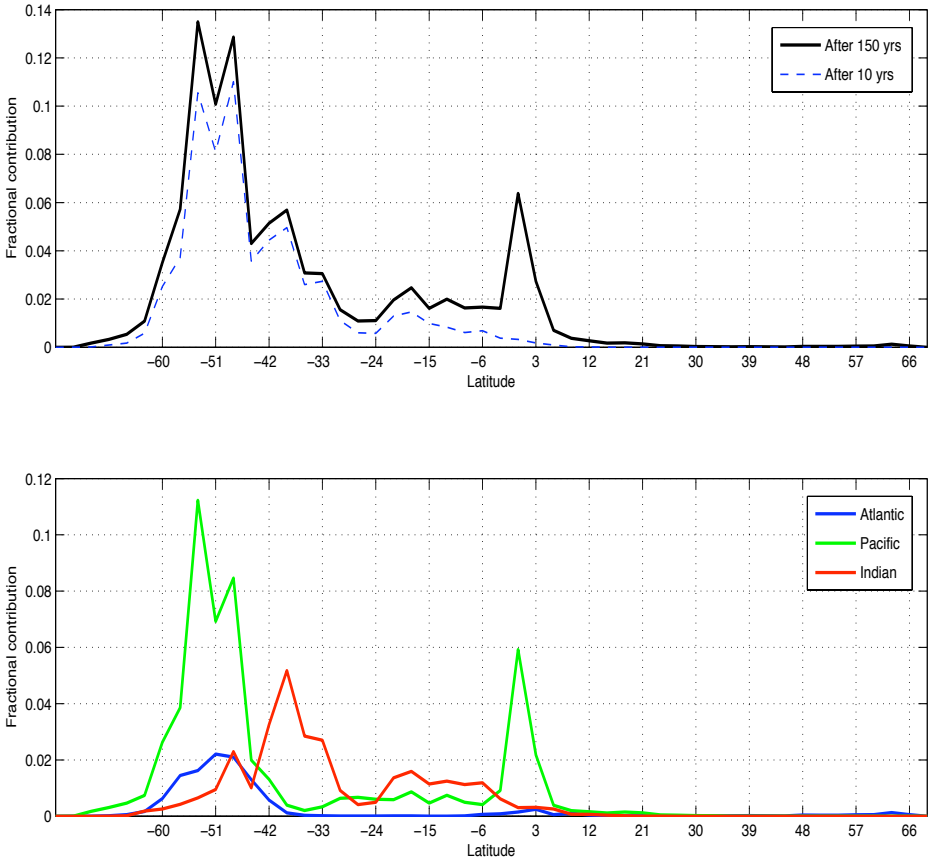

FIGURE 4.9: Zonal integral of fractional contribution of tracer re-emergence over latitude (top) global and (bottom) in different ocean basins after 150 yrs' integration. Horizontal axis with a interval of 3 degrees is determined by the model resolution.

with more details describing the physical/numerical mechanisms responsible for tracer upwelling in the model.

As we can see in Fig. 4.11, the most important component of $kppflx$ is due to thickening of the mixed layer and entrainment from the underlying thermocline (Q_{ent}). As described in Chapter 3, mixed layer depth is determined by both the local stratification and turbulent velocity in our non-local K-Profile Parameterization scheme. Thickening of the mixed layer could be a result of surface cooling due to destruction of stratification (reduced bulk Richardson number Ri_b) and/or increasing surface mechanical flux input. Therefore, it is easy to understand that the tracer upwelling flux due to this entrainment Q_{ent} is significant over the global ocean except for the equatorial region, which is characterized by small seasonal variation of the surface temperature and wind

field. Comparatively, extensive tracer diapycnal mixing happens immediately below the equatorial mixed layer due to velocity shear instability and creates a strong tracer upwelling flux (Q_{shr}) there. Another fractional contribution maximum of this shear-induced tracer upwelling flux is centered at $25°N$ and is due to the velocity shear between the northward Gulf Stream and underlying southward deep boundary current. Apart from these two, background diffusion-induced upwelling also plays an important role in total tracer re-emergence in the subpolar gyres of both the North Atlantic ($> 40°N$) and the South Pacific ($< 40°S$), where it accounts for $\sim 30\%$ of the total upwelling. Because background diffusivity is constant (10^{-5}), the corresponding upwelling flux (Q_{bck}) is only determined by the vertical tracer gradient in these regions. As for the strong regridding mixing that accounts for over 30% of the total tracer upwelling flux in equatorial region, most of it is introduced by the minimum layer thickness constraint and is actually associated with Ekman divergence at this region (Q_{mlt}). More discussion can be found in Section 4.3 about this Ekman effect and its relationship with regridding mixing.

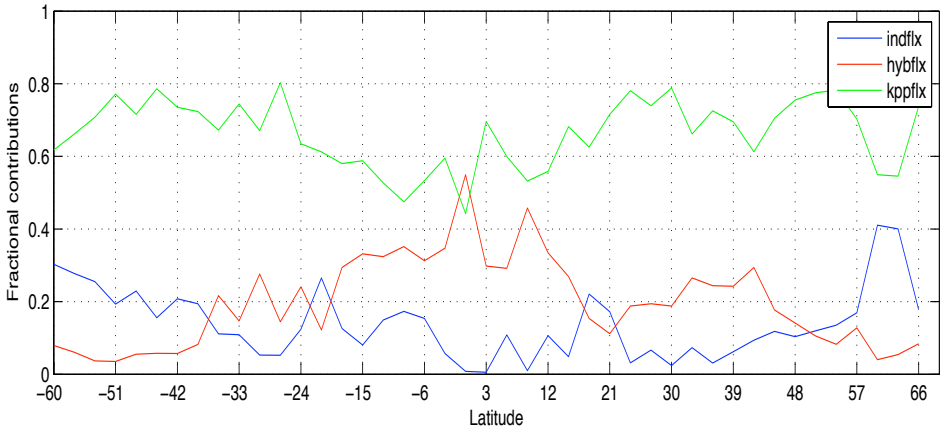

FIGURE 4.10: Fractional contribution of basic tracer upwelling fluxes (blue line represents lateral advection and diffusion introduced tracer upwelling, red line is the remapping upwelling, green line is the diapycnal upwelling) as a function of latitude.

Once the surface tracer consumption algorithm is applied (by resetting all tracer values within the mixed layer to zero), it induces a strong vertical gradient of tracer concentration which generates extensive diapycnal diffusion of tracer across the bottom boundary of the mixed layer, especially near the tracer release region in the Southern Ocean. Together with the strong vertical convection within the deep winter mixed layers, this diapycnal tracer flux injects

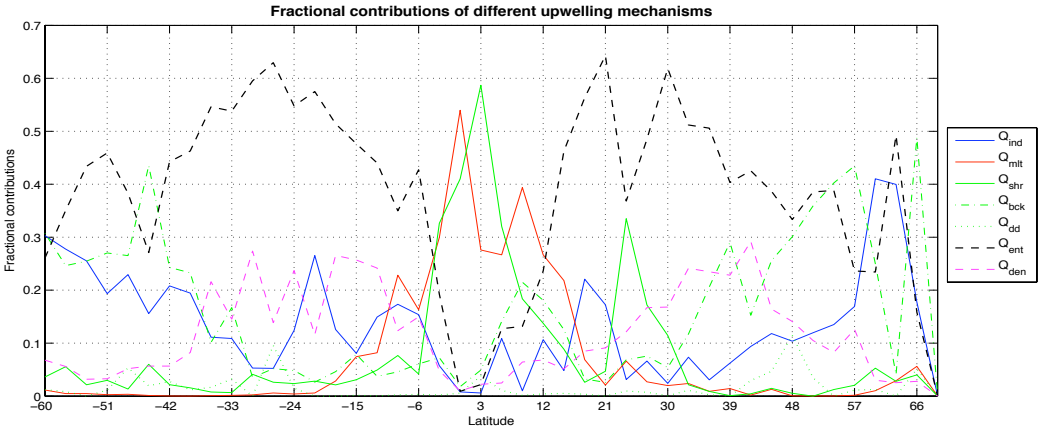

FIGURE 4.11: Fractional contribution of seven different tracer upwelling fluxes as a function of latitude. Q_{ind} for induction, Q_{dd} for double diffusion, Q_{shr} for shear diffusion, Q_{bck} for background diffusion, Q_{ent} for entrainment, Q_{mlt} for Ekman upwelling and Q_{den} for regridding mixing.

tracer back to the surface where it is then removed rapidly. Because this tracer re-emergence in the release region has little biogeochemical relevance, a mask has been introduced in our diagnostics in order to exclude the influence from this region. As shown in Fig. 4.12, the blue mask represents winter outcrop of the lightest SAMW layer (layer 4 with $\sigma_2 = 33.54$) for the Southern Hemisphere in our simulation (averaged over 10 years after model has reached a quasi-equilibrium state). The red mask is the formation region of SAMW following winter convection and mixing. Removing the upwelling contribution from the blue-shaded outcrop mask becomes critical for our following diagnostics of SAMW re-emergence of biogeochemical significance, especially for the North Hemisphere as the total upwelling of tracer north of $30°S$ only accounts for a quarter of T_{sub}.

As demonstrated by Fig. 4.13, upwelling within the winter outcrop region comprises much more induction and background mixing but much less regridding and shear mixing, when compared with upwelling north of the masked region. This difference can be understood in terms of the steep vertical tracer gradient due to closeness to the tracer source, and the strong isopycnal tracer flux in the ACC system within the Southern Ocean. As all SAMW related isopycnals are outcropping within the mask, this strong lateral tracer advection near its release region can generate extensive induction due to along-stream variation in mixed layer depth.

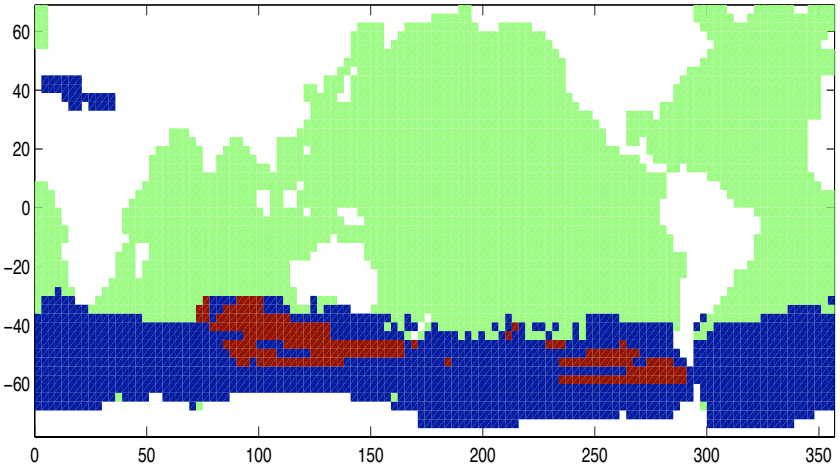

FIGURE 4.12: Mask of winter outcrop for layer 4 (with $\sigma_2 = 33.54$) in the Southern Hemisphere (blue) and tracer release region within the mixed layer (red).

Of all mechanisms responsible for SAMW upwelling over the global ocean, entrainment due to thickening of the mixed layer is the most important term and accounts for a third of the total tracer upwelling north of the winter outcropping mask (Fig. 4.13). Tracer induction generated by lateral advection and poleward thickening of the surface boundary layer accounts for 9% and also plays a significant part in upwelling. It is interesting to note that turbulent diapycnal diffusion (Q_{shr}+Q_{bck}+Q_{dd}) only accounts for $\sim$ 25% of the total upwelling of SAMW on the global average. It suggests that ventilation of the SAMW occurs through intrinsically different mechanisms than upwelling to mid depths of the abyssal ocean waters. Within this diapycnal diffusion induced upwelling flux, shear-induced diffusion is the most important term and accounts for 18% of T_{sub}. Background diffusion (set to a default value of $10^{-5} m^2 s^{-1}$) becomes a minor part and accounts for 7% of the total upwelling. Contribution from double diffusion is less than 1%. It is worth pointing out that $\sim$ 14% of the total upwelling is generated by vertical regridding mixing due to restoring the isopycnic condition (Q_{den}) of the surface layers (Fig. 4.13). Part of this mixing is triggered by density deviation induced by air-sea buoyancy exchange, while the other part is introduced as a supplement to the KPP mixing scheme. The remaining $\sim$ 19% of the total upwelling is associated with the Ekman divergence arising from the maintenance of the minimum layer thickness (Q_{mlt}) within the surface fixed coordinate region in HYCOM.

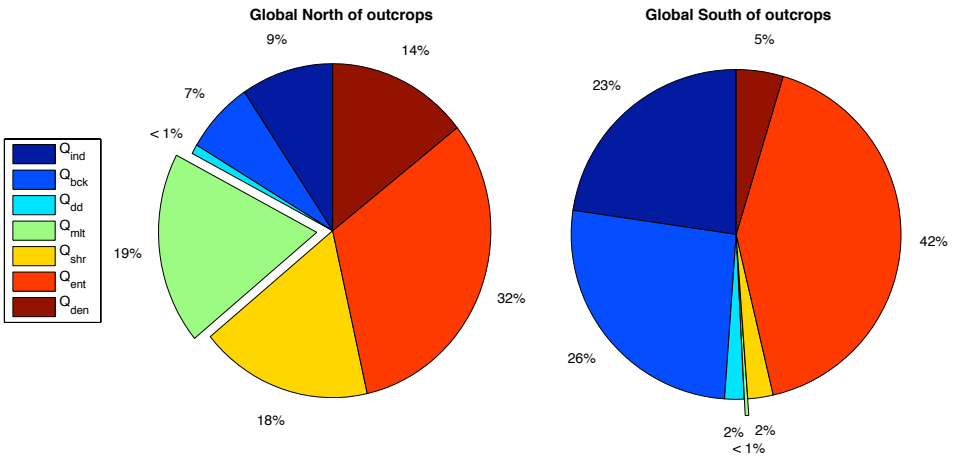

FIGURE 4.13: Global contributions of tracer upwelling north of the winter outcropping mask (left) and within the outcropping mask (right). The model has been integrated over a period of 150 years.

Figure 4.14 shows the fractional contributions of different SAMW upwelling mechanisms in the three major ocean basins, based on tracer re-emergence north of the winter outcropping mask. Induction happens when lateral advection and diffusion inject tracer from the ocean interior into the deep winter mixed layer epipycnally (along-isopycnal). There tracer ventilates to the surface through mixed layer convection and is consumed mimicking biogeochemical processes (Fig. 3.8). Thickening of the seasonal boundary layer by surface cooling and/or along the cyclonic circuit of subpolar gyres in the pathway of advection is the main reason for tracer induction in the model. Accordingly, this upwelling flux can be written in the form

$$Q_{\text{ind}} = \mathbf{v}_b \cdot H_b \tag{4.1}$$

where $\mathbf{v}_b = (u_b, v_b)$ is the lateral velocity and H_b is the isopycnal layer thickness at the base of the seasonal boundary layer. The fractional contribution of Q_{ind} to total tracer upwelling varies between 5% in the Pacific, to 15% in the Indian Ocean, with a global mean value of 9%. This value increases to 23% in the North Atlantic Ocean and reaches as high as 40% in the high-latitude North Atlantic ($> 55°N$), where cold salty outflows from the Arctic Mediterranean together with strong winter cooling in the Labrador and Irminger seas generate deep winter mixed layers. It is interesting to consider the temporal evolution of the induction contribution in the Atlantic Ocean. The fractional contribution of

Q_{ind} to total upwelling in Atlantic is 8% (20% in North Atlantic) after 70 years of integration, but increases to 11% (23% in North Atlantic) after 150 years. It suggests that of all the upwelling occurring between years 70 - 150 within the Atlantic Ocean, the bulk happens in the high-latitude North Atlantic and is due to induction. Apart from the North Atlantic Ocean, another area where induction plays a significant role in SAMW upwelling is the Indian Ocean's subtropical gyre. In contrast, a minimum contribution of induction of around 1% appears in the equatorial Pacific where a very shallow thermocline is found.

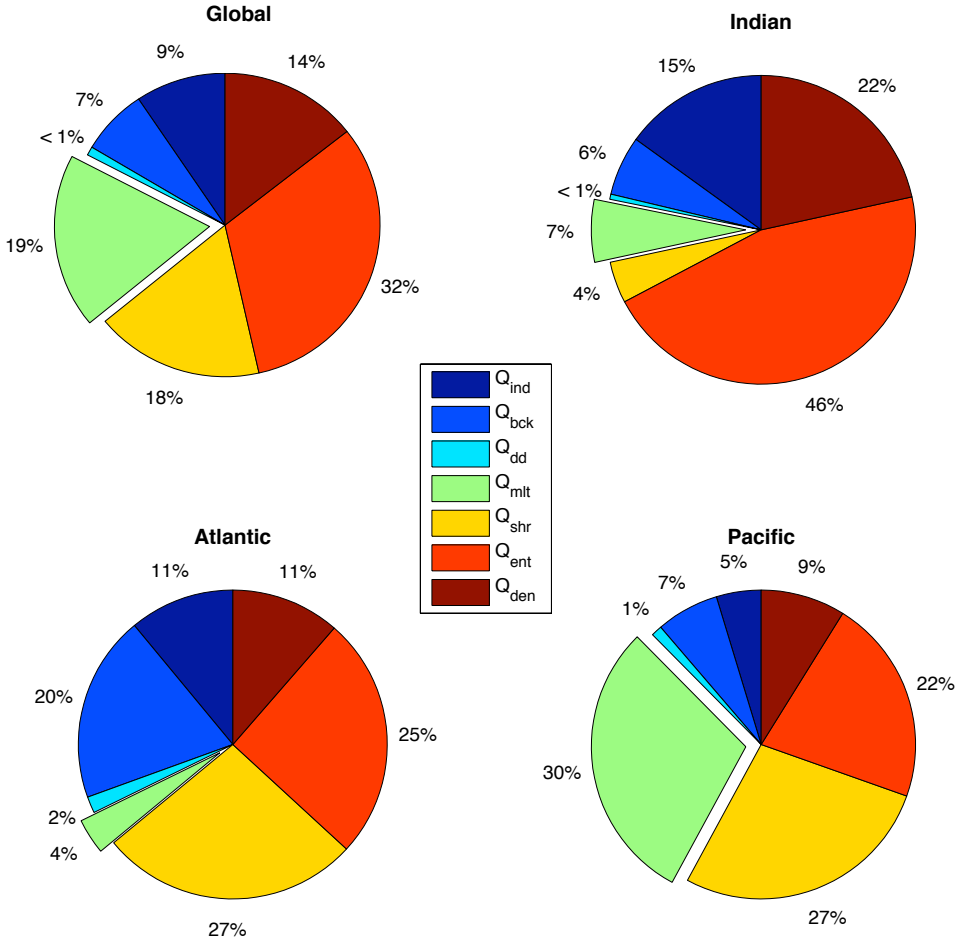

FIGURE 4.14: Contributions of tracer upwelling fluxes in different ocean basins north of the outcropping mask: a) Global, b) Indian, c) Atlantic, d) Pacific. The model has been integrated over a period of 150 years.

The combination of solar irradiance and atmospheric forcing induces characteristic diurnal and seasonal cycles in the mixed layer thickness. Tracer is entrained from the underlying thermocline whenever the mixed layer thickens,

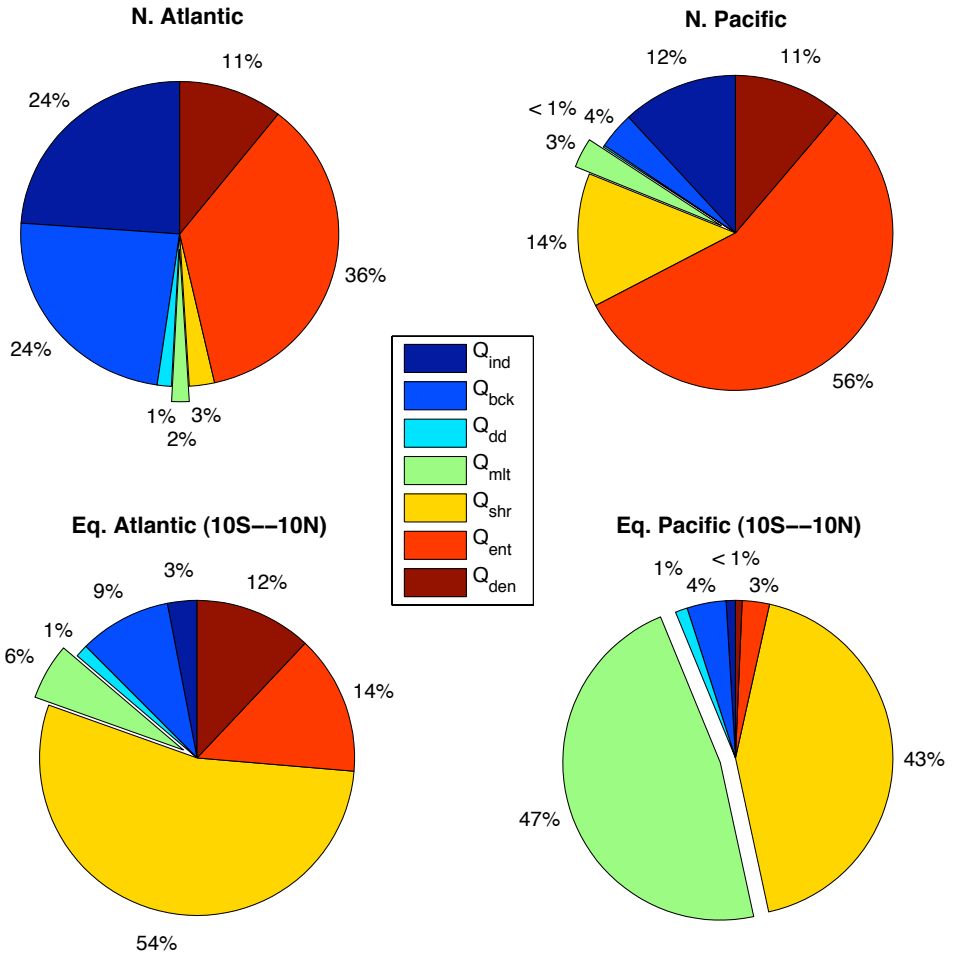

FIGURE 4.15: Contributions of tacer upwelling fluxes in: a) North Atlantic (> 20°N), b) North Pacific (> 20°N), c) Equatorial Atlantic (10°S - 10°N), d) Equatorial Pacific (10°S - 10°N). The model has been integrated over a period of 150 years.

and homogenized through-out the mixed layer by convection (Fig. 4.16). The maximum thickness of the mixed layer usually occurs at the end of winter when the surface buoyancy loss to the atmosphere ceases. Although it is the most important mechanism of SAMW/tracer upwelling in the global average, entrainment does not always play a dominant role in all three ocean basins. The fractional contribution of entrainment due to thickening of the mixed layer (Q_{ent}) varies from 22% (in the Pacific Ocean) to 46% (in the Indian Ocean), as depicted by Fig. 4.14. Although this value goes up to 56% in the North Pacific Ocean (Fig. 4.15), the maximum entrainment flux of tracer actually happens in the Indian Ocean because not much tracer reaches the North Pacific Ocean

($< 0.1\%\ T_{\text{sub}}$). The North Atlantic also hosts a large fraction of Q_{ent} ($\sim 36\%$) due to strong seasonal variation of the mixed layer thickness in the subpolar gyre and high-latitude North Atlantic due to strong winter cooling.

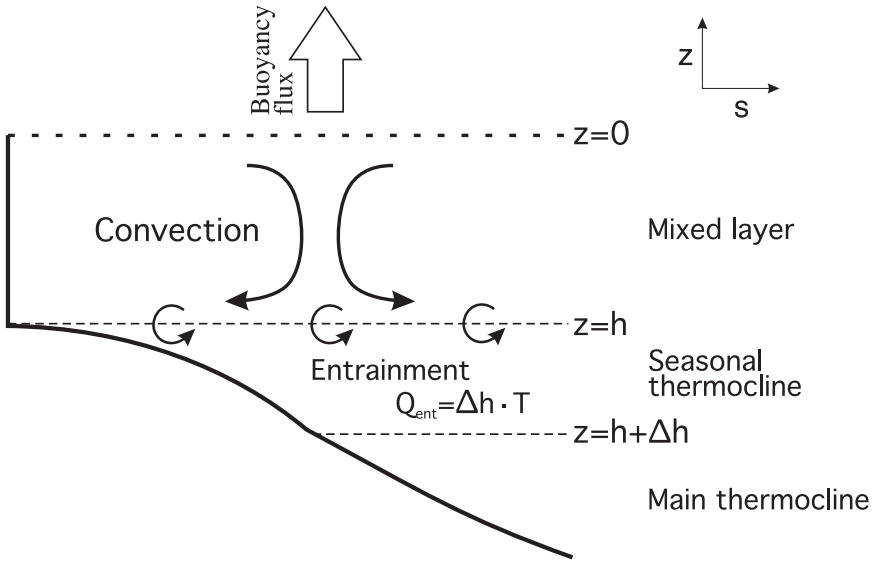

FIGURE 4.16: Schematic of entrainment due to thickening of the mixed layer, amended based on Fig. 2.7 from Williams and Follows (2003). Δh is the increase of the mixed layer thickness due to loss of buoyancy flux in the surface, T is the tracer concentration in the underlying thermocline.

The K-profile diffusivity used in HYCOM has been separated into three independent terms in the interior of the ocean as well as at the base of the mixed layer, where a smooth shape function has been used to ensure that the first vertical derivative of the boundary layer K-profile matches the value from the ocean interior. The effects of the internal wave-generated diffusion (Q_{bck}), salt-fingering and diffusive convection-generated double diffusion (Q_{dd}) and velocity shear instability-induced diffusion (Q_{shr}) have been included. The fractional contribution of total diapycnal diffusion induced tracer upwelling flux ($Q_{\text{bck}} + Q_{\text{dd}} + Q_{\text{shr}}$) reaches its maximum value in the Atlantic Ocean ($\sim 50\%$) due to a strong background diffusion, while the minimum contribution has been obtained within the Indian Ocean ($\sim 10\%$) due to lack of shear induced diffusion. Considering each term of the diapycnal tracer upwelling fluxes, Q_{shr} dominates over the equatorial region in both the Atlantic ($\sim 54\%$) and Pacific oceans ($\sim 43\%$) due to strong velocity shear instability between the surface and subsurface equatorial current systems. A minimum value of 4% is obtained in the Indian ocean due to lack of a significant equatorial current system there.

The fractional contribution from background diffusion shares a similar magnitude ($\sim$ 7%) for the Indian and Pacific oceans, but reaches its maximum value of 24% in the North Atlantic Ocean (19% for the whole Atlantic Ocean basin). Unlike as suggested by Oschlies et al. (2003) and Glessmer et al. (2008), double diffusion is insignificant for most of the ocean basin in our experiment ($<$ 1%). It is probably because we have set the reference density ratio (R_ρ^0 = 1.9) smaller in our model than that used in Oschlies et al. (2003) (there is no general agreement on the value of R_ρ^0 regarding to the type of OGCMs and model resolutions). Therefore, double diffusive mixing is only triggered within limited regions with density ratio exceeding R_ρ^0. However, our result does show the contribution from double diffusion reaches its maximum value in the Atlantic Ocean ($\sim$ 2%).

In order to maintain isopycnic conditions and minimum layer thickness for each model layer, HYCOM remaps layer interfaces at the end of the main loop. The tracer upwelling due to this regridding process was integrated and saved as $Q_{\rm mlt}$ and $Q_{\rm den}$. In Fig. 4.14 we can see that the fractional contribution of $Q_{\rm mlt}$ varies between 4% in the Atlantic Ocean, to 30% in the Pacific Ocean, with a global mean value of 19%. Although this regridding mixing only plays a minor role in the Northern Hemisphere (2% $\sim$ 3%), the fractional contribution can reach values as high as $\sim$ 47% in the equatorial Pacific region between $10^\circ S$ - $10^\circ N$ (Fig. 4.15), as it is a well recognized region with extensive Ekman upwelling. An interesting contrast also exists between the upwelling mechanisms in the two equatorial regions. The tracer upwelling flux in the equatorial Pacific is mainly comprised of contributions from velocity shear-induced diapycnal mixing and MLT constraint-induced regridding mixing; together these two terms account for over 90% of the total upwelling in this region. In the equatorial Atlantic region, the shear term also plays a major role in the total upwelling. However, $Q_{\rm mlt}$ only accounts for 6% in this region, while the regridding mixing due to density restoration ($Q_{\rm den}$) accounts for 12% of the upwelling. It suggests that the permanent thermocline is generally deeper within the equatorial Atlantic than in the equatorial Pacific. Entrainment and background diffusion also play significant roles in upwelling in the equatorial Atlantic (23%) but not in the equatorial Pacific, suggesting that a robust seasonal cycle of the mixed layer thickness only exists in the equatorial Atlantic in the model.

4.2.2 Geographical location of tracer upwelling

The spatial distribution of tracer upwelling fluxes due to different mechanisms is illustrated in Figs. 4.17 and 4.18. Only regions with significant upwelling (> 0.5 *tracer unit* m^{-2}) are shown here. Maximum SAMW upwelling can be seen along the western boundary of South Pacific Ocean, in the equatorial Pacific region, and following the subtropical gyre of Indian Ocean. Minimum upwelling regions are in the subtropical gyres of Pacific and Atlantic oceans. One can see certain similarities between oxygen isolines derived from WOCE Hydrographic Program (WHP) based on numerous global hydrographic surveys (WHP-SAC) (Karstensen et al., 2008) and the geographical location of SAMW upwelling in the model. As proposed by Karstensen et al. (2008), the Oxygen Minimum Zone (OMZ) located along the equatorial and eastern tropical oceans of Atlantic and Pacific basins can be explained by the high productivity induced by extensive nutrient upwelling. It is consistent with the result of our model, which also suggests that this nutrient supply is associated with the SAMW upwelling. Correspondingly, minimum SAMW upwelling in the subtropical gyres suppresses the respiration and leads to a high concentration of dissolved oxygen in these regions. In this section, the different upwelling patterns in three major ocean basins will be discussed separately, as well as the driving mechanisms of SAMW upwelling.

4.2.2.1 North Atlantic

To sustain the patterns of primary production over the subpolar gyre and high-latitude North Atlantic, strong nutrient upwelling is required. If the fluxes were supplied by diapycnal mixing alone, an extraordinarily large turbulent mixing coefficient ($\sim 10^{-3}\ m^2 s^{-2}$) would be needed across the thermocline (Jenkins, 1988), about 2 orders of magnitude higher than the observed value (Ledwell et al., 1993, 1998). Eddy enhancement of the nutrient upwelling in the North Atlantic Ocean has been suggested by McGillicuddy and Robinson (1997); McGillicuddy et al. (1998) and supported by several eddy resolving model experiments in this region (Oschlies and Garcon, 1998; McGillicuddy et al., 2003). However, McGillicuddy's results are under question due to the artificial re-mineralization

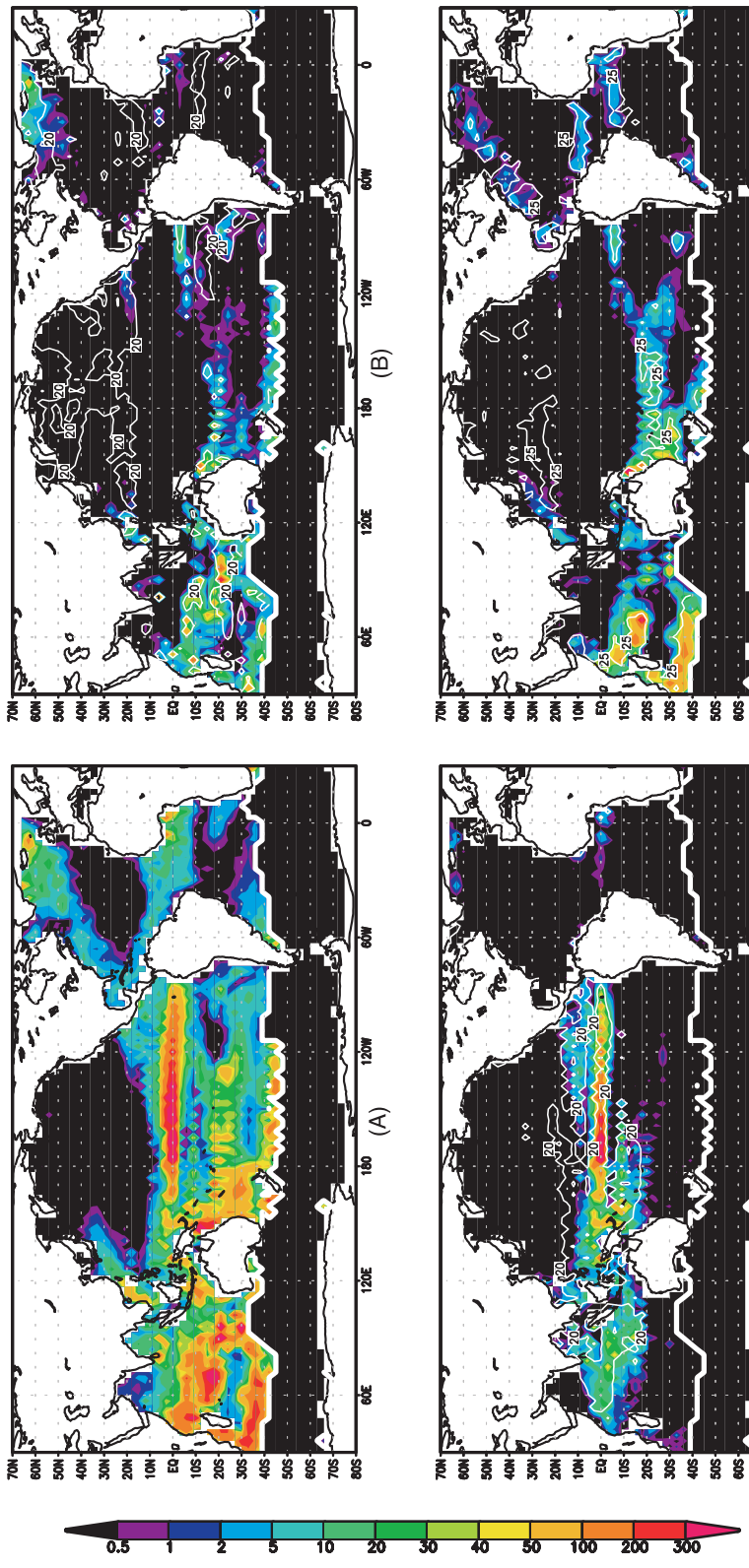

FIGURE 4.17: Time integral of the upwelling tracer flux (*tracer unit m-2*) components into the mixed layer (150 years after tracer release): A) Q_t is the total tracer upwelling flux, B) Q_{ind} is the induction flux, C) Q_{mlt} is the regridding mixing flux due to MLT constraint, and D) Q_{den} is the regridding entrainment due to density restoration. Also shown are ratios of corresponding tracer flux components to total upwelling flux (thin white contour in percentage) and winter outcrops of the lightest SAMW isopycnal in the Southern Ocean (thick white contour).

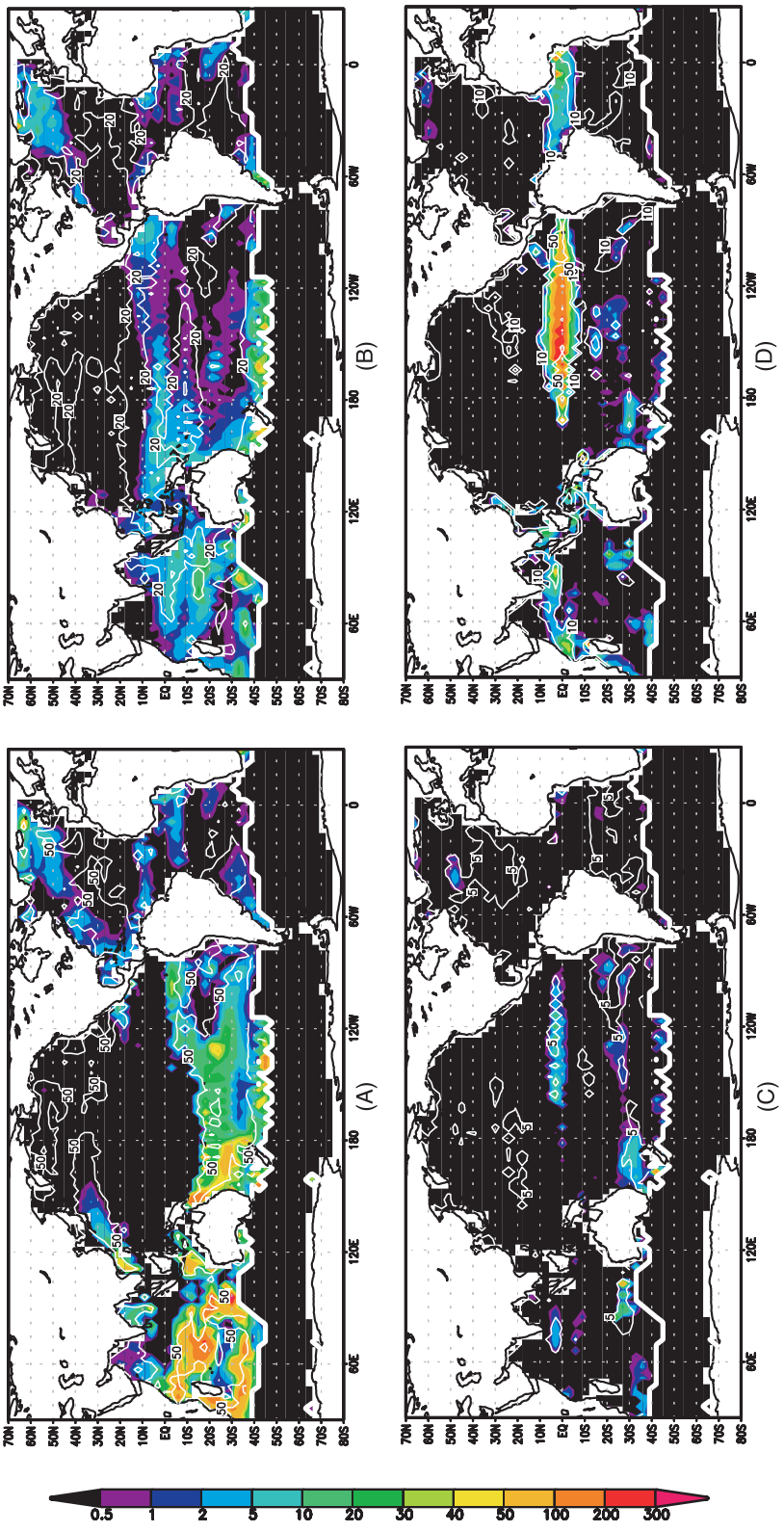

FIGURE 4.18: Same as in Fig. 4.17, except for: A) Q_{ent} as the tracer entrainment due to thickening of mixed layer, B) Q_{bck} as the background diffusion flux, C) Q_{dd} as the double diffusive flux, and D) Q_{shr} as the shear instability induced upwelling flux.

rate used at depth that recharges the nutrient back to depleted seasonal thermocline. Lévy (2001) conducts a careful model study of the instability of a jet examining the new production enhancement related to the increase of model resolution (from mesoscale to sub-mesoscale process). Further analysis about the eddy/wind interaction and its impact on the nutrient supply to the mixed layer has been discussed by Martin and Richards (2001); McGillicuddy et al. (2007) and investigated by model simulation (Eden and Dietze, 2009). Considering the importance of lateral advection and enhanced diapycnal mixing along the WBC, Jenkins and Doney (2003) proposed a gyre-scale nutrient circulation model for explaining the sustainable nutrient supply to the subtropical gyre in the North Atlantic Ocean. A alternative hypothesis has been proposed by Williams et al. (2006), which also emphasized the importance of isopycnal transports of nutrient and suggested that induction is the key mechanism in supplying nutrient to the subpolar gyre in the North Atlantic Ocean. However the relative importance of diapycnal diffusion and its contributions to the total upwelling were not discussed in their diagnostics. Pelegrí et al. (2006) support the importance of isopycnal advection in supplying nutrient to the northern flank of the North Atlantic subtropical gyre, but claim that high diapycnal mixing is also important during the last phase of nutrient transfer to the euphotic layers.

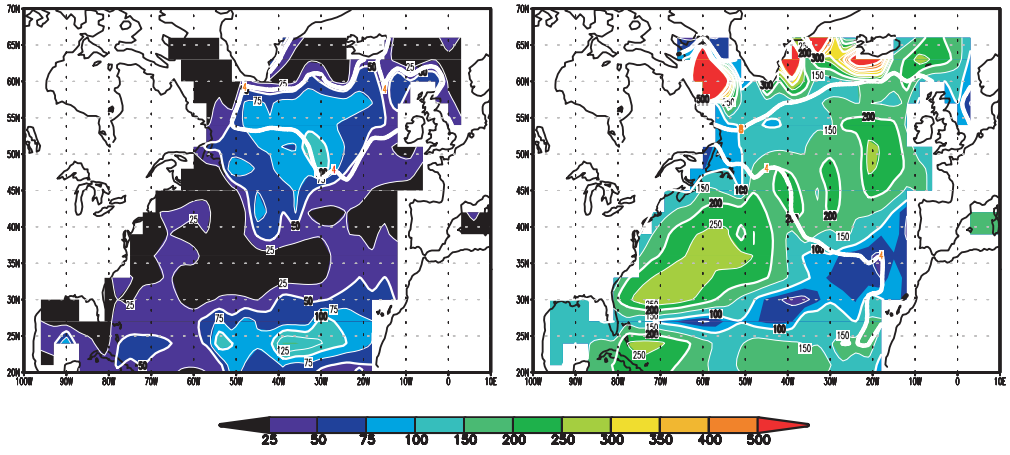

FIGURE 4.19: Mixed layer thickness [m] for the North Atlantic Ocean in (left) September and (right) March. Averaged over a period of ten years after model reached a quasi-equilibrium state. The thick white lines denote the outcrops of lightest (layer 4) and main (layer 8) coordinates that are within the density range of SAMW.

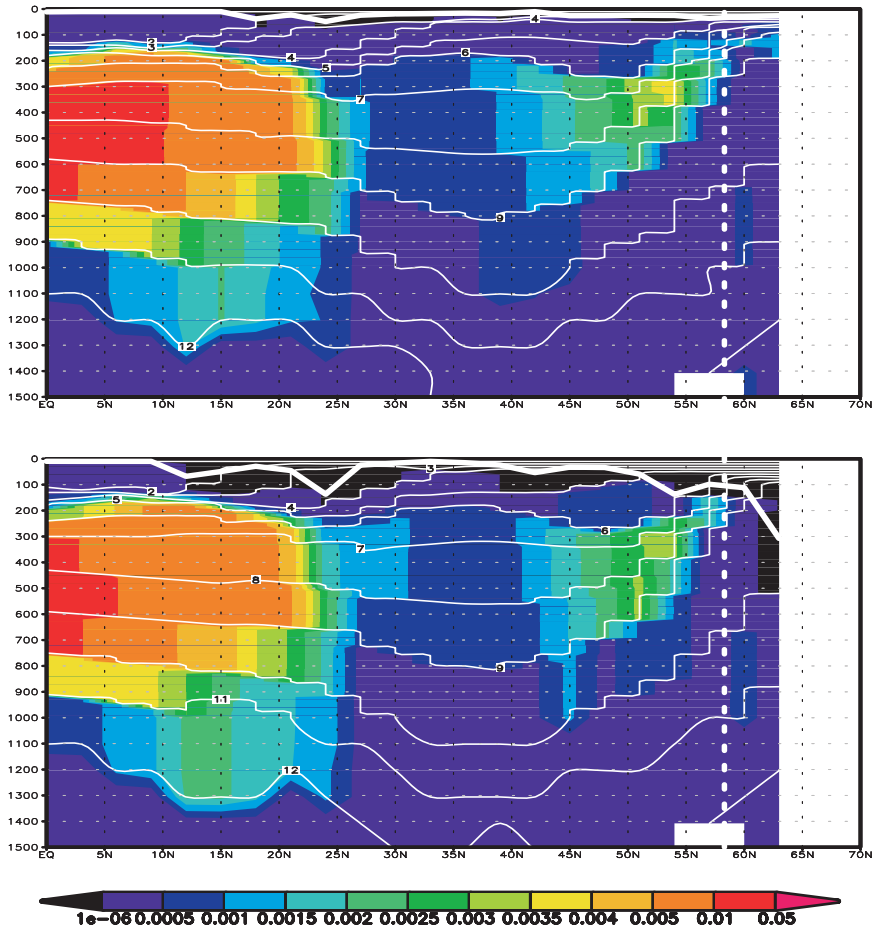

FIGURE 4.20: Tracer concentration along the meridional section of $20°W$ in the North Atlantic Ocean for boreal summer (top) and winter (bottom). The model has been integrated for a period of 70 years after tracer release. Also shown are the isopycnal surfaces with layer number (thin white contours) and mixed layer depth (thick white curve). The latitude of the winter outcrop point for the main SAMW layer (layer 8) has also been marked out by a dotted white line.

In our tracer experiment, induction driven tracer transfer is particularly strong following the cyclonic circuit of the subpolar gyre from the Gulf Stream extension to the high-latitude North Atlantic ($> 55°N$ in Fig. 4.17), where the winter mixed layer becomes progressively denser and thicker downstream. Our model results show a broadly similar magnitude of induction contribution as that suggested by Williams et al. (2006), the induction into the mixed layer accounts for typically $> 40\%$ of the total upwelling in the high latitude region of the North Atlantic. In addition, our results show that entrainment is also an important upwelling mechanism that becomes significant following the Gulf

Stream, subpolar gyre and in the high-latitude region (accounts for 30% $\sim$ 40% of total upwelling, as shown in Fig. 4.18). The geographical distribution of this entrainment upwelling simulated by our model is similar to that calculated by Williams et al. (2000) based on climatological estimation in the North Atlantic. Due to the lack of resolved shear in our model, diapycnal mixing is only significant when strong vertical tracer gradients exists, and therefore only important following the main advection pathway of tracer.

In our experiment, the spatial distribution of strong entrainment in the North Atlantic Ocean can be understood as a result of the seasonal variation of mixed layer thickness following the western boundary current and subpolar gyre in the North Atlantic. The late winter (March) mixed layer depth as well as that in summer (Sep) are illustrated in Fig. 4.19. Following the pathway of the Gulf Stream, significant thickening of the mixed layer is observed, as mixed layer depth increases from $\sim$ 25 m in summer, to over 250 m in winter. Part of the Gulf Stream breaks into two branches at about $45°N$ and flows northeastward across the mid-Atlantic Ridge following the anti-cyclonic subpolar gyre (NAC). There, the mixed layer also thickens from $\sim$ 50 m in summer, to about 200 m in winter. The largest change of mixed layer depth over the seasonal cycle is located in the high-latitude North Atlantic ($> 55°N$), or more precisely, in the Labrador Sea and around the boundary of the Irminger Sea. Mixed layer depth can reach as deep as > 600 m in winter due to strong surface cooling, while summer MLD is less than 50 m in these region. Despite the strong seasonal variation of MLD, the entrainment-induced tracer upwelling flux is not as important in the Labrador Sea as that in the nearby high latitude region (Fig. 4.18). It is because the southward flow of the Labrador Current blocks the northward flowing Gulf Stream by forcing it to turn eastward. Following the advection pathway of the subpolar gyre, most of the tracer has already been entrained/inducted into the mixed layer before it can reach the Labrador Sea from the underlying thermocline by following the south Greenland current system.

It is also worth pointing out that while the winter outcrop of SAMW's main isopycnal (layer 8) tilts equatorward from east to west and extends as far as $55°N$ following the outflow of the Labrador Current, the same density surface never outcrops into the surface mixed layer during the boreal summer (except for the lightest SAMW isopycnals), not even in the extreme high latitudes of

the North Atlantic (Fig. 4.19). Therefore, the subsurface tracer circulation can extend to as far north as the Irminger and Labrador seas during boreal summer following the NAC system underneath the thin mixed layer. However, with the mixed layer reaching its maximum thickness in later winter, tracer circulation following the SAMW layers becomes short-circuited and starts injecting tracer into the mixed layer in the form of induction, that is by isopycnal transfer across the base of the surface boundary layer at winter outcropping regions (Fig. 4.20).

Therefore, considering the seasonal cycle of the thermocline and its influence on the consumption and lateral circulation/recharging of the tracer (and nutrients) into the subpolar gyre and high-latitude region of the North Atlantic, here we propose a 4-D (3-D plus time) nutrient circulation and upwelling model in the North Atlantic Ocean by combining the models of Williams et al. (2006) and Jenkins and Doney (2003). As demonstrated by a schematic plot in Fig. 4.21, the tracer upwelling can be understood as a sequence of processes following a seasonal cycle:

- Step-one: during boreal summer when the mixed layer is at its minimum thickness, subsurface isopycnal/lateral advection of tracer following the GS conveys tracer to the northern flanks of the subtropical gyre, while the continued northward advection of the tracer in the NAC carries the tracer/nutrient to the Labrador Sea within the main SAMW-related isopycnal layers underlying the mixed layer. It can be seen as the fully extended tracer/nutrient circulation that reaches to the extreme northern latitudes of the basin.

- Step-two: the mixed layer thickens during boreal autumn and reaches its maximum thickness in late winter due to strong surface cooling and cold inflow from the Arctic Mediterranean and the Labrador Sea. During this period tracer from underlying seasonal thermocline is entrained into the surface mixed layer and consumed rapidly. Compared with the Ekman upwelling (induced only by surface winds), buoyancy loss is more important and plays a dominant role in controlling the entrainment rate here.

- Step-three: in boreal winter, the main SAMW-related isopycnals outcrop into thick mixed layers and the lateral transport of tracer generates strong

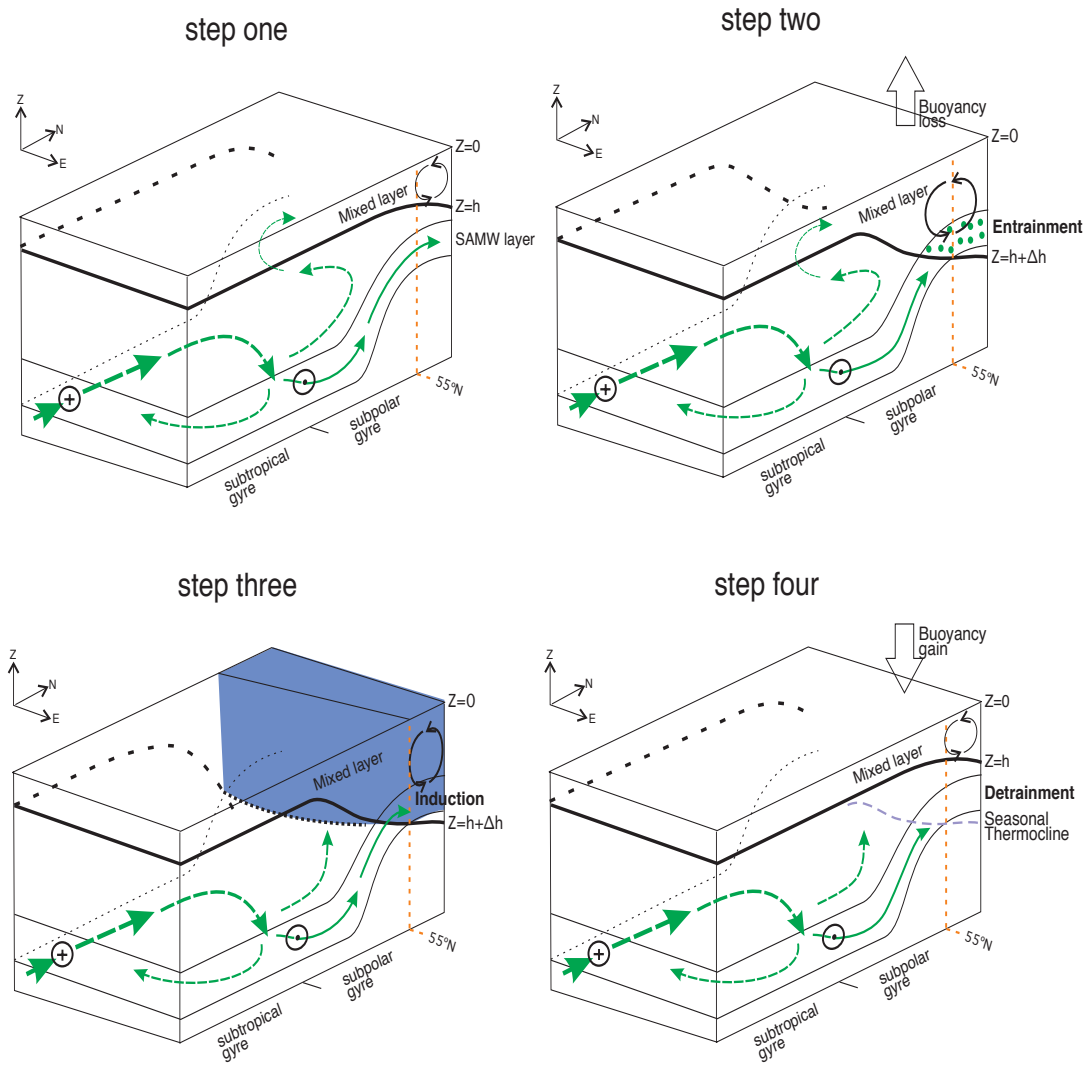

FIGURE 4.21: Schematic of tracer/nutrients pathways along the main density surfaces of SAMW in the North Atlantic ocean. Sustainment of tracer/nutrient upwelling can be understood as a sequence of processes following the seasonal cycle of mixed layer thickness: (**Step-one**) boreal summer with the subsurface tracer circulation extending to the extreme northern latitude of the basin; (**Step-two**) tracer is entrained from the thermocline into the mixed layer due to surface buoyancy loss during boreal autumn and early winter; (**Step-three**) the mixed layer reaches its maximum depth in late winter and tracer circulation is confined to the subtropical and eastern part of subpolar gyres; outcropping of the main SAMW layers and lateral advection generate strong induction of tracer/nutrients into the mixed layer; (**Step-four**) during boreal spring and early summer, thinning of the mixed layer generates a tracer/nutrient depleted seasonal thermocline, sustainment of the tracer/nutrinet supply must be completed by subsequent summer tracer/nutrients circulation and replenishing.

induction following the pathway of the subpolar gyre, firstly at Iceland Basin and then at the Irminger Sea and Denmark Strait. During this period, the lateral circulation of the tracer is confined near the subtropical and eastern part of the subpolar gyres. Hardly any tracer reaches the Labrador Sea due to the southward extension of the thick winter mixed layer resulting from strong winter cooling. Tracer circulation in this period can be regarded as spatially restricted.

- Step-four: the mixed layer base rises during boreal spring and reaches its shallowest position in late summer, subsequently resulting in a tracer/nutrient depleted seasonal thermocline. Recharging of the tracer to this underlying seasonal thermocline depleted by entrainment, induction and rapid surface utilization must be done by another full extension of tracer/nutrient circulation in summer by step one.

As described in Chapter 3, the surface boundary layer depth in HYCOM is determined by both wind induced velocity shear and surface buoyancy flux. The combination of solar irradiance and atmospheric forcing induces characteristic seasonal cycle of the mixed layer thickness. Thickening of the mixed layer can be induced by surface buoyancy loss as well as enhanced wind stirring (increased wind induced velocity shear). Here we calculated the magnitude of wind stress over the Northern Hemisphere based on the NCEP reanalysis data that has been used as surface forcing during HYCOM simulation. The Net surface heat flux was then calculated and averaged over a period of ten years with the purpose of estimating an annual-mean value. Results are shown in Figs. 4.22 and 4.23.

Comparison of the spatial and temporal distributions of the wind stress magnitude and the net heat flux in the Northern Hemisphere suggests that in boreal winter (March), both strong surface buoyancy loss and enhanced wind stress appear to the north of $30°N$ in the Atlantic Ocean. The combination of these two effects results in a seasonal variation of the mixed layer thickness in the GS extension, subpolar gyre and the high-latitude North Atlantic regions (Fig. 4.19). However, the relative importance of surface diabatic flux and mechanical forcing in altering the MLD vary depending on the concerned regions. As demonstrated in Fig. 4.22, in boreal winter the magnitude of the surface wind stress increases from 0.02 to 0.1 Nm^{-2} between $30°N \sim 45°N$ in regions that

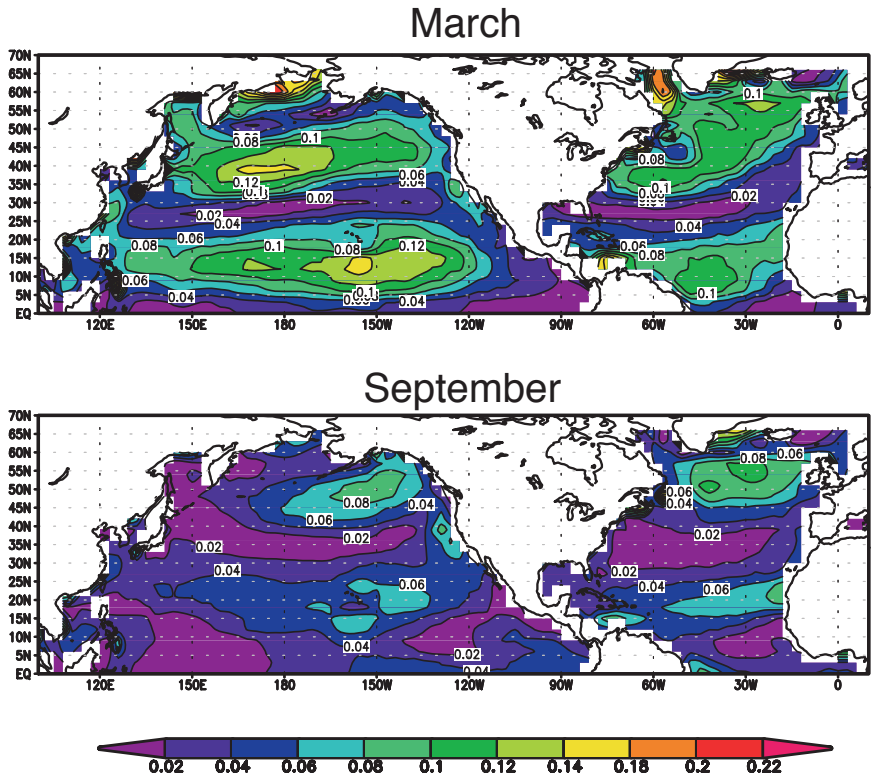

FIGURE 4.22: Magnitude of surface wind stress [Nm^{-2}] over the North Hemisphere in (top) March and (bottom) September. Contour intervals = 0.02 Nm^{-2}.

cover the GS, while little seasonal variance ($0.08 \sim 0.1\ Nm^{-2}$) of the wind stress can be observed over the center of the subpolar gyre. The maximum seasonal variation appears over the Labrador Sea regions where the magnitude of wind stress increases from 0.02 to 0.2 Nm^{-2} in boreal winter. Meanwhile, surface cooling has been found during boreal winter over the high-latitude North Atlantic and extends to as far south as $\sim 30°N$, covering most of the Gulf Stream region. In contrast, positive net heat flux has been found over almost all North Atlantic during boreal summer, except for the subpolar gyre along the pathway of NAC. As a result, entrainment in the North Atlantic subpolar gyre is mainly due to the strong winter cooling overlying this region, while the entrainment along the Gulf Stream and in the high-latitude North Atlantic is a result of both negative (from ocean to atmosphere) surface buoyancy flux and enhanced wind stirring effect.

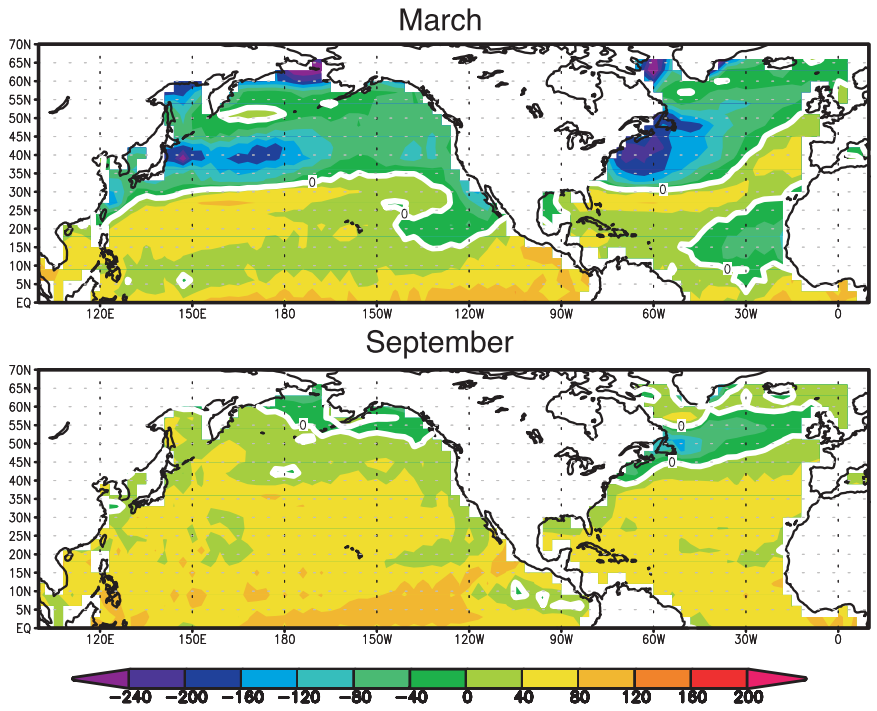

FIGURE 4.23: Sea surface net heat flux [wm^{-2}] (averaged over a period of ten years after tracer release) distribution in (top) March and (bottom) September for the Northern Hemisphere.

4.2.2.2 Indian Ocean

As for the Southern Hemisphere, following the subtropical gyre in the Indian Ocean there are strong tracer upwelling fluxes due to induction and entrainment. Unlike the North Atlantic Ocean, the mixed layer depth is never deep enough to outcrop the SAMW isopycnals following the subtropical gyre in the Indian Ocean, not even in the southern winter (Fig. 4.24) as there is no significant winter cooling or other cold water injection from nearby regions. Instead, most of the tracer upwelling following the subtropical gyre in the Indian Ocean is achieved through a sequence of processes. First, vertical convection (in the first year before applying the surface consumption) and diapycnal mixing (due to the strong tracer gradients) raises up a fraction of SAMW-tracer at the density surface that effectively entrains tracer into the near surface isopycnals (layers 2 to 3 with density σ_2 = 31.87 - 32.75) that lay just below the summer shallow surface boundary layer. Second, tracer is trapped in the subtropical gyre current system and circulates across the Indian Ocean following the SAMW layers as well as in the near-surface layers. Third, the mixed layer

thickens during the southern winter and part of the tracer is entrained from the near-surface layer into the mixed layer. Outcropping locations for near surface layers also shift due to the variation of the mixed layer thickness. Fourth, induction occurs due to tracer lateral advection following the near surface layers (mainly in layer 2) and by crossing the base of the mixed layer at the outcropping location during the southern winter. Seasonal variation of the MLD and its induced shifting of the outcropping locations for these near-surface layers play an important role in determining the induction region in the Indian Ocean. As demonstrated in Fig. 4.25, the maximum induction tracer flux appears close to the tracer release region in the southeast Indian Ocean, and is mainly a result of injection from the recirculation of subtropical gyre water as well as ACC-transported tracer into the deep winter mixed layer by following the SAMW isopycnals (layer 4 to 8). The outcropping location of near-surface isopycnals moves northward from April to July and retreats southward from Oct to Jan, leading to a seasonal cycle of the induction location in the Indian Ocean. Winter induction mainly occurs following the northern branch of the subtropical gyre, while the induction along the western boundary and the southern branch mainly takes place during the southern spring and autumn.

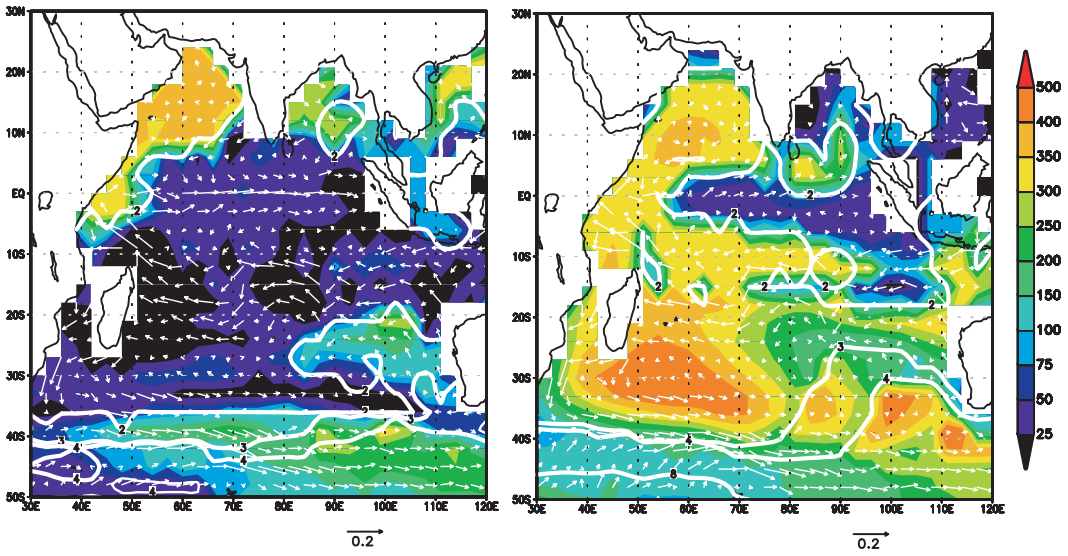

FIGURE 4.24: Mixed layer thickness $[m]$ and outcrops of SAMW and near-surface layers in the Indian Ocean for (left) Jan and (right) July. Also shown is averaged subsurface circulation (mean velocity field $[ms^{-1}]$ averaged over SAMW isopycnals).

In order to generate induction from near-surface layers, tracer must be raised

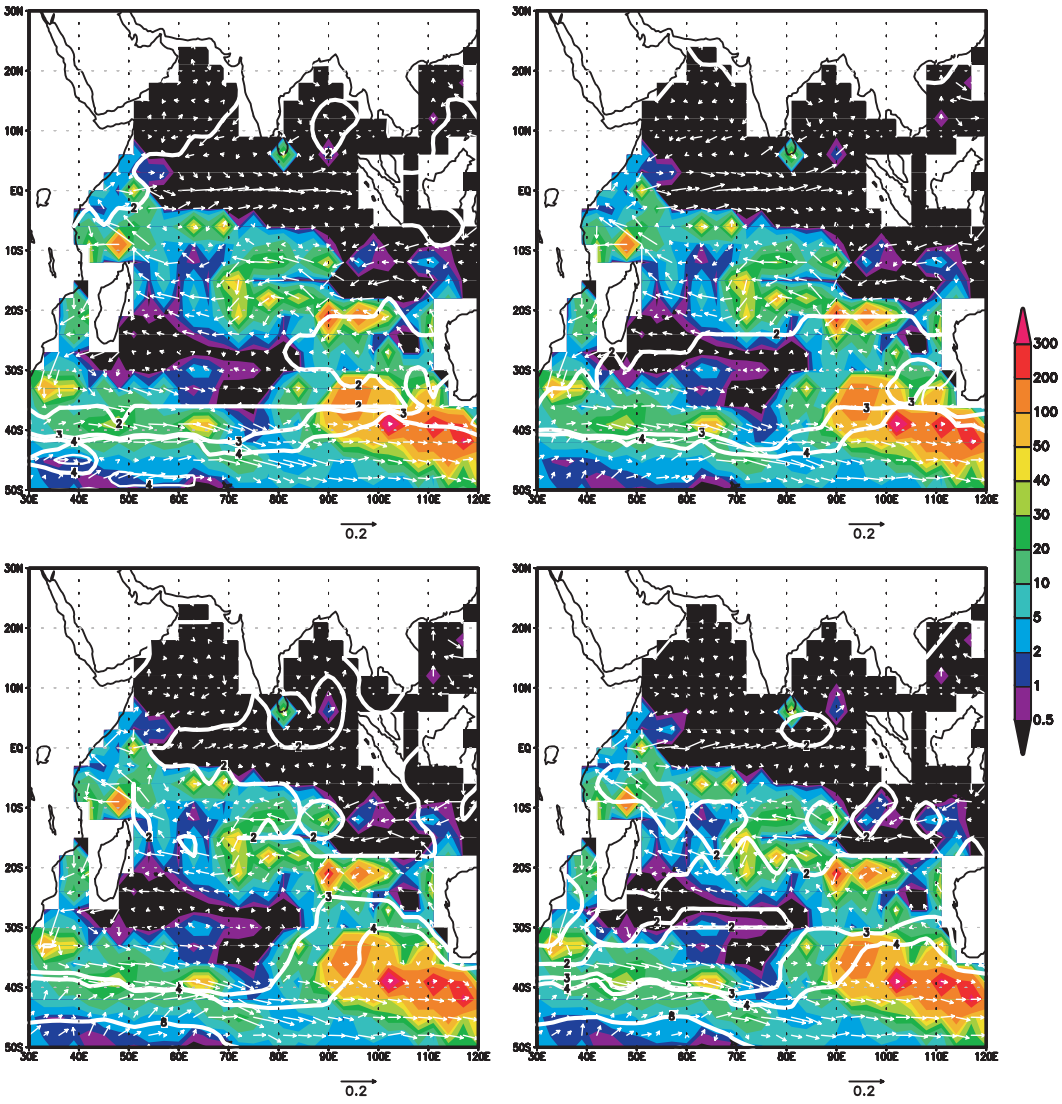

FIGURE 4.25: Mean velocity [ms^{-1}] of the SAMW circulation (averaged over the SAMW isopycnals) and outcrops of the SAMW and near surface layers in the Indian Ocean: (A) during the NE monsoon in Jan; (B) during the transition period in April; (C) during the SW monsoon in July; (D) during the transition period in October. Also shown is the magnitude of tracer induction flux [m^{-2}] as the shaded region (integrated for 20 years after tracer release).

at the density surfaces from SAMW isopycnals (layers 4 - 8) to the lighter layers (layer 2 - 3) first. Possible mechanisms have been investigated and we found that this diapycnal tracer uptake in the Indian Ocean is mainly a result of its closeness to the tracer release region in the southwest Indian Ocean, as well as the tracer release algorithm that has been applied during initialization. After the tracer is released in the winter mixed layer in the mode water density surfaces, strong vertical convection forces its mixing throughout the the surface boundary layer and thus injects tracer into near-surface layers (Fig. 3.8). Once released, tracer is allowed to be subducted into the interior of the ocean following the SAMW isopycnals as well as the density surfaces near the surface for one year, before any surface consumption algorithm is applied. Once escaped from the mixed layer, this part of tracer within the near-surface layers (layers 2 and 3) contributes as a source for the tracer induction in the Indian subtropical gyre (Fig. 4.26).

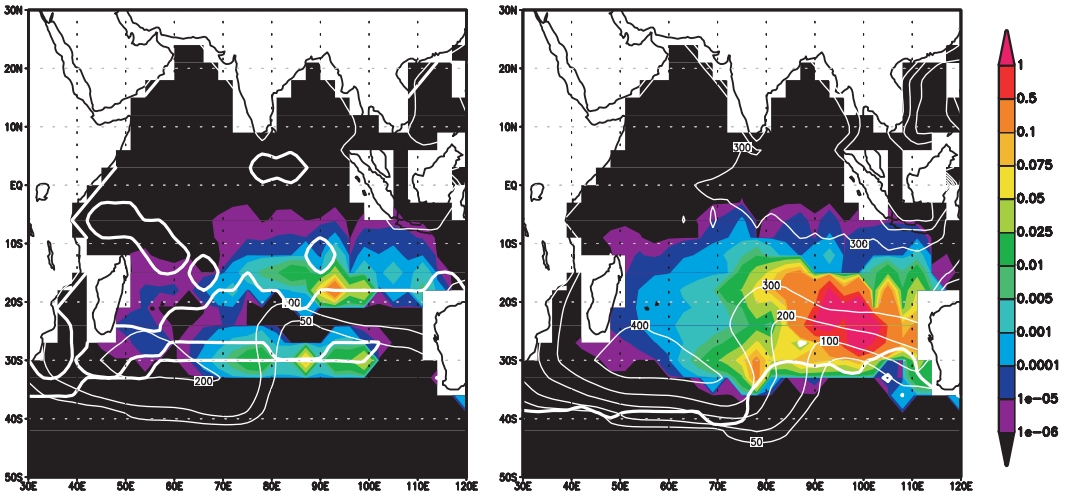

FIGURE 4.26: First Year tracer concentration in the Indian Ocean after subduction: (left) on the density surface $\sigma_2 = 31.87$ (layer 2); (right) on the density surface $\sigma_2 = 32.75$ (layer 3). The superimposed thin white contours show the mid-depth of the isopycnal. Outcrops of the density surface are also shown in thick white lines.

After being subducted into the ocean interior, tracer circulates following the subtropical gyre in the Indian Ocean. Due to its closeness to the tracer release region, high tracer concentrations are observed following the pathway of tracer circulation on the SAMW isopycnals below the mixed layer. Strong vertical tracer gradients emerge once induction and/or entrainment removes tracer from the near surface isopycnals (layers 2 and 3). Therefore, although the magnitude

of diapycnal diffusivity is only of 10^{-5} $m^2 s^{-1}$, there is still a strong diapycnal tracer uptake at density surfaces following the subtropical gyre in the Indian Ocean. However, it may seen in Fig. 4.14 that diapycnal mixing only accounts for $\sim$ 10% of the total upwelling in the Indian Ocean, suggesting that this turbulence induced diapycnal tracer flux is mainly responsible for raising-up tracer from the SAMW core density surfaces (layers 4 to 8) to near-surface isopycnals (layers 2 and 3), instead of injecting tracer into the surface boundary layer directly.

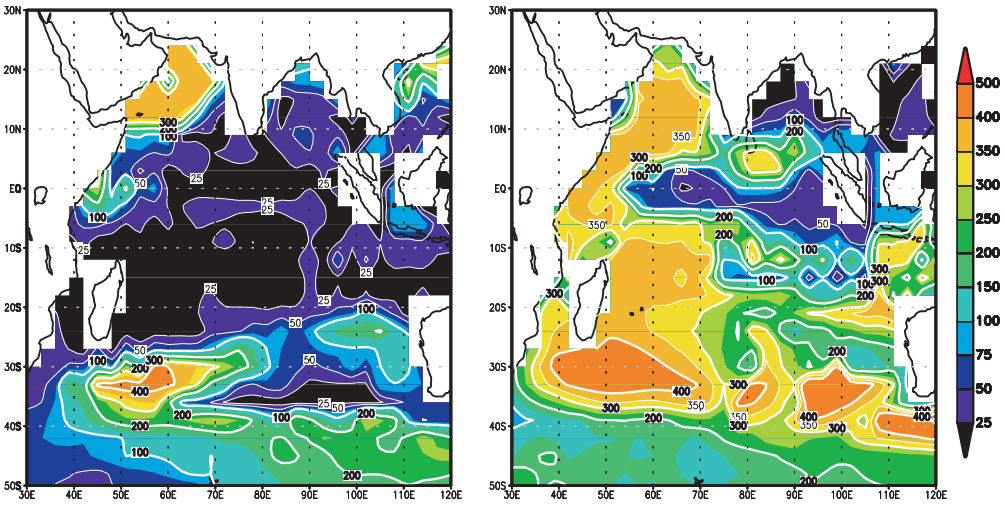

FIGURE 4.27: Mixed layer thickness [m] for the Indian Ocean in (left) March and (right) September. Averaged over a period of ten years after model reached a quasi-equilibrium state.

As demonstrated by Fig. 4.18 (A), extensive entrainment occurs following the subtropical gyre in the Indian Ocean, due to the thickening of the mixed layer during the southern winter. As for the North Atlantic, seasonal variations of the MLD in the Indian Ocean are illustrated in Fig. 4.27. Maximum differences between summer and winter MLD are found near the western boundary area (with $\Delta h \simeq 300$ m) and along the southern recirculation branch of the subtropical gyre (with $\Delta h \simeq 250$ m). A general trend is that following the advection pathway of the Indian Ocean subtropical gyre, seasonal variance of MLD is enhanced downstream, as MLD increases from < 25 m in summer to ~ 150 m in winter over the northern branch. Surface wind stress as well as surface diabatic forcing play important roles in determining this seasonal cycle of MLD and are illustrated in Figs. 4.28 and 4.29.

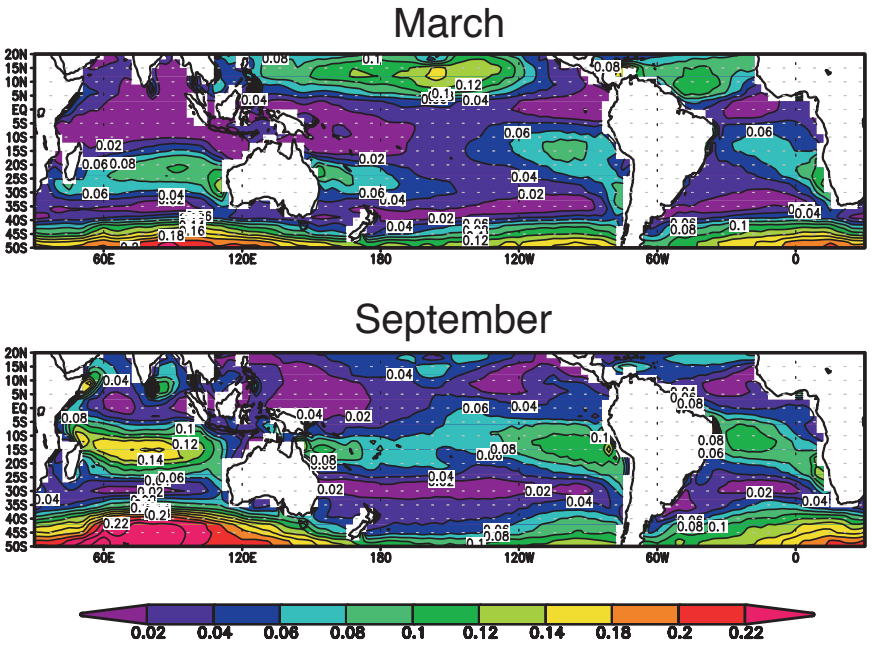

FIGURE 4.28: Magnitude of surface wind stress [Nm^{-2}] distribution in (top) March and (bottom) September for the Southern Hemisphere. Contour intervals = 0.02 Nm^{-2}.

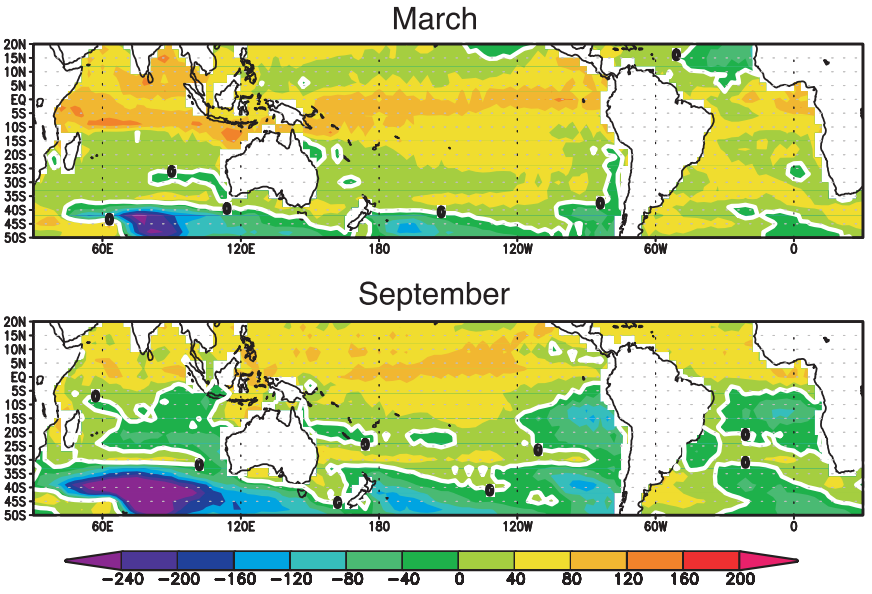

FIGURE 4.29: Sea surface net heat flux [wm^{-2}] (averaged over a period of ten years after tracer release) distribution in (top) March and (bottom) September for the Southern Hemisphere.

Under the influence of the unique southern Asia monsoon system, the prevailing winds in the Northern Indian Ocean (north of $10°S$) change from NE in Jan to SW in July. The ocean circulation responds to the seasonally varying monsoon winds and as a consequence presents well-defined seasonal characteristics. During the southern summer (December-March), the magnitude of the maximum wind stress in the model is $\sim$0.1 Nm^{-2} and is found in a belt between 15° S to 30° S. The influence of the NE monsoon is weak in the northern Indian Ocean where the wind stress magnitude is normally < 0.02 Nm^{-2}. This maximum wind stress belt moves northward to between 5° S - 25° S in the southern winter (June-September) and increases to 0.14 Nm^{-2} due to the strong SE trade winds and the vanishing of the NE monsoon. At the same time, strong surface wind stresses also appear in the Arabian Basin and Bay of Bengal due to the SW monsoon.

Considering the influences of both the surface wind stress and the air-sea net heat flux, the MLD variations and their induced tracer entrainment can be explained by following the pathway of SAMW in the subtropical gyre. First in the northern branch of the Indian subtropical gyre, thickening of the MLD is due to the combined effect of enhanced surface wind stirring and winter time surface cooling. Tracer is entrained into the mixed layer following the deepening of the mixed layer and is caused by both surface buoyancy loss and enhanced mechanical forcing. Along the western branch near Madagascar and the African coast, thickening of the MLD is mainly caused by a northward shift of the maximum wind stress belt in the southern winter (Fig. 4.28), following the reversal of the prevailing monsoon wind direction from the north. Therefore tracer entrainment in this region is primarily determined by the wind stirring effect. In the end, surface heat loss along the southern limit of the subtropical gyre and near the ACC plays a dominant role in determining the MLD and tracer entrainment there, and thickening of the MLD is mainly a result of strong surface cooling during southern winter.

Fig. 4.17-D also shows strong contributions ($> 20\%$) from Q_{den} following the subtropical gyre in the Indian Ocean. As a term induced by coordinate regridding process due to restoring the isopycnic conditions, it is considered as partly numerical. Diagnostics separating density discrepancy driven by surface buoyancy input and by density flux across the boundary layer base are challenging

under the frame of current HYCOM version and have not been included in this thesis due to the time limit of my PhD.

4.2.2.3 Equatorial tracer upwelling

As demonstrated in Fig. 4.17(A), our model predicts extensive upwelling in the eastern equatorial Pacific Ocean. This is consistent with the modeling results of Palmer and Totterdell (2001) with a coupled ecosystem model (HadOCC), which predicted a high primary production associated with strong nutrient upwelling fluxes in this region. Further diagnostics suggest that this strong upwelling is almost entirely due to three processes (see Fig. 4.17 and 4.18): the regridding mixing that is associated with Ekman divergence ($\sim$ 47% in Fig. 4.15); the diapycnal mixing due to resolved velocity shear ($\sim$ 43% in Fig. 4.15); the double diffusive mixing ($>$ 5% in the eastern equatorial Pacific, as shown in Fig. 4.18). In the physical ocean as well as in our model, equatorial upwelling into the mixed layer is very sensitive to the balance between Ekman divergence-induced upwelling (adiabatic) and upper-ocean mixing processes (diabatic). Despite the fact that Ekman upwelling is the most important mechanism of tracer re-emergence in the equatorial Pacific Ocean in the model, the discussion about this mechanism and its relationship with Q_{mlt} (regridding mixing triggered by numerical constraint, Fig. 4.17 (C)) in our model is deferred to Section 4.3. The present discussion is focussed on diapycnal mixing.

The relationship between turbulent mixing and vertical velocity shear in the equatorial region has been investigated extensively by Peters et al. (1995, 1994) as part of the the Tropic Heat Experiment. The focus of these studies was on assessing the importance of vertical turbulent mixing in balancing the zonal pressure gradient below the surface Ekman layer (Gill, 1982). Philander (1990) asserts that vertical mixing processes in the equatorial region are necessary for the upwelling to produce the surface temperature patterns. As a well recognized region with strong vertical shear, Gregg (1998) also suggested that vertical mixing should be strong in the stratified region above the Equatorial Under-Current (EUC) where it serves to maintain the balance between large upwelling transport and downward heat flux. According to Weisberg and Qiao (2000) the diapycnal diffusivity required for balancing the downward mixing of heat over the lower portion of the EUC is about 4×10^{-3} $m^2 s^{-1}$. In our model results,

a similar magnitude of diffusivity ($\sim 10^{-3}\ m^2 s^{-1}$) has also been found in the eastern equatorial Pacific. Considering the fractional contributions, diapycnal mixing (especially the large-scale shear-induced mixing) apparently plays a significant, and sometimes dominant role in the tracer/nutrient upwelling in the equatorial region (Fig. 4.18 (D)). Aside from Ekman upwelling (accounts for 47% of Q_t), velocity shear induced diapycnal mixing (Fig. 4.18(D)) is the most important upwelling mechanism for the equatorial Pacific Ocean in the model. This term accounts for $\sim 43\%$ (Fig. 4.15) of the total upwelling between $10°S$ and $10°N$, indicating the existence of a strong vertical shear in velocity at the base of the surface boundary layer, which is consistent with observations (Lien et al., 1995; Peters et al., 1995) and the theory of equatorial dynamics. The plume of this shear-induced upwelling is centered at $150°W$ and extends zonally from $170°E$ to the eastern boundary. There is no significant shear-induced upwelling in the western part of equatorial Pacific, between $120°E$ and $180°E$, which is consistent with Weisberg and Qiao (2000).

To understand this strong shear-induced upwelling, we need to comprehend the local current system in the equatorial Pacific first. The general circulation of the equatorial Pacific Ocean is characterized by strong wind-driven zonal flows (Reid, 1997). The surface currents are primarily wind-driven and relatively strong currents for a given wind stress are generated in association with the vanishing of the horizontal Coriolis force at the equator. The time-averaged surface flows are dominated by the westward South Equatorial Current (SEC; between about $3°N$ and $20°S$) in the equatorial Pacific, except for an eastward-flowing North Equatorial Countercurrent (NECC) between about $5°N$ and $10°N$ (Tomczak and Godfrey, 2003). The SEC and NECC are strongest in the central Pacific where the trade winds are strongest, but considerably weaker in the west than in the east, reflecting the greater variability of the winds in the western Pacific. This directly wind-driven flow vanishes below the mixed layer (usually shallower than 100 m) and the time-averaged subsurface flows are dominated by the eastward EUC, which is the strongest equatorial Pacific current found within the thermocline just below the westward SEC (Wyrtki and Kilonsky, 1984). Rodgers et al. (2003) proposed that the densest EUC waters originate from SAMW, suggesting a direct connection between the equatorial Pacific and the Southern Ocean. The strong mean shear above the core of the EUC (at the base of the mixed layer) gives rise to strong vertical mixing in the equatorial Pacific. Also the strong subsurface meridional shear of the zonal flow appears

between the SEC and NECC,associated with a subsurface maximum in the NECC near 50 m.

Despite the coarse resolution of our model, HYCOM reproduces the complicated equatorial Pacific current system reasonably well in our simulation, as demonstrated by Fig. 4.30. The strong westward SEC is centered at 140°W and extends zonally between 180°E and 100°W, almost coincident with the equatorial shear upwelling region (Fig. 4.18 (D)). This surface current is directly driven by the westerly Trade winds and can reach a maximum velocity of 0.7 ms^{-1} in the model. A well identified eastward flow of the EUC can be observed on the isopycnal surface $\sigma_2 = 31.87$ just below the mixed layer. It occupies the whole latitudinal band between 5°S and 5°N, with its core located between 180°E and 130°W in the Pacific Ocean. A vertical section of zonal flow along the equatorial Pacific has also been produced for the upper 1000 m (Fig. 4.31). The surface SEC weakens towards the west, when the thickness of the flow increases from $\sim$ 30 m to $\sim$ 100 m. Just below the SEC is the eastward EUC which is the dominant current in this region and normally occupies a depth between 100 m to 300 m. The westward Equatorial Intermediate Current (EIC) is found directly below the EUC across the Pacific. Both the EUC and EIC slope upward toward the east, tending to follow the shoaling isopycnal surfaces. With the weakening and thickening of the surface SEC flow towards the west, vertical shear in velocity at the mixed layer base also decreases westward. Therefore it is easy to understand why diapycnal mixing-induced tracer upwelling is only significant in the central-eastern Pacific. The tendency of this enhanced diapycnal mixing occurs in a seasonal cycle too. As winds strengthen in the second half of the year, the surface SEC and NECC both intensify thus strengthening the shear that drives turbulent mixing. Therefore, more tracer/nutrient upwelling occurs during June-December in the model.

The circulation of the tropical Atlantic has much in common with that in the tropical Pacific in the model because similar trade winds with similar seasonal fluctuations prevail over both oceans. In the equatorial Atlantic, surface flow is directly wind-driven and flows westward as the SEC. This current is particularly intense between July and September and can attain speeds of ~ 1 ms^{-1}. Below the westward surface flow is the intense eastward EUC; its core is at a depth of 100 m in the west, and shoals towards the east (Fig. 4.32). The current exists because the westward trade winds maintain an eastward pressure gradient by

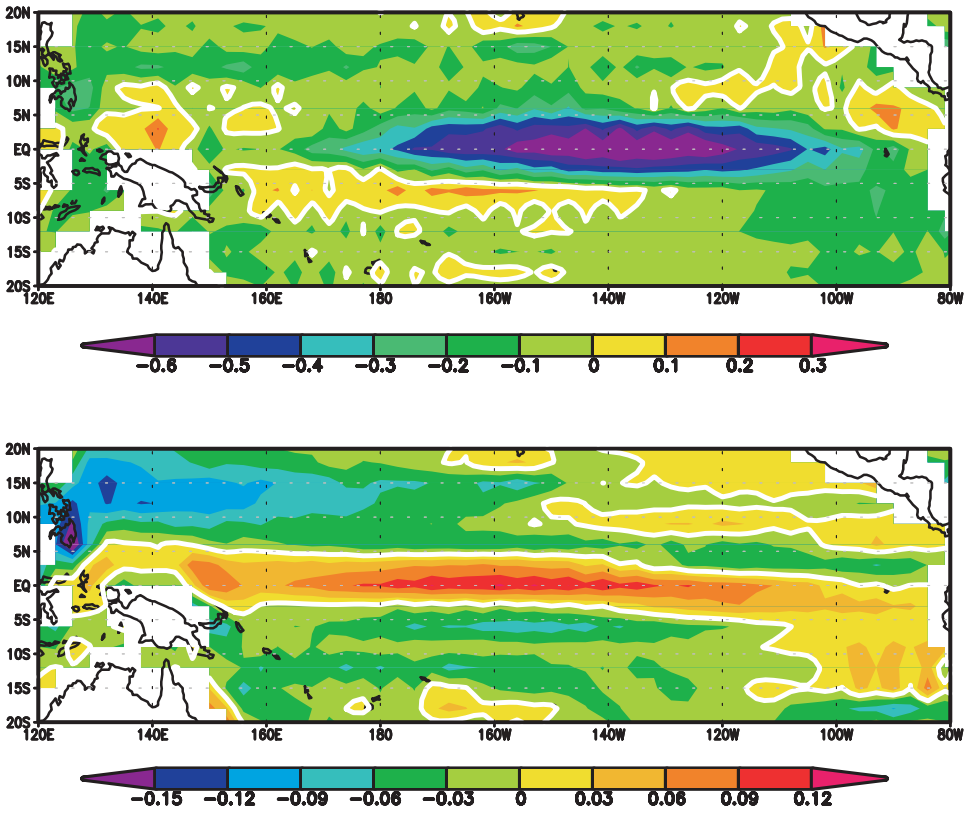

FIGURE 4.30: Map of long-term mean zonal velocity fields [ms^{-1} with positive values eastward] in the Tropical Pacific region at (top) surface with strong westwards SEC and (bottom) on the isopycnal surface $\sigma_2 = 31.87$ with strong eastwards EUC. Velocity fields have been averaged over a period of 10 years after model reaching the equilibrium state. White contours indicate zero zonal velocity.

piling up the warm surface waters in the western side of the Atlantic basin. As Coriolis force vanishes at the equator, this pressure force becomes the only source of momentum for the EUC (see Tomczak and Godfrey (2003)). The strong vertical shear between the EUC and overlying SEC produces continuous turbulent mixing in the equatorial Atlantic region and accounts for a similar fractional contribution in tracer upwelling as that in the equatorial Pacific ocean (Fig. 4.15). However, unlike the Pacific upwelling pattern, this shear induced upwelling occupies the whole equatorial Atlantic between $10°S$ and $10°N$ and extends zonally from African coast to the South American coast (see Fig. 4.18 (D)).

Unlike in the Atlantic and Pacific oceans, shear-induced upwelling only exists near the northern boundary of the Indian Ocean, within the Somali Basin and

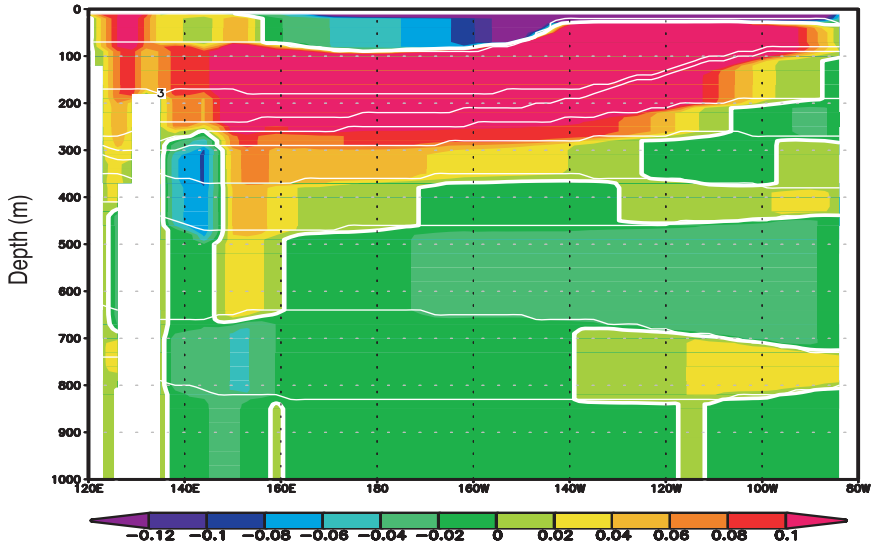

FIGURE 4.31: long-term mean zonal velocity fields $[ms^{-1}]$ in a vertical section along the equatorial Pacific Ocean. Annual mean velocity has been averaged over a period of 10 years. Thick white contours indicate zero zonal velocity. Also shown are the isopycnal coordinate interfaces in thin white lines.

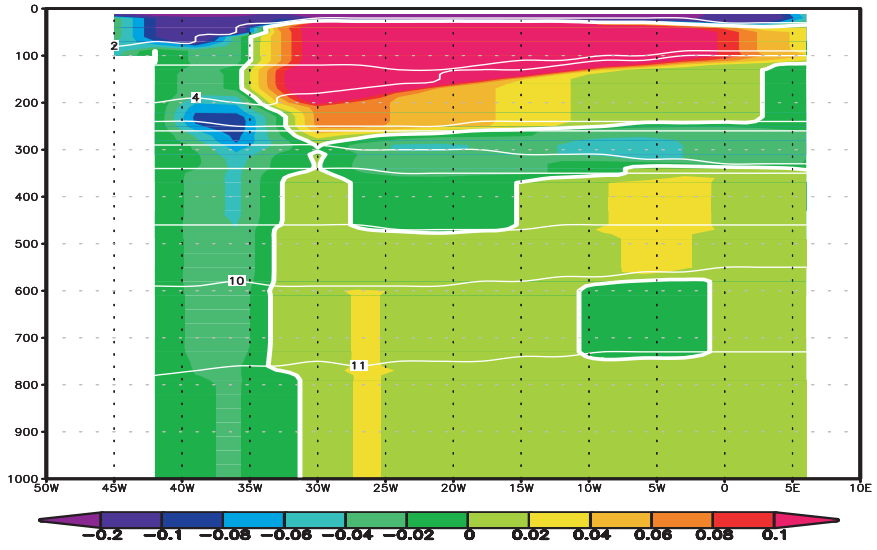

FIGURE 4.32: Same as 4.31 except for the equatorial Atlantic Ocean.

at the southern edges of the Arabian Basin and Bay of Bengal (Fig. 4.18 (D)). This pattern of shear induced upwelling is generated by the unique monsoon system in the Indian Ocean. A detailed description of the wind-driven surface circulation in the Indian Ocean can be found in Tomczak and Godfrey (2003). An observation-based geostrophic circulation pattern in the Indian Ocean has been discussed by Wyrtki (1971) and Reid (2003). Comparison with these results show that our model has reproduced the characteristics of major currents in the Indian Ocean reasonably well. At the equator, a semi-annual cycle of zonal winds occurs in the Indian Ocean, which is profoundly different from the largely westward winds in the Atlantic and the Pacific tropical oceans. The corresponding equatorial surface current changes direction in a semi-annual pattern in phase with the local winds, but with a prevailingly eastward flow for most of the year (Wyrtki, 1973). Therefore no strong velocity shear is produced as the whole upper layer flows eastward during the NE monsoon and two transition seasons. During the SW monsoon, the eastward EUC flows under a westward current. However the shear contribution is still insignificant because the currents at the equator are weak and variable for this season (Tomczak and Godfrey, 2003). The northern Indian Ocean, however, presents a current system similar to those found in the other oceans, but only during the NE monsoon. A well-developed Northeast Monsoon Current (NMC) flows westward in the surface, extending south to about $2°S$, with speeds between 0.3 and 0.8 ms^{-1} in January (Fig. 4.33). For the thermocline, an eastward current is found in the Arabian Basin and around the equator between $5°S$ and $5°N$ as part of the EUC and/or SECC. Therefore, a vertical shear is generated during the NE monsoon and thus produces tracer upwelling in this season just north of the equator in the Indian Ocean.

Although a lot of effort has been made to estimate the magnitude of Ekman pumping and horizontal velocity divergence and their importance in equatorial upwelling (Wyrtki, 1981; Quay et al., 1983; Bryden and Brady, 1985; Johnson et al., 2001), it was only recently that the contributions from enhanced turbulent mixing in this region have been added (Lien et al., 1995). Weisberg and Qiao (2000) found an imbalance of the advective temperature flux at the EUC, and proposed a diapycnal (eddy) vertical velocity with magnitude comparable to that of the kinematic vertical velocity assuming that the upward heat flux is attributed to vertical eddy diffusion. However, as far as the nutrient supply is concerned, the model simulations suggest that almost half of the total tracer

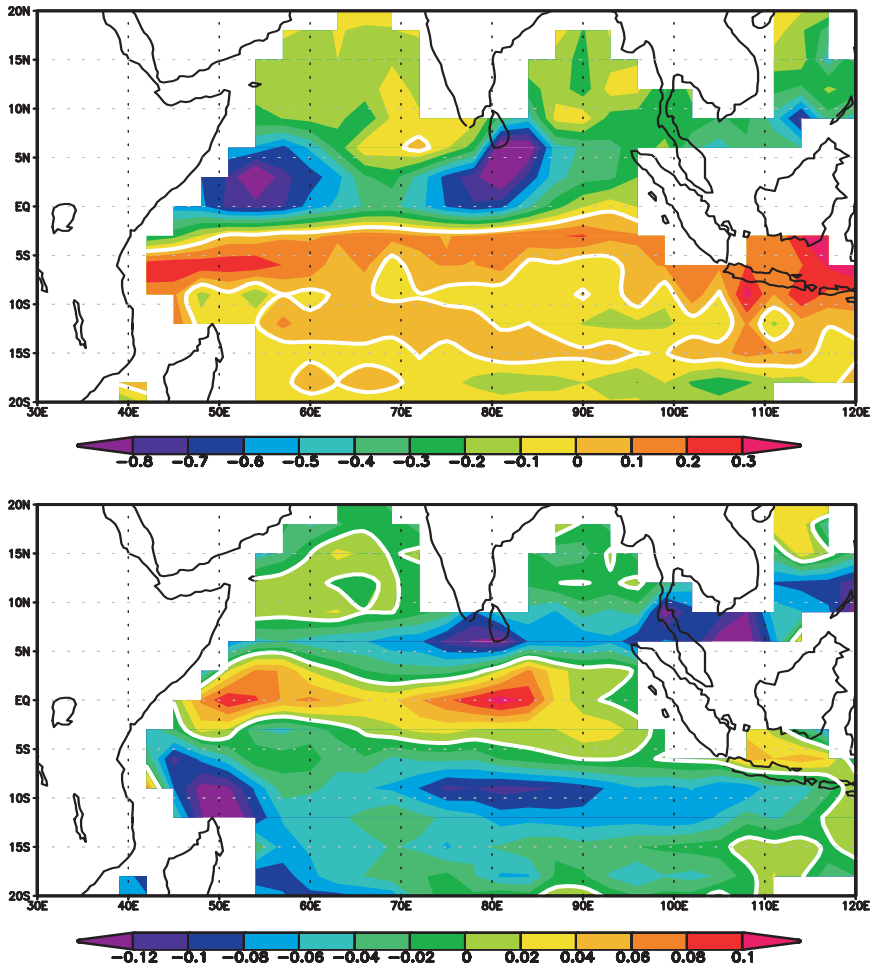

FIGURE 4.33: Maps of zonal velocity fields [ms^{-1} with positive values eastward] in the Indian Ocean at (top) surface and (bottom) on the isopycnal surface $\sigma_2 = 31.87$ in January. White contours indicate zero zonal velocity.

upwelling in the equatorial oceans is actually due to strong diapycnal mixing ($\sim$ 43% for the equatorial Pacific and $\sim$ 54% for the equatorial Atlantic). It is possible that the fractional contribution of this diapycnal mixing may vary depending on the choice of mixing scheme parameters (*e.g.*, Large and Gent (1999)) and may have been amplified by the surface consumption scheme implemented in our model (a rapid nutrient utilization rate has been set in the surface and therefore enhanced the tracer vertical gradient beyond what is realistic for a nutrient in the real ocean). Still, our results suggest that apart from horizontal divergence induced upwelling, which will be discussed in Section 4.3, diapycnal mixing also plays a significant (sometimes dominant) role in controlling the nutrient supply to the surface in equatorial regions, and should

be considered as an O(1) mechanism for equatorial upwelling.

4.2.3 Temporal evolution of tracer upwelling

A time mask has been introduced into the model for tracking the temporal evolution of tracer upwelling and the results are depicted in Fig. 4.34. For each grid box, assuming that all tracer upwelling has been accomplished after 150 years of integration since tracer release (near 97% of the total subducted tracer returned to the surface in the model), then the number of years to reach a prescribed percentage (i.e. 50%) of the total upwelling within each grid cell has been calculated in all significant tracer upwelling region ($Q_t > 0.5$ *tracer unit* m^{-2}).

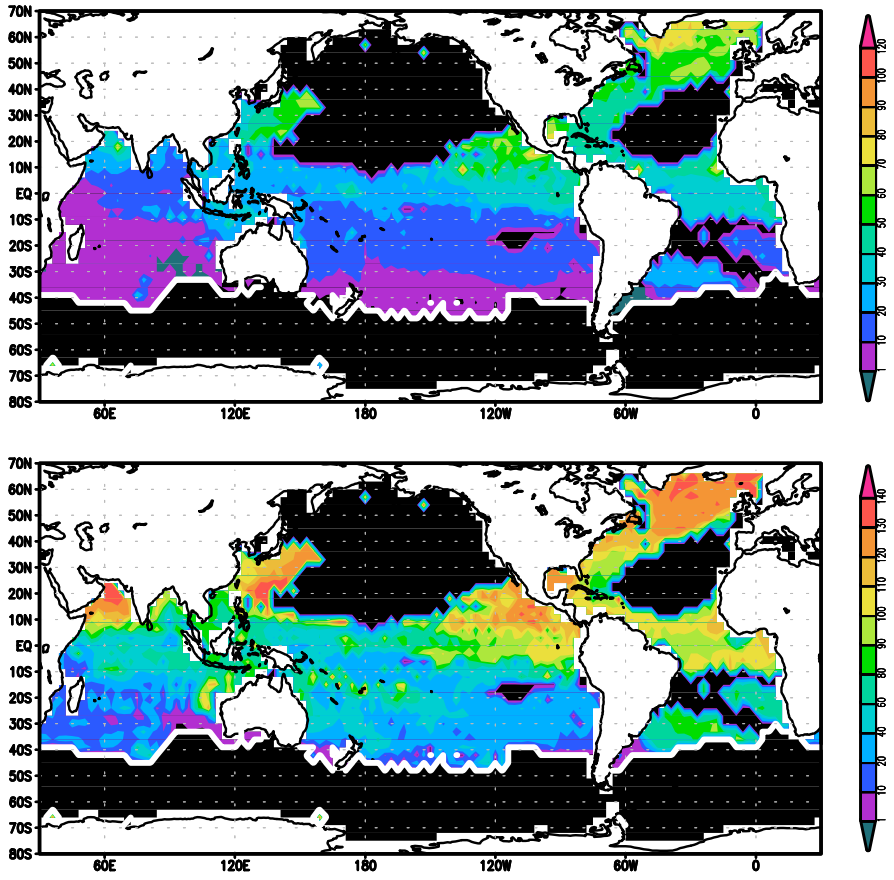

FIGURE 4.34: Maps of tracer age [*year*] required to reach (top) 50% and (bottom) 95% of the total upwelling flux (Q_t). Only regions with significant tracer upwelling ($Q_t > 0.5$ *tracer unit* m^{-2}) are depicted here.

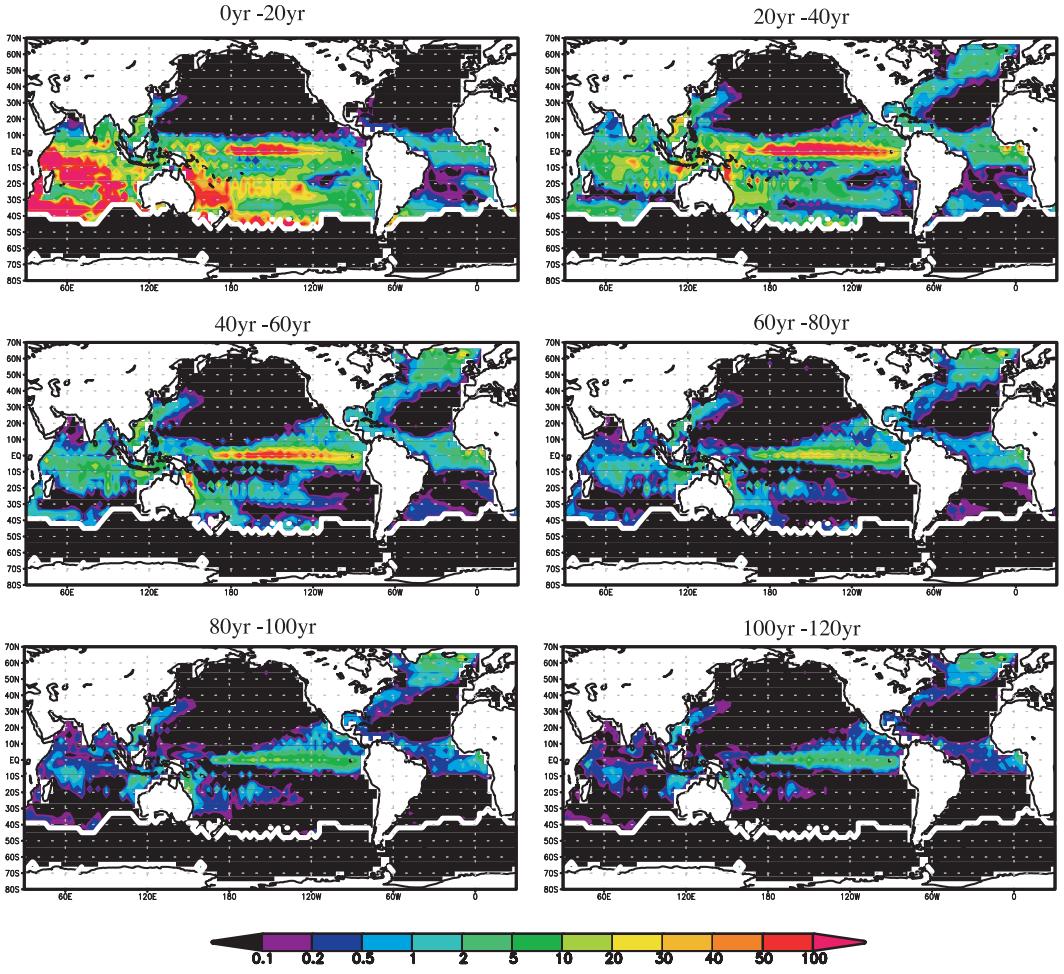

FIGURE 4.35: Spatial distributions of tracer upwelling flux (*tracer unit* m^{-2}) within an integration time interval of every 20 years after tracer release, in each case integrated over denoted time periods.

It is not surprising to see a general northward increase of the tracer ages required to exceed 50% of the total upwelling in Fig. 4.34. The fastest tracer re-emergence occurs in the subtropical gyre and western boundary of the tropical Indian Ocean, with less than 10 years required to reach 50% Q_t. This value increases to $\sim$ 20 years for the subtropical Pacific and to $\sim$ 30 years for the subtropical Atlantic, as there is no tracer release in the Atlantic Ocean. For equatorial upwelling, this value varies between 30 years, for the western part of the equatorial Pacific, to 60 years, for the eastern part of the equatorial Pacific, to reach 50% Q_t. Even though it may only take a year for the EUC to cross the Pacific basin, tracer upwelling does not persist for the whole equatorial Pacific region for the integration period of 150 years. Continuous upwelling only

occurs even after 100 years integration for the eastern part of the equatorial Pacific and in the eastern boundary upwelling regions (Fig. 4.35). It is also worth noticing that after 70 years of integration only 50% of the total upwelling has returned at the high-latitude North Atlantic, but increases to 95% after 120 years of integration, which suggests that a time scale of the order of 100 years is required for the re-emergence of Southern Ocean originated SAMW in the northern Atlantic.

Important regions responsible for continuous upwelling even in the later period of the simulation (after 100 years) can be identified from Fig. 4.35 and include mainly the eastern part of the equatorial Pacific, the subpolar gyre and the high-latitude North Atlantic regions. Tracer upwelling was dramatically slowed down in the last 30 years of integration, as over 95% of the total upwelling has already been generated within the first 120 years.

4.3 Ekman divergence-induced tracer upwelling

4.3.1 Ekman upwelling and its calculation

The atmospheric winds induce a horizontal (Ekman) volume flux over the surface Ekman layer of the upper ocean, directed to the right of the wind stress in the northern hemisphere and to the left of the wind stress in the southern hemisphere. A horizontal divergence of this volume flux in turn drives upwelling into the surface Ekman layer, referred to here as Ekman upwelling. A good example of this Ekman upwelling can be found in the Equatorial region. There the surface Trade winds are generally directed westwards and equatorwards. Accordingly, this wind pattern drives a horizontal polewards Ekman volume flux on either side of the equator and an off-shore Ekman flux along the eastern boundary of an ocean basin. It is compensated by the geostrophic convergence within and below the surface Ekman layer. Consequently, the divergence of this horizontal Ekman volume flux drives a band of upwelling along the equator and extends along the eastern boundary. This process has been well demonstrated by Fig. 4.36. Similar effects can also be found in the subpolar gyres, which are characterized by a cyclonic circulation, upwelling and a raised thermocline (Fig. 4.37).

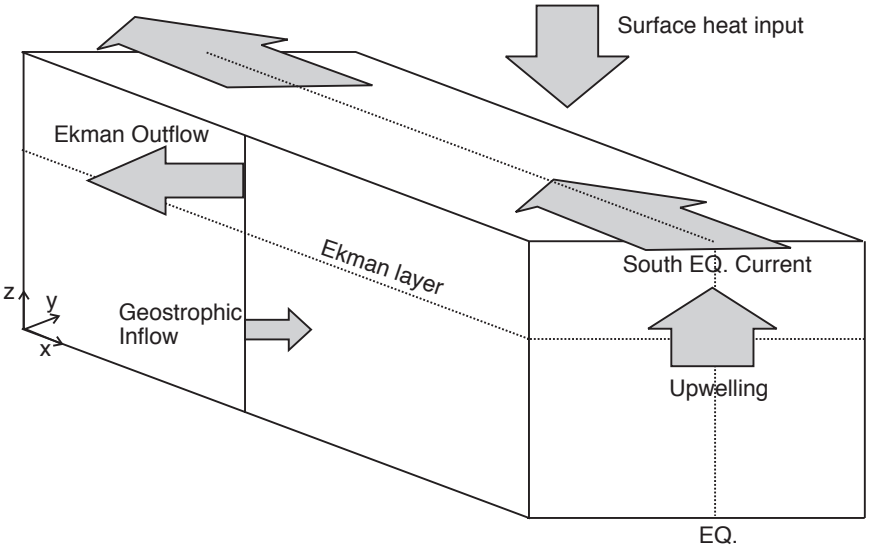

FIGURE 4.36: Schematic of Ekman divergence induced upwelling in the equatorial Pacific Ocean, adpated from Wyrtki (1981).

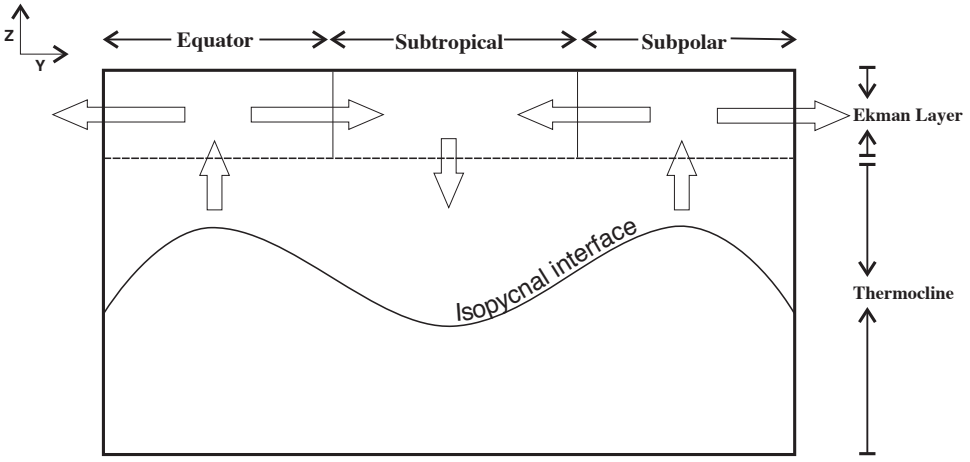

FIGURE 4.37: Schematic of Ekman upwelling in tropical and subpolar regions. The wind forcing leads to a horizontal divergence over the equator and subpolar gyre, inducing upwelling, and convergence over the subtropical gyre, inducing downwelling.

It is generally believed that equatorial upwelling is not only an important element of the general circulation, but also plays an important role in global biogeochemical cycles (Philander, 1990) as it is one of the most pronounced nutrient upwelling regions in the world. Equatorial upwelling in the Pacific Ocean has been estimated in various ways over a number of spatial and temporal scales. Wyrtki (1981) and Bryden and Brady (1985) used large-scale calculations assuming Ekman and geostrophic dynamics to diagnose upwelling in the Equatorial Pacific Ocean. Chemical tracers have been used with mixing models to estimate upwelling transports (Quay et al., 1983). Surface drifter velocities have been used to estimate meridional divergence and infer upwelling (Poulain, 1993). Local direct estimates of horizontal divergence from moored current meter arrays have been integrated vertically to estimate vertical velocity at the equator by continuity (Halpern et al., 1989). Estimations from direct measurements have been done by Weisberg and Qiao (2000) through using arrays of moored velocity profilers, and by Johnson et al. (2001) through using shipboard observation data. All these studies have estimated upwelling velocities on the order of a few m day^{-1}, with total vertical transport of 30-50 Sv over the east-central Pacific.

Vertical Ekman supply of nitrate to the surface euphotic layer has been diagnosed based on a wind-stress climatology over the North Atlantic by Williams and Follows (1998) and Williams et al. (2000). In their calculation, these Ekman upwelling fluxes were considered to result from horizontal Ekman volume flux divergence, which can be calculated from climatological NCEP wind-stress fields from the following equation

$$\mathbf{U}_e = \frac{\mathbf{k} \times \tau}{\rho_0 f} \tag{4.2}$$

and its divergence induces the vertical Ekman velocity at the base of Ekman layer,

$$w_e = \nabla \cdot \mathbf{U}_e = \frac{\mathbf{k}}{\rho_0} \cdot \nabla \times \frac{\tau}{f} \tag{4.3}$$

where f is the Coriolis parameter, $\mathbf{k}$ is the vertical unit vector, τ is the wind-stress, and ρ_0 is a reference density. Then nitrate fluxes to the euphotic zone are estimated by combining the mixed-layer thickness cycle and wind stress data with climatological nitrate profiles. Karstensen et al. (2008) also estimated the Ekman upwelling flux for tropical oceans based on wind field climatology. A significant positive contribution from Ekman upwelling has been identified for

the surface nutrient supply in the subpolar gyre of the North Atlantic Ocean as well as along the eastern equatorial Pacific Ocean.

4.3.2 Diagnosing Ekman upwelling in HYCOM

This wind-driven divergent velocity field in the equatorial Pacific as described by Wyrtki (1981) and demonstrated by Fig. 4.36 has been well captured in our model (Fig. 4.38).

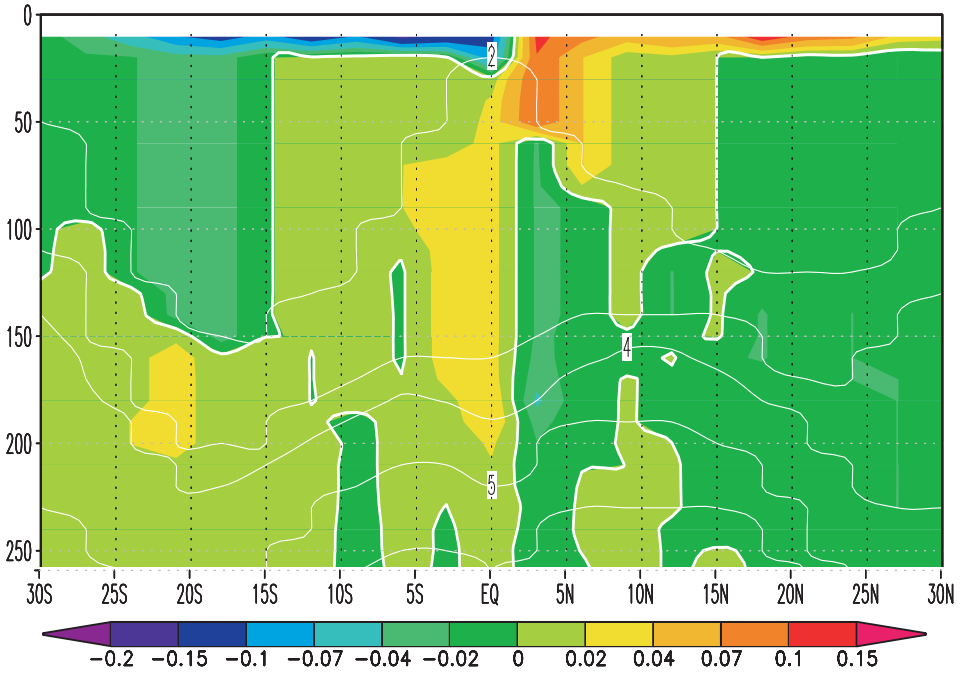

FIGURE 4.38: Meridional velocity section (ms^{-1}) along the 200°E in the Pacific Ocean. Positive velocity is northward. Also shown are the model layer interfaces (white contours) with overlaying layer numbers. A strong surface Ekman divergence (magnitude $>$ 0.2 ms^{-1} above 50 m) and weak geostrophic convergence underneath (magnitude $<$ 0.05 ms^{-1} below 50 m) are well resolved in our simulation.

However, Eq. (4.2) and (4.3) can not be applied directly to HYCOM for the calculation of Ekman upwelling fluxes into the mixed layer. If we consider the Ekman upwelling in an isopycnal way, based on mass conservation the vertical Ekman velocity calculated through Eq. (4.3) becomes the vertical velocity as Ekman layer base rises. Under the influence of continuous Ekman pumping, all isopycnal layers that are affected by Ekman divergence would bend upwards and eventually connect with the surface mixed layer (assuming that the mixed

layer depth is maintained by a diabatic process). Therefore isopycnal advection can contribute to transporting nutrients/tracer from the interior of the ocean to the surface mixed layer by following these shoaling density surfaces in the ocean (Fig. 4.39).

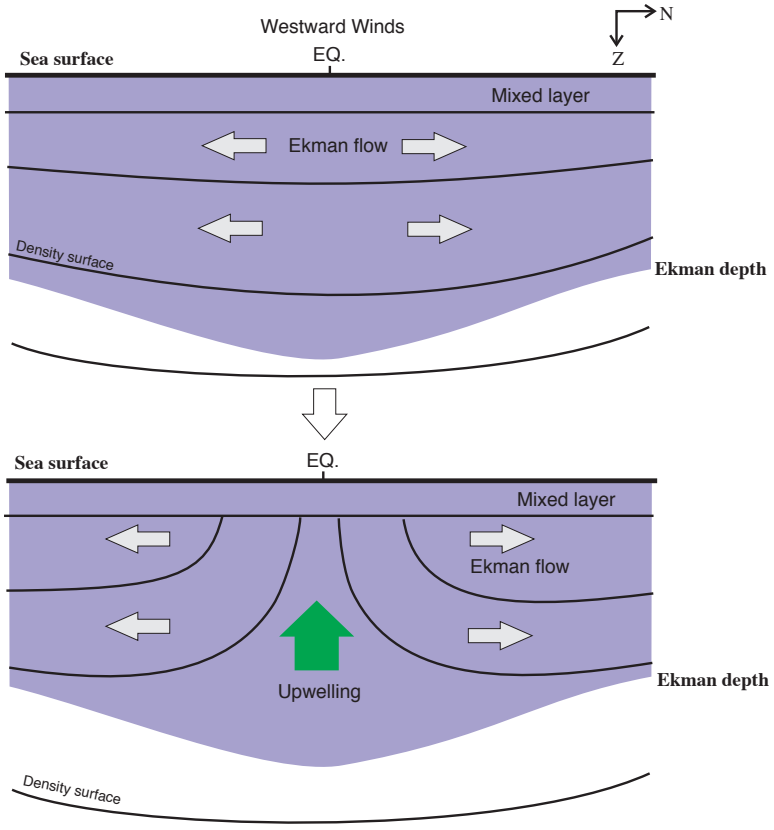

FIGURE 4.39: Schematic of Ekman divergence induced upwelling by following a shoaling density surface.

The remapping scheme used in HYCOM does not allow any coordinate layer to collapse into zero thickness, as an approach to improve the model resolution near the surface in some weakly stratified region, *e.g.*, Weddell Sea and Labrador Sea during winter. Consequently in regions of strong divergent Ekman volume flux (such as the equatorial Pacific), the remapping algorithm would stop coordinate layer tilting upwards by restoring the layer thickness and allowing deviation of layer density from the prescribed target density. As a result, the regional coordinate system becomes z-level within the Ekman depth but the density surfaces still bend upward to the surface due the Ekman pumping effect (Fig. 4.40).

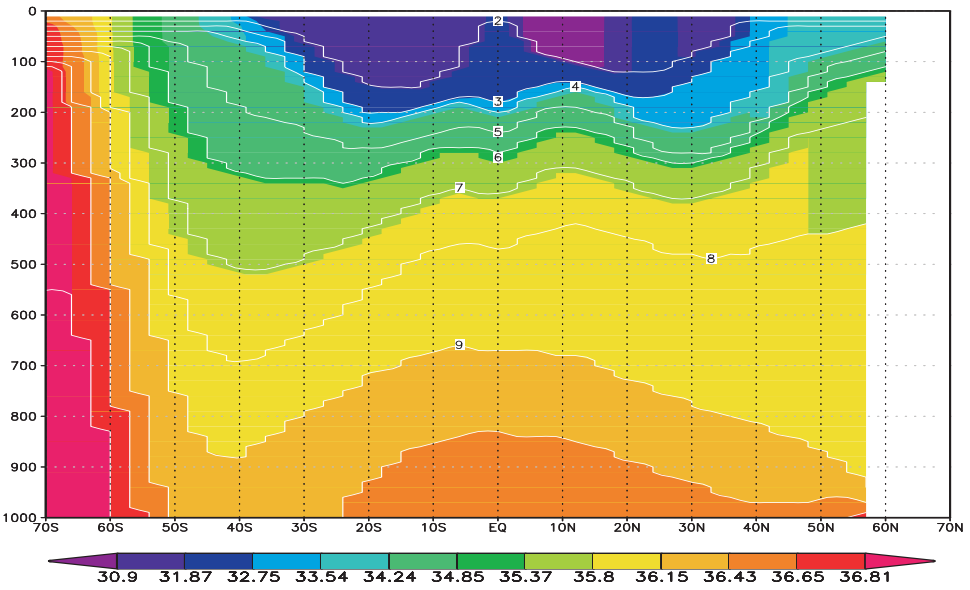

FIGURE 4.40: Meridional density section (σ_2) along 200°E across the Pacific Ocean. Also shown are the model layer interfaces with overlaying layer numbers. It is clear that even though the density interfaces (shaded) bend upwards and are connected to the sea surface due to Ekman divergence in the equatorial regions, the model layers (white contours) remain level and transfer to z-level coordinate near the surface in the equator (layer 2).

Extra mixing terms are introduced in HYCOM for resolving this upwelling flux into the mixed layer that are driven by the divergent Ekman volume flux. First, Ekman upwelling is applied through coordinate regridding mixing if the rising of isopycnal interfaces (due to Ekman divergence) triggers the MLT constraint in the remapping scheme. This process is illustrated in Fig. 3.20 and the diagnostic algorithm for separating this wind driven regridding mixing (Q_{mlt}) from numerical mixing (Q_{den}) in the remapping scheme of HYCOM has already been explained in Chapter 3.

Second, this wind-driven divergence and resulting rising density surfaces in the Ekman layer could change the local stratification and therefore modify the depth of the mixed layer (see Fig. 4.41). In this case Ekman upwelling is applied as extra entrainment in the KPP mixing scheme. This wind-driven entrainment only applies when the following conditions are satisfied: (1) the influence of this Ekman pumping effect reaches to the mixed layer base ($h_E > h_{\text{mix}}$), and (2) the number of coordinate layers within surface active mixing region increases ($h_b^{\text{t+1}} > h_{\text{mix}}^t$) due to surface buoyancy loss (cooling) and/or the divergence of this horizontal Ekman volume flux (Fig. 4.41-(B)).

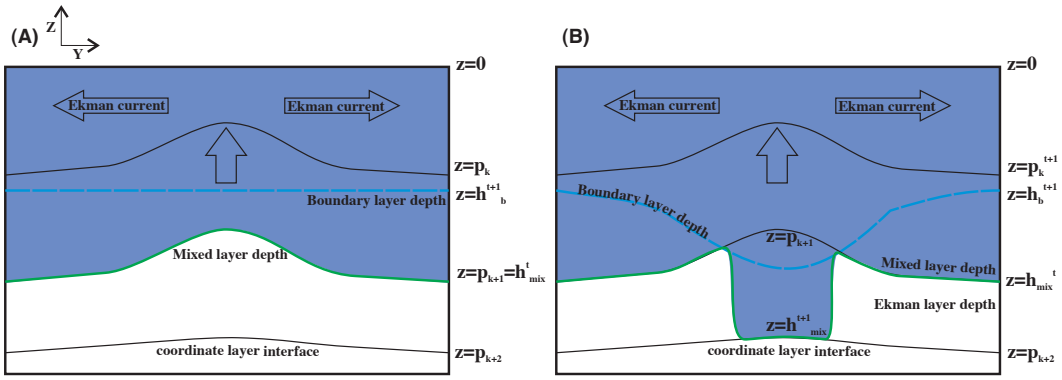

FIGURE 4.41: Schematic of Ekman pumping-induced entrainment in HYCOM: (A) no wind-driven entrainment because after Ekman divergence $h_b^{t+1} < h_{\mathrm{mix}}^t$ (B) with wind-driven entrainment because new boundary layer depth $h_b^{t+1} > h_{\mathrm{mix}}^t$, here h_b^{t+1} is the boundary layer depth after apply divergent Ekman volume flux and surface buoyancy flux, h_{mix}^t is the previous mixed layer depth before applying the vertical mixing scheme.

Assuming that geostrophic convergence in the Ekman layer is insignificant compared to the Ekman convergence, then any displacement of the coordinate layer interface (Δp_k) within the mixed layer can be considered as a result of the Ekman divergence. If entrainment happens, as demonstrated in Fig. 4.41-(B), after calling the KPP vertical mixing scheme ($h_b^{\mathrm{t+1}} > h_{\mathrm{mix}}^t$ and $h_{\mathrm{mix}}^{\mathrm{t+1}} = p_{\mathrm{k+1}}^{\mathrm{t+1}}$), then the total entrainment due to thickening of the mixed layer can be separated into entrainment driven by surface wind forcing ($widflx$) and entrainment induced by surface buoyancy loss ($buoflx$).

A schematic plot explaining the algorithm that has been used in our diagonstics of the Ekman- and buoyancy-driven entrainments is presented here as Fig. 4.42. Three coordinate layers ($K, K+1$ and $K+2$) and the positions of h_b and h_{mix} are depicted in the plot. Due to the architecture of this model, all entrainments are diagnosed after calling the vertical mixing scheme even though the Ekman divergence is calculated in the continuity equation in the beginning of the loop. Total tracer entrainment ($entflx$) in Eq. (3.27) is separated into two terms by the following equation

$$widflx = \frac{\Delta p_{\mathrm{k+1}}}{\Delta p_{\mathrm{k+1}} + \Delta h_b} \Delta h_{\mathrm{mix}} T_{\mathrm{k+1}} \tag{4.4}$$

$$buoflx = \frac{\Delta h_b}{\Delta p_{\mathrm{k+1}} + \Delta h_b} \Delta h_{\mathrm{mix}} T_{\mathrm{k+1}} \tag{4.5}$$

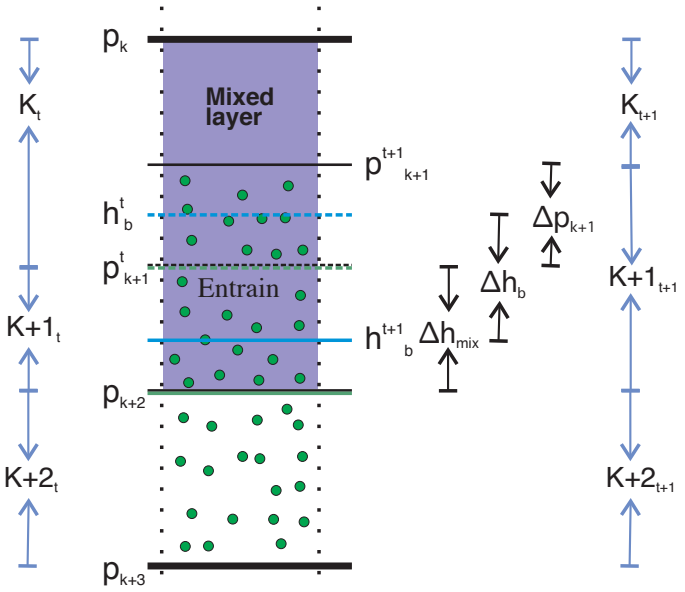

FIGURE 4.42: Schematic of wind- and buoyancy-induced entrainments calculation algorithm in HYCOM. The dashed and solid lines denote interfaces before and after applying the vertical mixing scheme, respectively. Black lines represent coordinate layer interfaces (p), blue lines are boundary layer depth (h_b) and green lines are mixed layer depth (h_{mix}), which are always superposed with coordinate layer interfaces. Green dots represent the tracer. Here the subscribe (k) denotes the coordinate layer number and superscribe (t) denotes time step.

where $T_{\mathrm{k+1}}$ is the tracer in layer $k+1$, $\Delta h_{\mathrm{mix}} = h^{\mathrm{t+1}}_{\mathrm{mix}} - h^{t}_{\mathrm{mix}}$ accounts for displacement of the mixed layer depth after applying the vertical mixing scheme. $\Delta h_b = h^{\mathrm{t+1}}_{b} - h^{t}_{b}$ is the displacement of boundary layer depth and is mainly controlled by the air-sea buoyancy exchange at the surface (Δh_b is actually decided by both surface buoyancy flux and local stratification, see Eq. (3.11)). Considering a constant surface buoyancy flux, if Ekman divergence leads to a rising lower interface bounding the mixed layer, then it would also increase the local stratification and may lead to a negative Δh_b (Here we assume that this effect is negligible comparing to the Δh_b caused by surface buoyancy flux). $\Delta p_{\mathrm{k+1}} = p^{t}_{\mathrm{k+1}} - p^{\mathrm{t+1}}_{\mathrm{k+1}}$ is the displacement of coordinate layer interface $k+1$ bounding the mixed layer due to Ekman divergence before applying the vertical mixing scheme (Eq. (3.25)).

As a result, Ekman divergence-induced tracer upwelling flux can be calculated in our simulation as the sum of $widflx$ from the KPP entrainment and $mltflx$ from the regridding mixing.

$$Q_{\mathrm{Ekm}} = Q_{\mathrm{wid}} + Q_{\mathrm{mlt}} \tag{4.6}$$

The two important assumptions used here for this diagnostic scheme of Ekman upwelling were first tested, in order to validate the scheme. As shown in Fig. 4.43, it is clear that in the tropical regions, Ekman layer depth normally exceeds 200 m, while mixed layer depth is very shallow at less than 50 m. It means that the Ekman divergence effect would affect the whole mixed layer (the mixed layer bottom would bend upward due to this Ekman pumping effect as long as $h_E > h_{\mathrm{mix}}$) for most of the tropical regions. Also the barotropic speed is at least an order of magnitude smaller than the mixed layer speed in the tropical regions (Fig. 4.44), suggesting that the wind-driven current plays a dominant role within the surface Ekman layer.

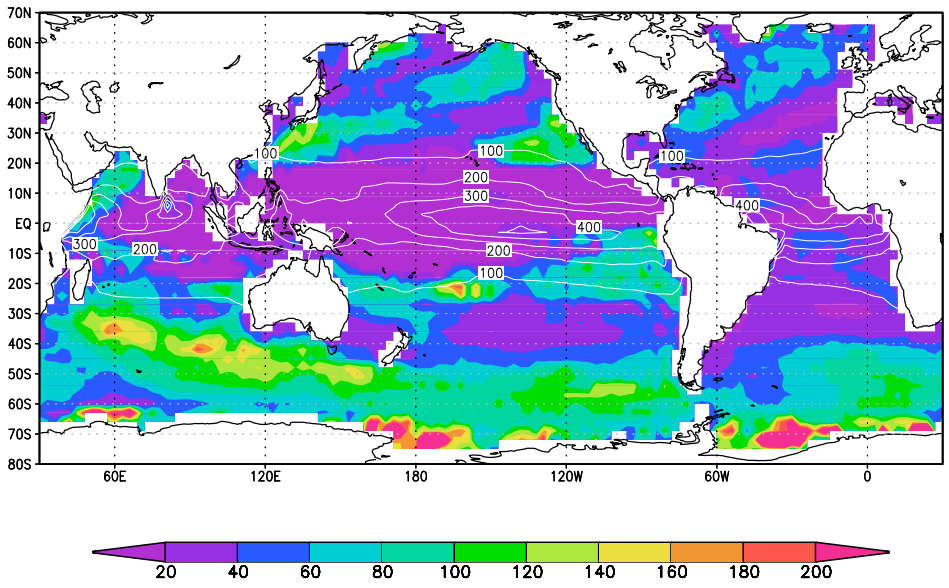

FIGURE 4.43: Annual mean mixed layer depth (color shaded [m]) and Ekman layer depth (solid contours with intervals of 100 m) for the control run.

Based on the above diagnostic scheme the Ekman divergence-induced tracer upwelling flux in our experiment has been calculated and the result is presented in Fig. 4.45, after being integrated over a period of 150 years following the release of tracer in the SAMW formation region. Comparison with Fig. 4.17-(C) shows that upwelling due to remapping process in HYCOM's coordinate generator (Q_{mlt}) accounts for majority of the Ekman upwelling in this model. Most of the Ekman divergence-induced tracer upwelling regions with

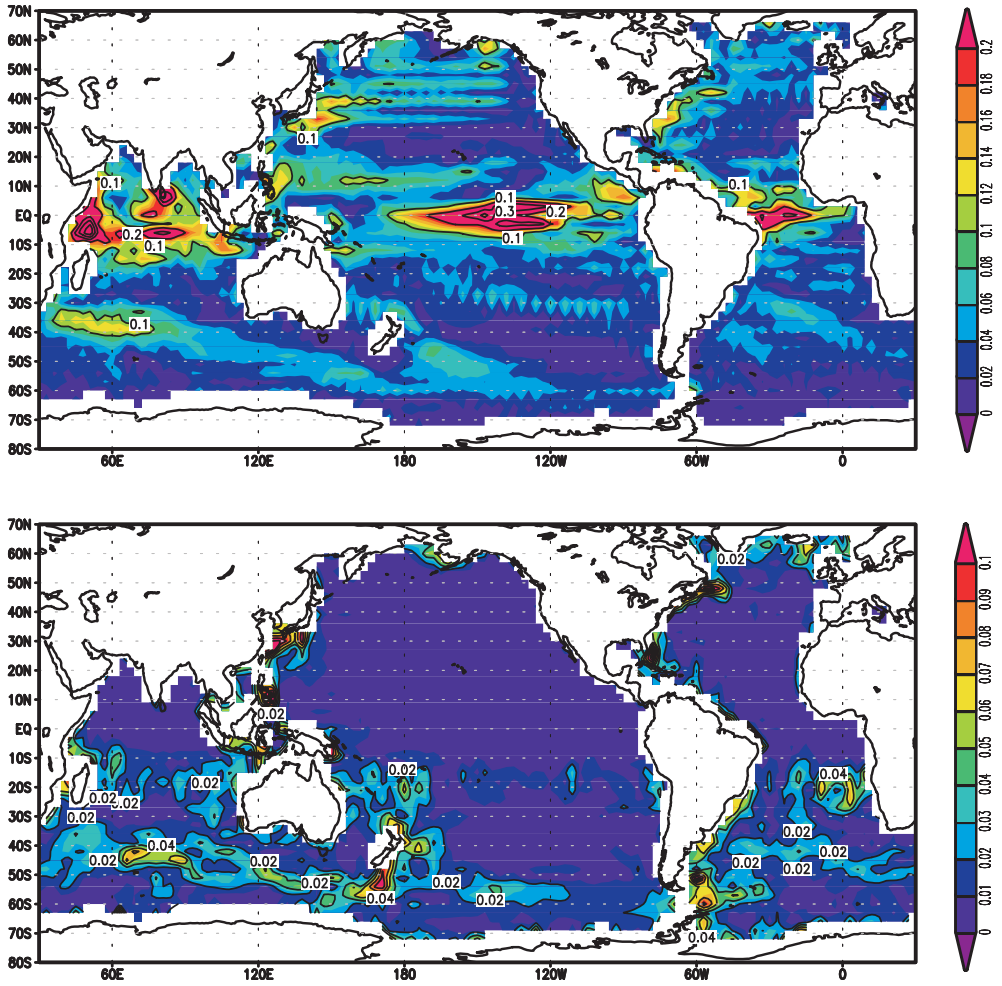

FIGURE 4.44: (Top) Mixed layer speed (contour interval 0.1 ms^{-1}) and (bottom) barotropic speed (contour interval 0.02 ms^{-1}) in September. Velocity field was averaged over ten years after model reaches a quasi-equilibrium state. The mixed layer speed is an averaged speed for all coordinate layers within the mixed layer.

significant Q_{Ekm} in our simulation are superimposed on regions with strong physical Ekman upwelling, like the equatorial Pacific ocean and tropical Indian ocean as suggested by Karstensen et al. (2008) based on SODA (NCEP/NCAR) wind field average 1992-2001. Though strong nutrient upwelling induced by Ekman divergence has also been estimated in the equatorial Atlantic Ocean and along the Gulf Stream (Williams and Follows, 1998), our simulation provides no significant Q_{Ekm} in these regions (Fig. 4.45). However, our diagnostics only accounts for tracer upwelling associated from the SAMW, instead of capturing the total local nutrient upwelling induced by surface mechanical forcing.

Therefore, it is possible that the Ekman induced nutrient upwelling as estimated in Williams and Follows (1998) in the equatorial Atlantic is associated with sources other than the Southern Ocean.

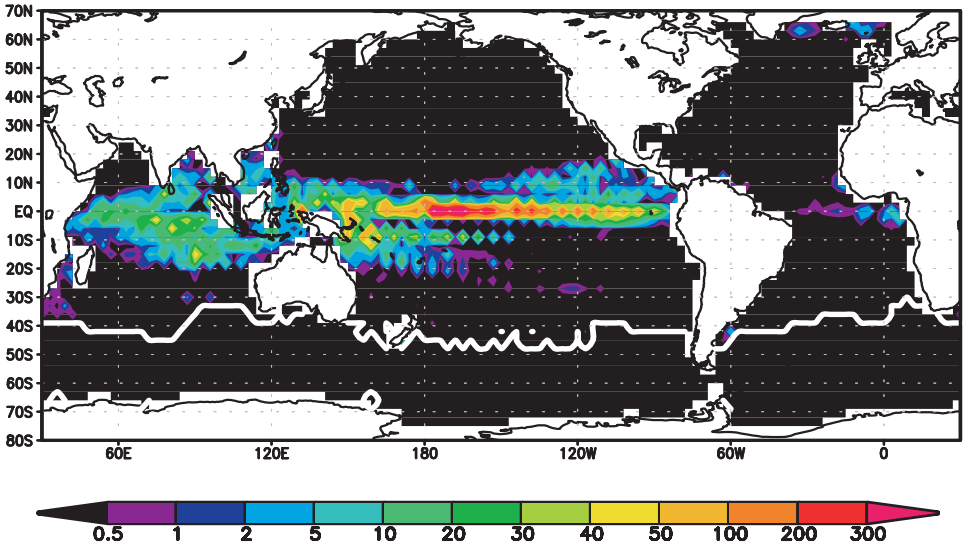

FIGURE 4.45: Ekman divergence induced tracer upwelling (Q_{Ekm} in *tracer unit* m^{-2}) due to regridding mixing and KPP entrainment (Integrated over a period of 150 years after tracer release). The white contour marks the outcropping region during southern winter.

Considering the re-emergence of the tracer after being subducted at the formation region of SAMW in the Southern Ocean, this Ekman divergence term accounts for $\sim$ 20% of the total upwelling and therefore stands as the second most important mechanism in driving the Southern Ocean originated nutrient supply to the global surface ocean in the model. If only the nutrient supply in the tropical region is considered, then Q_{Ekm} becomes the most important mechanism and is responsible for over 37% of the total tracer/nutrient upwelling between $10°S$ - $10°N$. At the same time, the fractional contribution of this wind-driven tracer upwelling varies between 7% to $\sim$ 50%, for the equatorial Atlantic and the equatorial Pacific regions, respectively. Such a difference is mainly caused by the distinguishing overlaying surface wind systems in these two equatorial regions. As already explained above, HYCOM can only numerically resolve the Ekman divergence induced upwelling as a regridding process in its remapping scheme. Therefore, even though wind physically drives an Ekman divergent volume flux and generates a rising velocity for the lower interface bounding the mixed layer (Eq. (4.3)), no upwelling flux would actually enter the mixed layer before the MLT constraint is violated following the thinning

of the model layer. Fig. 4.46 shows the zonal surface wind stress field in the tropical regions in boreal winter (March) and summer (September). Unlike the tropical Pacific, the zonal component of the surface wind stress in the equatorial Atlantic only remains westward during boreal summer, but changes to eastward (at the eastern boundary) due to the southward shift of the southeast trade wind. Correspondingly, no significant Ekman divergent volume flux is generated during boreal winter in this region. In boreal summer the lower interface bounding the mixed layer moves upwards due to the surface Ekman divergence, together with the thinning of all surface model layers. With the turning of the zonal component of the surface wind stress in the tropical Atlantic Ocean, this process ceases in boreal winter before most rising layer interfaces trigger the MLT constraint. The stratification would be rebuilt during the following transition period (boreal spring) with the restoring of the thermocline and descent of the mixed layer base. As a result, the seasonal Ekman divergent volume flux in the equatorial Atlantic drives an upward-downward annual cycle of the mixed layer base without inducing much tracer upwelling flux into the surface boundary in the model.

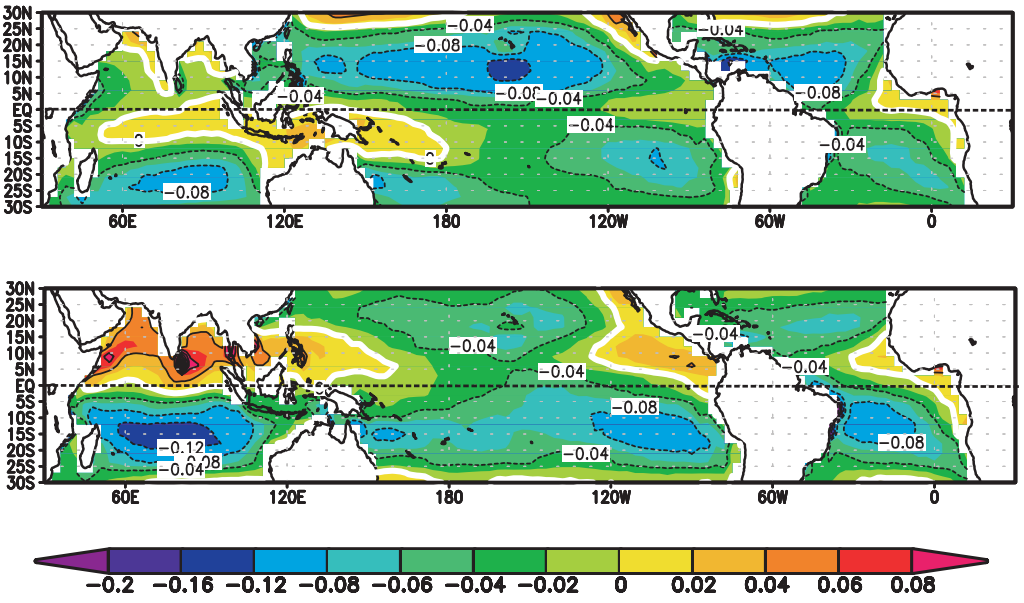

FIGURE 4.46: Zonal surface wind stress (Nm^{-2}) in (top) March and (bottom) September at the tropical regions. Wind stress derived from NCEP climatology wind field and used as surface forcing field during our simulation.

In contrast, the westward trade wind persists throughout the year in the eastern part of the tropical Pacific and the divergence of the Ekman flow causes

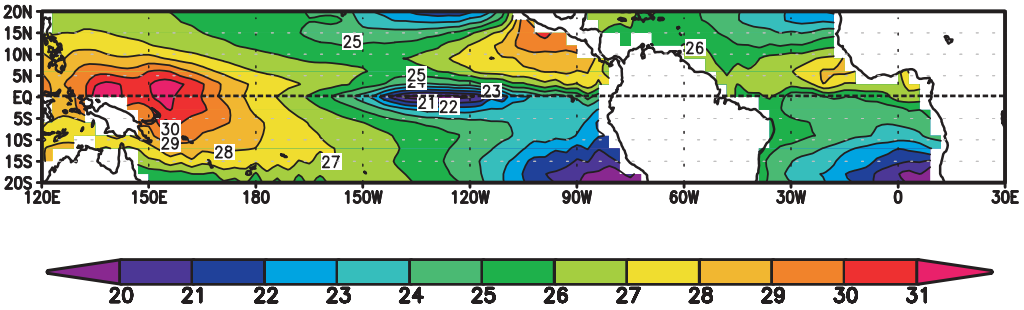

FIGURE 4.47: The cool equatorial tongue as shown by the annual mean mixed layer temperature at the tropical Pacific Ocean. Averaged over a period of ten years after the model reaches a quasi-equilibrium state.

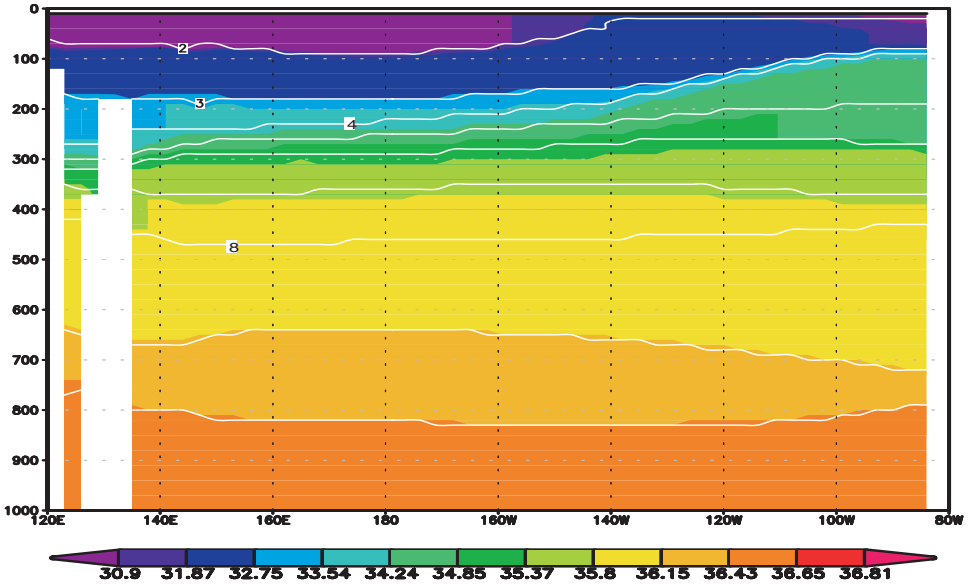

FIGURE 4.48: Annual mean potential density (σ_2) section along the equatorial Pacific Ocean. X axis is longitude and Y axis is depth [m].

upwelling at the equator. In the west, the upwelled water is warm. But in the east the upwelled water is cold because of the shallow thermocline. This leads to a cold tongue of water at the sea surface extending from South America to near the dateline (Fig. 4.47). The position of the Ekman tracer upwelling patch in the tropical Pacific is consistent with the location of this surface cold tongue. This Ekman pumping-induced shoaling of isopycnals in the eastern part of Pacific can be seen in Fig. 4.48, which shows the potential density section along the equator in the Pacific. This figure also demonstrates why the Ekman-induced tracer upwelling is more significant in the eastern part of the equatorial Pacific. As the surface isopycnals shoal eastward, tracer carried

by EUC can reach the surface by simply following the rising isopycnals in the equatorial Pacific region.

SUMMARY

In this Chapter the results of the control run with tracer released in the SAMW formation area are discussed. Once subducted into the ocean interior, tracer advection follows subtropical gyres in the Southern Hemisphere and reaches the South Atlantic Ocean via the ACC flow across the Drake Passage in the model. The tracer circulation patterns in three major ocean basins are in good agreement with the previous GCM simulations (Ribbe and Tomczak, 1997; Sloyan and Kamenkovich, 2007; Sen Gupta and England, 2007) and inverse models based on hydrographic sections (Sloyan and Rintoul, 2001a,b). Two types of SAMW (SAMW-light and SAMW-dense) have been identified entering the Atlantic Ocean and are found to follow distinct pathways at different density levels. No significant tracer transport following the Agulhas Leakage (Schmitz, 1995) has been found in our model, probably because of the coarse mesh grid and rapid surface consumption algorithm implemented for mimicking the biogeochemical process of nutrient depletion in the euphotic zone. The budget analysis of tracer circulation in major ocean basins shows that the Pacific Ocean plays the most important role ($\sim$ 55% T_{sub}) in SAMW re-emergence, however, continuous tracer upwelling also persists in the North Atlantic Ocean. For the global ocean, the most important mechanism responsible for SAMW upwelling is the entrainment (33%) due to surface buoyancy loss and/or enhanced mechanical flux input. Ekman divergence induced regridding mixing and diapycnal mixing induced by velocity shear are the second and the third most important mechanisms, accounting for 19% and 18% of total upwelling, respectively. Double diffusive mixing is found to be insignificant in contributing to the SAMW re-emergence, but maybe underestimated due to the small reference density ratio used in the model.

The geographical location of tracer upwelling produced by our model is similar to the SAMW re-emergence pattern proposed by Sarmiento et al. (2004) and the OMZ calculated by Karstensen et al. (2008), suggesting that the reproduction of the SAMW circulation in the model is handled reasonably well. Three distinct provinces of re-emergence are discussed, each governed by different physical processes: (1) nutrient circulation and upwelling in the North Atlantic Ocean can be explained by a new model based on our tracer experiment and inspired

by Williams et al. (2006), which comprises four steps following the seasonal cycle of the thermocline. In this model, nutrient upwellings are mainly driven by entrainment due to buoyancy loss during boreal autumn, and induction due to outcropping into the GS extension during boreal winter in the subpolar gyre and high-latitude North Atlantic. Recharging of the nutrient in the underlying seasonal thermocline is achieved by imported SAMW via GS and isopycnal advection of nutrient following the subpolar and the subtropical gyres during boreal summer; (2) SAMW upwelling in the Indian Ocean is found to be largely determined by the unique Monsoon system; (3) the equatorial upwellings in the Atlantic and Pacific oceans are mainly controlled by Ekman divergence induced upwelling and diapycnal diffusion. As suggested by Weisberg and Qiao (2000), our results also show that shear induced turbulent mixing in the equatorial regions is of O(1) importance in the model.

The temporal distribution of tracer upwelling in the global ocean suggests that a time scale of the order of 100 years is required for the re-emergence of Southern Ocean originated SAMW in the northern Atlantic Ocean. Diagnostics of Ekman divergence induced upwelling in the physical ocean and its solution in a numerical model like HYCOM have been discussed. It appears that extra mixing (regridding process) is needed in the remapping scheme for a hybrid coordinate system model to resolve this wind-driven upwelling process. In our simulation, the Ekman upwelling is of the most importance in the equatorial Pacific Ocean, but becomes less important when the equatorial Atlantic is concerned. The difference can be understood as a result of the unique surface wind systems overlaying the tropical regions in these two ocean basins.

Chapter 5

Perturbation Experiments

In this Chapter, the differences of tracer penetration pathways in the North Atlantic and North Pacific basins are presented and the formation of a nutrient barrier in the North Pacific is discussed. The northward transports of SAMW resides at comparatively deeper and denser isopycnal layers in the Atlantic Ocean than in the Pacific Ocean. The differences of the SAMW core density in these two ocean basins, together with the unique features of EUC and WBC serve as the key factors in determining the distinguishing circulation pathways of the SAMW in the North Hemisphere. A perturbation experiment with reduced Indonesian Through Flow suggests that the ITF transports is not vital in controlling the penetration of SAMW to the North Pacific. Instead, it plays an important role in the circulation pattern of SAMW in the equatorial and southern Pacific Ocean, as well as the SAMW supply into the Atlantic Ocean. In the end of the Chapter, a set of perturbation experiments with an enhanced diapycnal diffusivity profile in the Gulf Stream region are carried out for testing the "Nutrient Spiral" theory (Jenkins and Doney, 2003) and assessing the SAMW recirculation and corresponding nutrient supply to the gyre systems in the North Atlantic Ocean.

5.1 Tracer upwelling in the Northern Hemisphere

5.1.1 Different tracer upwelling patterns in the North Atlantic and North Pacific oceans

After reaching the equator, a strong eastward-flowing tracer pathway appears following the Equatorial Counter Current systems in both the Pacific and Indian oceans. Although this equatorial eastward tracer flow also exists in the Atlantic Ocean, the effect seems much weaker when compared with the Pacific and Indian oceans. A penetration of the tracer tongue from the Pacific to the Indian Ocean following the ITF is also clear in our simulation (Fig. 5.1), centered on layer 6 and significant in the upper part of SAMW isopycnals (σ_2 = 33.54 - 34.85). It is believed that this Pacific-to-Indian leakage is connected to the southward Leeuwin Current and ultimately supplies the "warm" return route of the global thermohaline circulation via the the Indian Ocean subtropical gyre and the Agulhas leakage (Speich et al., 2001). Tracer crosses the equator after 10 yr and enters the Northern Hemisphere primarily in association with western boundary current systems.

In Fig. 5.1 we can see that tracer follows the pathway of the western boundary current in the North Atlantic Ocean much more clearly than in the North Pacific Ocean. If we take 0.01 tracer units (0.1% of the release zone concentration) as the significant tracer concentration, then after 30 years of integration the tongue of tracer associated with the western boundary current reaches as far north as $67°N$ in the Atlantic Ocean while its counterpart in the Pacific Ocean is much weaker and limited to about $20°N$. In the North Atlantic, this tracer tongue is advected in the northeastward Gulf Stream and NAC before encountering the mixed layer outcrops between $50°N$ to $60°N$ at isopycnal surfaces from σ_2 = 34.24 - 35.37. Therefore, lateral advection is seen to play a dominant role in suppling tracer to the mixed layer of the subpolar North Atlantic. In the North Pacific, however, there is no significant tracer tongue following the pathway of the Kuroshio Current and the SAMW cannot appreciably penetrate into the high latitudes of the North Pacific.

Correspondingly, there is much more nutrient/tracer upwelling in the North Atlantic Ocean than in the North Pacific Ocean, as demonstrated by Fig. 4.17-(A). The lateral supply of tracer from underneath the thermocline (following

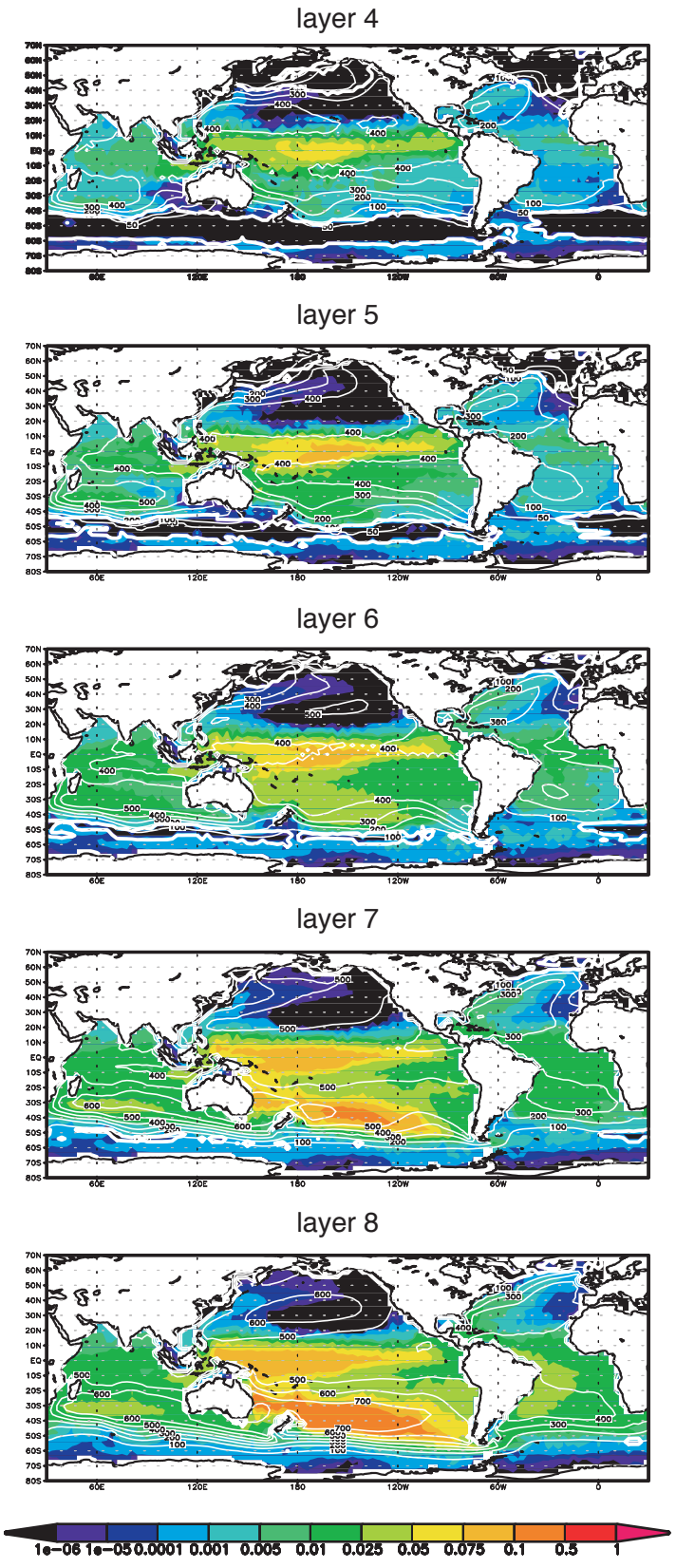

FIGURE 5.1: Tracer concentration in SAMW isopycnals ($\sigma_2 = 34.24 \sim 36.15$) after 30 years of integration in Sep. The thick white lines denote the outcrops and the thin white contours show layer depths (with contour interval = 100 m).

the isopycnals of SAMW density range) supplies re-emergence into the mixed layer due to induction, entrainment and diapycnal mixing in the subpolar gyre and high latitude of North Atlantic Ocean, as well as along the Gulf Stream. Comparatively, there is no significant tracer upwelling in the North Pacific Ocean because tracer can hardly penetrate north of $20°N$ here. Considering the tracer upwelling outside of the southern outcropping mask (Fig. 4.12), of all tracer that upwelled in the Atlantic Ocean, $\sim 36\%$ did so in the North Atlantic (north of $20°N$). However this fractional contribution reduces to $\sim 1\%$ for the tracer upwelling in the North Pacific. This result is generally consistent with the global thermocline nutrient study of Sarmiento et al. (2004), which suggested that North Pacific Intermediate Water (NPIW), instead of SAMW, may play a dominant role in controlling the nutrient supply to the main thermocline in the North Pacific. However, the hydrodynamic conditions that control the circulation pathway of the SAMW were not discussed in their paper. It is believed that the zonal Equatorial Current System in the Pacific may also play an important role in explaining the confined meridional transports of SAMW in the Pacific Ocean (Wyrtki and Kilonsky, 1984; Firing et al., 1998). Zenk et al. (2005) find that AAIW, which forms with the deepening and density increase of SAMW, is trapped in the zonal equatorial flows of the Southern and Northern Intermediate Countercurrents (SICC, NICC) within about $\pm 2°$ off the equator in the Pacific, and never reaches to the north of $12°N$. In order to understand the different behaviors of tracer circulations in the two ocean basins in the Northern Hemisphere, the influences of the ITF is assessed, as well as the differences of the Equatorial Under Currents and two Western Boundary Current systems in North Atlantic and North Pacific Oceans. The formation of NPIW and the distribution of Potential Vorticity (PV) in the North Pacific will also be investigated.

5.1.2 Perturbation experiment with reduced Indonesian Through Flow

As the only channel in the tropical regions through which inter-basin exchange of water masses occurs, the Indonesian Through Flow is thought to be important not only in the water circulation in the Pacific and Indian oceans (Godfrey, 1996), but also in the global climate and thermohaline circulation (Gordon, 1986) and equatorial biogeochemistry (Gorgues et al., 2007). As a

well established heat channel, ITF transports ~ 1.4 PW of heat from the Pacific to the Indian ocean, as well as 16 ± 5 Sv of water (Ganachaud and Wunsch, 2000). This heat flux was found to have an overall effect of warming the Indian and cooling the Pacific Ocean (Hirst and Godfrey, 1993). This process leads to a well-know fact that the net heat transport to the North Pacific Ocean is zero, while the same transport in the Atlantic Ocean is about 1.3 PW, which is of the similar magnitude as that transported to the Indian Ocean through the ITF. Simulations with a variety of models (Hirst and Godfrey, 1993; Rodgers et al., 1999; Lee et al., 2002) all indicate that closing the ITF warms the Pacific Ocean, and transports more nutrients to the eastern part of the equatorial Pacific (Gorgues et al., 2007). Apart from these, modeling studies evaluating the effects of the ITF on the circulation of the Pacific and Indian Oceans and the global climate system show that the ITF is also responsible for the strengthening of the South Equatorial Current (SEC) and Agulhas Current in the Indian Ocean, and weakening of the East Australian Current (EAC) in the South Pacific. A blocked ITF may also affect the nutrient supply to the Atlantic Ocean, as the return flow of the Atlantic thermohaline circulation from the "warm route" would be reduced too.

In order to assess the importance of the ITF in controlling the SAMW/tracer circulation pattern in the Global Ocean, a perturbation experiment with a modified bathymetry configuration has been carried out. In this experiment the Timor strait that connects the Pacific and Indian oceans was blocked (replaced with the minimum depth of 100 m, as demonstrated in Fig. 5.2). The perturbation experiment with reduced ITF (hereafter referred to as ITB) starts with the same initial state as the control run (hereafter, REF) and has been spun up for 120 years using the same climatological forcing fields derived from NCEP reanalysis data. After reaching a quasi-equalibrium state the tracer was released in the formation region of SAMW and then the model was integrated over a period of 150 years, during which the consumption algorithm mimicking the biogeochemical process was applied in the surface mixed layer. All mixing parameters are exactly the same as used in the control run.

Various direct and indirect measurements of the ITF transports were made and magnitudes range from nearly zero to 20 Sv into the Indian Ocean. Based on high-resolution trans-oceanic hydrographic sections and current meter data during the World Ocean Circulation Experiment (WOCE), Ganachaud and

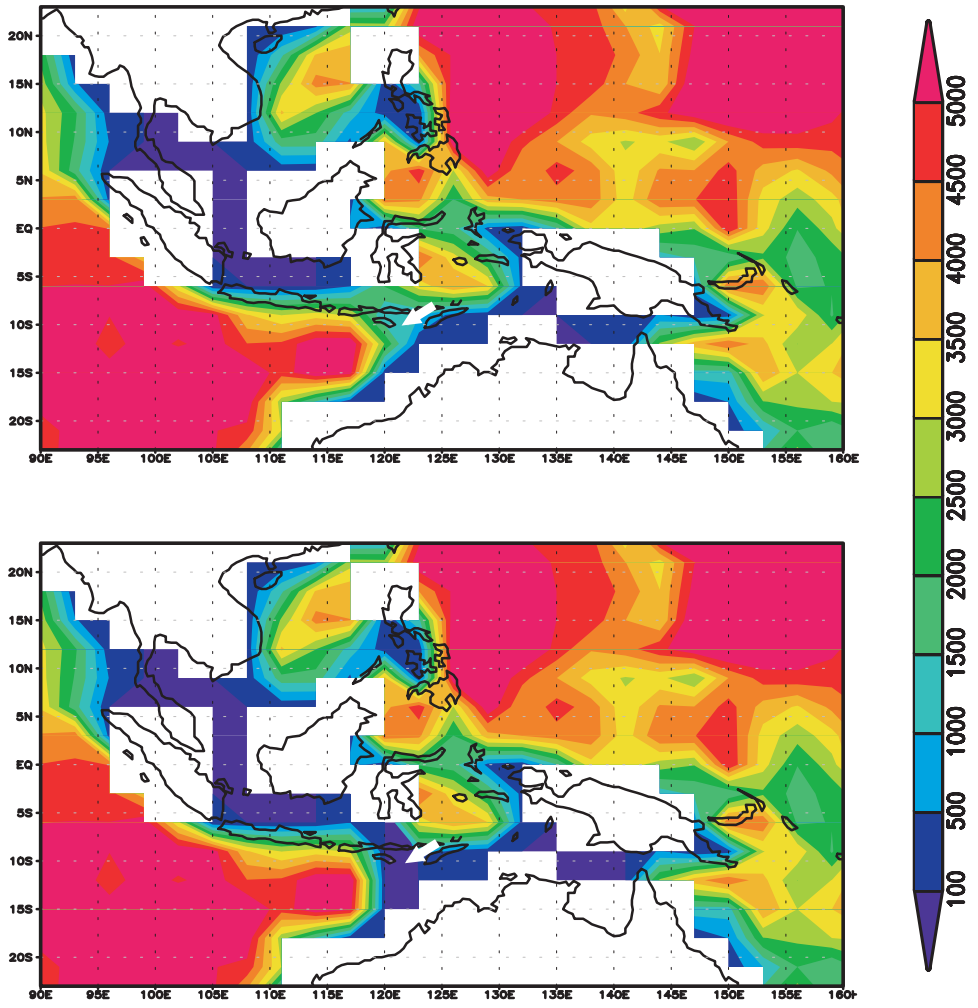

FIGURE 5.2: Bathymetry derived from (top) Etopo5 grid and (bottom) with shallowed Timor strait (marked with white arrow) for ITB simulation (unit m).

Wunsch (2000) obtained an estimated mean ITF transport of 16 ± 5 Sv. It is consistent with the ITF transport value generated by the control run (Fig. 5.3), which stabilized near 14 Sv after 120 years of spin-up. The ITF transports were significantly reduced (to ~ 3 Sv) in the ITB experiment due to the shallower Timor Strait. It suggests that about 10 Sv of water mass that originally enters the Indian from the Pacific was stopped in the ITB simulation.

Fig. 5.4 shows the magnitudes of Meridional Overturning Circulation in three different ocean basins and in the global scale in the simulation of ITB after a quasi-equlibrium state was obtained. For the Pacific Ocean, reduced ITF transports through Timor Strait do not seem to change the deep overturning

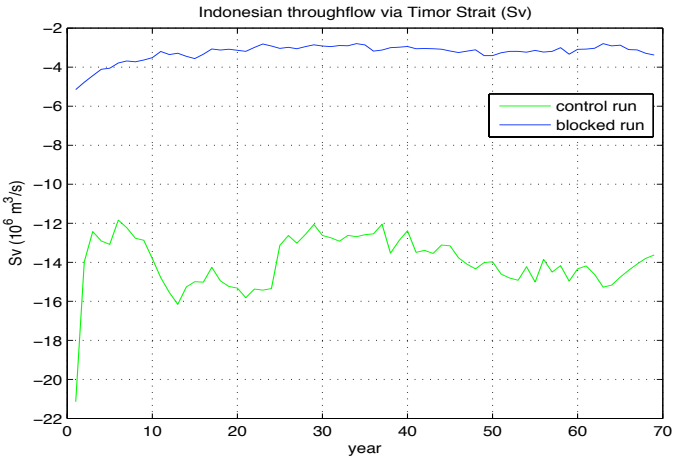

FIGURE 5.3: Time series of the ITF transports derived from REF and from ITB, calculated from the annual mean volume flux across the Timor Strait (unit Sv).

streamfunction below 1500 m but weaken the shallow MOC in the South Pacific above the maximum ITF sill depth of 1500 m (Fig. 5.5), with its maximum value reduced from 27 Sv in REF to 18 Sv in ITB. Correspondingly, the direction of subsurface transports (between 100m to 500m) in the Indian Ocean changes from southward in REF to northward in ITB due to the reduction of the ITF transports and approximately 10 Sv of the difference in meridional transport occurs in the lower part of the shallow cell streamfunction (Fig. 5.5). This result is consistent with Lee et al. (2002), who also suggest that a blocked ITF would lead to slow down of the shallow cell for the Pacific overturning circulation. As a result, the northward transport of the tracer that originated from the SAMW formation region in the Southern Ocean also slows down in the Pacific Ocean, as the shallow overturning cell is the main channel that carries tracer northward there. The ITB-simulated MOC streamfunction in the Atlantic Ocean has a maximum value of 16 Sv and shares a similar spatial distribution pattern as in the REF simulation. Reduced ITF transports did not affect the AMOC very much in this perturbation experiment, probably because the coarse resolution of our model limits its ability of resolving the Agulhas Current properly, which is believed to be the key factor in returning the upper brach of AMOC from the "warm route".

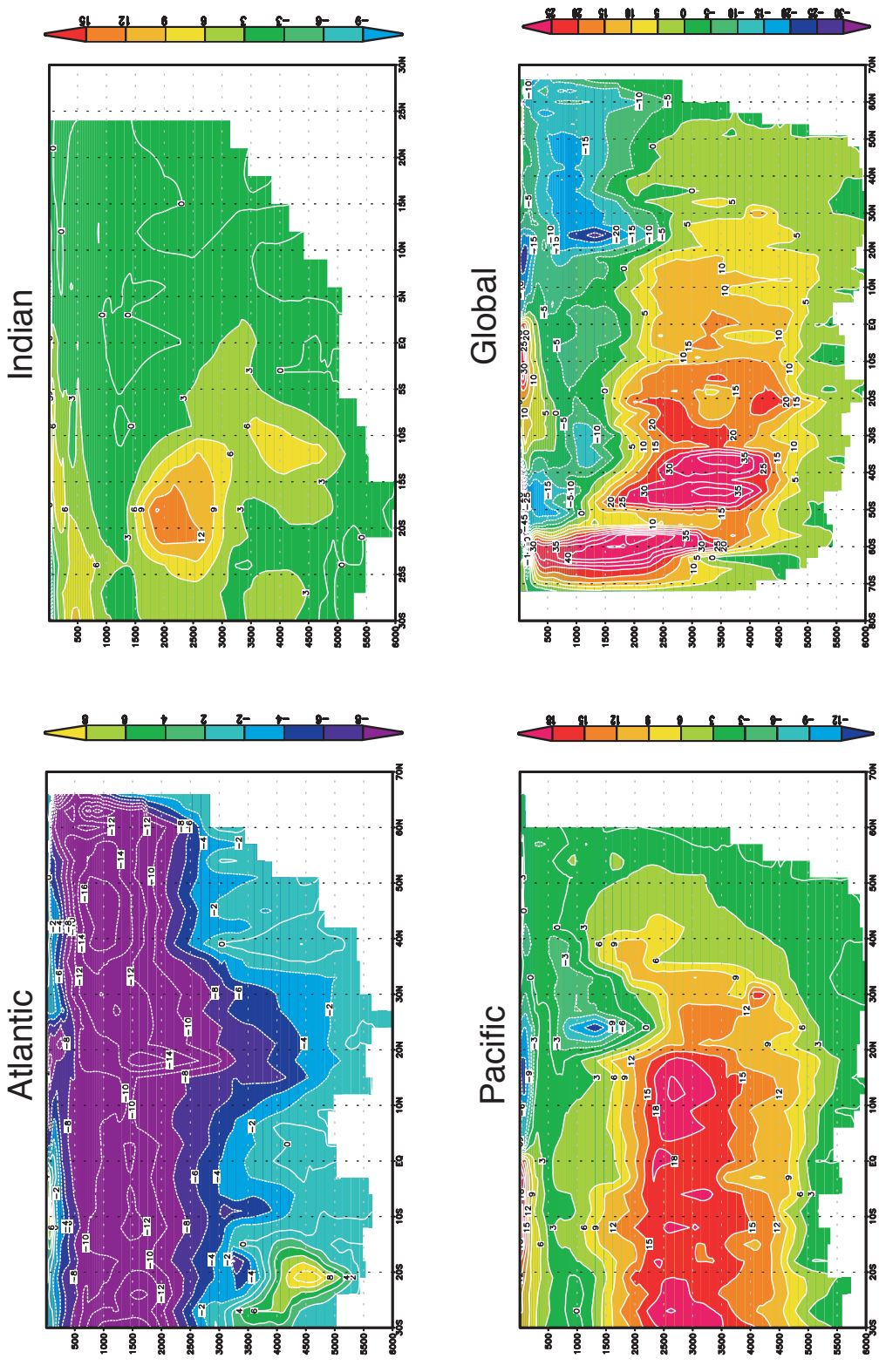

FIGURE 5.4: Meridional overturning stream functions (Sv) for the (A) Atlantic; (B) Indian and (C) Pacific and (D) Global oceans for the perturbation experiment with shallower Timor Strait. Model has been integrated over a period of 120 years and reached a quasi-equilibrium state.

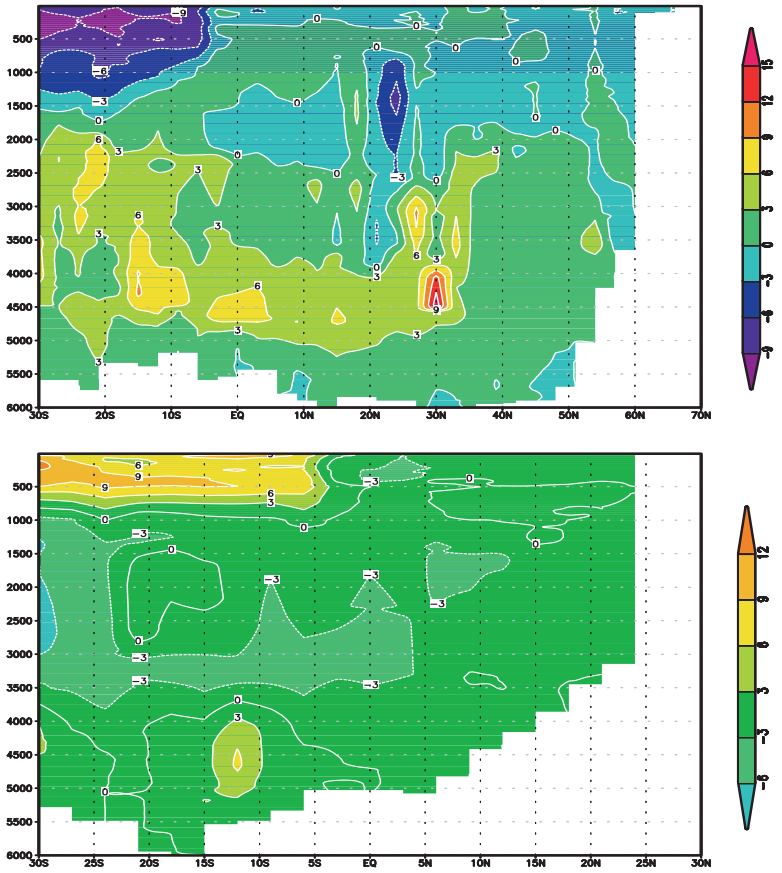

FIGURE 5.5: Difference plot of MOC for (top) Pacific and (bottom) Indian ocean basins between ITB and REF simulations (ITB - REF in Sv). Model has been integrated over a period of 120 years.

Despite the fact that AMOC remains almost unchanged in ITB simulation, we found that the magnitudes of SAMW-related tracer that entered the Atlantic ($> 30°N$) increased by $\sim 80\%$ in the ITB simulation (Table 5.1) as compared to the REF simulation. In addition, among all tracer that entered the Atlantic Ocean (hereafter, T_{atl}), 68% returned to the surface in the North Atlantic Ocean in the ITB simulation, while in the REF simulation only 36% of T_{atl} (Table 4.1) penetrated into the North Atlantic Ocean. Temporal analysis shows that for all upwelling that happened in the North Atlantic Ocean, over 65% upwelling appears in the later half duration of integration (from year 70 to 150) in the ITB simulation, in contrast to the REF simulation in which $\sim$ 65% (Table 4.1) of the North Atlantic upwelling happens in the early period of integration. This enhanced tracer upwelling flux in the North Atlantic Ocean in the ITB experiment can also been seen in Fig. 5.7 as the geographic distribution of integrated tracer upwelling fluxes in Global Ocean. Comparison with the REF

TABLE 5.1: Tracer re-emergence in different ocean basins after 150 years of integration in ITB simulation. All values are normalized against the total subducted tracer after tracer release in the SAMW formation region (unit T_{sub}).

	N. of $30°S$	S. of $30°S$	Equatorial	N. of $20°N$
Global	0.275	0.698	0.115	0.019
Atlantic	0.025	0.098	0.005	0.017
Pacific	0.122	0.446	0.059	0.002
Indian	0.129	0.153	0.052	

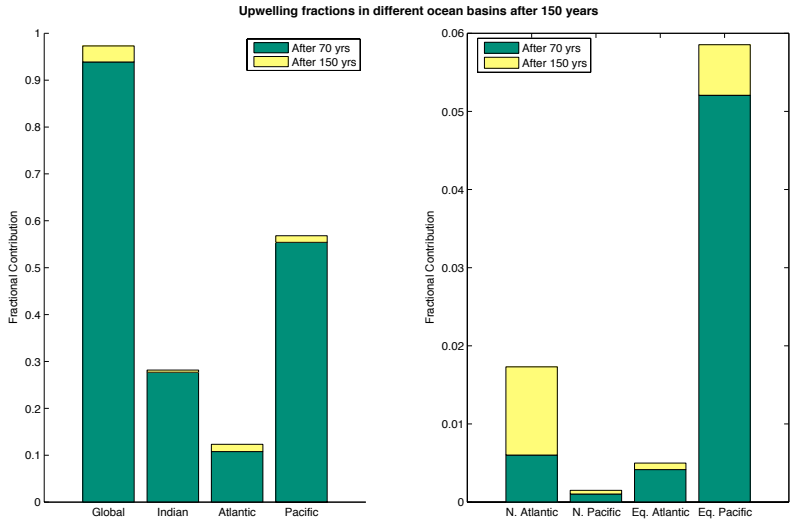

FIGURE 5.6: Fractional contributions of tracer upwelling fluxes in different ocean basins, after being integrated over a period of 150 years in the perturbation experiment with shallower ITF transports. All values are normalized against the total subducted tracer (T_{sub}). (North Atlantic/Pacific $> 20°N$; Equatorial Atlantic/Pacific between $10°S \sim 10°N$).

simulation (Fig. 4.17) shows that there is a great enhancement in the tracer upwelling in the high-latitude of North Atlantic Ocean, mainly in the form of entrainment upwelling.

The above results suggest that a long lasting tracer supply into the Atlantic Ocean exists if the ITF is closed. Fig 5.8 suggests that this continuous tracer supply into the Atlantic Ocean comes from both the Pacific Ocean via crossing the Drake Passage and Indian Ocean through the Agulhas leakage. A closed Timor Strait slows down the Pacific surface overturning cell as well as the northward transport of the SAMW-related tracer. Therefore, significant tracer still remains in the subpolar region of the South Pacific Ocean even after 100 years of integration and serves as a reservoir for the tracer supply to the Atlantic Ocean.

The temporal and spatial variations of the tracer upwelling in the North Atlantic in the ITB experiment are also associated with the unique feature of SAMW transports in the Atlantic basin. Unlike the Pacific Ocean, the SAMW circulation pathway (in both ITB and REF) in the tropical Atlantic Ocean is less ventilated and generally located a few hundred meters below the surface mixed layer (Fig. 5.9), therefore only a small fraction of tracer upwells into the surface during the northward transportation process after it has been moved upward onto lighter densities by diapycnal mixing. This repartition of tracer at the density horizon along the pathway of tracer circulation in the Atlantic Ocean was comparatively fast in the early period after tracer released in the Southern Ocean due to the strong tracer concentration gradient between SAMW layers (with high tracer concentration) and overlying empty layers (with very low tracer concentration in the beginning). However after several decades this leveling up process was greatly slowed down due to the weakening of the tracer concentration gradient. As a result, the fraction of SAMW related tracer that can penetrate into the North Atlantic Ocean, before re-emerging into the surface boundary layer along the circulation pathway, keeps increasing as long as the tracer supply into the Atlantic persists, and reaches to a high value in the later period of model integration. Once tracer transports into the North Atlantic Ocean, it eventually upwells into the mixed layer either along the pathway of the Gulf Stream by diapycnal mixing, or by induction and entrainment in the subpolar gyre and the high latitudes of the North Atlantic.

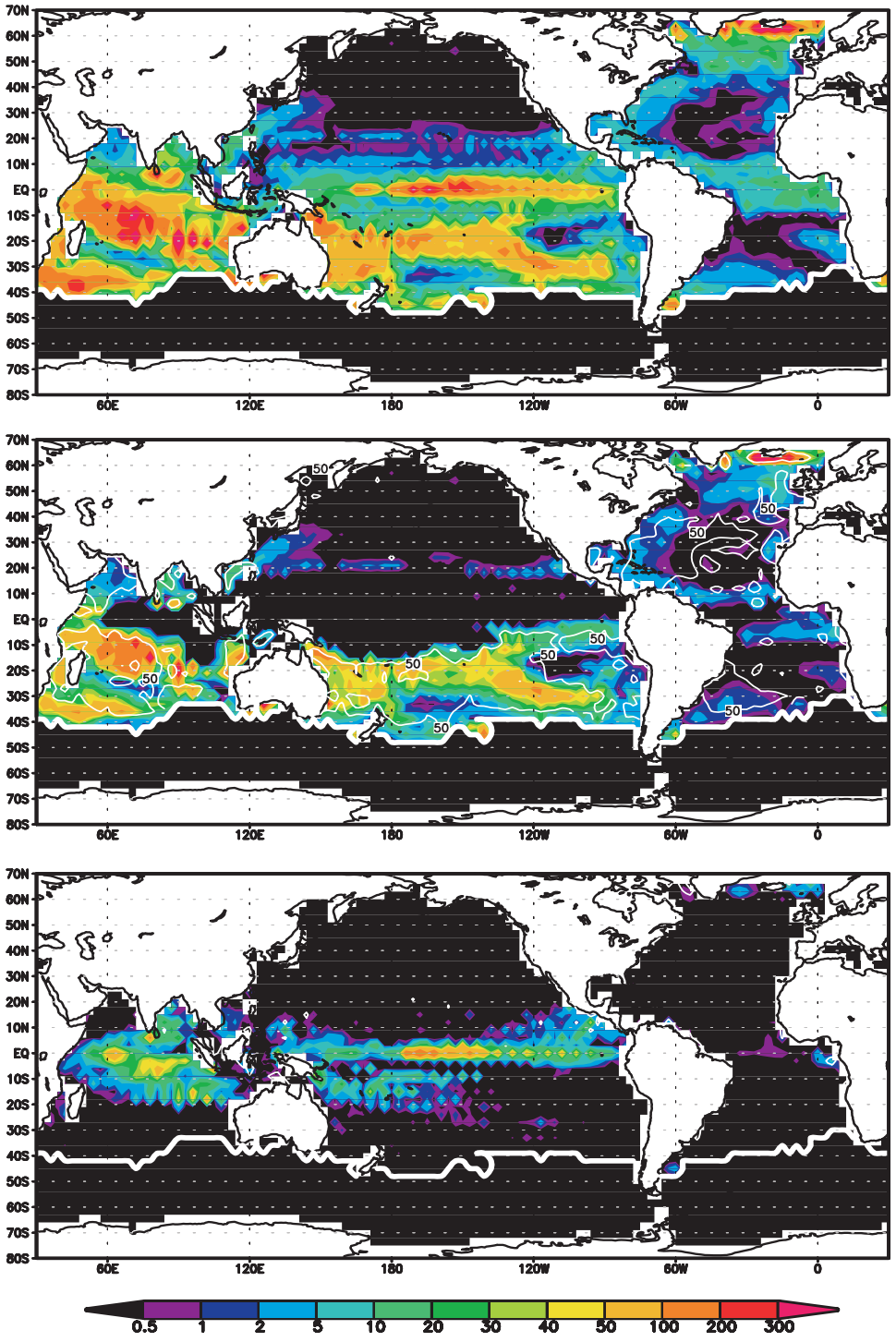

FIGURE 5.7: Time integral of the upwelling tracer flux (*tracer unit* m^{-2}) components in the ITB simulation after being integrated over a period of 150 years: (top) Q_{t} as total tracer upwelling flux; (middle) Q_{ent} as entrainment flux; (bottom) Q_{Ekm} as Ekman divergence induced tracer upwelling flux. Winter outcrops of the lightest SAMW isopycnal in the Southern Ocean are shown as the thick white contours.

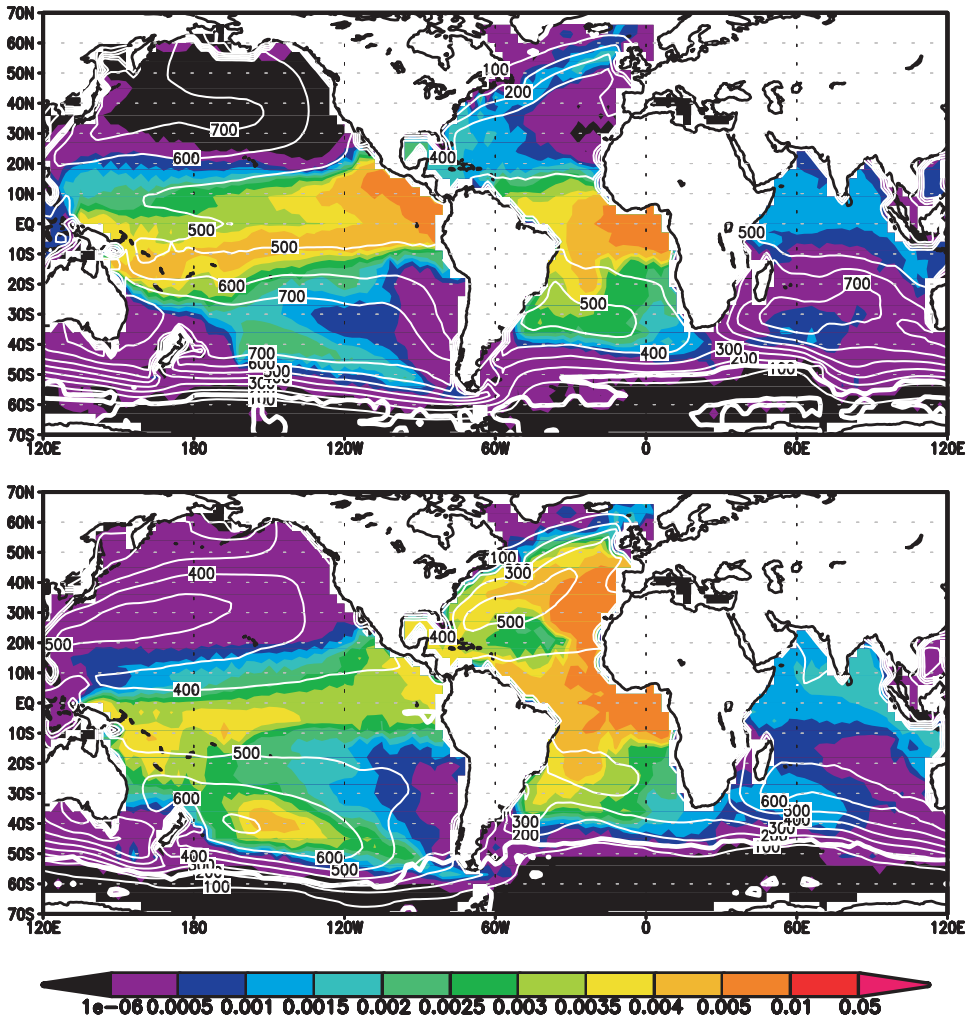

FIGURE 5.8: Tracer concentration distribution on the density surface of SAMW core (σ_2 = 35.80) in (top) the REF simulation and (bottom) ITB experiment after 100 years of integration.

Budget analysis suggests that a total of O(10^{-2}) T_{sub} tracer has been transported from the Pacific Ocean into the Indian Ocean by the ITF after 150 years of integration in the REF simulation. Correspondingly, a similar order of tracer upwelling flux increase appears in the Pacific Ocean (Table 5.1) after the ITF transports was reduced in the ITB experiment. However, even in the ITB simulation there is still no sign of tracer circulation that can penetrate to the high latitude of North Pacific Ocean, neither is there an enhancement of SAMW-related tracer upwelling in the North Pacific Ocean to the North of 20°N (Fig. 5.7). Instead, this extra tracer flux was deflected eastward by

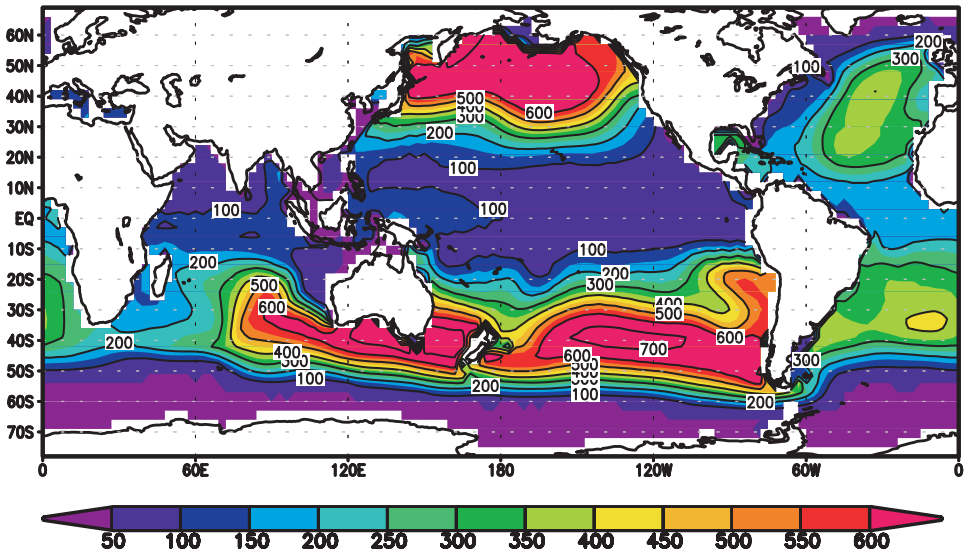

FIGURE 5.9: Distance $[m]$ between the bottom of surface boundary layer to the density surface of SAMW core ($\sigma_2 = 35.80$) in the ITB experiment. The core of SAMW locates $\sim 50\ m$ below the surface boundary layer in the tropical Pacific Ocean. In contrast, this value increases to $\sim 200\ m$ in the tropical Atlantic mainly because the mixed layer is comparatively thinner in the low latitude of Atlantic Ocean than in the Pacific Ocean.

following the zonal Equatorial Under Current system once it reached the tropical Pacific Ocean. Inter-comparison of the global upwelling patterns between REF (Fig. 4.17) and ITB experiments shows that total tracer upwelling along the equatorial Pacific actually decreases in the ITB simulation, despite the fact that reducing the ITF results in more tracer flux input at the origin of the EUC in the western boundary. This decreased tracer upwelling along the equatorial Pacific Ocean is mainly caused by the decrease of Ekman divergence induced tracer upwelling (Q_{Ekm} in Fig. 5.7) in this region induced by deepening of the mixed layer depth in the ITB simulation. As suggested by Rodgers et al. (2003), the stratification of the equatorial Pacific thermocline is determined by both local mixing and entrainment, as well as the advective exchanges with the Southern (via the circulation of SAMW) and Indian Oceans (via the ITF transports). Gorgues et al. (2007) claims that a decrease in primary production by 15% along the equator can appear if the ITF transports are closed, due to the deepening of the thermocline in the eastern Pacific, which is consistent with our results. Long-term mean mixed layer depth at the tropical Pacific Ocean for REF and ITB experiments are calculated and illustrated in Fig. 5.10. Reduced ITF leads to an increase of mixed layer depth at the eastern part of

equatorial Pacific between 60 $\sim$ 100 m, as an extra $\sim$ 10 Sv of water otherwise transferred to the Indian Ocean remains in the equatorial Pacific. This deepening decreases the tracer concentration of the equatorial wind driven upwelled water and cancels the tracer increase advected by the EUC (Lee et al., 2002). Extra upwelling can be observed between 20 - 30°S in the Pacific Ocean as the recirculation refills the tracer into the subtropical gyre in the ITB simulation.

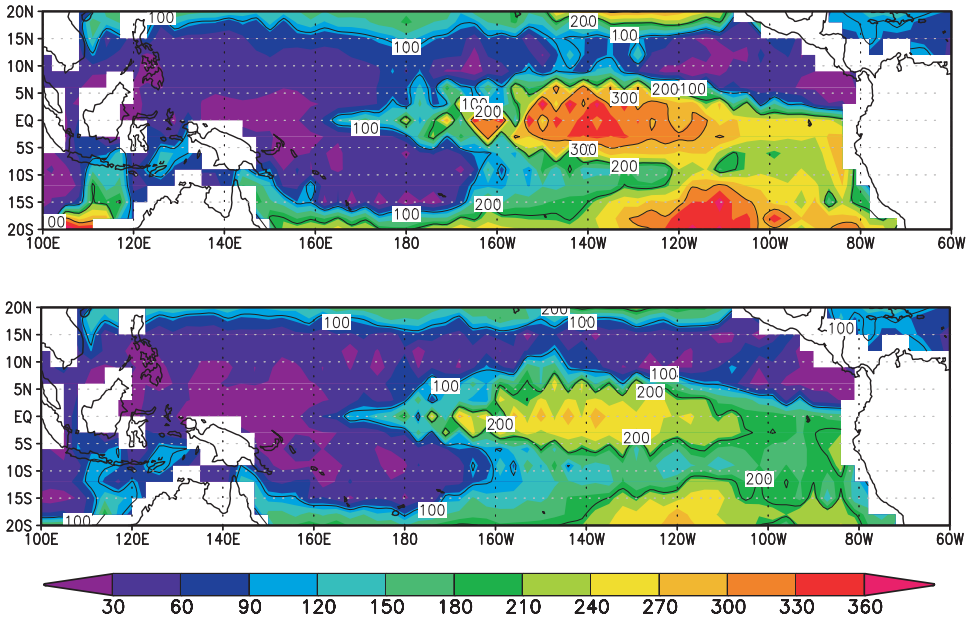

FIGURE 5.10: Ten year mean mixed layer depth (unit m) in the tropical Pacific Ocean in (top) ITB simulation and (bottom) REF simulation. The mixed layer depths are averaged over a period of ten years after both runs reach their quasi-equilibrium state.

Therefore, conclusion can be drawn from this perturbation experiment that ITF transport, though playing an important role in the circulation pattern of tracer in the equatorial and southern Pacific Ocean, is not the key factor controlling the penetration of SAMW to the North Pacific Ocean. Instead, reduced ITF transport leads to enhancement of nutrient supply into the Atlantic Ocean because nutrients are continuously supplied into the Atlantic Ocean from the Pacific Ocean via the Drake Passage due to the slow down of the Pacific meridional overturning circulation. Also the total SAMW upwelling in the North Atlantic Ocean increases to almost three times as large as in the REF simulation.

5.1.3 Importance of the EUC and WBC in the circulation of SAMW

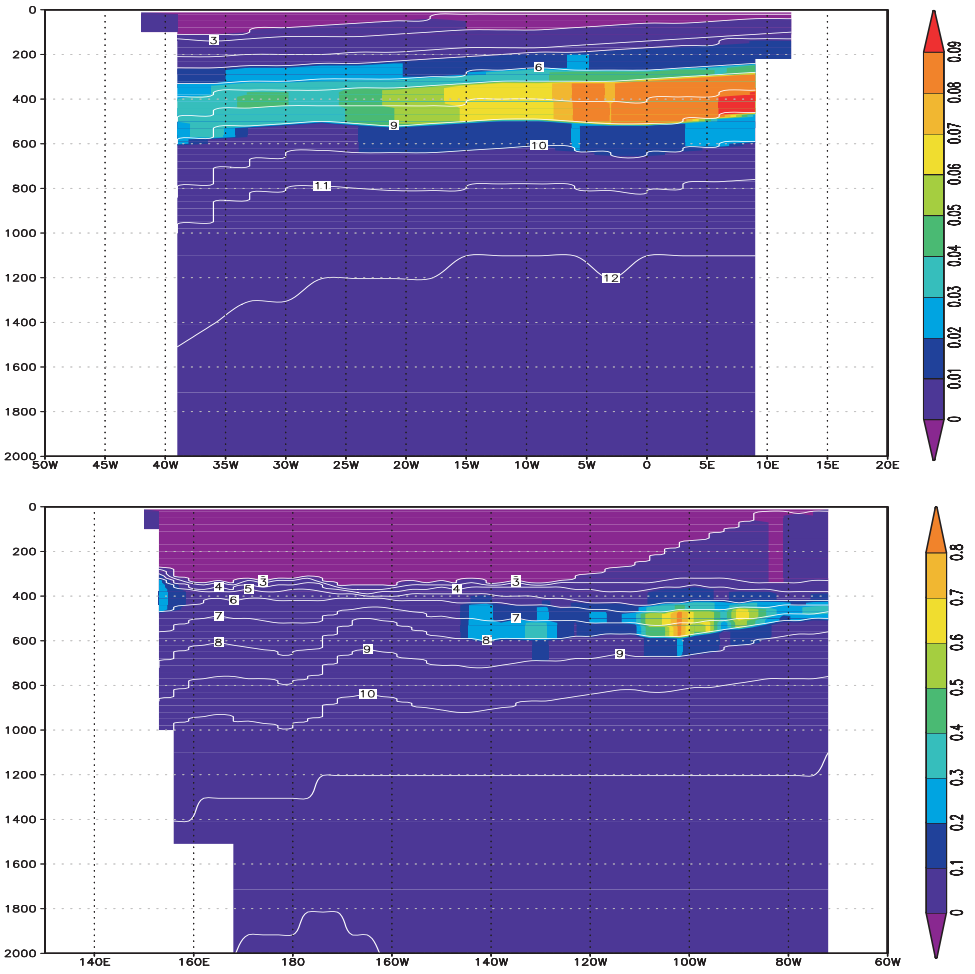

FIGURE 5.11: Tracer concentration sections at 20°S in the (top) Atlantic Ocean and (bottom) Pacific Ocean for the REF simulation. The model has been integrated over a period when the maximum tracer concentration crossed this latitude belt (8 years for the Pacific Ocean and 14 years for the Atlantic Ocean) after tracer release.

The EUC is expected to be important in controlling the pathway of SAMW-related tracer by deflecting it to the eastern part of equatorial Pacific (Wyrtki and Kilonsky, 1984; Firing et al., 1998). In order for this Southern Ocean originated tracer to cross the Equator and penetrate into the Northern Hemisphere, it must be associated with the Western Boundary Currents instead of being captured by the zonal equatorial current system, once it reaches the equator by following the circulation of the southern subtropical gyres. First we examine the density levels that the tracer resides at in the equatorial Pacific

and Atlantic oceans. As described in Chapter 3, this SAMW-related tracer was initially released in the Southeastern Pacific and Indian Oceans, within the density range between $\sigma_2 = 33.54$ and 36.15 and then circulated to the north in these two ocean basins by following the anticyclonic subtropical gyres and Ekman current (Fig. 4.2), with its core residing on density levels $\sigma_2 =$ 35.37 to 35.80 (layer 7 and 8). However, due to progressive cooling following the circumpolar pathway of the ACC, the tracer sinks in density range after crossing the Drake Passage and entering the Atlantic Ocean (Fig. 4.5), mimicking the process of transformation from SAMW to AAIW (McCartney, 1982). As a result, the core of tracer patch circulating in the Atlantic Ocean resides on somewhat deeper density levels (between $\sigma_2 = 35.80$ to 36.15 at layer 8 and 9) than its counterpart in the Pacific Ocean, as demonstrated by Fig. 5.11.

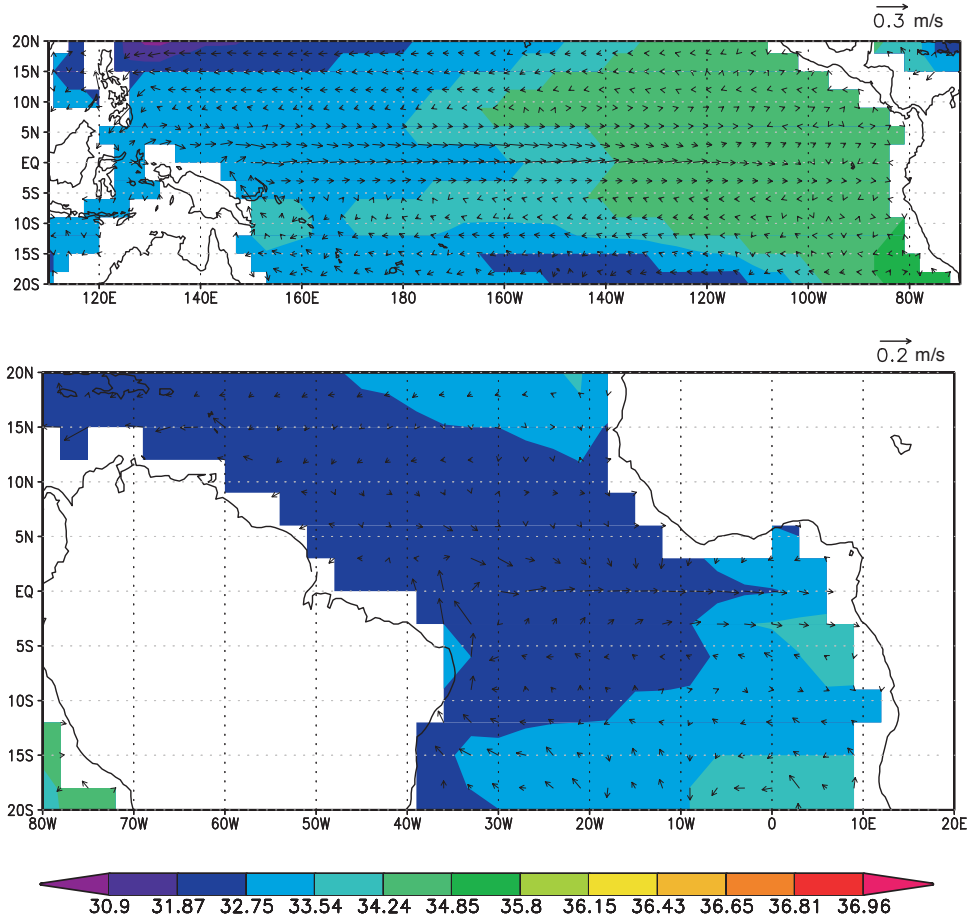

FIGURE 5.12: Long-term averaged potential density distribution at the depth of centre EUC (top) in the Pacific Ocean (200 m) and (bottom) in the Atlantic Ocean (100 m) for the REF simulation. Also shown are the velocity fields (ms^{-1}).

The zonal equatorial current system in the Pacific is dominated by a strong subsurface eastward EUC that lays just below the surface westward South Equatorial Current (SEC) and occupies depth levels from 100 m to 300 m (Fig. 4.31). The core of this EUC system resides on the density levels $\sigma_2 = 33.54 \sim 34.85$ (layers 4 to 6) in the tropical Pacific, with its densest constituent water mass residing in the density range of SAMW. Despite the coarse resolution of our model, the depth and density levels where this EUC resides in the Pacific Ocean are in good agreement with field observations and other model simulation results (Zenk et al., 2005; Rodgers et al., 2003). The annual mean velocity is of about 0.1 ms^{-1} and is weaker than observations, which is expected as a result of the coarse resolution model. A similar EUC also exists in the equatorial Atlantic Ocean, but residing at somewhat shallower depth and density levels, i.e. between 50 to 150 m depth, or near $\sigma_2 = 32.75$ to 33.54 (layers 3 and 4), respectively (Fig. 4.32). In addition, the simulated annual mean zonal velocity of EUC is also weaker in the Atlantic than in the Pacific Oceans (Fig. 5.12).

Like the EUC, the WBC systems in the North Atlantic (Gulf Stream) and Pacific Oceans (Kuroshio Current) also reside on different density levels, but in an opposite way if we consider their contributions to the northward transports of SAMW. As demonstrated by Fig. 5.13, the core of Kuroshio Current (> 0.1 ms^{-1}) in the North Pacific Ocean occupies the surface 400 m and a density range between $\sigma_2 = 30.90$ to 35.37 (from layers 1 to 7), with a maximum velocity of 0.2 ms^{-1}. These simulated results are in general agreement with previous observations (Zhang et al., 2001; Johns et al., 2001; Oka and Kawabe, 1998). In contrast, the core of Gulf Stream in the North Atlantic Ocean, though also occupying a depth range of about 400 m, is found at somewhat denser density levels between $\sigma_2 = 30.90$ to 36.15 (from layers 1 to 9) due to the shoaling isopycnals westwards (Fig. 5.13), and therefore extends to the density level where the core SAMW in the Atlantic Ocean resides.

As a result, once the lateral advection transports the SAMW-related tracer to the Equatorial region in the Atlantic Ocean, most of the SAMW-related tracer would keep moving northward by following the Florida Current and Gulf Stream due to the deep extension of this WBC that occupies the core density range of the SAMW circulating in the Atlantic Ocean. Also because the Atlantic EUC reaches to depths that cover only the lightest part of SAMW, only a small fraction of the SAMW-related tracer would be deflected eastward.

Consequently, the circulation of the SAMW can extend to the subtropical and subpolar gyres in the North Atlantic Ocean and be responsible for supplying nutrient back to the thermocline even in the high latitude regions (Fig. 4.17). In contrast, the SAMW circulation in the Pacific Ocean flows in a different way because of the hydrodynamic conditions of the Pacific EUC and WBC. After reaching the Equator by following the subtropical gyre in the South Pacific Ocean, most of the light SAMW (between $\sigma_2 = 33.54$ and 34.85 in layers 4 - 6) would be trapped in the zonal equatorial current system (Fig. 4.31) due to the wide density range it occupies. This part of the SAMW-related tracer deflects eastward following the Pacific EUC and emerges into the surface boundary layer mainly in the eastern part of equatorial Pacific Ocean driven by Ekman divergence (Fig. 4.45) and shear-induced diapycnal mixing. Only the upper part of the dense SAMW (in layer 7) follows the densest part of the Kuroshio Current as the WBC in the North Pacific Oceans resides at comparatively shallower density levels (from layer 1 to 7) as compared to its counterpart in the North Atlantic Ocean(Fig. 5.13).

Apart from the different hydrodynamic conditions of EUC and WBC in these two ocean basins, isopycnal Potential Vorticity (PV), as an important diagnostic parameter for tracking water masses in physical oceanography, can also be used for demonstrating the different circulation behaviors of the SAMW in the Northern Hemisphere. Isopycnal PV distributions in the northern Atlantic and Pacific oceans have been defined and calculated in our model simulation using Eq. (3.1)$\sim$(3.3) and results are illustrated in Fig. 5.14. As we can see, the northward transports of SAMW/tracer carried out by the densest Kuroshio Current (with $\sigma_2 = 33.54$ in layer 7) encounter a steep PV gradient once across $10°N$ in the Pacific Ocean. This strong PV gradient acts as a barrier in the North Pacific Ocean between 10 - 20° N and blocks the deepest Kuroshio Current and the northward transports of SAMW/tracer. In the North Atlantic Ocean, however, the Gulf Stream extends as deep as the SAMW core (layers 8 and 9 with density $\sigma_2 = 35.80 \sim 36.15$), where no significant PV gradient exists in the pathway of this WBC. Therefore, this part of the Gulf Stream transported SAMW/tracer can easily penetrate into the subpolar gyre and high latitude region in this ocean basin.

As a diagnostic variable, the distribution of the PV is determined by both surface adiabatic and diabatic fluxes, as well as boundary frictions. Traditionally,

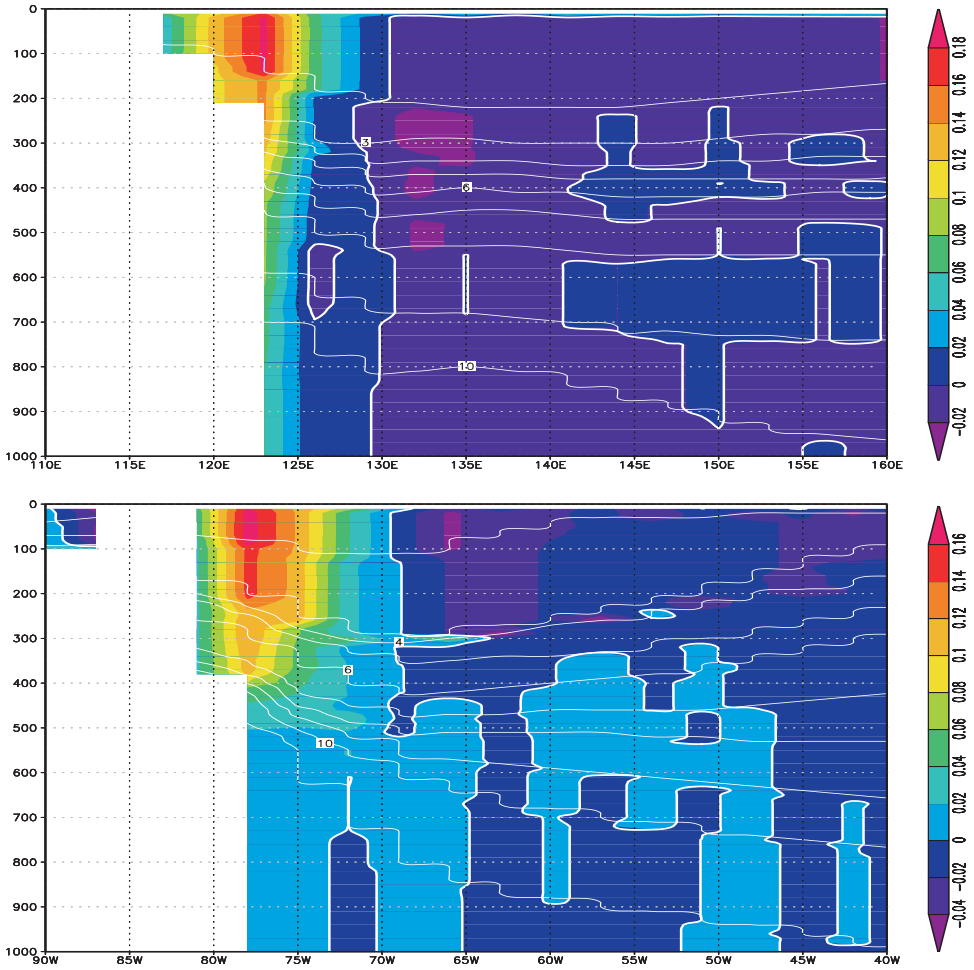

FIGURE 5.13: Seasonal mean sections of model meridional velocity (ms^{-1}) at $28°N$ for (top) the Kuroshio Current and (bottom) the Gulf Stream for the REF simulation. Positive meridional velocity indicates northward currents.

anti-cyclonic wind stress curl, which is often found in the northern subtropical gyres, is thought of as a sink of PV. Conversely, surface PV gain happens in the north subpolar gyre due to cyclonic wind stress curl (Marshall, 1984). For the diabatic contribution, surface cooling is an important mechanism of PV loss due to destruction of stratification and, conversely, surface heating a mechanism of PV gain due to creation of stratification. However, when considering the surface entry/exit of PV for any isopycnal layers below the mixed layer, the PV content can only be modified through fluxes where a layer intersects a boundary (outcrops the mixed layer) as PV flux cannot cross isopycnals (Haynes and McIntyre, 1987). Here we calculated the wind stress curl over the Northern Hemisphere based on the NCEP reanalysed climatology and results

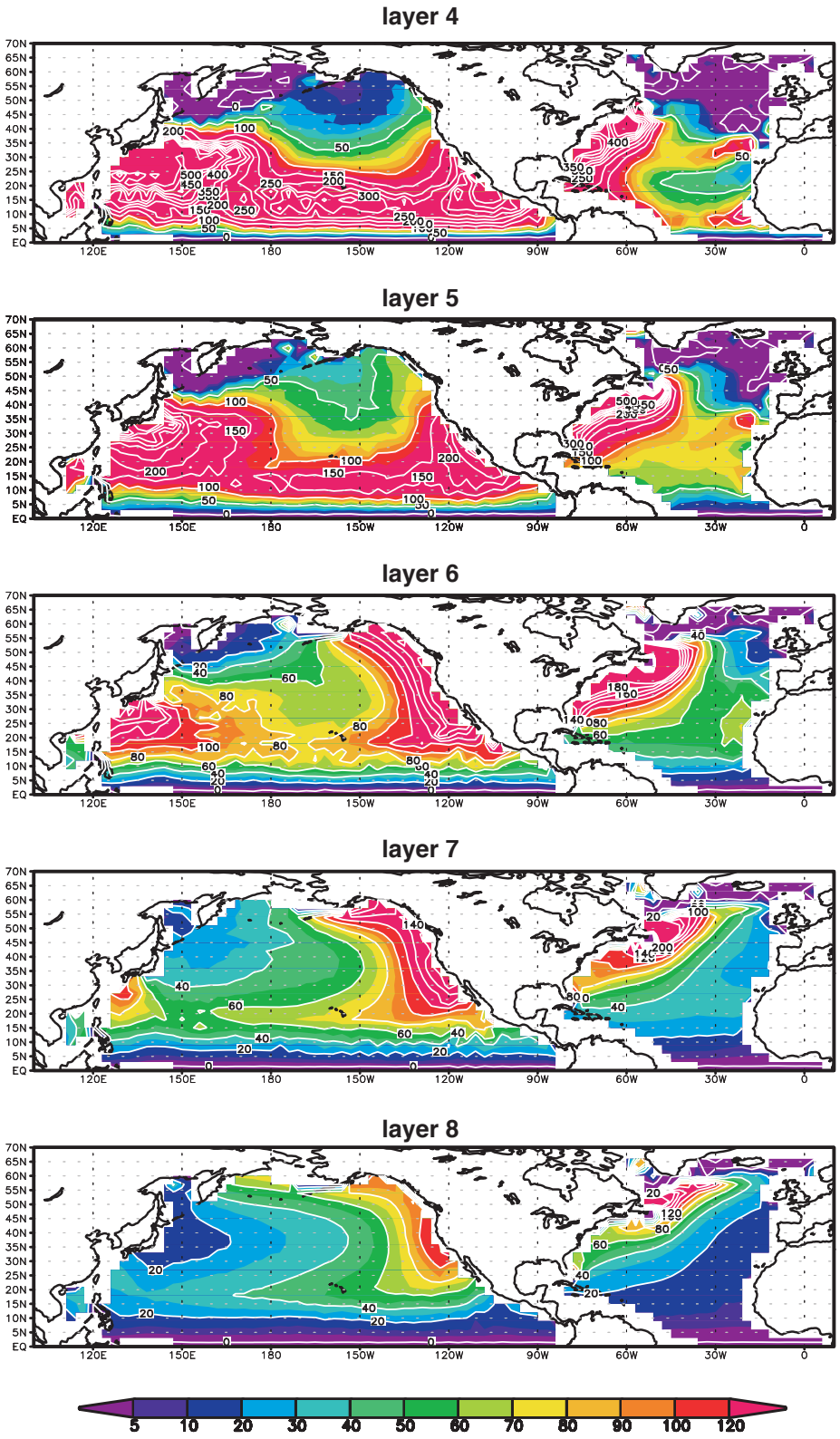

FIGURE 5.14: Averaged winter (Mar) distribution of PV $[\times 10^{-11}(ms)^{-1}]$ in the Northern Hemisphere following SAMW related isopycnal layers (σ_2 = 33.54 $\sim$ 35.80). Model has been integrated over a period of 120 years until reaching a quasi-equlibrium state.

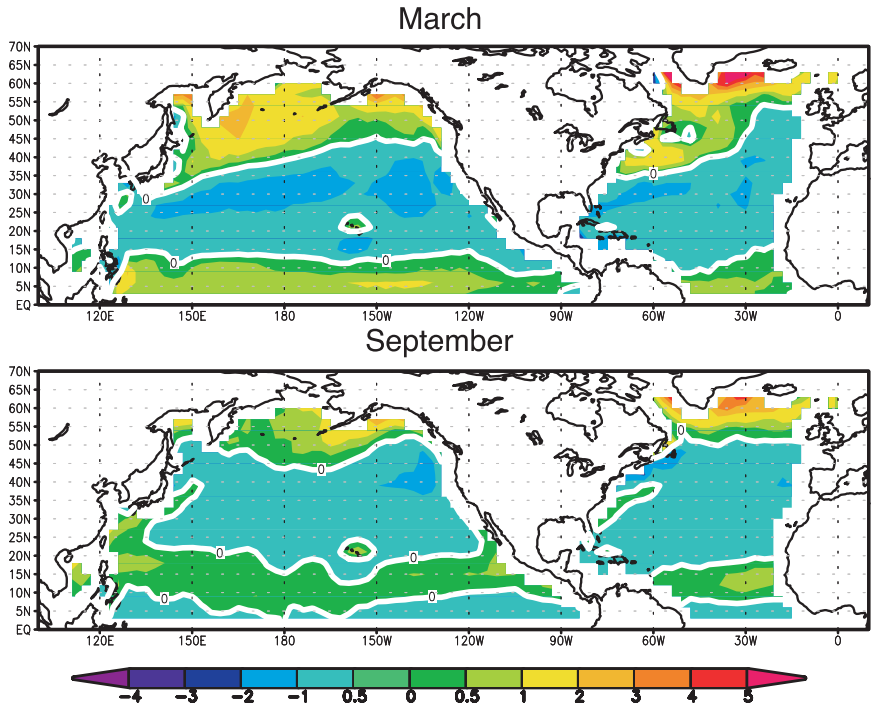

FIGURE 5.15: Surface wind stress curl [$\times 10^{-7} Ns^{-2}$] distribution in winter (Mar) and summer (Sep) for the Northern Hemisphere (based on NCEP reanalysis monthly mean wind stress climatology).

are shown in Fig. 5.15. As we can see, strong winter time cooling (Fig. 4.23) together with the cyclonic wind field at the north outcropping region around the Sea of Okhotsk generates a deep winter mixed layer with minimum PV in our simulation, which is believed to be associated with the ventilation of the NPIW (Talley, 1997; Yasuda et al., 2002). The spreading pathway of this PV minimum water mass follows the Subarctic Current eastward and then the southward recirculation of the subtropical gyre, filling up the western part of North Pacific Ocean to the north of $10°N$ on the density levels between $\sigma_2 =$ 35.37 to 35.80 (layers 7 and 8), in contrast to confinement of water masses at the lighter density levels between $\sigma_2 = 33.54$ to 34.85 (layers 4 - 6) (Fig. 5.14). Increased isopycnal PV for the subsurface water in layers $4 \sim 7$ in the western tropical Pacific is associated with strong local stratification (reflected in small layer thickness as the density discrepancy is always constant for an isopycnal layer) (Fig. 5.16) and the frictional PV gain at the western boundary. Investigation of the external forcing that determines the local stratification of the subsurface water there has not been completed and therefore is not included in this thesis. A discussion about the entry and exit of PV in the Northern

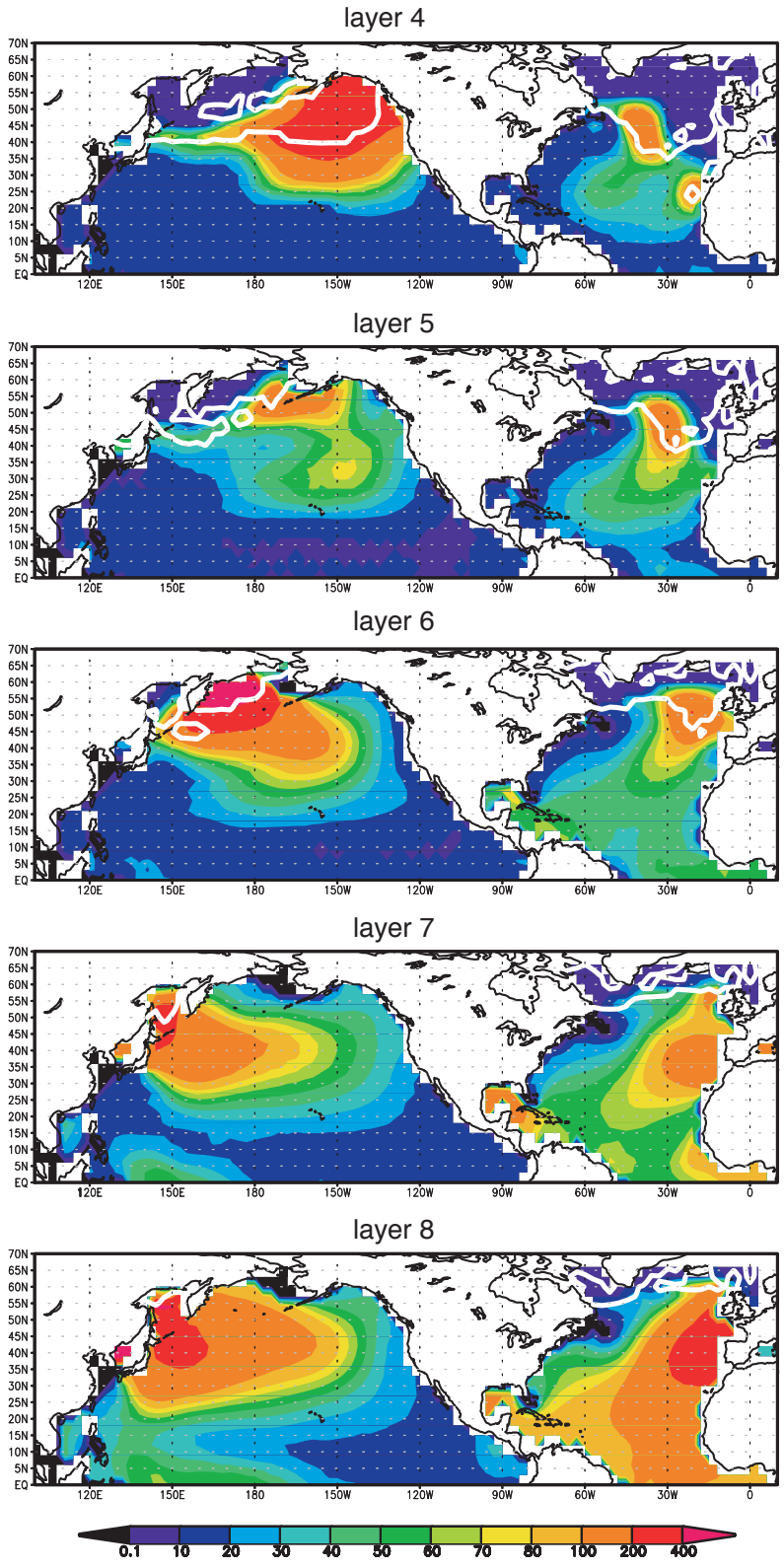

FIGURE 5.16: Same as Fig. 5.14 except for isopycnal layer thickness $[m]$.

Hemisphere has been carried out by Czaja and Hausmann (2009), and the surface winds are suggested to be particularly important in setting surface PV exchange in the tropical Pacific region.

The NPIW, with a similar density range as SAMW, can extend over the entrie North Pacific to the equator in the dense isopycnals (Fig. 5.14) and may bring nutrient to the mixed layer (Sarmiento et al., 2004). Here our simulation suggests that it is the structure/characteristics of EUC and WBC in the North Pacific Ocean that serve as the key factors in blocking the northward transport of SAMW. Strong local stratification induced by surface forcing (wind and heat flux) and western boundary friction in the pathway of Kuroshio Current acts as a nutrient barrier (as demonstrated by the steep meridional PV gradient there) between 10 - 20°N in the North Pacific Ocean, blocking the deepest Kuroshio Current and the northward transports of SAMW/tracer (Fig. 5.1). Additional contributions affecting the circulation pathway of SAMW in the North Pacific Ocean may come from the north-east Monsoon wind during boreal winter that deflects Kuroshio water into the Luzon Strait and the formation of a loop current in the South China Sea.

5.2 Perturbation experiments with enhanced turbulent mixing

Turbulent mixing modifies water masses, maintains ocean stratification and contributes to driving the global thermohaline circulation (Munk and Wunsch, 1998; Ganachaud and Wunsch, 2000). In some locations (*e.g.*, Gulf Stream), it also believed to play an important role in terms of nutrient upwelling to the surface layers (Jenkins and Doney, 2003; Pelegrí et al., 2006). In order to assess the sensitivity of the SAMW upwelling and global thermocline nutrient supply to the diffusivity profile used in our model, a set of twin experiments have been carried out with modified diffusion coefficients. The set up of the perturbation experiments is described first, followed by the SAMW upwelling patterns in the global ocean based on simulations with enhanced diapycnal mixing. In the end, the "Nutrient Spiral" theory proposed by Jenkins and Doney (2003) to explain the nutrient supply to the subtropical gyre in the North Atlantic Ocean is discussed against the backdrop of these perturbation experiments.

5.2.1 Vertical diffusivity profile in HYCOM

Based on an inverse analysis of high-resolution hydrographic sections and current meters, Ganachaud and Wunsch (2000) calculated globally averaged diapycnal diffusion coefficients of $3 \sim 4 \times 10^{-4}\ m^2 s^{-1}$ in the deep ocean (2000 - 3500 m) and $9 \pm 2 \times 10^{-4}\ m^2 s^{-1}$ for the abyssal ocean (3500 m - bottom). Other estimations also suggest that a diapycnal diffusivity of $O(10^{-4}\ m^2 s^{-1})$ is needed to maintain the abyssal stratification against global upwelling associated with 25 Sv of deep water formation (Munk, 1966; Munk and Wunsch, 1998). Although recent microstructure measurements (Gregg, 1987) and tracer-release experiments (Ledwell et al., 1993, 2000) have only established a vertical mixing of $O(10^{-5}\ m^2 s^{-1})$ in the stratified midlatitude ocean interior, strong turbulent mixing of 10 - 1000 times the ocean interior values is found over the boundaries and bottom rough topography regions (Toole et al., 1994; Heywood et al., 2002), suggesting that elevated mixing maybe confined to several key regions of the global ocean (Garabato et al., 2004).

As for numerical models, many early simulations used constant vertical diffusion coefficient. Guided by the characteristic microstructure profile in the equatorial ocean, Robinson (1966) started to use large diffusion coefficients in the high shear zones and low ones in the velocity core, where current shear is minimal. This idea was adopted by the subsequent modelers, such as Pacanowski and Philander (1981) and Large et al. (1994), both of whom proposed mixing schemes in which the vertical diffusivities are associated with the turbulent Richardson number. The K-Profile Parameterization scheme used in our model includes a constant background diffusion, a shear-dependent diffusion and double diffusion (Eq. (3.14)). To the best approximation, a background value of $O(10^{-5}\ m^2 s^{-1})$ should be used in the stratified ocean, except for regions with strong currents, *e.g.*, the equatorial and WBC regions, where the shear-driven turbulent mixing dominates and diffusivity reaches maximum values of order $50 \times 10^{-4}\ m^2 s^{-1}$.

The vertical diffusivity profiles calculated from our standard simulation (REF) are depicted in Fig. 5.17 as basin averaged values. It is clear that except for the surface boundary layer regions, the diffusion coefficients in the interior of the ocean are about $10^{-5}\ m^2 s^{-1}$. In addition, no significant enhancement of the diapycnal diffusivity can be observed even in the equatorial and WBC regions,

as velocity shears are too small to trigger any shear-dependent diffusion in the REF simulation.

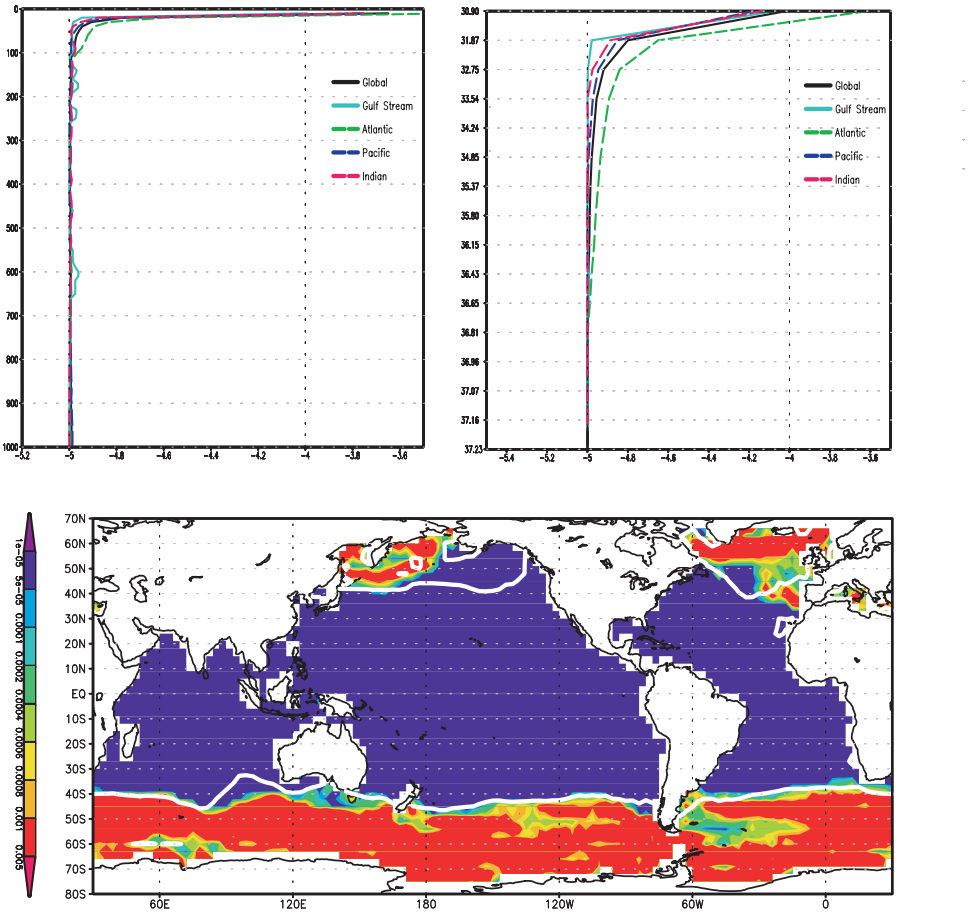

FIGURE 5.17: (Top) Basin-averaged vertical diffusivity profiles [$\log(K_v)$ $m^2 s^{-1}$] with respect to depth [m] and potential density ($\sigma 2$) used in the REF simulation; (bottom) long-term averaged diapycnal diffusivity distribution at the lightest density level (layer 4 with potential density $\sigma 2 = 33.54$) of the SAMW. Also shown are the outcrops of the layer 4 in thick white contours.

As explained in Chapter 3, the KPP mixing scheme used in our model for calculating the vertical diffusion coefficients has been finely tuned to achieve the most realistic simulation regarding large-scale observable quantities (surface currents, temperature, tracer circulation, etc.). Although the diffusion coefficients in the interior of the ocean are also shear-dependent in the KPP scheme, the horizontal velocities calculated by our model are unavoidably weaker than the observations (Fig. 5.13), after been smoothed over the grid box due to the coarse resolution. As a result, the weak velocity shear between two isopycnal layers can not generate enough diapycnal mixing and the nutrient upwelling

along the equatorial and Gulf Stream regions may be underestimated in our REF simulation.

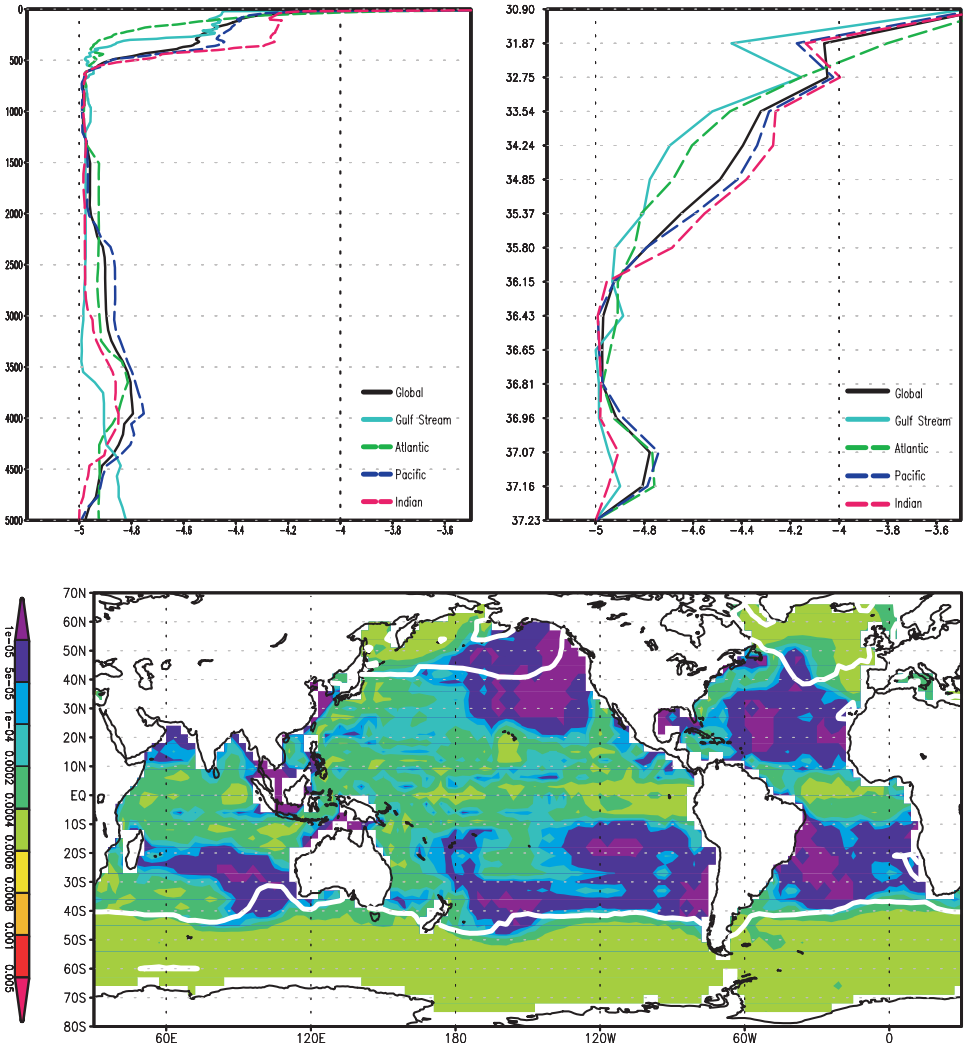

FIGURE 5.18: Same as Fig. 5.17 except with enhanced turbulent mixing, note that the depth scale is also changed to 5000 m. This profile has been used in the twin perturbation experiments.

The Gulf Stream turbulent diffusivities have been measured and estimated from a myriad of methodologies and data sets (Ledwell et al., 1998; Houghton and Visbeck, 1998; Pelegrí and Csanady, 1994). A general agreement has been achieved based on both tracer studies (Ledwell et al., 1993; Winkel et al., 2002) and measurements based on isopycnal floats and hydrography (Barth et al., 2004) (after long-term averaging), suggesting a mean diapycnal diffusion in the Gulf Stream of O(10^{-4} m^2 s^{-1}) below the surface boundary layer. Therefore, in order to assess the sensitivity of the SAMW upwelling and associated nutrient

supply to the vertical diffusivity profile used in our model, a modified KPP scheme has been implemented in HYCOM, with enhanced turbulent mixing in regions of known strong geostrophic velocities (*e.g.*, Gulf Stream). As illustrated in Fig. 5.18, diapycnal diffusivities increase to 5×10^{-4} m^2 s^{-1} along the Gulf Stream in this profile (it has been achieved by increasing the critical Richardson number from 0.7 to 1000 in Eq. 3.17), to replicate the WBC enhancement of the turbulent mixing. In the upper 500 m in the ocean this K_v varies between 10^{-5} - 10^{-4} m^2 s^{-1}, but is reduced to a background value in the interior. Based on this modified diffusivity profile, a set of twin experiments has been carried out: one run with this enhanced diffusivity profile (Fig. 5.18) only applied to the tracer mixing (hereafter referred as EDT); and the other run with the same enhanced diffusion coefficients but applied to all thermodynamic variables (T/S), momentum and tracer mixing (hereafter, EDC). The perturbation experiments were designed as an attempt to separate the contributions of hydrodynamic transports from the diapycnal mixing alone. Both experiments have been integrated over a period of 120 years, starting with the same initial state. A tracer release and consumption scheme as in the control run has been applied, and a further 150-years spin-up was carried out after tracer release.

5.2.2 Twin experiments results

Diapycnal mixing has been considered by some (Munk and Wunsch, 1998) as one of the main driving mechanisms for the global MOC, and model studies also show that the deep overturning circulation and the heat transport are very sensitive to the employed diapycnal diffusivity coefficients (Bryan, 1987; Zhang et al., 1999; Mignot et al., 2006), especially in the boundary regions (Marotzke, 1997; Scott and Marotzke, 2002). Streamfunctions of the MOC in different ocean basins from the simulation of EDC are illustrated in Fig. 5.19. Comparing with the REF results (Fig. 2.23), we can see a general enhancement of the overturning circulation for both the Atlantic Ocean and in a global scale (Fig. 5.20).

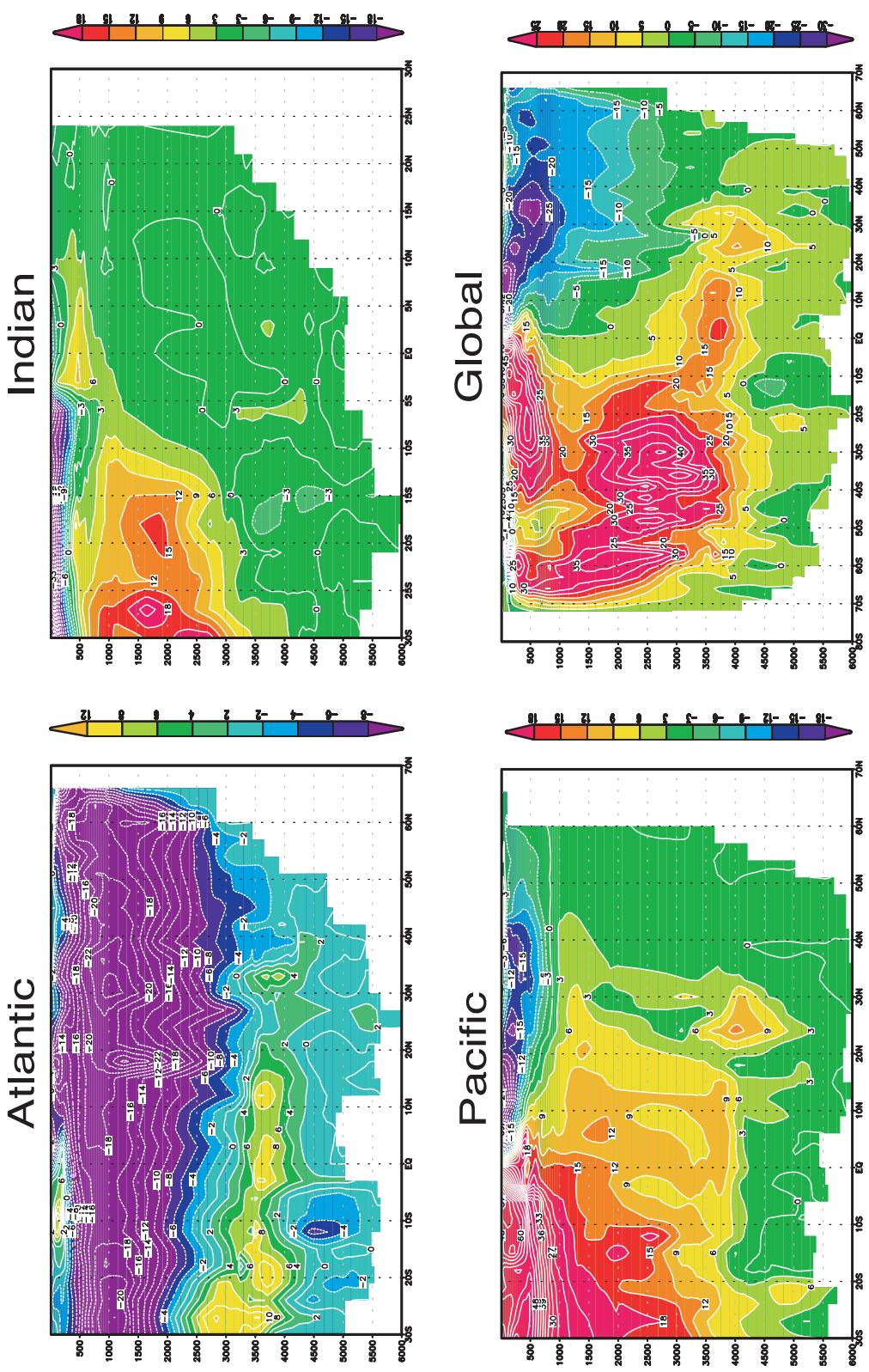

FIGURE 5.19: Meridional Overturning Streamfunctions (Sv) for the (A) Atlantic; (B) Indian and (C) Pacific and (D) Global Oceans for the perturbation experiment with enhanced vertical diffusivity coefficient (EDC). Model has been integrated over a period of 120 years and reached a quasi-equilibrium state.

The maximum overturning circulation in the global deep cell increased from ∼30 Sv (REF) to about 45 Sv (EDC), while the surface Ekman cell to the south of the equator reached a maximum value of about 65 Sv and to a depth of about 1000 m in the EDC simulation. For the AMOC, the maximum overturning of the North Atlantic Deep Water increased from 15 Sv in the REF to about 24 Sv in the EDC. At the same time, the southward advection of the deep cell resides on shallower depths in the EDC (at 1500 - 2000 m) than in the REF (at 2000 - 3500 m), with the streamfunction contours also shoaling southwards in the deep cell circulation in the EDC simulation. The maximum northward advection of the AABW in the abyssal cell is 12 Sv (at about 30°S and 3500 m depth), with an average value of 8 Sv penetrating to 20°N in the EDC simulation. Comparatively, the maximum overturning of AABW in the REF simulation is only 6 Sv and restricted to south of 10°S.

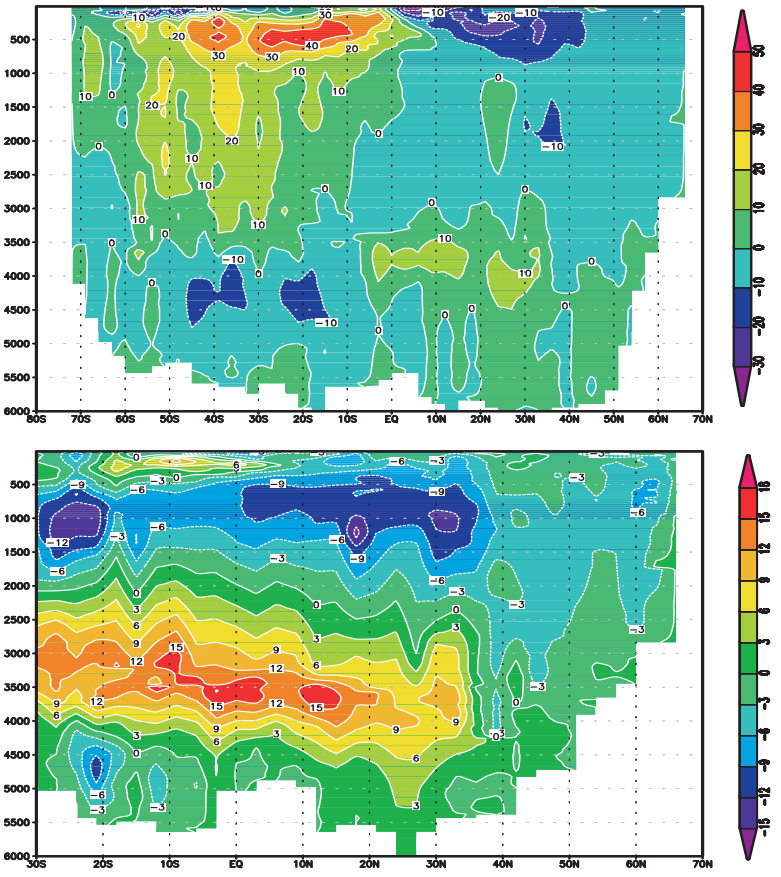

FIGURE 5.20: Difference plot of MOC for (top) Global and (bottom) Atlantic Ocean basins between EDC and REF simulations (EDC - REF in Sv). Model has been integrated over a period of 120 years.

The SAMW-related tracer upwelling budget in three ocean basins in the EDC simulation is shown in Table 5.2. After 150 years of integration about 97.3% of the total subducted tracer has returned to the surface. As a result of the enhanced thermohaline circulation, tracer re-emergence in the Northern Hemisphere ($> 20°N$) significantly increased from $0.007T_{\text{sub}}$ (REF) to $0.018T_{\text{sub}}$ (EDC), while the SAMW upwelling in the North Atlantic increased from $0.005T_{\text{sub}}$ (REF) to $0.013T_{\text{sub}}$ (EDC). In contrast, tracer upwelling in the equatorial regions reduced from $0.15T_{\text{sub}}$ (REF) to $0.09T_{\text{sub}}$ (EDC), as the equatorial Pacific upwelling reduced almost 50% in the EDC simulation. The magnitude of tracer upwelling decreased in almost every region of the Indian Ocean, mainly as a result of the shifted tracer release region (there is less tracer released in the Indian Ocean in the EDC than in the REF because of the modified mixed layer depth).

TABLE 5.2: Tracer re-emergence in different ocean basins after 150 years of integration in the EDC simulation. All values are normalized against the total subducted tracer after tracer release in the SAMW formation region (unit T_{sub}).

	N. of $30°S$	S. of $30°S$	Equatorial	N. of $20°N$
Global	0.230	0.743	0.091	0.018
Atlantic	0.039	0.133	0.019	0.013
Pacific	0.119	0.412	0.052	0.005
Indian	0.072	0.198	0.020	

Significantly different fractional contributions from the upwelling mechanisms exist between the REF and the twin perturbation experiment, if we focus on the North Atlantic Ocean (Table. 5.3). With increased diffusivity coefficients, the tracer upwelling fraction driven by diapycnal mixing ($Q_{\text{shr}}+Q_{\text{bck}}$) increased from 27% (REF) to 35% (EDT). However, this value dropped to about 19% in the EDC simulation in which the enhanced diffusion coefficients also affected hydrodynamics. The induction-driven tracer upwelling fraction reduced from its maximum value of 24% (REF) to 17% (EDT), and finally to 14% in the EDC simulation. Simply changing the diffusion coefficients for the tracer alone did not affect the entrainment, however, the Q_{ent} contribution increased to over 55% in the EDC simulation.

TABLE 5.3: Summary of fractional contributions of different upwelling mechanisms for tracer re-emergences in the North Atlantic Ocean. The model has been integrated over a period of 150 years after tracer release.

	Q_{shr}	Q_{bck}	Q_{ind}	Q_{ent}
REF	3%	24%	24%	36%
EDT	29%	6%	17%	36%
EDC	16%	3%	14%	55%

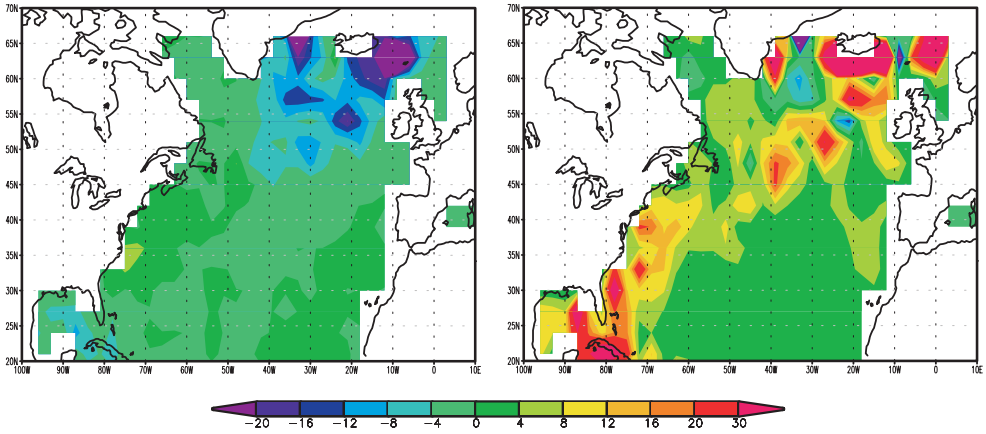

FIGURE 5.21: Difference in total tracer upwelling (Q_{t}) [*tracer unit* m^{-2}] between the twin experiments and the control run in the North Atlantic Ocean: (left) EDT-REF and (right) EDC-REF after 150 years of integration.

This enhanced diffusivity profile was employed in the EDT simulation but only for the tracer mixing. Therefore, comparing with the REF, no changes have been introduced for the lateral tracer circulation following the Gulf Stream underneath the thermocline. Even though the diapycnal diffusion coefficients increased from 10^{-5} to O(10^{-4}) $m^2\ s^{-1}$ along the Gulf Stream region, no significant enhancement of the tracer upwelling in this region can be observed in the EDT simulation (Fig. 5.21). Extra upwelling along the Gulf Stream and in the subpolar gyre of the North Atlantic Ocean appears in the EDC simulation because the enhanced AMOC transports more SAMW to the North Atlantic Ocean. Despite the fact that diapycnal diffusivity coefficients also increased 10 times in the EDC compared to the REF simulation, Fig. 5.22 shows that this extra tracer upwelling in the EDC simulation is mainly due to the entrainment instead of the diapycnal mixing, especially for the regions along the WBC and in the high latitude of the North Atlantic Ocean. In contrast, the fractional

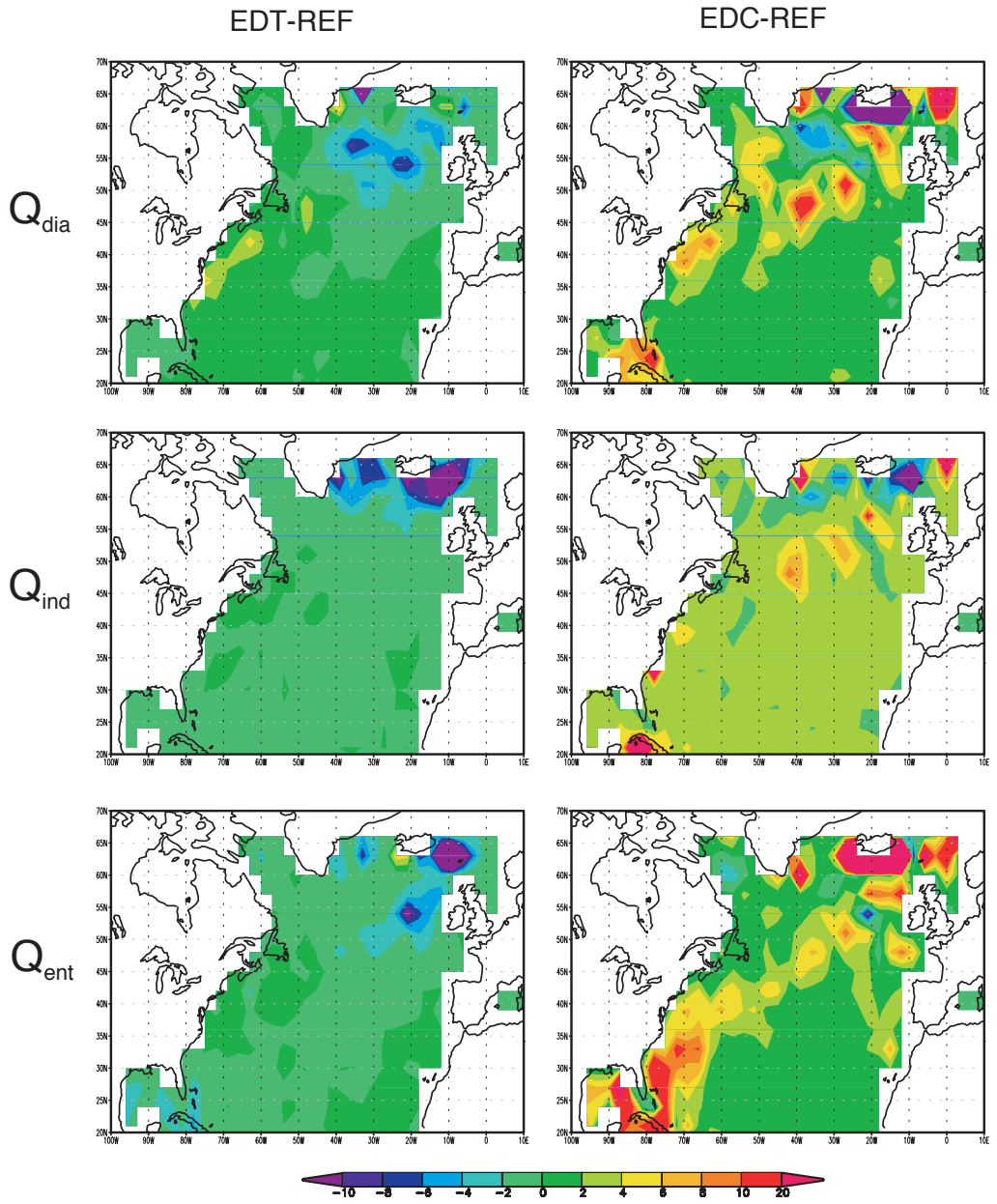

FIGURE 5.22: Difference in tracer upwelling fluxes in the North Atlantic Ocean: (top row) diapycnal mixing driven upwelling, (middle row) upwelling due to induction, (bottom row) upwelling due to entrainment; (left column) EDT - REF, (right column) EDC - REF.

contribution from the diapycnal mixing decreased from 27% in REF to 19% in EDC (Q_{shr}+Q_{bck} in Table 5.3).

The new hydrodynamic conditions, including the mixed layer thickness and the core depth of the SAMW circulating in the North Atlantic Ocean have been calculated and illustrated in Figs. 5.23 and 5.24, as an attempt to understand the changing fractional contributions to tracer upwelling from different mechanisms in the EDC simulation. Comparing to the results from REF (Fig. 4.19), end of winter (March) mixed layer in the EDC becomes slightly thinner along the Gulf Stream and in subpolar gyre region. At the same time, the core depth of the SAMW circulation sinks from 400 m in the REF to over 500 m in the EDC simulation. As a result, the winter outrcropping region recedes northwards in the EDC simulation and leads to reduced fractional contribution from induction in the high latitudes of the North Atlantic Ocean (Fig. 5.22). In addition, the increased vertical distance between the SAMW core and surface mixed layer base also makes it harder for the interior mixing-driven tracer fluxes to reach the surface, therefore causing a reduced contribution from diapycnal diffusion-induced tracer upwelling.

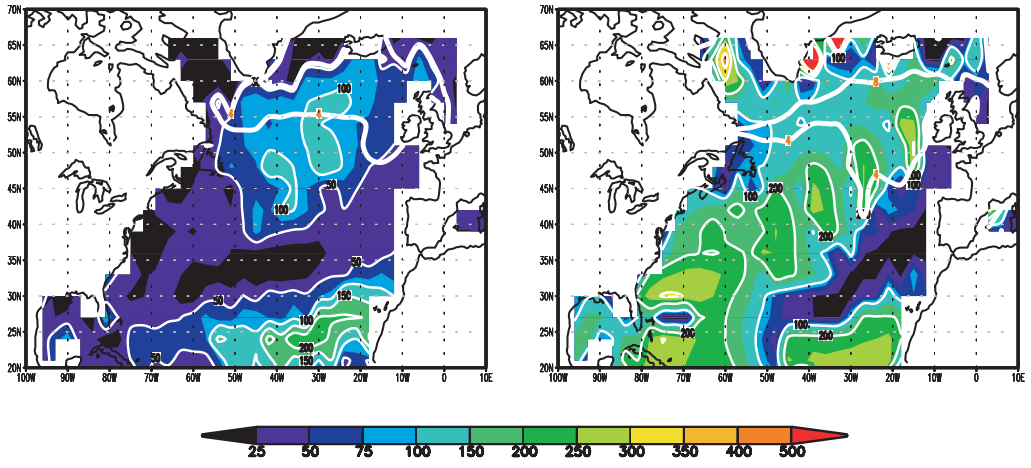

FIGURE 5.23: Mixed layer thickness [m] in (left) September and (right) March for the EDC simulation in the North Atlantic Ocean, after model reached a quasi-equilibrium state. The thick white lines denote the outcrops of lightest (layer 4) and core (layer 8) density layers of the SAMW.

By comparing the results from EDC and REF experiments, the conclusion can be drawn that although an enhanced diapycnal diffusion profile does increase the SAMW upwelling in the North Atlantic Ocean, it is mainly due to the hydrodynamic process that advects more tracer from the Southern Hemisphere

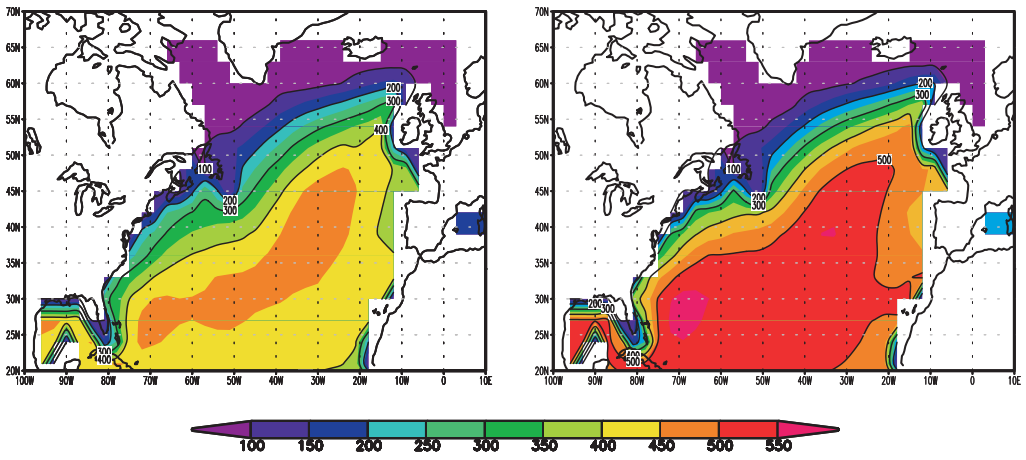

FIGURE 5.24: Long-term averaged depths [m] for the core density level (layer 8 with $\sigma_2 = 35.80$) that SAMW resides in the North Atlantic Ocean: (left) in the REF simulation and (right) in the EDC simulation. Contour intervals 100 m.

into the Gulf Stream NAC system instead of the small-scale turbulent process that brings up more tracer to the surface. Modified mixed layer depth (Fig. 5.23) and stratification conditions (Fig. 5.24) along the Gulf Stream in the EDC simulation slow down the diapycnal tracer upwelling flux and partly cancel the effect of increased import of SAMW from the Southern Ocean. As a result the fractional contribution of diapycnal mixing-induced upwelling actually decreased in the EDC simulation. Increasing diapycnal diffusion coefficients also leads to a enhancement of the northward upper branch of the MOC in the North Atlantic Ocean (Fig. 5.20), as well as the upper-ocean heat flux. This results in an increased surface temperature in the subtropical gyre of the North Atlantic and reduces the surface cooling effect during boreal winter along the Gulf Stream. As a result, this increases the density difference between the surface boundary layer and the SAMW core.

In both REF and our perturbation experiments, the Gulf Stream serves as a conduit of SAMW tracer (nutrient) from the Southern Ocean to the mixed layers of both the subpolar and subtropical North Atlantic, a concept that has been referred to as a "Nutrient Stream" by Pelegrí and Csanady (1991). However, the sources of nutrients and the mechanisms that sustain the relatively high nutrient concentrations and primary production in the surface and upper thermocline isopycnals within the Gulf Stream are a matter of debate with two dominant hypotheses proposed. Pelegrí and Csanady (1991), based

on the spatial coincidence of the Gulf Stream's enriched nutrients with low-gradient Richardson numbers and strong velocity shear, suggested that it is the strong diapycnal mixing along the length of the current that augments the Gulf Stream's nutrient concentrations on the lighter density surfaces. A conceptual model of gyre-scale nutrient cycling called the "Nutrient Spiral Theory" was then proposed by Jenkins and Doney (2003), in which they claimed that the persistent sustainment of the nutrient supply to the subtropical gyre is a result of entrainment, enhanced diapycnal mixing and recharge by remineralization, and the sources for this nutrient-enriched water in the Gulf Stream comes from the recirculation of the subtropical gyre in the North Atlantic.

An alternative hypothesis, proposed by Williams et al. (2006) based on an idealized nutrient-like tracer experiment in a GCM, suggested that the elevated nutrient concentrations of the Gulf Stream are caused by the along-isopycnal advection of high-nutrient waters from the tropical and South Atlantic, *e.g.*, the nutrient-rich SAMW. This result is consistent with the inference from temperature and salinity data that over 40% of the transport through the Strait of Florida has its origin in the Southern Hemisphere (Schmitz and McCartney, 1993). Based on a historical hydrographic data set, Palter and Lozier (2008) also suggested that the imported Southern Hemisphere waters are the primary source of the elevated nutrient concentrations along the Gulf Stream.

If only the SAMW carried nutrients are concerned, then part of the above two hypotheses can be tested with the help of our twin perturbation experiments. Comparing with the REF, tracer upwelling patterns in the EDT simulation (Fig. 5.21) show that even with the vertical diffusivity coefficient of about O(10^{-4}) $m^2 s^{-1}$ along the WBC, there is no significant enhancement of the SAMW/nutrients upwelling along the Gulf Stream, nor did it cause any tracer cycle following the recirculation of the subtropical gyres. Instead, almost all SAMW-related tracer still follows the NAC and is transported to the northern flank of the subtropical gyre and into the subpolar gyre. In the EDC simulation the new diffusivity profile was applied to all hydrodynamic variables and the model reached a new quasi-equalibrium state with an enhanced AMOC. Tracer advection following the recirculation of the subtropical gyre underneath the thermocline occurs in this experiment (not shown here). However, this recirculated tracer all re-emerged to the surface in the eastern boundary upwelling region before reaching the Gulf Stream again. Increased tracer concentration

in the light isopycnals and upwelling to the surface along the stream can be observed in the EDC experiment, but this is because the enhanced AMOC transports more SAMW/tracer to the tropics and source regions of the Gulf Stream. This, in addition, suggests that the relatively high nutrient concentrations in the Gulf Stream are primarily imported from the south. Although our model did not resolve the fallout and remineralization processes following the recirculation in the subtropical gyre, our results suggest that the diapycnal flux term alone is unlikely to be large enough to alter the nutrient concentrations during the WBC's rapid transit from the Straits of Florida to Cape Hatteras, and therefore is unlikely to be critical in bringing up nutrients into the surface boundary layer from this nutrient conduit. It is the imported Southern Ocean SAMW that is more likely to control the nutrient supply to the thermocline in the North Atlantic Ocean, as suggested by Sarmiento et al. (2004); Williams et al. (2006) and Palter and Lozier (2008).

Chapter 6

Conclusion

The main purpose of the this study is to investigate the circulation and re-emergence of SAMW, which is thought to be important in providing the source of nutrients to drive biological production over large proportions of the worlds oceans, following subduction in the Southern Ocean (Sarmiento et al., 2004). Even though the formation and circulation of SAMW in the Southern Hemisphere have previously been investigated by means of OGCMs (Ribbe and Tomczak, 1997; Sloyan and Kamenkovich, 2007; Sen Gupta and England, 2007), the geography and mechanisms of SAMW upwelling have never been fully resolved before, as either a off-line tracer method or a simplified vertical/lateral mixing scheme is always implemented in the previous climate-scale ocean models.

In this study, a HYbrid isopycnic-cartesian Coordinate Ocean general circulation Model (HYCOM, Bleck (2002)) with an advanced vertical mixing scheme (KPP, Large et al. (1994)) is adapted and configured to simulate the global ocean circulation for timescales of up to centuries. The isopycnic nature of the modelled ocean interior is ideally suited to investigating SAMW formation, subduction, spreading pathways, transit times, upwelling sites and driving mechanisms, as well as their sensitivity to perturbations in mixing parameters (see Table 6.1 for an intercomparison between HYCOM and previous OGCMs used in SAMW investigations). For this purpose, the formation of the SAMW in our model is carefully examined on the basis of a wintertime MLD criterion (Aoki et al., 2007; Dong et al., 2008) and a conservative tracer is released in the SAMW formation regions as a one-off event after a spin-up of 120 years. After release, tracer is subducted into the ocean interior and a surface consumption

scheme is implemented to mimic the the biological removal of nutrients at the surface euphotic zone. Both the formation regions of SAMW and its circulation pathways in our simulation are validated against previous OGCMs (Ribbe and Tomczak, 1997; Sen Gupta and England, 2007; Sloyan and Kamenkovich, 2007) and hydrographic data-based inverse models (Sloyan and Rintoul, 2000, 2001a,b). The circulation pattern of SAMW in our tracer experiment also shows a good degree of consistency with the oxygen distributions along the equatorial ocean and in the subtropical gyres, as derived by Karstensen et al. (2008), and is broadly consistent with the SAMW upwelling pattern in the Northern Hemisphere described by Sarmiento et al. (2004).

TABLE 6.1: Critical model settings of HYCOM and previous tracer experiments with respect to SAMW simulation.

	FRAM in Ribbe and Tomczak (1997)	OGCM in Sen Gupta and England (2007)	HYCOM
methodology	offline model	offline model	fully prognostic model
coordinate	z-level	z-level	hybrid coordinate system
mixing scheme	constant vertical diffusion coefficient	Pacanowski and Philander (1981)	KPP scheme
tracer release	around the Antarctic Polar Front	in discrete regions bounded by the density surface outcrops and the $30°S$ latitude line	in the SAMW formation region defined by mixed layer depth
tracer type	conservative tracer	conservative tracer	conservative tracer with surface consumption scheme

After following the SAMW circulation in the ocean interior, upwelling regions in which SAMW is returned to the upper-ocean mixed layer are identified across global ocean. As well as the familiar upwelling regions (*e.g.*, eastern boundary upwelling regions and the subpolar gyre and high-latitudes of the North Atlantic) pointed out in other studies (Sarmiento et al., 2004; Williams et al., 2006), significant tracer re-emergence has also been identified following the subtropical gyre of the Indian Ocean and in the equatorial Pacific (accounting for over 10% of the total subducted SAMW). Among all major ocean basins, the Pacific Ocean plays the most important role in SAMW re-emergence ($\sim$ 55%

of the total subducted SAMW). For tracer release as a one-off event in the formation region of SAMW in the Southern Ocean, a time scale of the order of O(100) years is required for the re-emergence of SAMW in the northern Atlantic Ocean.

A diagnostic scheme has been developed for interpreting tracer upwelling fluxes in terms of physical and numerical driving mechanisms to facilitate understanding the processes that control the upwelling of SAMW (and the thermocline waters) that sustains the nutrient supply to the upper ocean mixed layer. The total tracer upwelling flux has been decomposed into seven terms: **induction** due to lateral transport along outcropping isopycnal layers; **diapycnal mixing** due to double diffusion, shear instability and background internal wave breaking; **entrainment** due to the deepening of the mixed layer driven by surface buoyancy loss and/or enhanced wind stirring; **regridding mixing** driven by the Ekman pumping effect (wind-induced divergent volume flux in the mixed layer) and regridding mixing driven by the surface buoyancy flux as well as diapycnal flux across the base of the mixed layer.

In addition, an integration method under the leapfrog scheme has been developed to overcome the computational instabilities due to the strong nonlinearity effect induced by our surface consumption scheme, and has been applied for the tracer integration for a period of 150 years. The budget analysis of tracer re-emergences show that the important mechanisms responsible for SAMW upwelling to the north of $30°S$ are, in the sequence of their fractional contributions: (1) the entrainment from underneath the mixed layer (accounting for 33% of the total upwelling); (2) regridding mixing driven by Ekman pumping (19%); and (3) shear-induced mixing (18%). However, the fractional contributions from different driving mechanisms vary widely with different ocean regions, *e.g.* the contribution of induction increases to over 40% when considering the SAMW upwelling in the high latitudes of North Atlantic, Ekman upwelling dominates the equatorial Pacific (47%) and the shear-induced turbulent mixing dominates the equatorial Atlantic (54%).

In order to examine the two hypotheses as proposed by Jenkins and Doney (2003) and Williams et al. (2006) for explaining the maintenance of relatively high nutrient concentrations in the Gulf Stream and the nutrient supply into the subtropical and subpolar North Atlantic, a set of twin experiments with

enhanced diapycnal diffusion coefficients in the model have been setup. Intercomparison between the twin experiments shows that no significant enhancement of tracer upwelling occurs along the Gulf Stream even with enhanced diapycnal diffusion coefficients, suggesting that the diapycnal mixing alone is unlikely to play a central role in bringing up nutrients into the surface boundary layer from this "Nutrient Stream" (Pelegrí and Csanady, 1991). Instead, the relatively high nutrients concentration in the Gulf Stream are likely to originate from the Southern Ocean through isopycnal transport of the SAMW. This imported SAMW does not follow the recirculation in the subtropical gyre, but flows with the NAC along the northern flank of the subtropical gyre and into the subpolar gyre.

Based on our tracer experiment and inspired by both the "Nutrient Spiral" theory (Jenkins and Doney, 2003) and the nutrient circulation model proposed by Williams et al. (2006), a three-dimensional nutrient circulation and upwelling model for the North Atlantic Ocean in association with the nutrient imported from the Southern Ocean is postulated, which can be understood as a sequence of processes following the seasonal cycle of the thermocline. In this model, nutrient upwelling into the mixed layer is mainly driven by entrainment due to buoyancy loss during boreal autumn, and induction due to outcropping into the GS extension during boreal winter in the subpolar gyre and high-latitude North Atlantic. Recharging of nutrients in the underlying seasonal thermocline is achieved by imported SAMW via the GS and isopycnal advection of nutrients following the subpolar and the subtropical gyres during boreal summer (Fig. 4.21). Comparing with Williams et al. (2006)'s model, additional elements (entrainment and diapycnal mixing) are added and the importance of thermocline seasonal cycle is addressed with respect to the SAMW upwelling.

The results of our twin perturbation experiments confirm the importance of lateral advection in supplying nutrients into the subpolar gyre and high latitudes North Atlantic (Williams et al., 2006; Palter and Lozier, 2008), and present a direct connection between the sources of the "Nutrient Stream" and the northward transport of the SAMW. Sustainment of the high primary production in the surface euphotic zone in the subpolar gyre and high-latitude North Atlantic is found not to be dominated by any single upwelling mechanism but due to a set sequence of events associated with both surface buoyancy loss and wind forcing, as well as the isopycnal transport of nutrient and diapycnal

turbulent mixing towards the mixed layer. The relative importance of each mechanism is diagnosed quantitatively and emphasis was given to entrainment due to deepening of the mixed layer depth, induction due to isopycnal advection and shear-induced diapycnal mixing.

The circulation of SAMW in the Northern Hemisphere was investigated by Sarmiento et al. (2004) and the exception of North Pacific Ocean from the dominance of SAMW is suggested to be related to the influence of NPIW. However, here we show that the confined penetration distance of SAMW to the North Pacific is associated with the relative lighter density levels that the SAMW core resides at in the Pacific Ocean, and the hydrodynamic conditions of the Equatorial Under Current (EUC) and Kuroshio Current (KC) there. Our tracer experiment shows that the SAMW advects in the Atlantic Ocean residing at relatively denser density surfaces after crossing the Drake Passage. Instead, in the Pacific Ocean the relatively deeper and denser EUC (compared to the Atlantic EUC) deflects most of the Pacific SAMW eastward once it reaches the equator, and little is captured by the Kuroshio Current as this WBC system barely reaches the core density levels of the SAMW in the North Pacific Ocean. The nutrient barrier between $10^\circ - 20^\circ N$ in the North Pacific is associated with the steep isopycnal Potential Vorticity (PV) gradient along the KC.

In addition, the ITF is found to be important in association with the inter-basin circulation of SAMW. Reduced ITF transports can alter the SAMW circulation in the Southern Pacific Ocean and lead to enhancement of nutrient supply into the Atlantic Ocean due to the slow down of the overturning circulation in the upper 1000 m of the South Pacific. The above results imply that both the strong current systems (*e.g.*, EUC and WBC) and the critical channels in the world ocean (*e.g.*, the Indonesian Channel and Drake Passage) play important roles in determining the SAMW circulation in the global thermocline.

In order to resolve the upwelling processes of the thermocline waters into the mixed layer in a numerical model, a vertical mixing scheme that can be applied seamlessly from the surface boundary layer to the ocean interior must be implemented. Diagnosis of the surface active mixing layer depth must be treated carefully as it is not only important in determining the range of the convection process, but is also critical in calculating the entrainment flux driven by the atmospheric forcing. Numerical mixing due to horizontal advection in a z-level model or regridding mixing in a hybrid model can be important in

some ocean regions and the reliability of model results are subject to the relative importance of this numerical/spurious term with respect to other physical mechanisms.

Future Work

One key disadvantage of the model that may affect the simulation of SAMW re-emergence to the surface mixed layer is the lack of eddy-resolving ability due to the coarse resolution of the model ($3^\circ \times 3^\circ$), as both the mesoscale eddy and sub-mesoscale processes can be important in determining the vertical velocity structure and the subsequent vertical exchange of nutrients (Jenkins, 1988; McGillicuddy and Robinson, 1997; McGillicuddy et al., 1998; Oschlies and Garcon, 1998; Lévy, 2001, 2008; Lapeyre and Klein, 2006). Eddy-induced lateral stirring along isopycnal may be as important as the vertical pumping effect with respect to the nutrient supply (Oschlies, 2002). In addition, baroclinic instability of the turbulent eddies can lead to an increase in the stratification and hence a reduction in the thickness of the mixed layer (Nurser and Zhang, 2000), which eventually alters the surface heat flux into the ocean. Danabasoglu et al. (2008) show significant improvement of the model results when an eddy flux parameterization scheme is implemented into the surface boundary layer. Further analysis about the eddy/wind interaction and its impact on the nutrient supply to the mixed layer has been discussed by Martin and Richards (2001); McGillicuddy et al. (2007) and investigated by model simulation (Eden and Dietze, 2009).

A significantly different nutrient budget and the annual new production on a basin scale might emerge when the model resolution increases. Take as an example, the main sources of nitrate at the Bermuda Atlantic Time-series Study (BATS) site as diagnosed by Fasham et al. (1993) in a coarse resolution model (2°) were horizontal advection and the winter convection. However, McGillicuddy et al. (2003), using an eddy-resolving model ($\frac{1}{10}^\circ$), show that the main sources of nitrate at the same site are the vertical advection due to the mesoscale eddies and the winter convection. As a result, revisiting a tracer experiment of the kind considered here in a eddy-resolving version of a hybrid coordinate model (on a basin scale), and comparing the result with the benchmark left by this study are necessary for us to assess the relative importance of eddy-induced upwelling in association with the nutrient supply

from the SAMW. In addition, high-resolution runs with properly resolved Agulhas leakage may have important influence on the tracer advection into the Atlantic Ocean via the "warm route" of the global thermohaline circulation and therefore, alter the tracer circulation and upwelling patter in the North Atlantic.

Appendix A

Target densities for HYCOM layers

layer number	potential density (σ_2)
layer 1	30.90
layer 2	31.87
layer 3	32.75
layer 4	33.54
layer 5	34.24
layer 6	34.85
layer 7	35.37
layer 8	35.80
layer 9	36.15
layer 10	36.43
layer 11	36.65
layer 12	36.81
layer 13	36.96
layer 14	37.07
layer 15	37.16
layer 16	37.23

Bibliography

Allen, C. B., Kanda, J., Laws, E. A., Jun. 1996. New production and photosynthetic rates within and outside a cyclonic mesoscale eddy in the North Pacific subtropical gyre. Deep-Sea Research Part I-Oceanographic Research Papers 43 (6), 917–936.

Aoki, S., Hariyama, M., Mitsudera, H., Sasaki, H., Sasai, Y., 2007. Formation regions of Subantarctic Mode Water detected by OFES and Argo profiling floats. Geophysical Research Letters 34.

Asselin, R. A., 1972. Frequency filter for time integration. Mon. Wea. Rev., 187–490.

Barth, J. A., Hebert, D., Dale, A. C., Ullman, D. S., MAR 2004. Direct observations of along-isopycnal upwelling and diapycnal velocity at a shelfbreak front. Journal of Physical Oceanography 34 (3), 543–565.

Behrenfeld, M. J., Falkowski, P. G., Jan. 1997. Photosynthetic rates derived from satellite-based chlorophyll concentration. Limnology and Oceanography 42 (1), 1–20.

Bleck, R., 2002. An oceanic general circulation model framed in hybrid isopycnic-Cartesian coordinates. Ocean Modelling 37, 55–88.

Bleck, R., Benjamin, S. G., JUN 1993. Regional weather prediction with a model combining terrain-following and isentropic coordinates, Part 1: Model description. Monthly Weather Review 121 (6), 1770–1785.

Bleck, R., Halliwell, G. R., Wallcraft, A. J., Carroll, S., Kelly, K., Rushing, K., 2002. Hybrid coordinate ocean model (HYCOM) user's manual: details of the numerical code.

Bleck, R., Rooth, C., Hu, D., Smith, L. T., 1992. Salinity-driven thermocline transients in a wind- and thermohaline forced isopycnic coordinate model of the North Atlantic. JPO 22, 1486:1505.

Bleck, R., Smith, L. T., MAR 15 1990. A wind-driven Isopycnic Coordinate Model of the North and Equatorial Atlantic Ocean 1. Model development and supporting experiments. Journal of Geophysical Research 95 (C3), 3273–3285.

Bryan, F., JUL 1987. On the parameter sensitivity of primitive equation ocean general circulation models. Journal of Physical Oceanography 17 (7), 970–985.

Bryan, K., 1969. Climate and the ocean circulation. iii: The ocean model. Monthly Weather Review 97, 806–827.

Bryden, H. L., Brady, E. C., 1985. diagnostic model of three-dimensional circulation in the upper equatorial Pacific Ocean. Journal of Physical Oceanography 5, 1255–1273.

Canuto, V. M., Howard, A., Cheng, Y., Dubovikov, M. S., 2001. Ocean turbulence. Part I: One-point closure model - Momentum and heat vertical diffusivities. Journal of Physical Oceanography 31 (6), 1413–1426.

Canuto, V. M., Howard, A., Cheng, Y., Dubovikov, M. S., 2002. Ocean turbulence. Part II: Vertical diffusivities of momentum, heat, salt, mass and passive scalars. JPO 32, 240–264.

Chassignet, E. P., 1996. A model comparison: numerical simulations of the North and Equatorial Atlantic oceanic circulation in depth and isopycnic coordinates. Journal of Physical Oceanography 26, 1849–1867.

Chassignet, E. P., Hurlburt, H. E., Smedstad, O. M., Halliwell, G. R., Hogan, P. J., Wallcraft, A. J., Baraille, R., Bleck, R., Mar. 2007. The HYCOM (HYbrid Coordinate Ocean Model) data assimilative system. Journal of Marine Systems 65 (1-4), 60–83.

Chassignet, E. P., Hurlburt, H. E., Smedstad, O. M., Halliwell, G. R., Hogan, P. J., Wallcraft, A. J., Bleck, R., 2006. Ocean prediction with the HYbrid Coordinate Ocean Model (HYCOM). In: An Integrated View of Oceanography: Ocean Weather Forecasting in the 21st Century. Kluwer Academic Publishers.

Chassignet, E. P., Smith, L. T., Halliwell, G. R., Bleck, R., Dec. 2003. North Atlantic Simulations with the Hybrid Coordinate Ocean Model (HYCOM): Impact of the vertical coordinate choice, reference pressure, and thermobaricity. Journal of Physical Oceanography 33 (12), 2504–2526.

Cox, M. D., 1984. A primitive equation, 3-dimensional model of the ocean. In: Ocean Technical Report No. 1. Tech. rep., Ocean Group, Geophysical Fluid Dynamic Laboratory, Princeton University, Princeton, NJ.

Czaja, A., Hausmann, U., 2009. Observations of entry and exit of Potential Vorticity at the sea surface. Journal of Physical Oceanography: In press.

Danabasoglu, G., Ferrari, R., McWilliams, J. C., Mar. 2008. Sensitivity of an ocean general circulation model to a parameterization of near-surface eddy fluxes. Journal of Climate 21 (6), 1192–1208.

Dong, S., Sprintall, J., Gille, S. T., Talley, L., JUN 13 2008. Southern Ocean mixed-layer depth from Argo float profiles. Journal of Geophysical Research-Oceans 113 (C6).

Drange, H., Bleck, R., Apr. 1997. Multidimensional forward-in-time and upstream-in-space-based differencing for fluids. Monthly Weather Review 125 (4), 616–630.

Eden, C., Dietze, H., MAY 30 2009. Effects of mesoscale eddy/wind interactions on biological new production and eddy kinetic energy. Journal of Geophysical Research-Oceans 114.

England, M. H., Godfrey, J. S., Hirst, A. C., Tomczak, M., Jul. 1993. The mechanism for Antarctic Intermediate Water renewal in a world ocean model. Journal of Physical Oceanography 23 (7), 1553–1560.

Fasham, M., Sarmiento, J. L., Slater, R. D., Ducklow, H. W., Williams, R., Jun. 1993. Ecosystem behavior at bermuda station "S" and ocean weather station "India": a general circulation model and observational analysis. Global Biogeochemical Cycles 7 (2), 379–415.

Firing, E., Wijffels, S., Hacker, P., SEP 15 1998. Equatorial subthermocline currents across the Pacific. Journal of Geophysical Research-Oceans 103 (C10), 21413–21423.

Ganachaud, A., JUL 2 2003. Large-scale mass transports, water mass formation, and diffusivities estimated from World Ocean Circulation Experiment (WOCE) hydrographic data. Journal of Geophysical Research-Oceans 108 (C7).

Ganachaud, A., Wunsch, C., 2000. Improved estimates of global ocean circulation, heat transport and mixing from hydrographic data. Nature 408, 453–457.

Garabato, A. C. N., Polzin, K. L., King, B. A., Heywood, K. J., Visbeck, M., Jan. 2004. Widespread intense turbulent mixing in the Southern Ocean. Science 303 (5655), 210–213.

Garcon, V. C., Oschlies, A., Doney, S. C., McGillicuddy, D., Waniek, J., 2001. The role of mesoscale variability on plankton dynamics in the North Atlantic. Deep-Sea Research Part Ii-Topical Studies In Oceanography 48 (10), 2199–2226.

Gill, A. E., 1982. Atmosphere-Ocean Dynamics. Academic Press, New York.

Glessmer, M. S., Oschlies, A., Yool, A., AUG 16 2008. Simulated impact of double-diffusive mixing on physical and biogeochemical upper ocean properties. Journal of Geophysical Research-Oceans 113 (C8).

Godfrey, J. S., 1996. The effects of the Indonesian throughflow on ocean circulation and heat exchange with the atmosphere: A review. Journal of Geophysical Research 101 (12), 217–237.

Gordon, A. L., 1986. Interocean exchange of thermocline water. Journal of Geophysical Research 91, 5037–5046.

Gordon, A. L., 2001. Interocean Exchange, in Ocean Circulation and Climate. Academic Press, San Diego, Calif, Ch. 4.7, pp. 303–316.

Gorgues, T., Menkes, C., Aumont, O., Dandonneau, Y., Madec, G., Rodgers, K., MAR 13 2007. Indonesian throughflow control of the eastern equatorial Pacific biogeochemistry. Geophysical Research Letters 34 (5).

Gregg, M. C., MAY 15 1987. Diapycnal mixing in the thermocline: A review. Journal of Geophysical Research-Oceans 92 (C5), 5249–5286.

Gregg, M. C., 1998. Estimation and geography of diapycnal mixing in the stratified ocean. Coastal and Estuarine Studies 54, 305–338.

Griffies, S. M., Pacanowski, R. C., Hallberg, R. W., Mar. 2000. Spurious diapycnal mixing associated with advection in a z-coordinate ocean model. Monthly Weather Review 128 (3), 538–564.

Haidvogel, D. B., Wilkin, J. L., Young, R., May 1991. A semi-spectral primitive equation ocean circulation model using vertical sigma and orthogonal curvilinear coordinates. Journal of Computational Physics 94 (1), 151–185.

Halliwell, G., 2004. Evaluation of vertical coordinate and vertical mixing algorithms in the HYbrid-Coordinate Ocean Model (HYCOM). Ocean Modelling 7 (3-4), 285–322.

Halliwell, G. R., 1998. Simulation of North Atlantic decadal/multi-decadal winter SST anomalies driven by basin-scale atmospheric circulation anomalies. Journal of Physical Oceanography 28, 5–21.

Halpern, D., Knox, R. A., Luther, D. S., Philander, S. G. H., 1989. Estimates of equatorial upwelling between 140 and 110 W during 1984. Journal of Geophysical Research 94, 8018–8020.

Hanawa, K., Talley, L. D., 2001. Mode waters, in Ocean Circulation and Climate. Academic Press, San Diego, Calif, Ch. 5.4, pp. 373–386.

Haynes, P. H., McIntyre, M. E., 1987. On the evolution of vorticity and potential vorticity in the presence of diabatic heating and frictional or other forces. Journal of Atmospheric Science 44, 828–841.

Heywood, K. J., Garabato, A. C. N., Stevens, D. P., 2002. High mixing rates in the abyssal Southern Ocean. Nature 415, 1011–1014.

Hirst, A. C., Godfrey, J. S., JUN 1993. The role of Indonesian throughflow in a Global ocean GCM. Journal of Physical Oceanography 23 (6), 1057–1086.

Houghton, R. W., Visbeck, M., AUG 1 1998. Upwelling and convergence in the Middle Atlantic Bight shelfbreak front. Geophysical Research Letters 25 (15), 2765–2768.

Hutchings, L., Pitcher, G. G., Probyn, T. A., Bailey, G. W., 1995. The chemical and biological consequences of coastal upwelling. In: Upwelling in the ocean: modern processes and ancient records. John Wiley and Sons, New York.

Jenkins, W. J., MAY 25 1988. The use of anthropogenic tritium and HE-3 to study sub-tropical gyre ventilation and circulation. Philosophical Transactions of the Royal Society of London Series A-Mathematical Physical and Engineering Sciences 325 (1583), 43–61.

Jenkins, W. J., Doney, S. C., DEC 4 2003. The subtropical nutrient spiral. Global Biogeochemical Cycles 17 (4).

Johns, W., Lee, T., Zhang, D., Zantopp, R., Liu, C., Yang, Y., 2001. The Kuroshio east of Taiwan: Moored transport observations from the WOCE PCM-1 array. Journal of Physical Oceanography 31 (4), 1031–1053.

Johnson, G., McPhaden, M., Firing, E., 2001. Equatorial Pacific ocean horizontal velocity, divergence, and upwelling. Journal of Physical Oceanography 31 (3), 839–849.

Kara, A. B., J., W. A., Martin, P. J., Chassignet, E. P., 2008. Performance of mixed layer models in simulating SST in the equatorial Pacific Ocean. Journal of Geophysical Research 113.

Kara, A. B., Rochford, P. A., Hurlburt, H. E., Mar. 2003. Mixed layer depth variability over the global ocean. Journal of Geophysical Research-Oceans 108 (C3).

Karstensen, J., Quadfasel, D., NOV 2002. Formation of southern hemisphere thermocline waters: Water mass conversion and subduction. Journal of Physical Oceanography 32 (11), 3020–3038.

Karstensen, J., Stramma, L., Visbeck, M., JUN 2008. Oxygen minimum zones in the eastern tropical Atlantic and Pacific oceans. Progress In Oceanography 77 (4), 331–350.

Kraus, E. B., Turner, J. S., 1967. A one-dimensional model of the seasonal thermocline: II. The general theory and its consequences. Tellus 19, 98–106.

Kremeur, A. S., Levy, M., Aumont, O., Reverdin, G., JUL 17 2009. Impact of the subtropical mode water biogeochemical properties on primary production in the North Atlantic: New insights from an idealized model study. Journal of Geophysical Research-Oceans 114.

Kuhlbrodt, T., Griesel, A., Montoya, M., Levermann, A., Hofmann, M., Rahmstorf, S., 2007. On the driving processes of the Atlantic meridional overturning circulation. Reviews of Geophysics 45.

Lapeyre, G., Klein, P., Nov. 2006. Impact of the small-scale elongated filaments on the oceanic vertical pump. Journal of Marine Research 64 (6), 835–851.

Large, W., Gent, P., MAR 1999. Validation of vertical mixing in an equatorial ocean model using large eddy simulations and observations. Journal of Physical Oceanography 29 (3), 449–464.

Large, W. G., Mc Wiliams, J. C., Doney, S. C., November 1994. Oceanic vertical mixing: A review and a model with a nonlocal boundary layer parameterization. Reviews of Geophysics 32 (4), 363–403.

Ledwell, J. R., Montgomery, E. T., Polzin, K. L., St. Laurent, L. C., Schmitt, R. W., Toole, J. M., 2000. Evidence for enhanced mixing over rough topography in the abyssal ocean. Nature 403, 179–182.

Ledwell, J. R., Watson, A. J., Law, C. S., 1993. Evidence for slow mixing across the pycnocline from an open-ocean tracer-release experiment. Nature 364 (701–703).

Ledwell, J. R., Watson, A. J., Law, C. S., 1998. Mixing of a tracer in the pycnocline. Journal of Geophysical Research 103, 21499–21529.

Lee, T., Fukumori, I., Menemenlis, D., Xing, Z., Fu, L., MAY 2002. Effects of the Indonesian Throughflow on the Pacific and Indian oceans. Journal of Physical Oceanography 32 (5), 1404–1429.

Levitus, S., 1982. Climatological atlas of the world ocean. In: NOAA professional paper 13. Tech. rep., NOAA, Silver Spring, Md.

Levitus, S., 1998. World Ocean Database Vol. 1, Introduction. Tech. rep., NOAA NESDIS, Washington DC.

Lévy, M., 2001. Impacts of sub-mesoscale physics on phytoplankton production and subduction. Journal of Marine Research 59, 535–565.

Lévy, M., 2008. Lecture Notes in Physics. Vol. 744. Springer Berlin, Ch. The Modulation of Biological Production by Oceanic Mesoscale Turbulence, pp. 219–261.

Lien, R. C., Caldwell, D. R., Gregg, M. C., Moum, J. N., APR 15 1995. Turbulence variability at the equator in the central Pacific at the beginning of the 1991-1993 El-NINO. Journal of Geophysical Research-Oceans 100 (C4), 6881–6898.

Longhurst, A. R., Harrison, W. G., 1989. The biological pump: profiles of plankton production and consumption in the upper ocean. Progress In Oceanography 22, 47–123.

Lumpkin, R., Speer, K., 2007. Global ocean meridional overturning. Journal of Physical Oceanography 37, 2550–2562.

Luyten, J. R., Pedlosky, J., Stommel, H., 1983. The ventilated thermocline. Journal of Physical Oceanography 13 (2), 292–309.

Mahadevan, A., Archer, D., Jan. 2000. Modeling the impact of fronts and mesoscale circulation on the nutrient supply and biogeochemistry of the upper ocean. Journal of Geophysical Research-Oceans 105 (C1), 1209–1225.

Marotzke, J., AUG 1997. Boundary mixing and the dynamics of three-dimensional thermohaline circulations. Journal of Physical Oceanography 27 (8), 1713–1728.

Marra, J., 1978. Phytoplankton photosynthetic response to vertical movement in the mixed layer. Marine Biology 46, 203–208.

Marshall, J., Schott, F., Feb. 1999. Open-ocean convection: Observations, theory, and models. Reviews of Geophysics 37 (1), 1–64.

Marshall, J. C., 1984. Eddy-mean-flow interaction in a barotropic ocean model. Quarterly Journal of the Royal Meteorological Society 110 (465), 573–590.

Marshall, J. C., Nurser, A. G., Williams, R. G., JUL 1993. Inferring the Subduction rate and period over the North-Atlantic Ocean. Journal of Physical Oceanography 23 (7), 1315–1329.

Martin, A., Richards, K., 2001. Mechanisms for vertical nutrient transport within a North Atlantic mesoscale eddy. Deep-Sea Research Part Ii-Topical Studies In Oceanography 48 (4-5), 757–773.

Martin, A. P., 2003. Phytoplankton patchiness: the role of lateral stirring and mixing. Progress In Oceanography 57 (2), 125–174.

McCartney, M. S., 1977. Subantarctic Mode Water. In: A voyage of discovery, George Deacon 70th anniversary volume. Gergamon Press, Oxford.

McCartney, M. S., 1982. The subtropical circulation of Mode Waters. Journal of Marine Research 40, 427–464.

McCartney, M. S., Curry, R. A., Jun. 1993. Transequatorial flow of Antarctic Bottom Water in the Western Atlantic Ocean: abyssal geostrophy at the Equator. Journal of Physical Oceanography 23 (6), 1264–1276.

McDougall, T., Dewar, W., JUL 1998. Vertical mixing and cabbeling in layered models. Journal of Physical Oceanography 28 (7), 1458–1480.

McGillicuddy, D., Anderson, L., Doney, S., Maltrud, M., APR 11 2003. Eddy-driven sources and sinks of nutrients in the upper ocean: Results from a 0.1 degrees resolution model of the North Atlantic. Global Biogeochemical Cycles 17 (2).

McGillicuddy, D., Robinson, A., AUG 1997. Eddy-induced nutrient supply and new production in the Sargasso Sea. Deep-Sea Research Part I-Oceanographic Research Papers 44 (8), 1427–1450.

McGillicuddy, D., Robinson, A., Siegel, D., Jannasch, H., Johnson, R., Dickeys, T., McNeil, J., Michaels, A., Knap, A., JUL 16 1998. Influence of mesoscale eddies on new production in the Sargasso Sea. Nature 394 (6690), 263–266.

McGillicuddy, D. J., Johnson, R., Siegel, D. A., Michaels, A. F., Bates, N. R., Knap, A. H., Jun. 1999. Mesoscale variations of biogeochemical properties in the Sargasso Sea. Journal of Geophysical Research-Oceans 104 (C6), 13381–13394.

McGillicuddy, Dennis J., J., Anderson, L. A., Bates, N. R., Bibby, T., Buesseler, K. O., Carlson, C. A., Davis, C. S., Ewart, C., Falkowski, P. G., Goldthwait, S. A., Hansell, D. A., Jenkins, W. J., Johnson, R., Kosnyrev, V. K., Ledwell, J. R., Li, Q. P., Siegel, D. A., Steinberg, D. K., MAY 18 2007. Eddy/wind interactions stimulate extraordinary mid-ocean plankton blooms. Science 316 (5827), 1021–1026.

McWilliams, J. C., 1996. Modeling the oceanic general circulation. Annual Review of Fluid Mechanics 28, 215–248.

Mellor, G. L., Yamada, T., 1982. Development of a turbulence closure model for geophysical fluid problems. Reviews of Geophysics 20 (4), 851–875.

Michaels, A. F., Knap, A. H., Dow, R. L., Gundersen, K., Johnson, R. J., Sorensen, J., Close, A., Knauer, G. A., Lohrenz, S. E., Asper, V. A., Tuel, M., Bidigare, R., Jul. 1994. Seasonal patterns of ocean biogeochemistry at the U.S. JGOFS Bermuda Atlantic Time-series Study site. Deep-Sea Research Part I-Oceanographic Research Papers 41 (7), 1013–1038.

Mignot, J., Levermann, A., Griesel, A., APR 2006. A decomposition of the atlantic meridional overturning circulation into physical components using its sensitivity to vertical diffusivity. Journal of Physical Oceanography 36 (4), 636–650.

Montoya, M., Griesel, A., Levermann, A., Mignot, J., Hofmann, M., Ganopolski, A., Rahmstorf, S., Aug. 2005. The earth system model of intermediate complexity CLIMBER-3 alpha. Part 1: description and performance for present-day conditions. Climate Dynamics 25 (2-3), 237–263.

Munk, W. H., 1966. Abyssal recipes. Deep-Sea Research 13, 207–230.

Munk, W. H., Wunsch, C., DEC 1998. Abyssal recipes ii: energetics of tidal and wind mixing. Deep-Sea Research Part I-Oceanographic Research Papers 45 (12), 1977–2010.

New, A., Bleck, R., Jia, Y., Marsh, R., Huddleston, M., Barnard, S., 1995. An isopycnic model of the North Atlantic, part I: model experiments. Journal of Physical Oceanography 25, 2667–2699.

New, A. L., Alderson, S. G., Smeed, D. A., Stansfield, K. L., Jan. 2007. On the circulation of water masses across the Mascarene Plateau in the South Indian Ocean. Deep-Sea Research Part I-Oceanographic Research Papers 54 (1), 42–74.

Nurser, A., Zhang, J., Sep. 2000. Eddy-induced mixed layer shallowing and mixed layer/thermocline exchange. Journal of Geophysical Research-Oceans 105 (C9), 21851–21868.

Oberhuber, J. M., May 1993. Simulation of the Atlantic circulation with a coupled sea ice-mixed layer-isopycnal general circulation model. Part I: model description. Journal of Physical Oceanography 23 (5), 808–829.

Oka, E., Kawabe, M., 1998. Characteristics of variations of water properties and density structure around the Kuroshio in the East China Sea. Journal of Oceanography 54, 605–617.

Oschlies, A., 2001. Model-derived estimates of new production: New results point towards lower values. Deep-Sea Research Part Ii-Topical Studies In Oceanography 48 (10), 2173–2197.

Oschlies, A., May 2002. Nutrient supply to the surface waters of the North Atlantic: A model study. Journal of Geophysical Research-Oceans 107 (C5).

Oschlies, A., Dietze, H., Kahler, P., DEC 6 2003. Salt-finger driven enhancement of upper ocean nutrient supply. Geophysical Research Letters 30 (23).

Oschlies, A., Garcon, V., JUL 16 1998. Eddy-induced enhancement of primary production in a model of the north Atlantic Ocean. Nature 394 (6690), 266–269.

Pacanowski, R. C., Philander, S. G. H., 1981. Parameterization of vertical mixing in numerical models of tropical oceans. Journal of Physical Oceanography 11 (11), 1443–1451.

Paiva, A. M., Chassignet, E. P., Mariano, A. J., Aug. 2000. Numerical simulations of the North Atlantic subtropical gyre: sensitivity to boundary conditions. Dynamics of Atmospheres and Oceans 32 (3-4), 209–237.

Palmer, J., Totterdell, I., MAY 2001. Production and export in a global ocean ecosystem model. Deep-Sea Research Part I-Oceanographic Research Papers 48 (5), 1169–1198.

Palter, J. B., Lozier, M. S., JUN 20 2008. On the source of Gulf Stream nutrients. Journal of Geophysical Research-Oceans 113 (C6).

Pelegrí, J. L., Csanady, G. T., FEB 15 1991. Nutrient transport and mixing in the Gulf Stream. Journal of Geophysical Research-Oceans 96 (C2), 2577–2583.

Pelegrí, J. L., Csanady, G. T., SEP 15 1994. Diapycnal mixing in Western Boundary Currents. Journal of Geophysical Research-Oceans 99 (C9), 18275–18304.

Pelegrí, J. L., Csanady, G. T., Martins, A., 1996. The North Atlantic nutrient stream. Journal of Oceanography 52, 275–299.

Pelegrí, J. L., Marrero-Diaz, A., Ratsimandresy, A. W., 2006. Nutrient irrigation of the North Atlantic. Progress In Oceanography 70 (2-4), 366–406.

Peters, H., Gregg, M. C., SANFORD, T. B., APR 15 1994. The diurnal cycle of the upper equatorial ocean - turbulence, fine-scale shear, and mean shear. Journal of Geophysical Research-Oceans 99 (C4), 7707–7723.

Peters, H., Gregg, M. C., Sanford, T. B., SEP 15 1995. On the parameterization of equatorial turbulence - effect of fine-scale variations below the range of the diurnal cycle. Journal of Geophysical Research-Oceans 100 (C9), 18333–18348.

Peterson, R. G., Stramma, L., 1991. Upper-level circulation in the South-Atlantic Ocean. Progress In Oceanography 26 (1), 1–73.

Philander, S. G. H., 1990. EL NINO, LA NINA, and the Southern Oscilation. Academic Press, New York.

Piola, A. R., Georgi, D. T., 1982. Circumpolar properties of Antarctic Intermediate Water and Subantarctic Mode Water. Deep-Sea Research Part A-Oceanographic Research Papers 29 (6), 687–711.

Poulain, P. M., 1993. Estimates of horizontal divergence and vertical velocity in the equatorial Pacific. Journal of Physical Oceanography 23, 601–607.

Price, J. F., Weller, R. A., Pinkel, R., Jul. 1986. Diurnal cycling: observations and models of the upper ocean response to diurnal heating, cooling and wind mixing. Journal of Geophysical Research-Oceans 91 (C7), 8411–8427.

Quay, P. D., Stuiver, M., Broecker, W. S., 1983. Upwelling rates from the equatorial Pacific Ocean derived from the bomb C-14 distribution. Journal of Marine Research 41 (4), 769–792.

Reid, J. L., 1997. On the total geostrophic circulation of the Pacific Ocean: flow patterns, tracers, and transports. Progress In Oceanography 39 (4), 263–352.

Reid, J. L., 2003. On the total geostrophic circulation of the Indian Ocean: flow patterns, tracers, and transports. Progress In Oceanography 56, 137–186.

Ribbe, J., Tomczak, M., OCT 1997. On convection and the formation of Subantarctic Mode Water in the Fine Resolution Antarctic Model (FRAM). Journal of Marine Systems 13 (1-4), 137–154.

Rintoul, S. R., FEB 15 1991. South-Atlantic interbasin exchange. Journal of Geophysical Research-Oceans 96 (C2), 2675–2692.

Robbins, P. E., Toole, J. M., 1997. The dissolved silica budget as a constraint on the meridional overturning circulation of the Indian Ocean. Deep-Sea Research 32, 619–664.

Roberts, M. J., Marsh, R., New, A. L., Wood, R. A., Aug. 1996. An intercomparison of a Bryan-Cox-type ocean model and an isopycnic ocean model .1. The subpolar gyre and high-latitude processes. Journal of Physical Oceanography 26 (8), 1495–1527.

Robinson, A. R., 1966. An investigation into the wind as the cause of the equatorial undercurrent. Journal of Marine Research 24, 179–203.

Robinson, A. R., McGillicuddy, D., Calman, J., Ducklow, H. W., Fasham, M., Hoge, F. E., Leslie, W. G., McCarthy, J. J., Podewski, S., Porter, D. L., Saure, G., Yoder, J. A., 1993. mesoscale and upper ocean variabilities during the 1989 JGOFS bloom study. Deep-Sea Research Part Ii-Topical Studies In Oceanography 40 (1-2), 9–35.

Rodgers, K., Blanke, B., Madec, G., Aumont, O., Ciais, P., Dutay, J., JAN 29 2003. Extratropical sources of equatorial Pacific upwelling in an OGCM. Geophysical Research Letters 30 (2).

Rodgers, K., Cane, M. A., Naik, N. H., Schrag, D. P., SEP 15 1999. The role of the Indonesian Throughflow in equatorial Pacific thermocline ventilation. Journal of Geophysical Research-Oceans 104 (C9), 20551–20570.

Sarmiento, J. L., Gruber, N., Brzezinski, M. A., Dunne, J. P., 2004. High-latitude controls of thermocline nutrients and low latitude biological productivity. Nature 427, 56–60.

Sarmiento, J. L., Hughes, T. M. C., Stouffer, R. J., Manabe, S., May 1998. Simulated response of the ocean carbon cycle to anthropogenic climate warming. Nature 393 (6682), 245–249.

Sathyendranathan, S., Longhurst, A., Caverhill, C. M., Platt, T., 1995. Regionally and seasonally differentiated primary production in the North Atlantic. Deep-Sea Research 42, 1773–1802.

Schmitz, W. J., MAY 1995. On the interbasin-scale thermohaline circulation. Reviews of Geophysics 33 (2), 151–173.

Schmitz, W. J., McCartney, M. S., 1993. On the North Atlatnic circulation. Reviews of Geophysics 31, 29–49.

Scott, J. R., Marotzke, J., DEC 2002. The location of diapycnal mixing and the meridional overturning circulation. Journal of Physical Oceanography 32 (12), 3578–3595.

Sen Gupta, A., England, M. H., NOV 2007. Evaluation of interior circulation in a high-resolution global ocean model. Part II: Southern hemisphere intermediate, mode, and thermocline waters. Journal of Physical Oceanography 37 (11), 2612–2636.

Shaji, C., Wang, C., Halliwell, G. R., Wallcraft, A., 2005. Simulation of tropical pacific and Atlantic oceans using a hybrid coordinate ocean model. Ocean Modelling 9 (3), 253–282.

Sigman, D. M., Boyle, E. A., Oct. 2000. Glacial/interglacial variations in atmospheric carbon dioxide. Nature 407 (6806), 859–869.

Sloyan, B. M., Kamenkovich, I. V., OCT 15 2007. Simulation of Subantarctic Mode and Antarctic Intermediate Waters in climate models. Journal of Climate 20 (20), 5061–5080.

Sloyan, B. M., Rintoul, S. R., 2000. Estimates of area-averaged diapycnal fluxes from basin-scale budgets. Journal of Physical Oceanography 30, 2320–2341.

Sloyan, B. M., Rintoul, S. R., 2001a. Circulation, renewal and modification of Antarctic mode and intermediate water. Journal of Physical Oceanography 31, 1005–1030.

Sloyan, B. M., Rintoul, S. R., 2001b. The Southern Ocean limb of the global deep overturning circulation. Journal of Physical Oceanography 31, 143–172.

Smagorinsky, J. S., 1963. General circulation experiments with the primitive equations. I: The basic experiment. Monthly Weather Review 91, 99–164.

Smith, R. L., 1995. The physical processes of coastal ocean upwelling systems. In: Upwelling in the ocean: modern processes and ancient records. John Wiley and Sons, New York.

Speer, K. G., Zenk, W., Dec. 1993. The flow of Antarctic Bottom Water into the Brazil Basin. Journal of Physical Oceanography 23 (12), 2667–2682.

Speich, S., Blanke, B., de Vries, P., Drijfhout, S., Doos, K., Ganachaud, A., Marsh, R., MAY 15 2002. Tasman leakage: A new route in the global ocean conveyor belt. Geophysical Research Letters 29 (10).

Speich, S., Blanke, B., Madec, G., 2001. Warm and cold water paths of a GCM thermohaline conveyor belt. Geophysical Research Letters 28, 311–314.

Stramma, L., Peterson, R. G., JUN 1990. The Southern-Atlantic Current. Journal of Physical Oceanography 20 (6), 846–859.

Talley, L. D., 1996. Antarctic Intermediate Water in the South Atlantic. In: The south Atlantic: Present and Past Circulation. Springer-Verlag, Ch. 5.4, pp. 219–238.

Talley, L. D., 1997. North Pacific Intermediate Water transports in the mixed water region. Journal of Physical Oceanography 27, 1795–1803.

Talley, L. D., Reid, J. L., Robbins, P. E., Oct. 2003. Data-based meridional overturning streamfunctions for the global ocean. Journal of Climate 16 (19), 3213–3226.

Toggweiler, J. R., Dixon, K., Broecker, W. S., Nov. 1991. The Peru upwelling and the ventilation of the South-Pacific thermocline. Journal of Geophysical Research-Oceans 96 (C11), 20467–20497.

Tomczak, M., Godfrey, J. S., 2003. Regional oceanography: an introduction, 2nd Edition. Daya Publishing House, Delhi.

Toole, J. M., Polzin, K. L., Schmitt, R. W., MAY 20 1994. Estimates of diapycnal mixing in the abyssal ocean. Science 264 (5162), 1120–1123.

Weisberg, R. H., Qiao, L., JAN 2000. Equatorial upwelling in the Central Pacific estimated from moored velocity profilers. Journal of Physical Oceanography 30 (1), 105–124.

Willebrand, J., Barnier, B., Boning, C., Dieterich, C., Killworth, P., Le Provost, C., Jia, Y., Molines, J., New, A., 2001. Circulation characteristics in three eddy-permitting models of the North Atlantic. Progress In Oceanography 48 (2-3), 123–161.

Williams, R., Follows, M., FEB-MAR 1998. The Ekman transfer of nutrients and maintenance of new production over the North Atlantic. Deep-Sea Research Part I-Oceanographic Research Papers 45 (2-3), 461–489.

Williams, R., McLaren, A., Follows, M., DEC 2000. Estimating the convective supply of nitrate and implied variability in export production over the North Atlantic. Global Biogeochemical Cycles 14 (4), 1299–1313.

Williams, R., Roussenov, V., Follows, M., MAR 22 2006. Nutrient streams and their induction into the mixed layer. Global Biogeochemical Cycles 20 (1).

Williams, R. G., 2001. Ocean subduction. In: Encyclopedia of ocean sciences. Academic Press.

Williams, R. G., Follows, M. J., 2003. Physical transport of nutrients and the maintenance of biological production, in Ocean Biogeochemistry: A JGOFS synthesis. Springer, New York.

Winkel, D. P., Gregg, M. C., Sanford, T. B., NOV 2002. Patterns of shear and turbulence across the Florida Current. Journal of Physical Oceanography 32 (11), 3269–3285.

Winther, N. G., Evensen, G., 2006. A hybrid coordinate ocean model for shelf sea simulation. Ocean Modelling 13 (3-4), 221–237.

Wyrtki, K., 1971. Oceanographic atlas of the international Indian Ocean Expedition. National Science Foundation Publication, Washington, DC.

Wyrtki, K., 1973. An equatorial jet in the Indian Ocean. Science 181, 262–264.

Wyrtki, K., 1981. An estimate of equatorial upwelling in the Pacific. Journal of Physical Oceanography 11 (9), 1205–1214.

Wyrtki, K., Kilonsky, B., 1984. Mean water and current structures during the Hawaii-to-Tahiti Shuttle experiment. Journal of Physical Oceanography 14, 242–254.

Yasuda, I., Kouketsu, S., Katsumata, K., Ohiwa, M., 2002. Influence of Okhotsk Sea Intermediate Water on the Oyashio and North Pacific Intermediate Water. Journal of Geophysical Research 107.

You, Y. Z., Apr. 2002. Quantitative estimate of Antarctic Intermediate Water contributions from the Drake Passage and the southwest Indian Ocean to the South Atlantic. Journal of Geophysical Research-Oceans 107 (C4).

Zalesak, S., 1979. Fully multidimensional flux-corrected transport algorithms for fluids. Journal of Computational Physics 31 (335-362).

Zenk, W., 2001. Abyssal current. In: Encyclopedia of ocean sciences. Academic Press.

Zenk, W., Siedler, G., Ishida, A., Holfort, E., Kashino, Y., Kuroda, Y., Miyama, T., Muller, T., 2005. Pathways and variability of the Antarctic Intermediate Water in the western equatorial Pacific Ocean. Progress In Oceanography 67 (1-2), 245–281.

Zhang, D., Lee, T., Johns, W., Liu, C., Zantopp, R., 2001. The Kuroshio east of Taiwan: Modes of variability and relationship to interior ocean mesoscale eddies. Journal of Physical Oceanography 31 (4), 1054–1074.

Zhang, J., Schmitt, R., Huang, R., APR 1998. Sensitivity of the GFDL modular ocean model to parameterization of double-diffusive processes. Journal of Physical Oceanography 28 (4), 589–605.

Zhang, J. B., Schmidt, R. W., Huang, R. X., JUN 1999. The relative influence of diapycnal mixing and hydrologic forcing on the stability of the thermohaline circulation. Journal of Physical Oceanography 29 (6), 1096–1108.